

A STUDY OF CARBON DIOXIDE CATALYTIC ACTIVATION FOR ITS CONVERSION TO VALUE-ADDED PRODUCTS

A Thesis Submitted to the College of
Graduate and Postdoctoral Studies
in Partial Fulfilment of the Requirements for
the Degree of Doctor of Philosophy in the
Department of Chemical and Biological Engineering
University of Saskatchewan
Saskatoon, Saskatchewan

By

Jinglin Gao

© Copyright Jinglin Gao, August 2020. All right reserved.

PERMISSION TO USE

In presenting this thesis in partial fulfillment of the requirements for a Postgraduate degree from the University of Saskatchewan, I agree that the Libraries of this University may make it freely available for inspection. I further agree that permission for copying of this thesis/dissertation in any manner, in whole or in part, for scholarly purposes may be granted by professors who supervised my thesis/dissertation work or, in their absence, by the Head of the Department or the Dean of the College in which my thesis work was done. It is understood that any copying or publication or use of this thesis or parts thereof for financial gain shall not be allowed without my written permission. It is also understood that due recognition shall be given to me and to the University of Saskatchewan in any scholarly use which may be made of any material in my thesis.

Requests for permission to copy or to make other use of material in this thesis in whole or parts shall be addressed to:

Head of the Department of Chemical and Biological Engineering

University of Saskatchewan

Saskatoon, Saskatchewan

S7N 5A9, Canada

Or

Dean

College of Graduate and Postdoctoral Studies

University of Saskatchewan

116 Thorvaldson Building, 110 Science Place

Saskatoon, Saskatchewan

S7N 5C9, Canada

ABSTRACT

To mitigate carbon dioxide (CO_2) emission, carbon capture and utilization seems to make more sense than carbon storage. Catalytic conversion plays key roles in the efforts to make the conversion of CO_2 into commodity chemicals or products feasible not only technically but also economically. Due to its thermodynamic stability, CO_2 conversion needs energy input as well as the participation of second molecules or reactants, for example, CH_4 in CO_2 reforming to produce syngas, or H_2 in CO_2 hydrogenation for methanol synthesis. It has been found that CO_2 and the second molecules are activated on different catalytic sites on a catalyst surface. This work studies the catalytic reaction mechanism of CO_2 reforming of methane (CRM) and CO_2 hydrogenation, focusing on the contiguity of the CO_2 activation sites and the activation sites for the second molecules, i.e., the orientation, distribution, and interaction of the two kinds of catalytic sites.

In CRM reaction, the Ni monometallic and NiM_2 ($\text{M}_2=\text{Co}$, Mn , Cu , and Fe) bimetallic catalysts supported by MgO -spinel prepared by the co-precipitation method were studied. It was observed that M_2 affected metallic particle sizes and slightly affected the basicity of the catalysts. During the reaction, the initial TOF of CO_2 and CH_4 based on the number of metallic sites had a good correlation with the average metallic particle size. The deactivation behavior of the catalysts was explained by a pushing-pulling theory proposed in this study. A stable or suitable carbon-resistant catalyst should let the CO_2 species on the basic sites can fully oxidize the carbon species formed from CH_4 dissociation on the metallic sites. This study also revealed the incomplete dissociation of CH_4 on the metallic sites, which may be the reason leading to lower H_2/CO instead of reverse water-gas shift reaction.

In CO_2 hydrogenation reaction to synthesize methanol, the ZnO over-coated Cu/SiO_2 catalysts prepared by the combination of strong electronic absorption (SEA) and the atomic layer deposition

(ALD) to form catalysts with Cu nanoparticles surrounded by ZnO with different uniformity were studied. The catalyst activity was correlated with the number of metallic sites. The catalyst containing 5 wt% Cu over-coated with a single atomic layer of ZnO exhibited higher methanol selectivity. This catalyst has comparatively more metallic sites (Cu particles with uniform distribution) and basic sites (with uniform ZnO layer) formation, and the good contiguity between them both with their physical location and chemical interaction, which provided necessary synergy for the CO₂ activation and hydrogenation to form methanol.

In conclusion, the mechanism of CO₂ catalytic activation was analyzed based on the CRM and CO₂ hydrogenation reaction, especially on the aspect of contiguity of metallic sites and basic sites. For CO₂ utilization, (a) enough and strong basic sites should be created on the catalysts for CO₂ activation; (b) the properties of metallic sites can lead to different products formation (CO or coke formation in CRM, methanol or CO formation in CO₂ hydrogenation reaction); (c) good contiguity of basic and metallic sites on the catalysts is necessary for these reactions to allow the activation of the reactants on these two catalytic sites so that they can reach and react with each other, further improving the stability and activity of the catalyst. These conclusions can be instrumental in developing effective catalysts for CO₂ utilization in future.

ACKNOWLEDGEMENTS

I would like to express my sincere appreciation and gratitude to my supervisor, Professor Hui Wang, for his patience, guidance, support, and encouragement during the doctoral study. I am so incredibly grateful for his mentorship in both of my research and my life. I am also sincerely grateful to my co-supervisor, Professor Ajay Kumar Dalai, for his thoughtful suggestions and invaluable support during the research and writing of the thesis. It is an honor to be supervised by two great supervisors. I have learned much from their creative, meticulous, industrious, and productive research style.

I would like to convey my great appreciation to my advisory committee: Dr. Yongfeng Hu, Dr. Robert Scott, Dr. Jafar Soltan, and Dr. Catherine Niu at the University of Saskatchewan for their constructive comments and suggestions that helped me to improve the quality of my work.

I am thankful to all the staff in the Department of Chemical and Biological Engineering, the University of Saskatchewan, especially Ms. Dushmanthi Jayasinghe, Mr. Richard Blondin, and Mr. RLee Prokopishyn for their technical support in the laboratory.

I would like to extend my thanks to the staffs of Soft X-ray Microcharacterization Beamline (SXRMB) at the Canadian Light Source for their assistance during the analysis and data interpretations of X-ray Absorption Spectroscopy. I am also grateful to Dr. Catherine Niu and Mr. Saeed Ghanbari at the University of Saskatchewan for their help during the N₂ Adsorption-Desorption analysis. Sincere thanks to Dr. Junjie Liao and Ms. MengMeng Liu at the Taiyuan University of Technology for their support during the CO chemisorption analysis.

I wish to convey many thanks to all members of Dr. Wang's research group and Dr. Dalai's research group for their support and advice for my research work, especially to Dr. Mohsen Shakouri and Dr. Philip Boahene for their help in the laboratory.

Special thanks and gratitude to my parents, my husband, and all my friends, who support, encourage, and help me to overcome numerous obstacles not only in these years but also in my life. Thank you all for your support, love, and encouragement.

I would like to acknowledge the China Scholarship Council (CSC) and Natural Sciences and Engineering Research Council of Canada (NSERC) for providing me with financial support.

DEDICATION

Dedicated to

My beloved parents, Mrs. Xiuli Li and Mr. Xinhua Gao, and my dear husband, Mr. Bailu Teng, who believed in me and encouraged me throughout my Ph.D. program.

TABLE OF CONTENTS

PERMISSION TO USE	i
ABSTRACT	ii
ACKNOWLEDGEMENTS	iv
DEDICATION	vi
TABLE OF CONTENTS	vii
LIST OF TABLES	xiii
LIST OF FIGURES.....	xvi
ABBREVIATION.....	xxiii
NOMENCLATURE.....	xxv
CHAPTER 1 Introduction.....	1
1.1 CO ₂ Emission and Utilization	1
1.2 Two Reactions for CO ₂ Utilization	3
1.3 Significance on Local Economy	5
1.4 Theoretical Consideration	7
1.5 Knowledge Gap.....	8
1.6 Hypotheses	8
1.7 Research Objectives	9
1.8 Organization of Thesis	11
CHAPTER 2 Literature Review.....	13

2.1 CO ₂ Reforming of Methane Reaction	13
2.1.1 Development of Ni-based bimetallic catalysts	15
2.1.2 Mechanism of CRM reaction	19
2.1.3 Contribution of our group to the development of Ni-based catalyst.....	21
2.2 CO ₂ Hydrogenation for Methanol Synthesis	23
2.2.1 Development of Cu-ZnO catalysts	25
2.2.2 Mechanism of the CO ₂ hydrogenation reaction	29
2.3 Atomic Layer Deposition Technique in Catalyst Development	31
CHAPTER 3 Experimental Methodology.....	34
3.1 Catalysts Preparation.....	34
3.1.1 Ni monometallic and NiM ₂ bimetallic catalysts.....	34
3.1.2 ZnO over-coated Cu/SiO ₂ catalysts.....	35
3.2 Catalyst Characterization	38
3.2.1 Inductively Coupled Plasma Mass Spectrometry (ICP-MS).....	38
3.2.2 N ₂ Adsorption-Desorption Experiment.....	39
3.2.3 H ₂ temperature-programmed reduction (H ₂ -TPR)	39
3.2.4 Transmission Electron Microscope (TEM) and Energy-Dispersive X-ray Spectroscopy (EDX)	40
3.2.5 CO Chemisorption.....	40
3.2.6 CO ₂ temperature-programmed desorption (CO ₂ -TPD).....	41

3.2.7 X-ray Diffraction (XRD).....	41
3.2.8 X-ray Absorption Spectroscopy (XAS)	42
3.3 Catalysts Evaluation	42
3.3.1 CO ₂ reforming of CH ₄ over Ni monometallic and NiM2 bimetallic catalysts...	42
3.3.2 CO ₂ hydrogenation reaction over ZnO over-coated Cu/SiO ₂ catalysts.....	44
CHAPTER 4 CO ₂ Catalytic Activation for CO ₂ Reforming of CH ₄ over Ni Monometallic and NiM2 Bimetallic Catalysts	46
4.1 Bulk Properties of Oxide Catalysts for CO ₂ Reforming of CH ₄	47
4.1.1 Metal composition by ICP analysis.....	47
4.1.2 Bulk structure by XRD analysis.....	48
4.1.3 Surface area and porous structures by N ₂ adsorption-desorption	50
4.2 Catalysts Characterization after Reduction	52
4.2.1 Reduction extent of metals	53
4.2.2 Particle size and distribution	59
4.2.3 Number of metallic sites and metal dispersion	63
4.3 Basicity of the monometallic Ni and bimetallic NiM2 catalysts	64
4.4 Pulse Adsorption Experiments and Pulling-Pushing Theory	68
4.4.1 Pulse adsorption experiments.....	69
4.4.2 The pulling-pushing theory	73
4.5 Catalyst Performances.....	77

4.6 Catalyst Study with Larger Metallic Particles.....	85
4.6.1 Reduction properties of active metals by XANES at higher reduction temperature	85
4.6.2 Particles formed at a higher reduction temperature	87
4.6.3 Performance of catalysts reduced at a higher temperature.....	88
4.7 Catalyst Study with Different Support	90
4.7.1 Extent of reduction of metals	91
4.7.2 Number of metallic and basic sites	91
4.7.3 Distribution of the active metal on the support	92
4.7.4 Performance of the catalyst	100
4.8 Conclusion.....	102
CHAPTER 5 CO ₂ Catalytic Activation for CO ₂ Hydrogenation to Synthesize Methanol over ZnO	
Over-coated Cu/SiO ₂ Catalysts	104
5.1 Formation of Cu Particles with Uniformed Distribution	105
5.1.1 Reduction properties of samples from H ₂ -TPR.....	106
5.1.2 Samples screened by TEM images.....	107
5.2 Bulk Properties of the CO ₂ Hydrogenation Catalysts of Oxide State	111
5.2.1 Metal composition by ICP analysis.....	111
5.2.2 Surface area and porous structures by N ₂ adsorption-desorption	112
5.3 Catalysts Characterization after Reduction	114

5.3.1	Reduction condition study by H ₂ -TPR.....	115
5.3.2	Crystal structure by XRD.....	116
5.3.3	ZnO and Cu phase distribution.....	117
5.3.4	Metallic particle size and distribution	119
5.3.5	Number of metallic sites and metal dispersion	122
5.4	Basicity of the catalysts from CO ₂ -TPD	123
5.5	Chemical Structure from XAS spectra.....	125
5.5.1	XANES for Cu K edge of SEA-5Cu and ZnO over-coated Cu/SiO ₂ catalysts	126
5.5.2	EXAFS for Cu K edge of SEA-5Cu and ZnO over-coated Cu/SiO ₂ catalysts	131
5.5.3	XANES for Zn K edge of ZnO over-coated Cu/SiO ₂ catalysts	133
5.5.4	EXAFS for Zn K edge of ZnO over-coated Cu/SiO ₂ catalysts	135
5.6	CO ₂ Conversion and Methanol Synthesis	137
5.7	Evidence from Others' Work	140
5.7.1	The catalyst CuZn/N-rGO with promising CO ₂ conversion	141
5.7.2	The catalyst Cu@ZnO _x with 100 % selectivity to methanol.....	144
5.8	Conclusion.....	147
CHAPTER 6 Conclusions and Recommendations		149
6.1	Conclusions	149
6.2	Recommendations	152
6.2.1	CO ₂ reforming of methane	152

6.2.2	CO ₂ hydrogenation reaction for methanol synthesis.....	153
6.2.3	Other CO ₂ utilization reactions	153
REFERENCES.....		155
Appendix A: Reproducibility of the Experimental Results		168
Appendix B: Calibration of Mass Flow Controller		173
Appendix C: Calibration of Gas Chromatography.....		175
Appendix D: Temperature Profiles of Reactors		178
Appendix E: Carbon and Hydrogen Balance		180
Appendix F: Performance of Monometallic Ni and Bimetallic NiM ₂ Catalysts for CRM Reaction at 750 °C.....		182
Appendix G: Characterization of Monometallic Ni and Bimetallic NiM ₂ Catalysts Reduced at 850 °C.....		184
Appendix H: Characterization of Catalysts with Different Supports.....		189
Appendix I: Permission to Use.....		191

LIST OF TABLES

Table 2-1 The performance of Cu-ZnO catalysts with different supports for CO ₂ hydrogenation to produce methanol.	26
Table 3-1 Catalysts prepared by Imp or SEA and ALD method and calcined under different calcination temperatures.	38
Table 4-1 Compositions of metals and Mg/Al ratio in monometallic Ni and bimetallic NiM ₂ catalysts	48
Table 4-2 BET surface area, pore volume and pore diameter of the monometallic Ni and bimetallic NiM ₂ catalysts.....	52
Table 4-3 The contents of metals and metal oxides in reduced catalysts measured by the linear combination fitting of XANES.	59
Table 4-4 Metal compositions on the monometallic Ni and bimetallic NiM ₂ catalysts after reduction at 750 °C for 4 h.....	59
Table 4-5 Average particle size and particle size distribution from the TEM micrographs of catalysts reduced at 750 °C	62
Table 4-6 The number of metallic sites and metal dispersion of catalysts based on CO chemisorption analysis	64
Table 4-7 Basic properties of Ni and NiM ₂ catalysts, support, Ni/Al ₂ O ₃ , and NiCo/spinel.....	66
Table 4-8 The formation rate of H ₂ and CO over the reduced and pre-chemisorbed catalysts in pulse adsorption experiments	71
Table 4-9 The pulling or pushing forces from metallic or basic sites based on the pulse adsorption experiments.	75

Table 4-10 The relative reaction rate of CH ₄ dissociation and CO ₂ decomposition and deactivation of catalysts	83
Table 4-11 The metal and metal oxide content in catalysts reduced at 850 °C for 4 h measured by the linear combination fitting of XANES.	86
Table 4-12 Average particle size and particle size distribution from the TEM micrographs of catalysts reduced at 850 °C	87
Table 4-13 Extent of Ni and Co reduction in catalysts.....	91
Table 4-14 Properties of metallic sites of catalysts from the analysis of CO chemisorption, and basic properties of catalysts based on CO ₂ -TPD analysis.....	92
Table 4-15 The element content in different parts of the catalyst.	100
Table 5-1 ICP results of SiO ₂ , SEA-5Cu, and ZnO over-coated Cu/SiO ₂ catalyst	112
Table 5-2 BET and XRD results of SiO ₂ , SEA-5Cu, and ZnO over-coated Cu/SiO ₂ catalysts.	114
Table 5-3 The content of elements on the reduced catalysts detected by TEM-EDX.....	118
Table 5-4 Metallic particle size measured by TEM and XRD	122
Table 5-5 Cu dispersion, metallic surface area of reduced catalysts, and number of metallic sites.	123
Table 5-6 Basic properties of the SEA-5Cu and Cu-ZnO catalysts.	124
Table 5-7 Cu species in the reduced SEA-5Cu and ZnO over-coated Cu/SiO ₂ catalysts based on linear combination fitting	130
Table 5-8 Basic information of Cu reference in EXAFS spectra	132
Table 5-9 Catalytic performances of the ZnO over-coated Cu/SiO ₂ catalysts: reaction rate and selectivity.	137
Table 5-10 Catalytic performances of the ZnO over-coated Cu/SiO ₂ catalysts: TOF of reactants.	138

Table 5-11 EDX results for Cu, Zn, and O on the catalyst Cu@ZnO _x . Spots refer to Figure 5-24.	146
Table A-1 Repeatability results for ICP analysis for catalyst NiMn.....	169
Table A-2 Repeatability results for ICP analysis for catalyst 5Cu-1CyZn-30s	169
Table A-3 Repeated catalytic performances of the catalyst 5Cu-1CyZn-30s	172
Table E-1 Carbon and Hydrogen balance for CRM over NiCo during 20 h. Reaction conditions: 0.05 g catalyst, temperatures: 750 °C, 1atm, GHSV of 110 L g ⁻¹ h ⁻¹ , CH ₄ /CO ₂ /N ₂ = 1/1/1	181
Table E-2 Carbon and Hydrogen balance for CO ₂ hydrogenation reaction over catalyst 5Cu- 1CyZn-30s during 24 h. Reaction conditions: 1.0 g catalyst, temperatures: 250 °C, 4 MPa, F = 9.6 L h ⁻¹ , H ₂ /CO ₂ = 3/1.....	181
Table H-1 ICP and BET results.....	189

LIST OF FIGURES

Figure 1-1 The trends of temperature anomaly and CO ₂ concentration in the atmosphere (https://www.climatelevels.org)	2
Figure 2-1 Equilibrium constant of CRM reaction and other reactions as a function of temperature (Zhang et al., 2007)	15
Figure 2-2 Schematic diagram of the dealloying-realloying process on Ni-Fe bimetallic catalyst in CRM reaction (Kim et al., 2017).....	18
Figure 2-3 Reaction steps for CRM. (a) step 1; (b) step 2; (c-d) step 3. (Papadopoulou et al., 2012)	21
Figure 2-4 Anthropogenic carbon cycles based on the methanol economy (Olah et al., 2009)...	24
Figure 2-5 Model representation of the CO ₂ hydrogenation: active sites for methanol and CO over a Cu/ZnO catalyst. (Tisseraud et al., 2015).....	30
Figure 2-6 Scheme of film ALD with a binary (AB) precursor system. a) substrate with reactive sites; b) exposed the substrate to the first precursor and first half-reaction occurred; c) purging of unreacted precursor and reaction byproducts; d) exposed to the second precursor and second half- reaction happened; e) purging; f) film resulting from several ALD cycles. (Oneill et al., 2015).	32
Figure 3-1 Reaction mechanism of ALD using DEZ and H ₂ O to form ZnO. (a) DEZ exposure; (b) monoethylzinc replaced H ₂ and connected to atomic O; (c) N ₂ purge; (d) monoethylzinc saturated surface; (e) H ₂ O exposure; (f) H ₂ O react with the monoethylzinc to form hydroxyls bonded with Zn; (g) N ₂ purge; (h) hydroxide saturated ZnO monolayer. (Janocha, 2011)	37
Figure 4-1 XRD patterns corresponding to the monometallic Ni and bimetallic NiM ₂ catalysts	49
Figure 4-2 N ₂ adsorption-desorption isotherms of monometallic Ni and bimetallic NiM ₂ catalysts	51

Figure 4-3 The Ni K-edge XANES spectra of monometallic Ni and bimetallic NiM2 catalysts after reduction at 750 °C for 4 h as well as those of Ni and its oxide standards	54
Figure 4-4 The Co K-edge XANES spectra of NiCo catalyst after reduction at 750 °C for 4 h as well as those of Co foil, and its oxide standards	55
Figure 4-5 The Mn K-edge XANES spectra of NiMn catalyst after reduction at 750 °C for 4 h as well as those of Mn foil, and its oxide standards	56
Figure 4-6 The Cu K-edge XANES spectra of NiCu catalyst after reduction at 750 °C for 4 h as well as those of Cu foil, and its oxide standards	56
Figure 4-7 The Fe K-edge XANES spectra of NiFe catalyst after reduction at 750 °C for 4 h as well as those of Fe foil, and its oxide standards.....	57
Figure 4-8 TEM images and the particle size distribution of the catalysts reduced at 750 °C	62
Figure 4-9 CO ₂ -TPD curves of the Ni and NiM2 catalysts, support, Ni/Al ₂ O ₃ , and NiCo/spinel65	
Figure 4-10 CH ₄ conversion as a function of time-on-stream over monometallic Ni and bimetallic NiM2 catalysts.....	78
Figure 4-11 Activity and stability of monometallic Ni and bimetallic NiM2 catalysts at reaction condition: T = 750 °C, P = 1 atm, GHSV = 110 L·g _{cat} ⁻¹ h ⁻¹ , CH ₄ /CO ₂ /N ₂ = 1/1/1, 0.05 g catalyst. (a) TOF of CH ₄ reacted based on the metallic sites on the surface of the catalysts; (b) TOF of CO ₂ reacted based on the basic sites on the surface of the catalysts; (c) TOF of CO ₂ reacted based on the metallic sites on the surface of the catalysts.....	81
Figure 4-12 Correlations of initial TOF _{CH4} and TOF _{CO2} and the average size of metallic particles	82
Figure 4-13 H ₂ /CO molar ratio as a function of time-on-stream over monometallic Ni and bimetallic NiM2 catalysts.....	84

Figure 4-14 Activity and stability of Ni monometallic and NiM2 bimetallic catalysts at reaction condition: reduction $T=850\text{ }^{\circ}\text{C}$, reaction $T = 750\text{ }^{\circ}\text{C}$, $P = 1\text{ atm}$, $F = 90\text{ mL/min}$, $\text{CH}_4/\text{CO}_2/\text{N}_2 = 1/1/1$, 0.05 g catalyst . (a) TOF of CH_4 reacted based on the metallic sites on the surface of the catalysts; (b) TOF of CO_2 reacted based on the metallic sites on the surface of the catalysts.....	89
Figure 4-15 STEM-EDX of Ni/ Al_2O_3 catalyst. Ni and Al interaction	93
Figure 4-16 STEM-EDX of Ni/MgO-spinel catalyst. Ni and Al interaction, Ni and Mg interaction, Mg and Al interaction	94
Figure 4-17 STEM-EDX of NiCo-spinel catalyst.	96
Figure 4-18 STEM-EDX of NiCo- MgO-spinel catalyst.	98
Figure 4-19 STEM-EDX of NiCo/MgO-spinel catalyst to calculate the element content in each part.....	99
Figure 4-20 Activity and stability of Ni/ Al_2O_3 and Ni/MgO-spinel catalysts at reaction condition: $T = 755\text{ }^{\circ}\text{C}$, $P = 1\text{ atm}$, $\text{GHSV} = 1200\text{ L}\cdot\text{g}_{\text{cat}}^{-1}\cdot\text{h}^{-1}$, $\text{CH}_4/\text{CO}_2/\text{N}_2 = 1/1/1$. The reaction rate of CH_4 as a function of time-on-stream (Alabi, 2018).	101
Figure 4-21 Activity and stability of NiCo/spinel and NiCo/MgO-spinel catalysts at reaction condition: $T = 755\text{ }^{\circ}\text{C}$, $P = 1\text{ atm}$, $\text{GHSV} = 1200\text{ L}\cdot\text{g}_{\text{cat}}^{-1}\cdot\text{h}^{-1}$, $\text{CH}_4/\text{CO}_2/\text{N}_2 = 1/1/1$. The reaction rate of CH_4 as a function of time-on-stream (Alabi, 2018).....	101
Figure 5-1 H_2 -TPR profiles of samples prepared by Imp or SEA method with different Cu content and different calcined temperature.	106
Figure 5-2 TEM images of samples Imp-5Cu, SEA-5Cu and SEA-10Cu calcined at $250\text{ }^{\circ}\text{C}$ and reduced at $250\text{ }^{\circ}\text{C}$, and samples calcined at $500\text{ }^{\circ}\text{C}$ and reduced at $500\text{ }^{\circ}\text{C}$	109
Figure 5-3 TEM images and particle-size distribution of samples Imp-5Cu, SEA-5Cu, and SEA-10Cu calcined at $250\text{ }^{\circ}\text{C}$ and reduced at $500\text{ }^{\circ}\text{C}$	110

Figure 5-4 N ₂ adsorption-desorption isotherms of SiO ₂ , SEA-5Cu, and ZnO over-coated Cu/SiO ₂ catalysts	113
Figure 5-5 H ₂ -TPR profiles of SEA-5Cu and catalysts ZnO over-coated Cu/SiO ₂	115
Figure 5-6 XRD patterns corresponding to support and reduced ZnO over-coated Cu/SiO ₂ catalysts	117
Figure 5-7 TEM images, particle size, and distribution of Cu-ZnO catalysts.....	121
Figure 5-8 CO ₂ -TPD curves of the SEA-5Cu and Cu-ZnO catalysts	124
Figure 5-9 Experimental XANES spectra registered Cu K edge of catalysts SEA-5Cu and Cu-ZnO	127
Figure 5-10 Experimental derivative XANES spectra registered Cu K edge of catalysts SEA-5Cu and Cu-ZnO.....	127
Figure 5-11 Experimental XANES spectra registered Cu K edge of reduced SEA-5Cu and ZnO over-coated Cu/SiO ₂ catalysts	129
Figure 5-12 Experimental derivative XANES spectra registered Cu K edge of reduced SEA-5Cu and ZnO over-coated Cu/SiO ₂ catalysts.....	130
Figure 5-13 Experimental EXAFS spectra registered Cu K edge of calcined ZnO over-coated Cu/SiO ₂ catalysts.....	132
Figure 5-14 Experimental EXAFS spectra registered Cu K edge of reduced ZnO over-coated Cu/SiO ₂ catalysts.....	133
Figure 5-15 Experimental XANES spectra registered Zn K edge of calcined ZnO over-coated Cu/SiO ₂ catalysts.....	134
Figure 5-16 Experimental XANES spectra registered Zn K edge of reduced ZnO over-coated Cu/SiO ₂ catalysts.....	135

Figure 5-17 Experimental EXAFS spectra registered Zn K edge of ZnO over-coated Cu/SiO ₂ catalysts	136
Figure 5-18 Experimental EXAFS spectra registered Zn K edge of reduced ZnO over-coated Cu/SiO ₂ catalysts	136
Figure 5-19 Mechanism of CO ₂ hydrogenation process to produce methanol on a common catalyst	140
Figure 5-20 Mechanism of CO ₂ hydrogenation process to produce methanol on the second catalyst model	141
Figure 5-21 Schematic illustration for the synthesis of Cu-Zn/N-rGO (Deerattrakul et al., 2018)	142
Figure 5-22 FE-SEM images of CuZn/N-rGO (a, b) and EDS mapping of CuZn/N-rGO catalyst showing Cu (c), Zn (d), C (e) and N (f) (Deerattrakul et al., 2017)	143
Figure 5-23 (a) Low- and (b) high-magnification TEM images of CuZn/N-rGO. (Deerattrakul et al., 2017).....	144
Figure 5-24 TEM images for the catalyst Cu@ZnO _x . Spots in figure correspond to EDX analysis. (Tisseraud et al., 2016)	145
Figure A-1 Reproducibility of XANES analysis for the reduced catalyst NiCo.....	170
Figure A-2 Reproducibility of XANES analysis for the reduced catalyst 5Cu-1CyZn-30s	170
Figure A-3 Repeated catalyst performance evaluation experiments. Activity test of NiCo catalysts at reaction condition: T = 750 °C, P = 1 atm, F = 90 mL·min ⁻¹ , CH ₄ /CO ₂ /N ₂ = 1/1/1, 0.05 g catalyst. (a) The reaction rate of CH ₄ as a function of time-on-stream; (b) The reaction rate of CO ₂ as a function of time-on-stream.....	171
Figure B-1 MFC calibration curves of each channel for CRM reaction	173
Figure B-2 MFC calibration curves of each channel for the reaction of CO ₂ hydrogenation....	174

Figure C-1 Calibration curves for the Agilent 6890N GC equipped with an TCD for CRM reaction	176
Figure C-2 Calibration curve of Methanol for the Agilent Technologies 7890A GC equipped with TCD and FID detectors	177
Figure C-3 Calibration curve of Methanol for the Agilent Technologies 7890A GC equipped with a DB-Wax capillary column and FID detector.....	177
Figure D-1 Temperature profiles of CRM reactor	178
Figure D-2 Temperature profiles of CO ₂ hydrogenation reactor	179
Figure F-1 Activity and stability of monometallic Ni and bimetallic NiM2 catalysts at reaction condition: T = 750 °C, P = 1 atm, GHSV = 110 L·g _{cat} ⁻¹ h ⁻¹ , CH ₄ /CO ₂ /N ₂ = 1/1/1, 0.05 g catalyst. (a) The reaction rate of CH ₄ as a function of time-on-stream; (b) The reaction rate of CO ₂ as a function of time-on-stream; (c) The formation rate of H ₂ as a function of time-on-stream; (d) The formation rate of CO as a function of time-on-stream.....	183
Figure G-1 The Ni K-edge XANES spectra of monometallic Ni and bimetallic NiM2 catalysts after reduction at 850 °C for 4 h as well as those of Ni and its oxide standards.....	184
Figure G-2 The Co K-edge XANES spectra of NiCo catalyst after being reduction 850 °C for 4 h as well as those of Co foil, and its oxide standards.....	185
Figure G-3 The Mn K-edge XANES spectra of NiMn catalyst after reduction at 850 °C for 4 h as well as those of Mn foil, and its oxide standards	185
Figure G-4 The Cu K-edge XANES spectra of NiCu catalyst after reduction at 850 °C for 4 h as well as those of Cu foil, and its oxide standards	186
Figure G-5 The Fe K-edge XANES spectra of NiFe catalyst after reduction at 850 °C for 4 h as well as those of Fe foil, and its oxide standards.....	186
Figure G-6 TEM images and the particle size distribution of the catalysts reduced at 850 °C .	188

Figure H-1 XRD patterns of Ni catalysts supported by Al₂O₃ and MgO-spinel (Alabi, 2018). 189

Figure H-2 XRD patterns of NiCo catalysts supported by spinel and MgO-spinel (Alabi, 2018)

..... 190

ABBREVIATION

ALD	Atomic layer deposition
BET	An analysis technique for the measurement of the specific surface area and porous structure of a solid material based on Brunauer-Emmett-Teller theory
CCS	CO ₂ capture and storage
CCU	CO ₂ capture and utilization
CO ₂ -TPD	CO ₂ temperature-programmed desorption
CRM	CO ₂ reforming of methane
DEZ	Diethyl zinc
DFT	Density functional theory
EDX	Energy-dispersive X-ray Spectroscopy
EXAFS	Extended X-ray absorption fine structure
FID	Flame ionization detector
GC	Gas chromatography
GtC	Gigatonnes of carbon
H ₂ -TPR	Temperature-programmed reduction
ICP-MS	Inductively coupled plasma mass spectrometry
K _{sp}	Solubility product
LCF	Linear combination fitting
Mt	Megatonnes
SEA	Strong electronic adsorption
TCD	Thermal conductivity detector
TEM	Transmission electron microscopy

TOF	Turnover frequency
XANES	X-ray absorption near-edge structure
XAS	X-ray absorption spectroscopy
XRD	X-ray diffraction

NOMENCLATURE

$\beta(2\theta)$	Full width at half maximum in radians in the XRD experiment
C^*	Carbon species formed by CH_4 dissociation on the metallic sites
CH_x^*	Methyl-like species, where $x = 1, 2, 3$ or 4 on the metallic sites
CO_2^*	Activated CO_2 on the basic sites
d	Spacing between the adjacent planes of atoms in the crystal lattice
E_0	edge energy of an element
H^*	Hydrogen species formed by CH_4 or H_2 dissociation on the metallic sites
k	Crystallite shape constant (0.94)
K-edge	Binding energy of the innermost electron shell of the atoms interacting with the photons
M2	The second (active) metal in addition to Ni in CRM catalysts
O^*	Oxygen species formed by CO_2 decomposition on the basic sites
P	Pressure
pH	Power of hydrogen, a measure of acidity or basicity
S	Metallic sites
T	Temperature
wt%	Weight percent
λ	X-ray wavelength
n	Order of diffraction in the XRD experiment

CHAPTER 1 Introduction

1.1 CO₂ Emission and Utilization

Carbon dioxide (CO₂) is commonly considered as one of the most severe greenhouse gases by the amount of anthropogenic emission since the industrial era. CO₂ emission from human activity is 12 gigatonnes of carbon (GtC) per year in 2018 (Friedlingstein et al., 2019). Naturally, the CO₂ fluxes containing 60 GtC are in the carbon cycle among land, ocean, and atmosphere (Hasan and Webly, 2017). With the industrial revolution and development, the carbon cycle has been disrupted due to the increase in CO₂ concentration in the ocean and the change in land use. The ability of land and ocean to take up CO₂ is not enough to complete the carbon cycle, resulting in an accumulation of CO₂ from the anthropogenic emission and also from the natural fluxes. Consequently, CO₂ is remained in the atmosphere, leading to an increase in CO₂ concentration, further global warming. The present CO₂ concentration in the atmosphere is unprecedented as compared to past 420 thousand years (<https://www.climatelevels.org>). Before the industrial revolution, the CO₂ concentration in the atmosphere was 285 ± 10 ppm for several thousand years. This value increased to 310 ppm by 1950 and to 410 by now, shown in Figure 1-1 (<https://www.climatelevels.org>). Considering past 20 thousand years, the rate of increase in CO₂ concentration in the atmosphere in last century has not been exceeded.

Undoubtedly, the increasing atmospheric CO₂ concentration may be beneficial for the photosynthesis process for the plants to a certain extent. But the severe consequence of global warming cannot be negligible. From the trend of temperature anomaly and CO₂ concentration in the atmosphere shown in Figure 1-1, the temperature keeps on increasing along with the increase in CO₂ concentration. Due to the dependence of fossil fuels in the near future, the emission of CO₂ will still keep rising. Thus, the CO₂ capture and storage (CCS) and CO₂ capture and utilization (CCU) arouse attention to slow down the increasing rate of CO₂ emission and the growing concentration of CO₂ in the atmosphere. Compared to CCU, CCS faces the challenges on site selection, transportation cost, and CO₂ leakage, which results in a loss of 64 % of CO₂ emitted into the atmosphere after 200 years. These challenges suggest more research on CO₂ utilization, alternative ways to solve the problem.

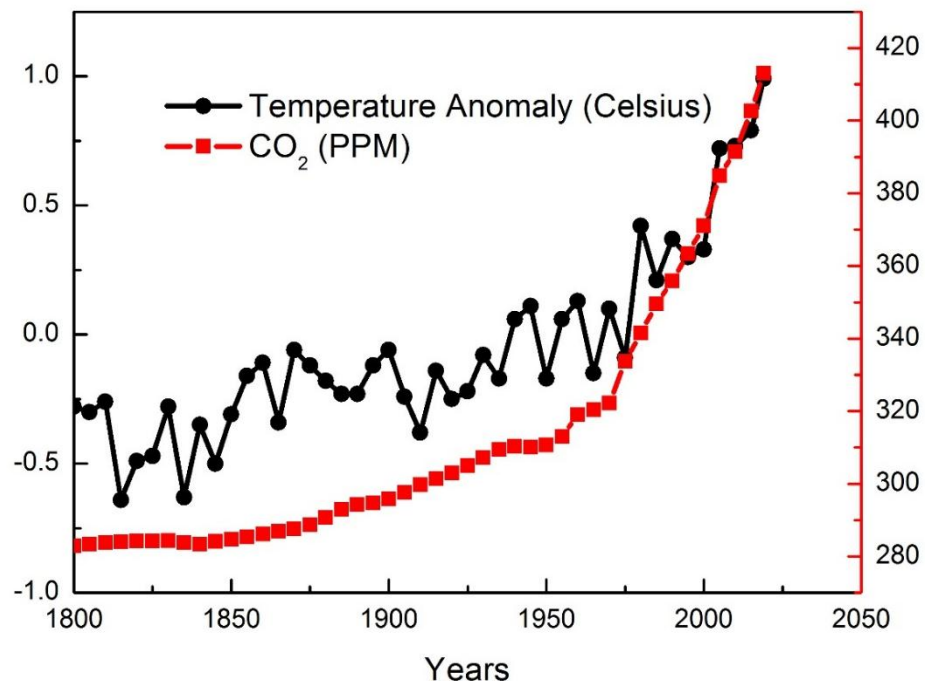


Figure 1-1 The trends of temperature anomaly and CO₂ concentration in the atmosphere
(<https://www.climatelevels.org>)

The attractive factors for CO₂ as the precursor for industrial purposes are (a) its abundant amount, good carbon source for existing applications to replace toxic precursors and intermediates; (b) a building block to construct new materials and polymers; (c) and a good substitute for organic solvents in recovery or separation application. Due to these advantages, CO₂ has been used as feedstock in the industry to produce chemicals and fuels since the 19th century. For example, CO₂ is used in the synthesis of chemicals such as syngas, urea, salicylic acid, pigments, and carbonates. CO₂ is also a carbon source for methanol, dimethyl carbonate, and dimethyl ether, which can be used as fuel (Centi and Perathoner, 2009). Based on CO₂ physicochemical properties, CO₂ can also be used directly in applications, for example in the supercritical state. Meanwhile, CO₂ is involved in biological conversions, for instance, CO₂ photo-conversion, CO₂ fermentation by bacteria, or in the algae bio-refinery (Pérez-fortes et al., 2016).

CO₂ has so many advantages in industrial utilization. However, after hundreds of years of study and attempt, only 0.5% of the emitted CO₂ has been used for industrial purposes (English et al., 2014). This is primarily because of the thermodynamic stability of CO₂ (Wang et al., 2011) and high energy required to transform CO₂ into other chemicals. CO₂ can barely be involved in a reaction if there are no catalysts and/or driving energy. Thus, it is essential to understand the mechanism of catalytic activation of CO₂ such that effective catalysts can be developed for the pursued reactions.

1.2 Two Reactions for CO₂ Utilization

To study the mechanism of CO₂ catalytic activation, further to develop effective and efficient catalysts, reactions such as CO₂ reforming of methane (CH₄) (CRM) and CO₂ hydrogenation for methanol synthesis are chosen in this research.

CRM reaction has attracted intense research interest due to the conversion of CO_2 and CH_4 into synthetic gas, which is in a more favorable ratio of H/C for the production of synthetic fuels via Fischer-Tropsch synthesis. Since the CRM reaction plays an important role in the development of gas-to-liquid (GTL) fuel technology, the published literature under the keywords of “ CO_2 ”, “reforming”, and “ CH_4 ” have increased from over one thousand during 2000-2010 to almost ten thousand during 2010-2020. Based on these new studies and results, the general agreement about the mechanism of CRM is summarized (Papadopoulou et al., 2012). During the reaction, CO_2 is commonly considered to be activated on the metallic oxide phase, which is the basic sites on the catalyst. Another reactant, CH_4 , is cracked into CH_x species on the surface of active metal, as well as metallic sites. Then at the interface of metallic and basic sites, surface hydroxyls or oxygen species from the basic sites oxidize the carbon species or CH_x from the metallic sites to form CO and H_2 . Thus, only at the point where the metallic sites and basic sites are close enough, the reaction can be completed. In other words, the CO_2 decomposition cannot occur to form CO unless the carbon species from CH_4 cracking on the metallic sites could reach and reduce the activated CO_2 on the basic sites. To evaluate the performance of the catalyst, not only the activity and number of catalytic sites but also the accessibility of basic sites to metallic ones should be identified.

Methanol synthesis directly from CO_2 hydrogenation is considered as a central technology for CO_2 utilization, as methanol could be a starting feedstock for the production of some chemicals and fuels (Olah et al., 2009). More researches have been done in this area. As the proof, the number of published papers about this reaction has increased from one thousand during 2000-2010 to five thousand during 2010-2020. To understand the mechanism of the reaction, a dual-site, bifunctional theory was summarized (Dang et al., 2019). The dual-site mechanism is widely accepted, which deems that CO_2 is activated as bicarbonate on the basic sites. At the same time, H_2 is adsorbed and dissociated on the active metal phase, as well as metallic sites. With the right orientation of metallic

and basic sites, methanol can be produced at the interface of these catalytic sites. Thus, how the metallic sites and basic sites are connected to each other, and how the connection affects the performance of the catalyst should be studied for effective preparation of catalysts with specific structures.

From the mechanism of these two reactions, there is something in common. Two catalytic sites exist on the catalysts. CO_2 is activated on the basic sites, and the reducing agent, CH_4 in the CRM reaction or H_2 in the CO_2 hydrogenation reaction, is adsorbed and dissociated on the metallic sites. For a homogeneous reaction, the molecules' collision frequency, orientation, and activation energy determine the reaction mechanism and kinetics. However, for a catalytic reaction involving two or more reactants to be activated on different types of activation sites, not only the number and activity of the sites but also the site distribution and orientation, namely site contiguity, determine the mechanism and kinetics. The reaction only can occur when two types of catalytic sites are close to each other. The contiguity here is a description of how dual or multiple catalytic sites exist next to each other in the desired orientation to allow collision among different active species to take place. CO_2 reforming of methane and CO_2 hydrogenation for methanol are such catalytic reactions where two reactants are activated by two types of sites. To develop an efficient catalyst for CO_2 utilization, the study on the contiguity of the CO_2 activation sites and the activation sites for the second molecules should be carried out.

1.3 Significance on Local Economy

The research on CO_2 utilization is not only significant scientifically but also impacts local economy. For example, the CRM reaction can be used at the locations where CO_2 and CH_4 coexist. Examples include biogas from biomass or biowaste degradation, coal gas from coal gasification

and pyrolysis processes, natural gas reservoirs with large CO₂ content, and petroleum field when CH₄ cannot be utilized effectively (Wang et al., 2013; Alabi et al., 2018). CO₂ reforming of methane has the potential to be used in the dairy industry where biogas is produced. The reaction on CO₂ hydrogenation to produce methanol can be combined with CO₂ capture in the energy industry and local biodiesel industry.

As a global landmark event, the first-ever, commercial-scale, coal-fired power plant which incorporates amine solvent adsorption for CO₂ capture, started operation in Saskatchewan, Canada, on October 2, 2014 (Preston, 2015). The amount of CO₂ captured in 2019 was 0.6 million tons. As planned, the CO₂ captured is geologically stored in an oil reservoir and a deep saline aquifer, with a sale of a portion for petroleum exploitation by CO₂ enhanced oil recovery. However, the revenue is not enough to balance the cost. The captured CO₂ should be considered in the utilization of chemicals and fuel industries.

In Saskatchewan, a major province in agriculture, biodiesel is produced from a certain amount of oilseed that is not qualified for the production of cooking oil. Biodiesel is produced by the reaction of transesterification or esterification of triacylglycerol (an ingredient in vegetable oil) and short-chain alcohols, like methanol or ethanol (Kurahde, 2019). Among the alcohols, methanol can lead to more excellent conversion of cooking oil to biodiesel, but it is expensive. Through the reaction of CO₂ hydrogenation for methanol synthesis, both the CO₂ utilization and methanol source can be solved. The H₂ for CO₂ hydrogenation reaction can be produced by the iodine-sulfur thermochemical cycle. SO₂ used in this cycle is a by-product of the process of CO₂ capture (Preston, 2015).

Except for the CO₂ capture project in Saskatchewan, there is another new carbon capture project in Alberta, which is operational in 2020. Up to 1.8 million tons of CO₂ each year will be

captured initially, and up to 15 million tons of CO₂ annually for the long-term potential. This amount of CO₂ can also be considered to produce value-added products as raw material. As a result, the biogas from the dairy industry and the CO₂ captured in the local power plant can be utilized via CRM and CO₂ hydrogenation reactions to produce value-added products.

1.4 Theoretical Consideration

As the Inspiration, the collision theory, where the molecules collision frequency, orientation and the activation energy determine the reaction mechanism and kinetics in a homogeneous reaction. However, during the study of a catalytic reaction involving two or more reactants to be activated on different types of active sites, the orientation and neighborhood of the types of active sites on catalysts are recognized to determine successful catalytic reaction. Thus, a conception, the site contiguity is proposed to describe the relationship between the types of active sites on catalysts. It is the quality of a catalyst by which how close different types of active sites are next to each other and how well they make the reacting molecules to desired orientations that lead to successful reactions.

Based on the literature and our study, a theory, pushing-pulling theory is proposed to explain the mechanism of CO₂ utilization reactions. When two or more types of sites play roles to complete a reaction, there must be two types of effects: pushing effect by which a molecule is activated by its adsorption site, and pulling effect which a species on one type of site receives from the species on other type of site or the site itself. Take CRM reaction as example, the CO₂ activation occurs on the basic sites. The pushing effect is CO₂ being activated to form activated CO₂ (CO₂*) or oxygen species (O*). The pulling effect is CO₂* or O* being react with species on metallic sites. Meanwhile, the CH₄ activation occurs on the metallic sites. The pushing effect is CH₄ being

activated to form carbon or methyl-like species (C^* or CH_x^*). The pulling effect is C^* or CH_x^* being oxidized by CO_2^* or O^* on the basic sites. Then there are regeneration of metallic sites and formation of CO and/or H_2O .

The conception, site contiguity, and the theory, pushing-pulling theory are used to understand the catalytic activation of CO_2 during the CO_2 reforming of CH_4 and CO_2 hydrogenation to methanol reactions in this study.

1.5 Knowledge Gap

Literature review (Chapter 2) was carried out related to the reaction mechanism and catalyst development for CO_2 reforming of methane and CO_2 hydrogenation for methanol synthesis, which led to the present knowledge gaps.

The Ni-based bimetallic catalysts for CRM reaction and Cu-ZnO catalysts for CO_2 hydrogenation reaction have been studied in terms of dispersion and distribution of active metal, modification of second metal, and effects of various support. But no careful and sufficient attention has been given to the effects of the neighborhood, accessibility, and the orientation on the catalytic performance when there are two or more sites are involved in activating the reactants. In other words, the contiguity of the catalytic sites when two or more sites are involved in these catalytic reactions has not been fully studied. Especially for CO_2 catalytic activation in CO_2 reforming of methane and CO_2 hydrogenation for methanol, no publications have been found discussing the effects of the interactions between CO_2 activation sites and the activation sites for CH_4 or H_2 .

1.6 Hypotheses

Based on the above knowledge gaps, the following hypotheses are proposed:

1. In a catalytic reaction involving two different catalytic sites, only those of which the active species on one site can access the species on the other site, or two catalytic sites in good contiguity, participate in the reaction.
2. In CRM, carbon formation can be mitigated only if the CH_4 dissociation sites are in close proximity of the CO_2 activation sites.
3. For CRM catalysts, a second metal in addition to Ni can change the contiguity and then the accessibility between the CH_4 dissociation sites, which are the metallic sites, and the CO_2 activation sites, the basic sites.
4. In CO_2 hydrogenation for methanol, CO_2 activation sites and H_2 activation sites must be next to each other and sit in the right locations so that H atoms can not only pull off one O from the activated CO_2 but also react with the CO to form C-H and O-H bonds for methanol.
5. The use of ALD and SEA to formulate CO_2 activation sites (the Zn sites), and the H_2 activation site (the Cu sites) can change the probability of the right site locations and thus change the methanol selectivity on the formulated catalyst.

1.7 Research Objectives

The principal research objective of this work is to study the CO_2 catalytic activation mechanism by considering the effect of contiguity of the two activation sites in the CO_2 reforming of methane system and CO_2 hydrogenation for methanol system. Then the desired catalyst surface designs for both reactions can be determined to achieve better catalytic performances, for example, to mitigate carbon formation in CRM, and to improve methanol selectivity in CO_2 hydrogenation. To meet the overall objective, the following sub-objectives are formulated:

1. Study the contiguity of CO₂ activation sites (metal oxide sites as well as basic sites), and the CH₄ activation sites (Ni-second metal sites as well as metallic sites) by using different second metals in addition to Ni on Ni-second metal bimetallic catalysts for CO₂ reforming of methane, and confirm the contiguity effects by analyzing the results with varying the strength of basic sites.
2. To reveal the reaction mechanism and the structure of the good catalyst, the Cu-ZnO/SiO₂ catalysts were prepared by strong electronic adsorption (SEA) method and atomic layer deposition (ALD) method.
3. We had two types of catalyst proposed, first one is metallic Cu particles isolated in ZnO layers, and the second is ZnO particles isolated in Cu layers.
4. We hypothesize that the second has more probability to have right Cu-ZnO orientation to form methanol. Due to the instrument limitation at this moment, only the first catalyst can be synthesized.
5. Study the contiguity of CO₂ activation sites (Zn sites as well as basic sites), and the H₂ activation sites (Cu sites as well as metallic sites) by switching the ALD method for one site and SEA for the other for CO₂ hydrogenation for methanol production. Two types of catalyst are proposed, first one is metallic Cu particles isolated in ZnO layers, and the second is ZnO particles isolated in Cu layers. The second is supposed to have more probability to have right Cu-ZnO orientation to form methanol. Due to the limitation of the ALD instrument, only the catalyst of ALD over-coated ZnO on Cu/SiO₂ is studied in this phase.

1.8 Organization of Thesis

This thesis is organized in 6 chapters, followed by the reference and appendix sections. In this chapter (Chapter 1), global warming due to the emission of greenhouse gases, especially CO₂, and one of the solutions, CO₂ capture and utilization, are introduced. The reactions such as CO₂ reforming of methane and CO₂ hydrogenation for methanol synthesis have significance on the study of catalysts for CO₂ utilization and the local economy. Based on the literature review in Chapter 2, the knowledge gap, hypotheses, and research objectives are stated.

Chapter 2 presents the literature review for reactions of CO₂ reforming of methane and CO₂ hydrogenation to methanol. For the reaction of CRM, the development of Ni-based bimetallic catalysts and the mechanism of the reaction, along with the contribution of our group in this area, are summarized. For the reaction of CO₂ hydrogenation, the catalyst Cu-ZnO and the reaction mechanism are stated. A special catalyst preparation method, atomic layer deposition, is also introduced in this section.

The experimental methodology, including the preparation, characterization, and evaluation of the catalysts are described in Chapter 3.

Chapter 4 is devoted to the studies for CRM reaction. Different second metals are used with Ni to modify the properties of catalytic sites, mainly the metallic ones, and the contiguity of basic and metallic sites to clarify the importance of sites contiguity on the activity and stability of the catalysts. Higher reduction temperature was used to prepare larger Ni particles to further certify the importance of contiguity on the stability of the catalyst. Then the effects of basic sites on the contiguity of basic and metallic sites on the catalysts are summarized based on Ni and NiCo catalyst with different supports.

Chapter 5 presents the studies related to CO₂ hydrogenation to methanol. Cu-ZnO catalysts containing isolated Cu-related particles distributed on ZnO atoms with different distributions are characterized and evaluated, to study the effects of properties of metallic sites on the activity of the catalyst, and the contiguity of basic and metallic sites on the catalyst selectivity to methanol.

Chapter 6 states the major conclusions as well as recommendations for further studies. References and Appendices are presented at the end of this thesis.

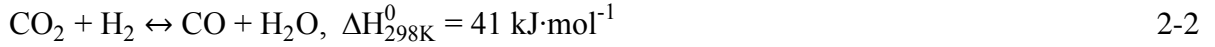
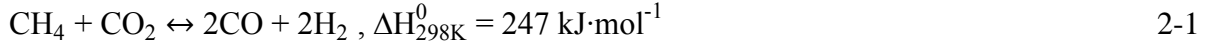
CHAPTER 2 Literature Review

The literature reviews on CO₂ reforming of methane, including the development of Ni-based catalysts, mechanism of the reaction, and contributions of Professor Wang's group in this area, are presented in the first part of this chapter. The reviews of the CO₂ hydrogenation reaction, including the development of Cu-ZnO catalysts, and the mechanism of the reaction, are presented in the second part of this chapter. The reviews mainly focused on the papers published in the last decade. Then one of the material growth techniques, atomic layer deposition (ALD), especially its utilization for the catalysts' preparation, is summarized in the last part of this chapter.

2.1 CO₂ Reforming of Methane Reaction

Carbon dioxide reforming of methane reaction has become an attractive process as a starting part of gas-to-liquid fuel technology. Meanwhile, it can convert CO₂ and methane, two major greenhouse gasses into value-added products (Muraza and Galadima, 2015). As a result, this process has the potential to constitute an essential unit in carbon capture and utilization technologies (Pakhare and Spivey, 2014; Rathod and Bhale, 2014; Arora and Prasad, 2016). Additionally, the flue gas can be directly used as the feedstock for this reaction and CO₂ need not to be separated. The syngas product can be used in the Fisher-Tropsch process to synthesize long-chain hydrocarbons (Kawi et al., 2015).

As an endothermic reaction, the heat of the CRM reaction is $247 \text{ kJ}\cdot\text{mol}^{-1}$ at 101.3 kPa and 298 K (equation 2-1). Simultaneously, the side reaction, reverse water-gas shift (RWGS) reaction (equation 2-2) happens between the chemisorbed CO_2 and produced H_2 , if H_2 does not leave the surface of the catalyst. The heat of this reaction is $41 \text{ kJ}\cdot\text{mol}^{-1}$ at the same condition.



The methane decomposition reaction and CO disproportionation reaction as shown in equations 2-3 and 2-4 lead to coke formation on the catalyst surface and consequently deactivate catalysts. (Nikoo and Amin, 2011)



The thermodynamics of reaction CRM and other reactions were studied by Zhang and co-workers (shown in Figure 2-1) (Zhang et al., 2007). The equilibrium constant of reaction CRM increases dramatically with the increase in temperature. However, the value of this constant for the RWGS reaction rises moderately. Thus, high reaction temperature is more favorable to the target reaction, but the higher temperature also enhances the equilibrium constant of the methane decomposition reaction, which is one of the reasons for carbon formation, leading to the deactivation of the catalysts.

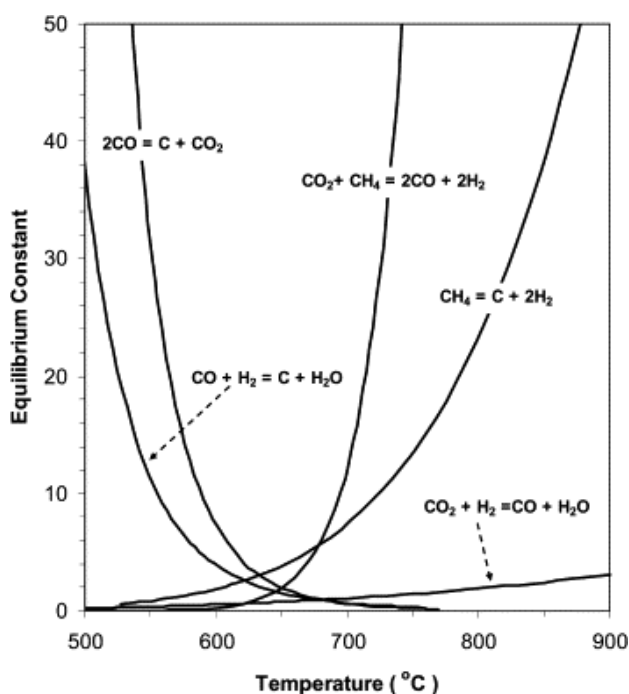


Figure 2-1 Equilibrium constant of CRM reaction and other reactions as a function of temperature (Zhang et al., 2007)

2.1.1 Development of Ni-based bimetallic catalysts

Noble metals usually are highly active towards CRM reaction and more resistant to coke formation than other transition metals, however they are expensive. For industrial applications, non-noble catalysts are studied widely. The nickel (Ni)-based catalysts, as the non-noble metal catalysts, show their high catalytic activity, excellent availability, and low cost, resulting in broader use for the CRM reaction. But Ni-based catalysts are prone to coke formation, which is the major concern during the reaction (Alabi, 2018; Wang and Zaidi, 2013).

The amorphous carbon species, generated from CO disproportionation reaction (equation 2-4) at low temperatures, is less active than most of the carbon species formed via methane decomposition. It deposits on the metal surface and causes deactivation of the catalysts. When the reaction temperature is above 700 °C, the CO disproportionation reaction is inhibited because it is

highly exothermic. The highly reactive carbon species (C^*), which is intermediate, primarily formed by methane decomposition (equation 2-3), is oxidized by CO_2 . As a result, coke deposition is not apparent (Fan et al., 2009). However, the least reactive carbon species, which is also the graphitic type of carbon, leads to the catalytic deactivation at a high temperature above 850 °C (Tomishige et al., 2002; Kawi et al., 2015).

The mechanism of whisker carbon growth on Ni-based catalysts is summarized as follows: The less reactive carbon species originating from CO disproportionation reaction or methane decomposition dissolves and diffuses into the Ni cluster to form nickel carbide, which is the crucial step for the growth of carbon whisker. Then the growing high strength carbon whisker pushes the Ni crystal out of the structure of Ni-based catalysts (Trimm, 1999; Rostrup-Nielsen et al., 2002; Annesini et al., 2007). Other important factors of coke deposition are attributed to the size of Ni metal clusters and purity of the Ni (111) phase. The size of the Ni particle, 9 nm, was reported as a critical size, above which carbon deposition cannot be mitigated effectively (Wang and Zaidi 2013). Compared to Ni (100) and Ni (110) surfaces, the Ni (111) plane shows more carbon resistance, as the carbon formation reaction is structure-sensitive (Y. H. Hu & Ruckenstein, 2004).

Due to the coke deposition of the Ni-based catalyst, second metals are introduced to improve the stability of the catalysts by enhancing the carbon resistance (Hu and Ruckenstein, 2004; Fan et al., 2009; Fan et al., 2010; Ahmad et al., 2017). The role of the specific transition metal is quite different because of their intrinsic characteristics (Kawi et al., 2015; Bian et al., 2017). The researches on the CRM reaction over the Ni-based bimetallic catalyst modified by Co, Fe, Cu, and Mn, which are most commonly used as the second metal, are reviewed and summarized.

Ni-Co-Mg-Al-O catalyst prepared by Zhang and coworkers (Zhang et al., 2007) using the co-precipitation method has turned out to be one of the best catalysts for CRM. During the 2000 h

stability test, the catalyst showed stable performance with very low carbon formation, attributing to its high surface area, high metal dispersion, strong metal-support interaction, and formation of different types of stable solid solutions. The conclusion, that the addition of Co can remarkably inhibit coke formation, is uncontroversial. The ratio of Ni/Co plays a crucial role in the activity of the catalyst. The NiCo catalyst with a small amount of Co has higher activity. The study on catalyst Co-Ni-Mg-O solid solution platelets enclosed by facets (Fan et al., 2015) revealed the role of Co in the catalyst. Co was enriched on the surface of NiCo alloy, enhanced the gasification of coke intermediates, and accelerated the chemisorption of oxygen in CO₂. These effects of Co on the catalyst modification are mainly attributed to the strong affinity of Co. Much lower energy is needed to oxidize metallic Co than other metals, like Ni or noble metals. The metallic Co on the catalyst can be oxidized by CO₂ to Co-O, then reduced to metallic Co by carbon species originating from CH₄ dissociation. As a result, the presence of Co improves the adsorption of CO₂ due to the strong interaction of Co-O, which helps to decrease the carbon deposition by enhancing carbon removal. (Ruckenstein and Wang, 2002; Bian et al., 2017) Furthermore, the Ni reduction was mitigated by Co because of the interaction between them, resulting in smaller metallic particle formation. This can improve the stability of the catalyst. (Wang and Zaidi, 2013) The Co monometallic catalyst supported by MgO, γ -Al₂O₃, and MgO-spinel has been studied (Wang and Ruckenstein, 2001; Ruckenstein and Wang, 2002; Wang et al., 2013). The Co catalyst supported by MgO-spinel shows higher activity and stability due to the properties of support.

The addition of Fe to Ni-based catalysts also improved its ability for carbon resistance. Research (Theofanidis et al., 2015, 2016; Kim et al., 2017) has been done to study the role of Fe in the Ni-Fe catalyst. It has been found that Ni and Fe were distributed uniformly in the alloy particles and the effect of Fe on carbon resistance was due to the redox properties of Fe. Fe partially

segregated from the NiFe alloy and formed FeO_x , then FeO_x was reduced by the surface carbon during the reaction. Thus, the carbon species on the catalysts can be rapidly removed, resulting in a lower amount of accumulated carbon. A similar conclusion was drawn based on the study of Ni-Fe bimetallic catalysts by Kim and co-workers (Kim et al., 2017). A dealloying-realloying process is exhibited in Figure 2-2. Through the $\text{Fe}^{2+}/\text{Fe}^0$ redox cycle, the stability of the catalyst was increased. But according to the study of Zhang et al., 2007, the NiFe catalyst prepared by the co-precipitation method had poor catalytic performance and higher amount of carbon formation than that by NiCo. To date, no Fe monometallic catalyst has been reported to have better activity for CRM reaction.

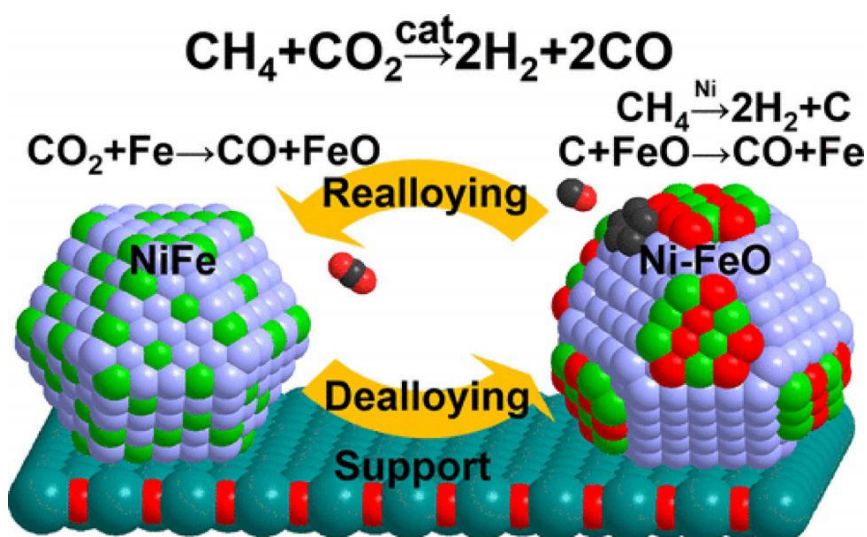


Figure 2-2 Schematic diagram of the dealloying-realloying process on Ni-Fe bimetallic catalyst in CRM reaction (Kim et al., 2017)

Compared to the studies on NiCo and NiFe catalysts, there are not much discussion on NiCu and NiMn bimetallic catalysts, especially in terms of the reaction mechanism. Lee et al., 2004 and Wu et al., 2015 have found that the addition amount of Cu on Ni-based catalysts was crucial. Less amount of Cu addition can promote the CRM activity and increase the coke resistance. It was found

that Cu-rich alloy was formed and facilitated carbon growth over the NiCu catalyst with higher Cu loading.

The addition of Mn to Ni/SiO₂ catalyst enhanced the dispersion of Ni particles and promoted the formation of smaller Ni particles (Yao et al., 2013). The study on the self-supported Ni-Mn catalyst prepared by Menezes et al., 2016 indicated that Mn had a significant promotion on the activity and stability of the catalyst. However, Rouibah et al., 2017 prepared a series of Ni-based bimetallic catalysts by co-precipitation and observed the most severe deposition of coke formed on the Ni-Mn catalyst due to the high Mn surface content and low Ni dispersion compared to the Ni-Cr and Ni-Co catalysts.

2.1.2 Mechanism of CRM reaction

The mechanism of CRM reaction was discussed in detail by Papadopoulou et al., 2012 and the scheme is shown in Figure 2-3.

Step 1: methane adsorption and activation. As the CH₄ is introduced into the system, it is activated on the metallic site, Ni or NiM₂ alloy, to form carbon species (C*) and H₂ (equation 2-5). The CH₄ dissociation to carbon species may not be completed by one step. There may be methyl-like species (CH_x) formed. It is reported that the degree of methane decomposition depended on the active metal and the nature of the support. It is generally agreed that CH₄ dissociation is a slow reaction and the rate-determining step during the reaction.

Step 2: carbon dioxide adsorption and activation. The catalytic sites for CO₂ adsorption and activation also depend on the nature of active metal and support of the catalytic system. It can be the active metal, the support (metal oxide), or the interface of metal and support. The most accepted statement was that CO₂ is activated on the basic sites. It is generally considered that CO₂

decomposition is a fast reaction. It occurs in three coordination geometries: carbon atom only adsorbs on the surface of catalyst; carbon atom and one of the oxygen atoms adsorb on the surface and the other oxygen atom exposed; both oxygen atoms form bonds with surface metal. The latter two are more favorable in CRM reaction. In this step, there are activated CO₂ (CO₂*) or CO and oxygen species (O*) formation (equation 2-6).

Step 3: surface reaction. This step is quite fast and contains hydroxyl group formation and intermediates oxidation and desorption. Surface hydroxyl groups are formed based on the spillover of hydrogen from CH₄ dissociation and oxygen from CO₂ decomposition. The surface hydroxyls or oxygen species oxidize the carbon species or CH_x to form eventually CO and H₂. In short, oxygen species or activated CO₂ from the basic sites react with carbon species on the metallic sites, forming CO and H₂ (equation 2-7). The accessibility of basic sites to the metallic sites (or accessibility of metallic sites to basic sites) is important in this step.

During the reaction, the relative rate of dissociation of CH₄ and oxidation of carbon species is crucial. Higher CH₄ dissociation rate leads to the formation of surface carbon, which cannot be oxidized by activated CO₂ or oxygen species from CO₂ decomposition immediately. As a result, the carbonaceous species begin to form and accumulate from the surface carbon, causing the deactivation of the catalyst.



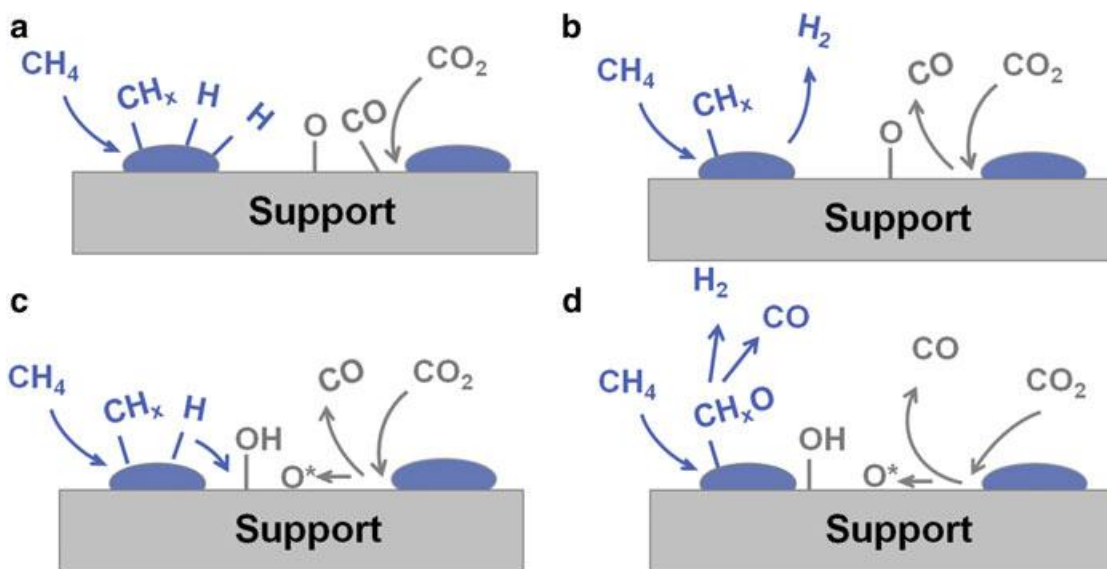


Figure 2-3 Reaction steps for CRM. (a) step 1; (b) step 2; (c-d) step 3. (Papadopoulou et al., 2012)

2.1.3 Contribution of our group to the development of Ni-based catalyst

Professor Wang's group at the University of Saskatchewan has patented a highly active and stable Ni-based catalyst for CRM reaction, which has been tested in lab and pilot plant scales for over 2000 h and 1500 h, respectively. The following studies were performed in this area.

1. To develop the CRM catalyst which can be used for industrial purpose, sophisticated analyses including stoichiometry, thermodynamics, and reaction mechanism of CRM system were conducted. This revealed that the properties of a suitable catalyst must have (a) thermal stability at reaction temperature, (b) relatively high surface area and proper pore size and volume, (c) strong support-metal interaction, and (d) small and stable metallic sites (Ni) with acceptable dispersion (Zhang, 2008; Wang and Zaidi 2013). Besides, the commonly available and low-cost materials and simple development procedures were the priorities of the selection of metals and preparation methods. After comparison of the performance of catalysts such as NiCo, NiFe, NiCu, and NiMn

supported by MgAlO_x oxide matrix prepared by co-precipitation method, it was found that NiCo catalyst with a lower amount of active metal loading displayed high activity and excellent stability, due to the high metal dispersion, the strong interaction of metallic and basic sites, and formation of stable solid solutions (Zhang et al., 2007; Zhang, 2008).

2. Since the property of metallic sites, such as the size of metallic particles and the number of metallic sites are the key factors for affecting the performance of the catalysts, the impact of reduction on the growth of the metallic nanoparticles was studied (Wang et al., 2013). Based on the synchrotron X-ray absorption spectroscopy study, it was found that the reduction of Ni was mitigated by Co, Co reduction promoted by Ni, and there was a strong interaction between Ni and Co atoms leading to the formation of alloy.
3. Then the effects of the support structures, namely the properties of basic sites on the surface properties of the catalyst, and thus the performance during the reaction were studied with changing the Mg/Al ratio in the catalysts (Alabi, 2018). It demonstrated that at a higher Mg/Al ratio there was MgO-solid phase and spinel structure on the catalyst, and only spinel structure was observed at the lower ratio. The MgO phase improved the basicity and reduction of the active metals, resulting in the higher activity and better stability of catalyst for CRM reaction.
4. To develop the catalyst suitable for the industrial application, the biogas, coal gas, and feed containing H_2S or SO_2 were used as feedstocks to study the catalysts' performance (Shakouri, 2018). It revealed that the steam content in the biogas can affect the performance of the catalyst, and the NiCo catalyst was more stable than other monometallic catalysts (Ni or Co). With the coal gas as feedstock, the activity of catalyst NiCo was influenced by the ratio of CH_4 and CO_2 . The investigation of the catalyst deactivation in sulfur-containing gases presented that the support of NiCo catalyst

provided additional active sites for CH₄ dissociation during catalyst poisoning by H₂S or SO₂.

5. Then the shaped NiCo catalysts, such as spherical catalysts and cylindrical/extrudate catalysts, prepared were stable and active for the CRM reaction during 800-900 °C with the strength similar to the commercial spherical alumina ones (Shakouri, 2018).

The literature study and Professor Wang's group research showed that the properties of metallic sites and basic sites were studied, however, no sufficient attention has been given to the contiguity of these two catalytic sites. For the CRM reaction involving two reactants to be activated on different types of activation sites, not only the number and activity of the sites but also the distribution and orientation of catalytic sites, namely site contiguity, determine the mechanism and kinetics. The contiguity of basic and metallic sites is later found as one of the key factors impacting the performance of the CRM catalyst. A study becomes necessary to explain the CO₂ catalytic activation process, further for the development of the catalyst with the right orientation of catalytic sites.

2.2 CO₂ Hydrogenation for Methanol Synthesis

Compared to nature's photosynthesis to recycle CO₂ and water into plant life, then fossil fuels, which take sufficient geological time, chemical recycling of CO₂ to methanol can be achieved in a short time via CO₂ capture and subsequent conversion to methanol. Related methanol economy is shown in Figure 2-4 (Olah et al., 2009). Through the reaction of carbon dioxide hydrogenation to methanol (equation 2-8), one of the greenhouse gases (CO₂) can be converted to value-added products, methanol. The product methanol is a feed for productions of many chemicals and clean liquid fuel, like dimethyl ether, ethylene, propylene, and other products, which are obtained from

petroleum or natural gas. The hydrogen for CO₂ hydrogenation reaction can be obtained from thermochemical cleavage of H₂O with solar or nuclear energy, which is an emission friendly energy source. After the combustion of methanol and its derivatives, CO₂ is released and the carbon cycle is completed (Olah, 2005; Olah et al., 2009; Goeppert et al., 2014). In this cycle, CO₂ hydrogenation to methanol is one of the key reactions, which may solve both the environmental issue and energy shortage in the modern industry.

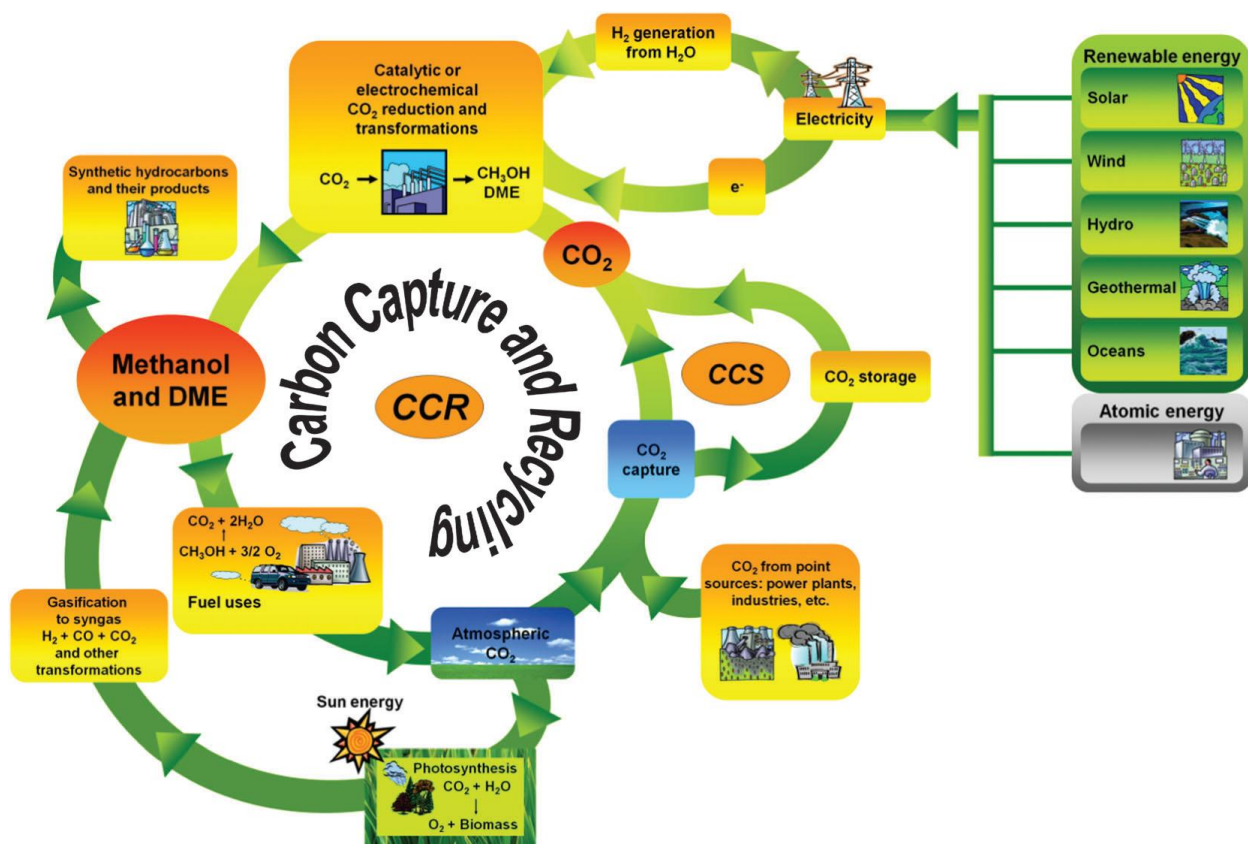
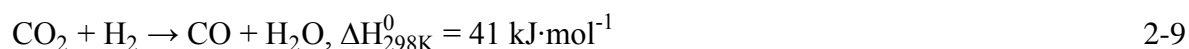
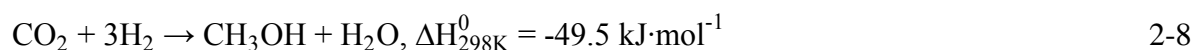


Figure 2-4 Anthropogenic carbon cycles based on the methanol economy (Olah et al., 2009)

Although CO₂ hydrogenation to produce methanol (equation 2-8) is an exothermic reaction, the high reaction temperature is in favor of the activation of CO₂. However, high temperature also contributes to the formation of by-products CO and other hydrocarbons, because these side reactions are endothermic. (Ma et al., 2009) Among the side reactions, the RWGS reaction

(equation 2-9) is the main one, which decreases the catalyst's selectivity to methanol significantly. The methanol synthesis from CO₂ is less favored thermodynamically as compared to that from CO (Fujimoto and Yu, 1993). The equilibrium yield of methanol from CO₂ hydrogenation is less than 40 % at 200 °C, but it is more than 80 % from CO hydrogenation (Jadhav et al., 2014). Thus, a catalyst with high activity and selectivity is essential for this reaction. The CO₂ hydrogenation for methanol synthesis reaction results in a reduction in the number of molecules. Therefore, it should be facilitated at high pressure.



2.2.1 Development of Cu-ZnO catalysts

Catalysts are developed in order to minimize or prevent the occurrence of side reactions. Lots of work have been done to study Cu-based catalyst for methanol synthesis with different modifiers, like Zn, Zr, Ce, Ga, Al, Si, V, Ti, etc, and various supports, such as ZnO, SiO, Al₂O₃ (Wang et al., 2011). Among all of these, the Cu-ZnO catalyst has been predominantly studied for CO₂ hydrogenation reaction (Wang et al., 2011). The summary of the performance of the Cu-ZnO catalysts is shown in Table 2-1.

Table 2-1 The performance of Cu-ZnO catalysts with different supports for CO₂ hydrogenation to produce methanol.

Catalyst	Preparation method	CO ₂ conversion (%)	Methanol selectivity (%)	Methanol formation rate (mmol·g ⁻¹ h ⁻¹)
Cu-ZnO/Al ₂ O ₃ (Tisseraud et al., 2015)	Co-precipitation	4.1	17.8	1.3
Cu-ZnO/Al ₂ O ₃ (Ahouari et al., 2013)	Co-precipitation	10.0	8.0	2.4
Cu-ZnO/Al ₂ O ₃ (Kobl et al., 2016)	Co-precipitation	19.5	37	9.7
Cu-ZnO/ Al ₂ O ₃ (Gesmanee and Koo-Amornpattana, 2017)	Incipient wetness impregnation	0.2	22.5	0.5
Cu-ZnO/Al ₂ O ₃ (Lei et al., 2016)	Citric acid as fuel by mechanical milling and combustion method	16.2	63.8	4.1
Cu-ZnO/Al ₂ O ₃ (Lei et al., 2016)	Carbonate co-precipitation	8.1	63.3	2.1
Cu-ZnO/Al foam (Z. Liang et al., 2017)	Hydrothermal	9.9	82.7	23.2
CuO-ZnO-Al ₂ O ₃ graphene nanosheet (Liu et al., 2014)	High energy ball milling method	14.6	62.3	11.3
Cu-ZnO/Al ₂ O ₃ (Arena et al., 2013)	Commercial	20.0	42.0	8.3
CuZn/NrGO (Deerattrakul et al., 2016)	Incipient wetness impregnation	26.0	5.1	13.3
Cu-Zn-Zr (Bonura et al., 2014)	Co-precipitation with NaHCO ₃	16.0	48.7	9.0
Cu-Zn-Zr (Bonura et al., 2014)	Complexation with citric acid	12.5	51.8	7.5

Catalyst	Preparation method	CO ₂ conversion (%)	Methanol selectivity (%)	Methanol formation rate (mmol·g ⁻¹ h ⁻¹)
Cu-Zn-Zr (Bonura et al., 2014)	Gel-oxalate co-precipitation	18.0	51.2	10.6
Cu-ZnO/CeO ₂ (Arena et al., 2013)	Reverse co-precipitation	8.0	70.0	5.5
Cu-ZnO/ZrO ₂ (Arena et al., 2013)	Reverse co-precipitation	10.0	62.0	37.5
Cu/ZnO/ZrO ₂ (Kobl et al., 2016) (Angelo et al., 2015)	Co-precipitation	23.2	33.0	10.3
Cu-ZnO-ZrO ₂ -MgO/Al ₂ O ₃ (Ren et al., 2015)	Impregnation	12.12	35.9	1.0
Cu/CuO-ZnO on Mesoporous carbon (Duan et al., 2014)	In-situ method without precipitate addition	4.0	10.2	0.2
Cu/CuO-ZnO on Mesoporous carbon (Duan et al., 2014)	In-situ method with precipitate addition	5.3	87.0	1.7
Cu/CuO-ZnO on Mesoporous carbon (Duan et al., 2014)	Ex-situ method with co-precipitate addition	27.0	69.0	7.3
Cu@ZnO _x (Le Valant et al., 2015)	Surface modification precipitation process	2.3	100.0	4.6
Cu/ZnO/Al ₂ O ₃ (Dasireddy and Likoza, 2019)	Ultrasonic co-precipitation	13.5	10.5	5.1
CuZnAl (Liang et al., 2019)	Commercial	≥50.0	≤1.0	5.7
Cu/ZnO plate (Huang et al., 2019)	Simple hydrothermal method and impregnation method	3.5	81.0	6.3

It is observed from the literature review that some catalysts exhibit high conversion but poor selectivity to methanol while the others show prominent selectivity of methanol but lower CO₂ conversion. There is no catalyst yet offering both high CO₂ conversion and high methanol selectivity. On the high conversion-low selectivity side, Duan et al., 2014 prepared Cu-ZnO catalyst supported on mesoporous carbon. The catalyst showed a relatively high CO₂ conversion of 27 %, and high methanol selectivity of 69 % due to the excellent contact between Cu/CuO and ZnO particles. The Cu-ZnO catalyst (Deerattrakul et al., 2016) supported by reduced graphene oxide nanosheets also showed CO₂ conversion of 26 % resulting from good dispersion of Cu-Zn particles enhanced by the support, but much low methanol selectivity of 5 %. Cu/ZnO/ZrO₂ catalyst (Dong et al., 2016) prepared by precipitation-reduction method showed CO₂ conversion of 23 % and selectivity to methanol of 57 %. The study found that the CO₂ conversion was related to the surface area of exposed Cu, and methanol selectivity is related to the number of basic sites.

On the high selectivity-low conversion side, Cu@ZnOx core-shell catalyst (Le Valant et al., 2015) prepared by precipitated ZnO on the surface of Cu powders showed 100 % of selectivity to methanol, and CO₂ conversion of 2 %. The excellent selectivity was due to the alloy formation and migration of Zn. Cu-Zn/Al foam catalyst (Z. Liang et al., 2017) prepared via hydrothermal method showed selectivity to methanol of 83 % and CO₂ conversion of 10 %. Compared with other Cu based catalysts, Cu-Zn/Al foam catalyst possessed a great heat and mass transfer properties and suitable amount of strong basic sites.

To develop the catalysts with high CO₂ conversion and selectivity to methanol, the mechanism of the CO₂ hydrogenation reaction over Cu-ZnO should be understood.

2.2.2 Mechanism of the CO₂ hydrogenation reaction

Cu or ZnO alone had little effect on methanol synthesis, shown by Karelovic et al., 2012. However, the combination of Cu and ZnO enhanced the catalyst performance dramatically, revealed by Gesmanee & Koo-Amornpattana, 2017. ZnO is regarded as structure-directing support to improve the dispersion of metallic Cu particles during reduction and acts as a spacer between the Cu particles (Behrens, 2009; Behrens et al., 2012). ZnO could provide active sites for spillover of hydrogen (Waugh, 1992; Fujimoto and Yu, 1993; Gesmanee and Koo-Amornpattana, 2017; Hu et al., 2018). According to a study of Cu-based catalysts modified by ZnO, ZrO₂, and MgO, Ren et al., 2015 observed that Cu⁰ sites were the catalytic active centers for hydrogenation of CO₂ to methanol. However, Choi et al., 2001 discovered that Cu-Zn sites were the active sites for CO₂ hydrogenation to methanol. Kanai et al., 1994 found that parts of ZnO migrated onto the surface to form Cu-Zn alloy, and that Cu⁺ species formed in the vicinity of ZnO_x were regarded as active sites for methanol synthesis. The group of Tisseraud and Le Valant (Le Valant et al., 2015; Tisseraud et al., 2015, 2016, 2018) have done much work to study the Cu-ZnO catalysts. They reported that the active sites for CO and methanol synthesis were different. CO was produced on ZnO sites and methanol was produced on ZnO_x, which were formed on the interface of Cu and ZnO through cross-diffusion of Cu and ZnO. The model of the CO₂ hydrogenation is presented in Figure 2-5. The activity of the catalysts was found to be related to the number of “contact points” of Cu and ZnO.

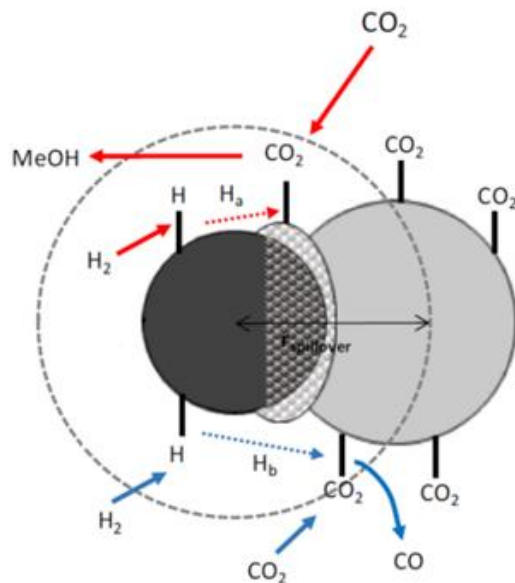


Figure 2-5 Model representation of the CO₂ hydrogenation: active sites for methanol and CO over a Cu/ZnO catalyst. (Tisseraud et al., 2015)

Although a variety of mechanisms were proposed and some of them were debatable, one recognized that CO₂ was activated by one type of sites, say ZnO or ZnO related, and H₂ by another type, say metallic Cu or Cu related. Each type alone cannot have the activity for the activation of either H₂ or CO₂. The metallic sites (Cu or Cu related) and basic sites (ZnO or ZnO related) must be next to each other to form the right structures to facilitate the formation of methanol. If not, the two active sites may form the wrong structures to help the formation of CO. The activated CO₂, still in molecular form, needs assistance from the activated H to pull one O away and to insert H in at the same time to form C-H and O-H bonds. In other words, the right structures must be able to perform two functions at the same time, pulling one O away to form H₂O and inserting H atoms in to form methanol. Beside one activated CO₂, there must be two units of activated H atoms available. There should be enough H atoms around the activated CO₂. In other words, enough metallic sites should be prepared around one basic site.

Based on the literature study related to the development of catalysts such as Cu-ZnO and the reaction mechanism over these catalysts, we have proposed two extreme catalyst models to ascertain how the right structure should be. The first model of catalyst contains isolated Cu-related particles distributed in a layer of ZnO atoms, and the second shows isolated ZnO phases distributed in a layer of Cu or surrounded by sufficient Cu nanoparticles. To develop the pursued catalysts, the atomic layer deposition method was used as one of the catalyst preparation methods.

2.3 Atomic Layer Deposition Technique in Catalyst Development

Atomic layer deposition (ALD) is a thin film growth technique. In this method, gaseous precursors are used to grow thin films on the surface of the substrate by atomic layers through self-limiting reactions (Lu et al., 2012). ALD was first used in transistor material preparation and battery manufacturing. In the past few years, ALD has been used to prepare catalysts to further study of the mechanism of the catalytic reaction and the structure-property relationships of the catalysts by preparing the catalysts with a controlled distribution of particle size, element composition, and catalytic sites.

The deposition process relies on discrete pulsing of chemical precursors that act as an element source of the desired film (see Figure 2-6). Typically, one of the precursors is a metal precursor with the high vapor pressure, which reacts with the substrate as the first half-reaction (Figure 2-6 a,b). The reactive ligands of the metal precursor reacted with the active sites on the substrate. The exposure of the substrate to the precursor stops and the unreacted precursor and reaction by-product are purged out of the system with an inert gas when the first half-reaction reaches completion (Figure 2-6 c). Through the second half-reaction between the substrate and the other precursor, the remaining ligands of the metal precursor are removed, the active sites are regenerated, and the

reaction cycle is completed (Figure 2-6 d). Then the system is purged again after the completion of the surface reaction (Figure 2-6 e). This procedure is repeated until the desired thickness of the metal oxide is achieved (Figure 2-6 f) (Janocha, 2011; Lu et al., 2012; Oneill et al., 2015).

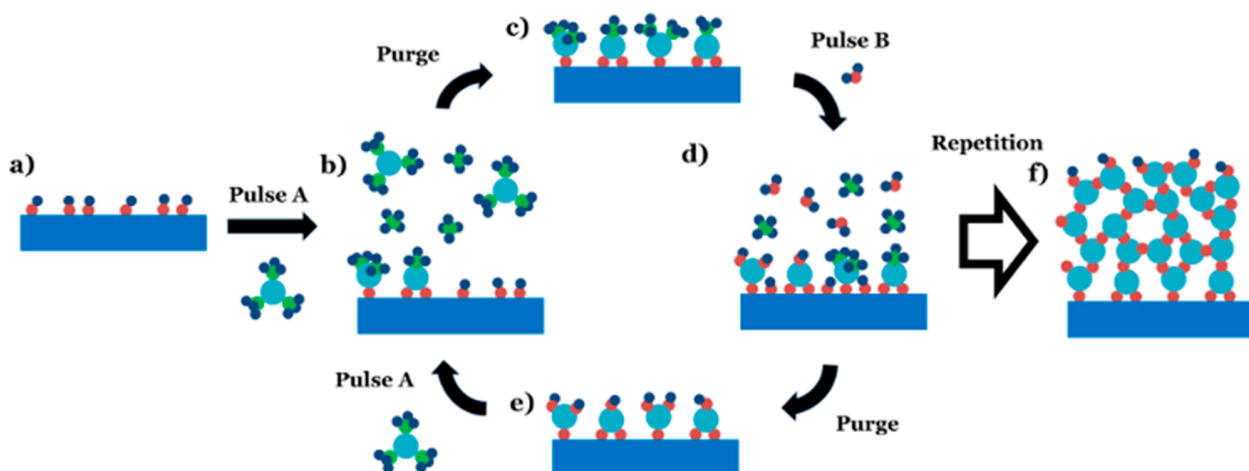


Figure 2-6 Scheme of film ALD with a binary (AB) precursor system. a) substrate with reactive sites; b) exposed the substrate to the first precursor and first half-reaction occurred; c) purging of unreacted precursor and reaction byproducts; d) exposed to the second precursor and second half-reaction happened; e) purging; f) film resulting from several ALD cycles. (Oneill et al., 2015)

The superiority of ALD in the development of catalysts is related to the deposition of active metals or nanoparticles in atomic layers uniformly (Oneill et al., 2015). During the deposition of the materials, the structure and component of the ALD layer are dependent on the chosen precursors. By selecting an appropriate substrate, precursor, and preparation condition, atomic layer(s) or nanoparticles can form on the surface of the catalyst. In the preparation of nanoparticles on the surface of the substrate, the initial metal particles deposited on the substrate could act as nucleation points, and subsequent precursors will form bonds with former metals instead of the substrate because of the Volmer-Weber growth mechanism. These interactions allow the formation of core-

shell metal nanoparticles (Feng et al., 2010; Rikkinen et al., 2011; Masango et al., 2014). However, if the precursor is allowed with enough time to react with all the active bonds on the substrate, a saturated metal oxide layer can be deposited on the surface of the substrate (Oneill et al., 2015).

Taking advantage of the ALD technique on the deposition of nanoparticles or atomic layer(s) via choosing an appropriate substrate, precursor, and preparation condition, the Cu-ZnO catalysts with a particular structure can be developed.

CHAPTER 3 Experimental Methodology

3.1 Catalysts Preparation

3.1.1 Ni monometallic and NiM2 bimetallic catalysts

The Ni monometallic and NiM2 bimetallic catalysts supported by MgO-spinel were synthesized by the co-precipitation method. The various metal nitrates [nickel (II) nitrate hexahydrate (98 to 102% purity; Alfa Aesar), cobalt (II) nitrate hexahydrate (98 to 102% purity; Alfa Aesar), magnesium nitrate hexahydrate (98 to 102% purity; Alfa Aesar) and aluminum nitrate nonahydrate (98 to 102% purity; Alfa Aesar)] were used as precursors to prepare the solution through dissolving in de-ionized water. The other NiM2 catalysts were prepared by replacing cobalt nitrate with manganese (II) nitrate hexahydrate (99.98% purity; Fisher Scientific), copper (II) nitrate hemi-(pentahydrate) (98 to 102% purity; Alfa Aesar), or iron (III) nitrate nonahydrate (99% purity, Lancaster Synthesis), respectively.

During the precipitation procedure, the salt solution and the base solution (ammonium hydroxide; 28 to 30 w/w%; Fisherbrand) were simultaneously pumped to a container to maintain the pH in the solution at the desired pH value of 8.5-8.7 at any time until a certain amount of salt solution is used up. Then the precipitate was collected using a Buchner vacuum filtration unit. The filtrate cake was washed until the pH value of the washing fluid was 7. Then the filtrate cake was

dried at 120 °C overnight to remove water and calcined at 850 °C for 6 hours. The calcined catalysts were ground and sieved to the desired size, with radius of 0.165 mm. In the heterogeneous catalytic reaction, the external mass transfer is associated with feed flow rate. The discussion about external mass transfer is shown in 3.3.1. The internal mass transfer is dependent on the radius of the catalyst particles. Based on the previous study in the group, it is determined that when catalyst particle size was less than 0.200 mm, the internal mass transfer can be neglected (Zhang, 2008). The catalysts prepared are named Ni, NiCo, NiMn, NiCu, and NiFe.

3.1.2 ZnO over-coated Cu/SiO₂ catalysts

Silica gel (6-12 mesh, grad 40; Fisher Chem) was ground and particles in the size of 255-350 nm range was chosen as the support. Silica gel was used as the support due to its high surface area and suitability as the substrate for the ALD procedure.

Cu nanoparticles were prepared by dry impregnation (Imp) method or strong electronic adsorption (SEA) method. Compared to the SEA method, Imp method is simpler and more manageable. If Imp can prepare Cu nanoparticles as small and uniform as SEA, it would be chosen. In the Imp method, a certain amount of copper nitrate hemi-pentahydrate ($\text{Cu}(\text{NO}_3)_2 \cdot 2.5 \text{H}_2\text{O}$, 98~102%; Aldrich), which can give 5 wt% of Cu in the catalyst, was dissolved in 2 mL distilled water. The ammonia hydroxide (28 wt%; Sigma-Aldrich) was added into the Cu precursor solution dropwise to form copper hydroxide solid, then the solid was re-dissolved to be a dark blue solution, which is tetraamine copper (II) ion, $[\text{Cu}(\text{NH}_3)_4]^{2+}$. Distilled water then was added into the solution of $[\text{Cu}(\text{NH}_3)_4]^{2+}$ until the volume was the same as the pore volume of the substrate. The prepared solution of $[\text{Cu}(\text{NH}_3)_4]^{2+}$ was added to silica gel dropwise with manual mixing. The resultant solid was dried overnight at 110 °C and calcined at 250 °C for 3 h. The sample was named as Imp-5Cu.

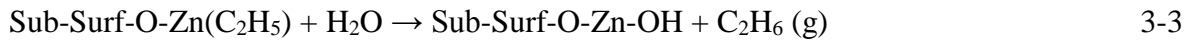
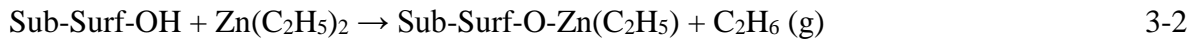
The resultant solid was also calcined at 500 °C, then named as Imp-5Cu-CT500. The names of the samples prepared are given in Table 3-1.

In the SEA method, the substrate (silica gel) was pretreated in 50 mL ammonia solution for 30 min to adjust the surface charge, which is opposite to the $[\text{Cu}(\text{NH}_3)_4]^{2+}$. The pH of the ammonia solution was higher than 10. The copper nitrate was dissolved in 50 mL of H_2O . Then ammonia solution was added to the solution of copper nitrate to form $[\text{Cu}(\text{NH}_3)_4]^{2+}$ solution. After the pretreatment of silica gel, the solution of $[\text{Cu}(\text{NH}_3)_4]^{2+}$ was added to the silica gel mixture and stirred for 2 h. The solid was filtered, washed, dried at 110 °C overnight, and calcined at 250 °C for 3 h. The samples were named as SEA-5Cu (with 5 wt% of Cu in the catalyst) and SEA-10Cu (with 10 wt% of Cu in the catalyst). The solids were also calcined at 500 °C, then named as SEA-5Cu-CT500 and SEA-10Cu-CT500 (Table 3-1).

ZnO layer(s) on the samples with Cu was prepared by the atomic layer deposition (ALD) method using a Beneq TFS 200 equipment. Diethyl zinc (DEZ) (Sigma-Aldrich) was used as the Zn precursor and H_2O employed as the oxidant. Nitrogen (UHP, Praxair Canada Inc.) was used to purge the gas lines and the reactor. The temperature of the reaction was set at 150 °C to avoid the formation of metallic Zn. The ALD cycle follows the reaction (Janocha, 2011):



This reaction splits into two half-reactions:



The first half-reaction (equation 3-2) in the ZnO deposition procedure is shown in Figure 3-1 a-d. DEZ vapor was first introduced to the chamber (Figure 3-1 a) and reacted with hydroxyls which were on the surface of the substrate to form monoethylzinc. The monoethylzinc replaced

hydrogen and connected to the oxygen atom with the release of ethane (Figure 3-1 b). The chamber was purged with N_2 to remove the unreacted precursor and gaseous products (Figure 3-1 c). Then a surface was saturated by monoethylzinc molecules (Figure 3-1 d). After well purging, the second half-reaction (Figure 3-1 f-h) began by allowing H_2O vapor to the chamber (Figure 3-1 e) to react with the monoethylzinc, forming hydroxyls bonded with Zn, and releasing ethane (Figure 3-1 f). The chamber was again purged with N_2 to remove the unreacted oxidant and the gaseous products (g). The hydroxide formed a chemical bond with Zn atom on the surface of SiO_2 , and the surface was ready for the next layer of over-coated ZnO. SiO_2 surface with saturated hydroxide is obtained by the first ZnO layer deposition followed by introducing H_2O to the chamber to pre-treat the surface of SiO_2 . In each ZnO ALD run, before steps (a) and (e), the pressure of the chamber was reduced to 1.2 kPa and the valve, which separated the chamber and the pump, was closed until the purging procedure started. Finally, exposure time and/or the number of cycles were changed to obtain catalysts with different atomic layers and properties. The samples were named as given in Table 3-1.

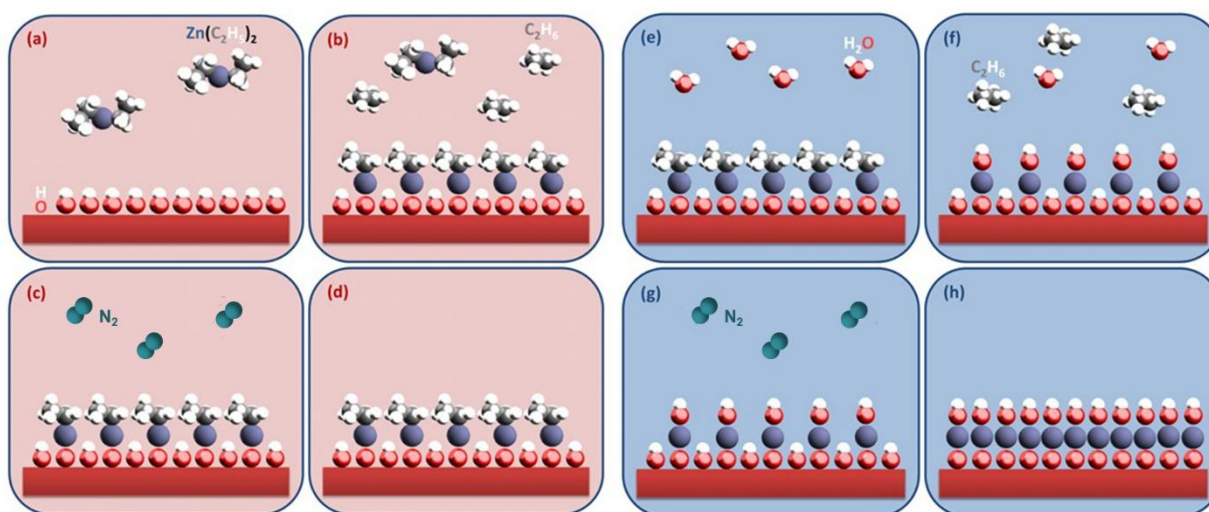


Figure 3-1 Reaction mechanism of ALD using DEZ and H_2O to form ZnO. (a) DEZ exposure; (b) monoethylzinc replaced H and connected to atomic O; (c) N_2 purge; (d) monoethylzinc saturated

surface; (e) H₂O exposure; (f) H₂O react with the monoethylzinc to form hydroxyls bonded with Zn; (g) N₂ purge; (h) hydroxide saturated ZnO monolayer. (Janocha, 2011)

Table 3-1 Catalysts prepared by Imp or SEA and ALD method and calcined under different calcination temperatures.

Samples ^a	Cu content (wt%)	Method	Calcination T (°C)	ALD exposure time (s)	ALD cycles
Imp-5Cu	5	Dry impregnation	250	-	-
SEA-5Cu	5	SEA	250	-	-
SEA-10Cu	10	SEA	250	-	-
Imp-5Cu-CT500	5	Dry impregnation	500	-	-
SEA-5Cu-CT500	5	SEA	500	-	-
SEA-10Cu-CT500	10	SEA	500	-	-
5Cu-1CyZn-5s	5	SEA	250	5	1
5Cu-1CyZn-30s	5	SEA	250	30	1
5Cu-5CyZn-5s	5	SEA	250	5	5

^a For the samples calcined at 250 or 500 °C, they are named as name-CT250 or 500. For the reduced samples at 250 or 500 °C for 2 h, they are named as name-RT250 or 500.

3.2 Catalyst Characterization

3.2.1 Inductively Coupled Plasma Mass Spectrometry (ICP-MS)

The elemental compositions of Ni monometallic and NiM₂ bimetallic catalysts and ZnO over-coated Cu/SiO₂ catalysts were obtained using ICP-MS analysis. The analysis was carried out by the equipment of PerkinElmer Optima 5300 DV/Optima 8300 DV at Saskatchewan Research

Council, Saskatoon, SK, Canada. The element could not be detected if it is less than $0.1 \text{ ug}\cdot\text{g}^{-1}$ ($1 \times 10^{-5} \text{ wt\%}$) in the catalyst.

3.2.2 N₂ Adsorption-Desorption Experiment

The textural properties of the Ni monometallic and NiM2 bimetallic catalysts and ZnO over-coated Cu/SiO₂ catalysts were determined by N₂ adsorption-desorption experiment. The experiment was carried out using Micromeritics ASAP 2020 with 100-200 mg sample. The degassing was carried out at 200 °C and 500 µmHg (66.6 Pa) for 2 h to remove the moisture and adsorbed gases from the surface of the samples. Then the N₂ adsorption was carried out at -196 °C. Brunauer–Emmett–Teller (BET) method was used to calculate the surface area of the catalysts. The pore volume and pore size were obtained from the N₂ isotherm adsorption branch by Barret – Joyner-Halenda (BJH) method.

3.2.3 H₂ temperature-programmed reduction (H₂-TPR)

The reduction of active metals on ZnO over-coated Cu/SiO₂ catalysts was studied using the Micromeritics 2950 HP Chemisorption Analyzer, equipped with a thermal conductivity detector (TCD). Approximately 50 mg sample was used for each run. Argon (UHP, Praxair Canada Inc.) was used to purge the U-shaped sample holder until the baseline of TCD was stable. Then, H₂-TPR analysis was conducted by heating samples from room temperature to 650 °C at a ramp of 10 °C/min. The flow rate of 10% H₂/Argon was maintained at 50 mL per minute.

3.2.4 Transmission Electron Microscope (TEM) and Energy-Dispersive X-ray Spectroscopy (EDX)

The metallic particle size and its distribution on Ni monometallic and NiM2 bimetallic catalysts and ZnO over-coated Cu/SiO₂ catalysts were investigated using TEM by scanning the reduced catalysts. 4 spots were randomly selected for each sample. The size of each particle on these spots was measured, based on which the average and distribution of particle size were determined. The distribution of the elements on the ZnO over-coated Cu/SiO₂ catalysts was determined by EDX. The analyses were both done using HITACHI HT-7700 with Bruker X-ray detector at Western College of Veterinary Medicine imaging center, University of Saskatchewan, SK, Canada.

3.2.5 CO Chemisorption

The number of active metallic sites and the dispersion of active metal of the Ni monometallic and NiM2 bimetallic catalysts and ZnO over-coated Cu/SiO₂ catalysts were obtained by CO chemisorption. The study of monometallic Ni and bimetallic NiM2 catalysts was performed using Micrometrics AutoChem II 2920 instrument. The sample (100 mg) was weighed and loaded in the quartz tube before it was reduced in-situ with 10 v/v% H₂/He at 750 °C for 4 h. Then the chemisorption analysis was conducted by passing the pulses of CO gas. The measurement of ZnO over-coated Cu/SiO₂ catalysts was carried out on the Micrometrics ASAP 2020 instrument at Taiyuan University of Technology, China. After the catalyst (100 mg) was loaded in the quartz tube and degassed, it was reduced at 500 °C for 2 h and cooled down under vacuum to 35 °C. Then the chemisorption analysis was conducted by passing the pulses of CO gas.

3.2.6 CO₂ temperature-programmed desorption (CO₂-TPD)

The basicity of the Ni monometallic, NiM2 bimetallic catalysts, and ZnO over-coated Cu/SiO₂ catalysts were studied using CO₂-TPD. The study was performed using the Micrometrics 2950 HP Chemisorption Analyzer, fitted with a thermal conductivity detector (TCD). The sample (50 mg) was placed in the U-shaped sample holder and pretreated at 250 °C for 20 min in a He atmosphere to remove physically adsorbed CO₂. Then the CO₂ adsorption was carried out at 50 °C. Afterward, the CO₂ desorption was performed with a linear temperature increase up to 800 °C at a rate of 10 °C/min.

3.2.7 X-ray Diffraction (XRD)

The X-ray diffraction (XRD) analysis of the reduced ZnO over-coated Cu/SiO₂ catalysts was conducted on the Bruker Advance D8 series II, equipped with Cu K α radiation ($\lambda=0.1541$ nm). The crystallite sizes of the reduced catalysts were estimated using Scherer's equation:

$$\text{size} = k\lambda / \beta(2\theta) \cos\theta \quad 3-4$$

where k is the crystallite shape constant (0.94), λ is the X-ray wavelength and $\beta(2\theta)$ is the full width at half maximum in radians. The lattice constants for the reduced catalysts were determined by Bragg's law.

$$n\lambda = 2d \sin \theta \quad 3-5$$

where n is the order of diffraction and d is the spacing between the different planes of atoms in the crystal lattice.

3.2.8 X-ray Absorption Spectroscopy (XAS)

The reduction extent of Ni, M2 was determined by X-ray absorption near edge structure (XANES) spectroscopy measurement for the Ni monometallic and NiM2 bimetallic catalysts. The measurements were conducted for Ni K-edge (8333 eV), Co K-edge (7709 eV), Mn K-edge (6539 eV), Cu K-edge (8979 eV) and Fe K-edge (7112 eV) at soft X-ray micro-characterization beamline (SXRMB) in Canadian Light Source. A few milligrams of powder calcined and reduced samples were loaded on carbon tape. The metal and metal oxide contents in reduced catalysts were calculated by linear combination fitting (LCF) of XANES in the range of -20 to +30 eV of edge jump.

The Cu K-edge and Zn K-edge XAS measurements of ZnO over-coated Cu/SiO₂ catalysts were conducted at the SXRMB and Industry, Development, Education, and Students (IDEAS) beamline, respectively. Both Cu K-edge and Zn K-edge were collected in fluorescence and transmission modes. The energy range for Cu was from 8879 eV to 9527 eV, and from 9507 eV to 10407 eV for Zn

3.3 Catalysts Evaluation

3.3.1 CO₂ reforming of CH₄ over Ni monometallic and NiM2 bimetallic catalysts

The reaction of CO₂ reforming of CH₄ over the Ni monometallic and NiM2 bimetallic catalysts was carried out in a fix-bed quart tube reactor of 1/8 inch of inner diameter and 15 inches of length. For a run, 50 mg catalyst was diluted with 450 mg of silica carbide and loaded into the temperature-constant zone of the reactor, which was then put into the furnace and connected with the gas-feeding and analysis system. The catalyst was first reduced at 750 °C or 850 °C in the 40

v/v% H₂ (99.9% purity, Praxair Canada Inc.) mixed with N₂ (99.9% purity, Praxair Canada Inc.) at a flow rate of 100 mL·min⁻¹ for 4 hours. Then the CRM reaction was carried out at 750 °C with an equimolar CH₄ (99.2% purity, Praxair Canada Inc.), CO₂ (99.9% purity, Praxair Canada Inc.), and N₂ at a flow rate of 90 mL·min⁻¹. The previous study indicated that when the feed flow rate was higher than 70 mL·min⁻¹, the external mass transfer effect can be neglected (Zhang, 2008). Thus 90 mL·min⁻¹ is used in this study. The product gas was analyzed using on-line gas chromatography (GC) (Agilent 6890N), equipped with a thermal conductivity detector (TCD) and a ShinCarbon ST100/12 packed column (RESTEK) with 1-mm ID and 2-m length. Helium (Ultra-high purity 5.0, Praxair Canada Inc.) was used as the carrier gas for GC.

To measure the relative reaction rate of CH₄ dissociation and CO₂ decomposition occurring during the CRM reaction, further evaluate the stability of the catalysts, pulse adsorption experiments were designed. The experiments were carried out by introducing only one of the reactants first to the reactor packed with freshly reduced catalyst, or the catalyst pre-adsorbed to saturated with the other reactant. Before the pulse adsorption experiment, the catalysts were reduced with a 40 % H₂/N₂ mixture at 750 °C for 4 h. After purging the reactor with pure N₂ for 10 min, only CH₄ or CO₂ (N₂: 30 mL·min⁻¹, CH₄ or CO₂: 30 mL·min⁻¹) was injected to the reactor. After 1 min, the product gas was analyzed by the on-line GC. Different waiting time before the analysis by GC was tested, determining 1 min was the most suitable time. Most products were detected at this time. The pulse adsorption experiment was also done with the pre-adsorbed catalyst. The well-reduced catalyst was first exposed to CO₂ or CH₄ until no gas was adsorbed by the catalyst. Then the other reactant, CH₄ or CO₂ was introduced into the system with the pre-adsorbed catalyst for 1 min before the product gas was analyzed.

Turnover frequency (TOF) of CH₄ was calculated based on the number of metallic sites on reduced catalysts, and the TOF of CO₂ was calculated based on the number of basic sites and the number of metallic sites, separately.

$$\text{TOF}_{\text{CH}_4} = \frac{\text{reaction rate of CH}_4}{\text{number of metallic sites}} \quad 3-6$$

$$\text{TOF}_{\text{CO}_2} = \frac{\text{reaction rate of CO}_2}{\text{number of basic sites}} \quad 3-7$$

$$\text{TOF}'_{\text{CO}_2} = \frac{\text{reaction rate of CO}_2}{\text{number of metallic sites}} \quad 3-8$$

3.3.2 CO₂ hydrogenation reaction over ZnO over-coated Cu/SiO₂ catalysts

The evaluation of the ZnO over-coated Cu/SiO₂ catalysts with CO₂ hydrogenation reactions was conducted in an Inconel fixed bed reactor (ID: 22 mm and length: 450 mm) with a single-pass downward flow. 1 g of catalyst was diluted with 90 mesh size silicon carbide particles and loaded in the constant temperature zone of the reactor. Other parts of the reactor were filled with different sizes of silicon carbide by layers. The catalyst was then reduced under H₂ (99.9% purity, Praxair Canada Inc.) flow (120 mL·min⁻¹) at atmospheric pressure (ramp from room temperature to 500 °C, rate 3 °C·min⁻¹, isothermal for 3 h). The reduced catalyst was cooled down to 250 °C under H₂ flow. The desired reaction gas flow rates were adjusted to a total volumetric flow rate of 160 mL·min⁻¹ (H₂:CO₂=3:1) (CO₂: 99.9% purity, Praxair Canada Inc.). Then the reactor was pressurized to the reaction pressure of 4.0 MPa. The gas product was cooled to 0 °C in a cold trap to separate the condensable gas in the product stream into the liquid phase at the reaction pressure.

The flow rate and compositions of non-condensable gases in the stream were measured by a bubble flow column installed at the exit of the reactor and an Agilent Technologies 7890A gas chromatograph instrument equipped with two thermal conductivity detectors (TCD) and a flame

ionization detector (FID). The liquid products were collected during a 24-h reaction period and analyzed with an off-line Agilent Technologies 7890A gas chromatograph equipped with a DB-Wax capillary column and FID detector. The weight of liquid products was measured after the collection to ensure the mass balance.

Conversion of CO₂ was calculated as average values for the total test duration.

$$X_{\text{CO}_2} = 100\% \times \frac{n_{\text{CO}_2,\text{in}} - n_{\text{CO}_2,\text{out}}}{n_{\text{CO}_2,\text{in}}} \quad 3-9$$

Methanol selectivity was calculated with respect to carbon-containing products (no other product obtained except CH₃OH and CO).

$$S_{\text{CH}_3\text{OH}} = 100\% \times \frac{n_{\text{CH}_3\text{OH}}}{n_{\text{CH}_3\text{OH}} + n_{\text{CO}}} \quad 3-10$$

Turnover frequency of CO₂ was calculated based on the number of basic sites on reduced catalysts.

$$\text{TOF}_{\text{CO}_2} = \frac{\text{reaction rate of CO}_2}{\text{number of basic sites}} \quad 3-11$$

Turnover frequency of H₂ was calculated based on the number of metallic sites on reduced catalysts.

$$\text{TOF}_{\text{H}_2} = \frac{\text{reaction rate of H}_2}{\text{number of metallic sites}} \quad 3-12$$

CHAPTER 4 CO₂ Catalytic Activation for CO₂ Reforming of CH₄ over Ni Monometallic and NiM₂ Bimetallic Catalysts

Based on the literature study, during the reaction of CO₂ reforming of CH₄ (CRM), CO₂ is activated on the metal oxide phase, which is basic sites in nature, and the other reactant, CH₄ is adsorbed and activated into CH_x or carbon (C*) species on the surface of active metal, as well as metallic sites. When the basic and metallic sites are close enough to each other, surface hydroxyls or oxygen species from the basic sites oxidizes the CH_x or C* from the metallic sites to form CO and H₂. The previous research in Professor Wang's research group had developed a highly active and stable Ni-based catalyst, and studied the effects of dispersion and distribution of active metal, modification of second metal, and various support on the performance of Ni-based catalysts. However, for this catalytic reaction involving two reactants to be activated on different types of activation sites, not only the number and activity of the sites but also the site distribution and orientation, namely site contiguity, impacted the reaction mechanism and kinetics. Thus, a study becomes necessary to determine the effects of the neighborhood, the accessibility, and the orientation of these two types of sites on their catalytic performances.

In this work, the contiguity of CO₂ activation sites, which are the basic sites, and the CH₄ activation sites, which are the metallic sites, are studied by using different second metals in addition to Ni on Ni-second metal bimetallic catalysts for CRM reaction. Then the contiguity effects were

confirmed by developing larger metallic particles on the catalysts, and analyzing the earlier results with varying the strength of basic sites.

4.1 Bulk Properties of Oxide Catalysts for CO₂ Reforming of CH₄

In this study, the catalysts for CO₂ reforming of CH₄ were made using co-precipitation method. The precipitates were calcined at 850 °C in air to form the desired oxides. The solid structure and basic sites were formed during calcination. The bulk properties, which include the composition, the crystal structures, and the specific surface area and porous structures were measured by ICP-MS, XRD, and N₂ adsorption, respectively. The detailed procedures are given in Chapter 3.

4.1.1 Metal composition by ICP analysis

The metal compositions, and Mg/Al ratio of the catalysts obtained from ICP-MS, are shown in Table 4-1. The target loading of metals was 6 % (Ni:M2 = 1:1). The reproducibility of the ICP results are shown in Appendix A. There was 5.1 wt% of Ni loaded on the catalyst Ni, with Mg/Al ratio of 1.8. The Ni and Co loadings on catalyst NiCo were 2.6 and 4.6 wt %, respectively, with Mg/Al ratio of 2.5. In the catalyst NiMn, the loadings of Ni and Mn were 1.8 and 1.2 wt %, respectively, with the Mg/Al ratio of 2.1. There were Ni and Cu loadings of 1.7 and 1.6 wt % respectively in NiCu catalyst, with Mg/Al ratio of 2.5. The catalyst NiFe had Ni and Fe loadings of 1.7 and 1.1 wt %, respectively, with Mg/Al ratio of 2.5.

The procedure for co-precipitation cannot control the elemental compositions precisely. Shifts in pH during the procedure led to different ratios of desired metals than the targeted values in precipitation method, especially for those whose solubility product (K_{sp}) values were large. Since the M2 had different K_{sp} and some of M2 precursors formed a complex in basic solution, it resulted

in different loadings of metals and Mg/Al ratio. Different Mg/Al ratios may lead to different activities of each basic site and the number of basic sites on the catalysts. But the monometallic Ni and bimetallic NiM2 catalysts prepared were very useful to study the contiguity effects of metallic and basic sites.

Table 4-1 Compositions of metals and Mg/Al ratio in monometallic Ni and bimetallic NiM2 catalysts

Catalysts	Ni	M2	Mg	Al	Mg/Al mole ratio
	(wt %)				
Ni	5.1	-	21.0	12.7	1.8
NiCo	2.6	4.6	26.0	11.6	2.5
NiMn	1.8	1.2	16.8	8.9	2.1
NiCu	1.7	1.6	20.6	9.0	2.5
NiFe	1.7	1.1	20.9	9.4	2.5

4.1.2 Bulk structure by XRD analysis

The XRD analysis was used to identify the bulk morphological phase of monometallic Ni and bimetallic NiM2 catalysts. The results are shown in Figure 4-1. The patterns of monometallic Ni and bimetallic NiM2 catalysts didn't show much difference from each other. The phase was assigned to the MgO-solid phase with characteristic diffraction peaks 2θ at 43.1° , 62.4° , 74.7° , and 78.6° . The diffraction peaks relative to spinel structure at 2θ can be seen at $2\theta = 19.1^\circ$, 31.4° , 34.7° , 36.9° , 39.0° , 45.9° , 60.6° , and 65.2° (Al-Daous et al., 2012; Foo et al., 2012; Klym, 2017). The MgO phase had the structure of the face cubic centre. The spinel phase was a cubic structure, which can

be expressed by general chemical formula AB_2O_4 . In the normal spinel structure, A was the divalent cations in tetrahedral sites, B represented trivalent cations in octahedral sites. In the inverse spinel structure, cations A occupied some of the octahedral sites, the cations B occupied the tetrahedral sites. These two spinels existed in the support MgO-spinel (Dugué et al., 2012). In addition, Al_2O_3 was also shown spinel structure. From the phase structure of different catalysts Ni or NiM2, it was determined that the addition of M2 barely had an effect on the bulk structure of catalysts.

According to the study of bulk properties of these five catalysts with the same support, MgO-spinel, the addition of various M2 had not much influence on the bulk structure of the catalysts.

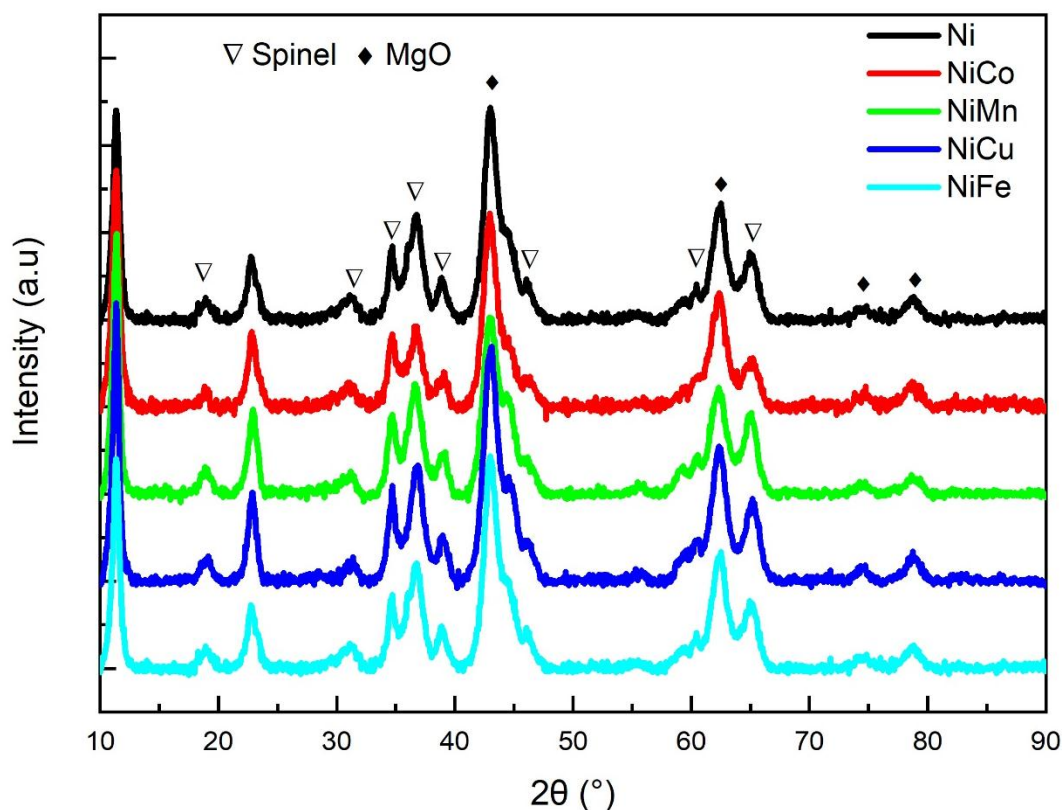


Figure 4-1 XRD patterns corresponding to the monometallic Ni and bimetallic NiM2 catalysts

4.1.3 Surface area and porous structures by N₂ adsorption-desorption

The isotherm results of N₂ adsorption-desorption of monometallic Ni and bimetallic NiM₂ catalysts are shown in Figure 4-2. According to the IUPAC classification (Sing et al., 1985), all the catalysts had the hysteresis loop which is the characteristic feature of the Type IV isotherm. The loop was associated with capillary condensation, which takes place in mesoporous material. However, the catalysts had different types of hysteresis loops as shown in Figure 4-2. The catalysts NiCo, NiCu, and NiFe displayed Type H1 hysteresis loop, which was often related to solid materials with a narrow distribution of pore size. The catalyst Ni and NiMn exhibited the loop of Type H3. The results of ICP-MS showed that the Mg/Al ratio in catalysts NiCo, NiCu, and NiFe was 2.5, but this value in catalyst Ni and NiMn was approximately 2.0. Thus, the uniformity of pores on the catalyst was associated with the Mg/Al ratio, as well as the amount of MgO in the support. The correlation also had been confirmed by the earlier work in Professor Wang's research group. It was found that significant amount of MgO can enhance the uniformity of the pores shown on the support (Alabi, 2018).

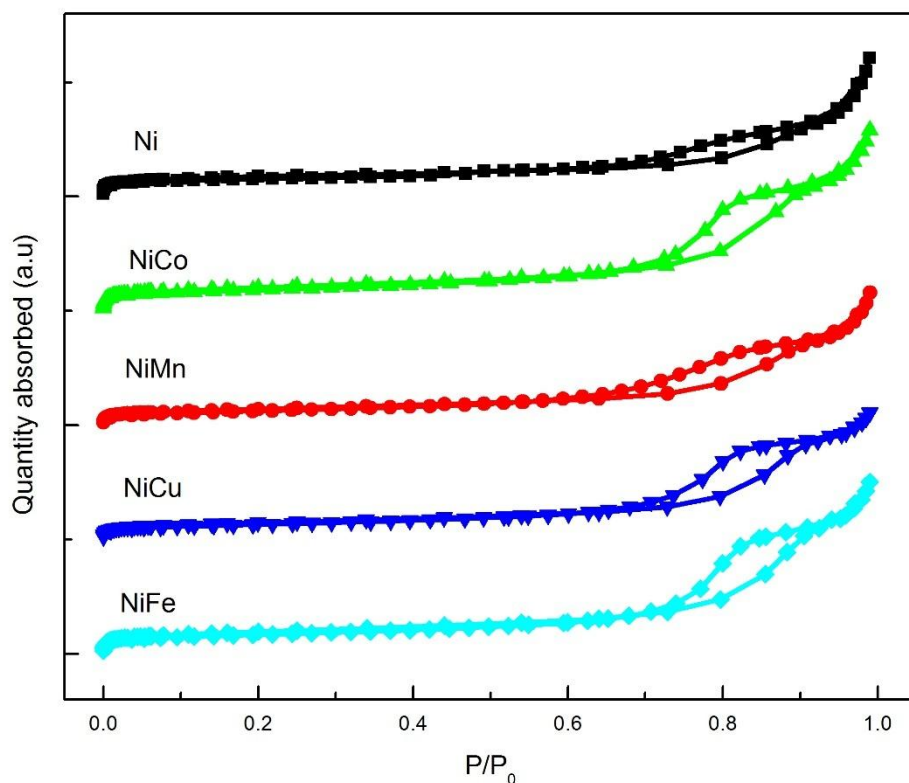


Figure 4-2 N₂ adsorption-desorption isotherms of monometallic Ni and bimetallic NiM₂ catalysts

The BET surface area, pore volume, and average pore diameter of the monometallic Ni and bimetallic NiM₂ catalysts from the N₂ adsorption are shown in Table 4-2. The BET surface areas of catalysts NiCo and Ni were similar and higher at 111-113 m²·g⁻¹. Meanwhile, NiMn, NiFe, and NiCu catalysts had a lower surface area at 58-81 m²·g⁻¹. Among these catalysts, the NiCu catalyst had the biggest pore volume of 0.31 cm³·g⁻¹ and the smallest average pore diameter of 13.8 nm. On the contrary, the Ni catalyst had the smallest pore volume of 0.18 cm³·g⁻¹ and the biggest average pore diameter of 19.8 nm. The pore volumes of NiCo, NiMn, and NiFe catalysts were 0.29, 0.26, and 0.24 cm³·g⁻¹, respectively. The average pore diameters of NiCo, NiMn and NiFe catalysts were 15.2, 15.3, and 16.7 nm, respectively.

Table 4-2 BET surface area, pore volume and pore diameter of the monometallic Ni and bimetallic NiM2 catalysts

Catalysts	BET surface area, $\text{m}^2\cdot\text{g}^{-1}$	Pore volume, $\text{cm}^3\cdot\text{g}^{-1}$	Average pore diameter, nm
Ni	113	0.18	19.8
NiCo	111	0.24	16.7
NiMn	81	0.26	15.3
NiCu	58	0.31	13.8
NiFe	75	0.29	15.2

Relative to monometallic Ni catalyst, the addition of the second metal generally made the pore volume larger and the average pore diameter smaller. Theoretically, larger pore volume and smaller pore diameter led to larger specific surface area. However, the use of a second metal in addition to Ni in catalyst preparation resulted in larger pore volume, smaller pore diameter, but similar or smaller specific surface area, which remained unclear. Based on XRD, MgO-spinel seemed to be the backbone of the material morphology structure, which did not change by varying the second metal.

4.2 Catalysts Characterization after Reduction

The catalysts, produced after reduction, were used for the reactions as their properties after reduction had more direct impacts on reaction performances. Therefore, its characterization appeared to be more important. The reduction was the key step where the metallic sites were formed. The reduction conditions for the catalysts developed in Professor Wang's research group had been

studied earlier. The present work used the conditions developed earlier in Professor Wang's laboratories, at which Mg and Al in the oxide phases did not reduce (Zhang, 2008).

The information on the valence of active metal, including Ni, Co, Mn, Fe, and Cu, on the reduced monometallic Ni and bimetallic NiM₂ catalysts, were studied by XANES, and the extents of reduction of active metals were fitted by the linear combination fitting (LCF) based on the XANES spectra. The size of metallic particles was measured from the TEM images and the metal dispersion and the number of metallic sites were determined by the CO chemisorption analysis.

4.2.1 Reduction extent of metals

The Ni K-edge XANES of monometallic Ni and bimetallic NiM₂ catalysts after being reduced at 750 °C for 4 h were scanned. The Ni spectra of the catalysts, as well as those of metallic Ni and its oxide standards, are shown in Figure 4-3. The reproducibility of the XANES results has been studied and shown in Appendix A. It displays that the XANES spectra of Ni on all the catalysts fall between XANES for the standards of respective metal foil and metal oxide. It demonstrates that after reduction at 750 °C for 4 h, Ni in all the catalysts was just partially reduced.

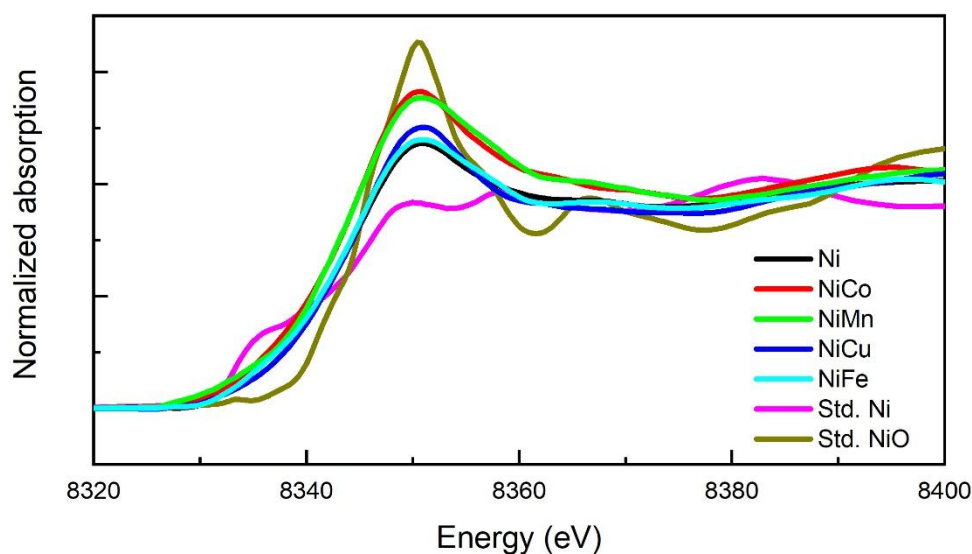


Figure 4-3 The Ni K-edge XANES spectra of monometallic Ni and bimetallic NiM2 catalysts after reduction at 750 °C for 4 h as well as those of Ni and its oxide standards

The K-edge XANES spectrum of each second metal in reduced catalyst was also scanned. The spectra of Co, Mn, Cu, or Fe K-edge XANES of the monometallic Ni and bimetallic NiM2 catalysts, as well as those of M2 foil and their oxide standards, are also shown in Figure 4-4,5,6 and 7. Obviously, the Co species on catalyst NiCo was not sufficiently reduced, and there were Co^0 , Co^{2+} , and no Co^{3+} species based on the comparison of Co XANES spectrum and those of Co foil, CoO, and Co_3O_4 standards. There are two components in Co_3O_4 . The reason for no Co^{3+} species in the reduced catalyst was due to the reduction of Co_2O_3 into CoO, which occurred at a lower temperature (Wang et al., 2013). According to Mn XANES spectrum and those of Mn foil, MnSO_4 , and MnO_2 in Figure 4-5, these were only Mn^{2+} and Mn^{4+} and no Mn^0 species present in the reduced NiMn catalyst. For NiCu catalyst (Figure 4-6), the Cu species was not sufficiently reduced, either. But from the XANES spectra of Cu on NiCu catalyst, Cu foil, Cu_2O , and CuO, the existence of Cu^{1+} species could not be determined. According to Fe XANES spectra of NiFe, Fe

foil, $\text{Fe}(\text{OH})_2$, and Fe_2O_3 in Figure 4-7, mixture of Fe^0 and Fe^{3+} species was present in the NiFe catalyst.

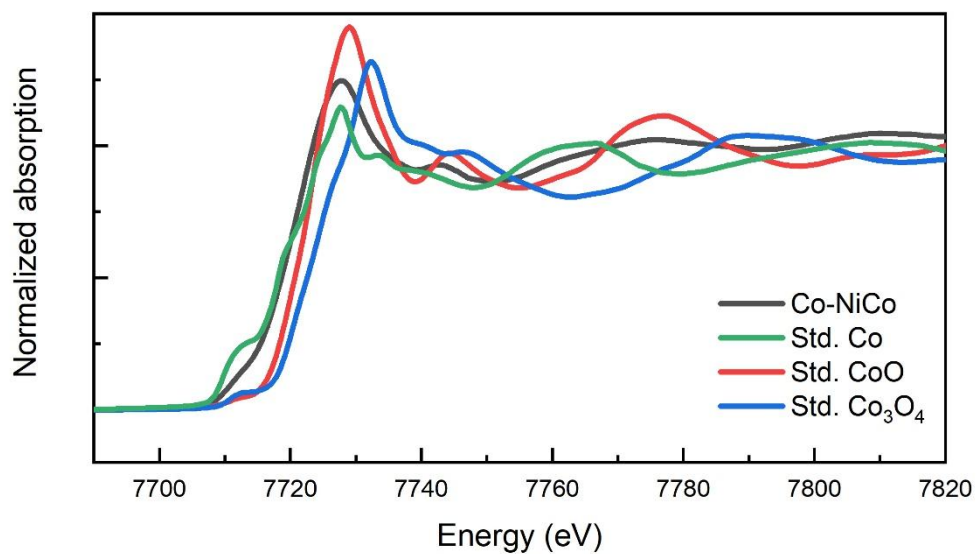


Figure 4-4 The Co K-edge XANES spectra of NiCo catalyst after reduction at 750 °C for 4 h as well as those of Co foil, and its oxide standards

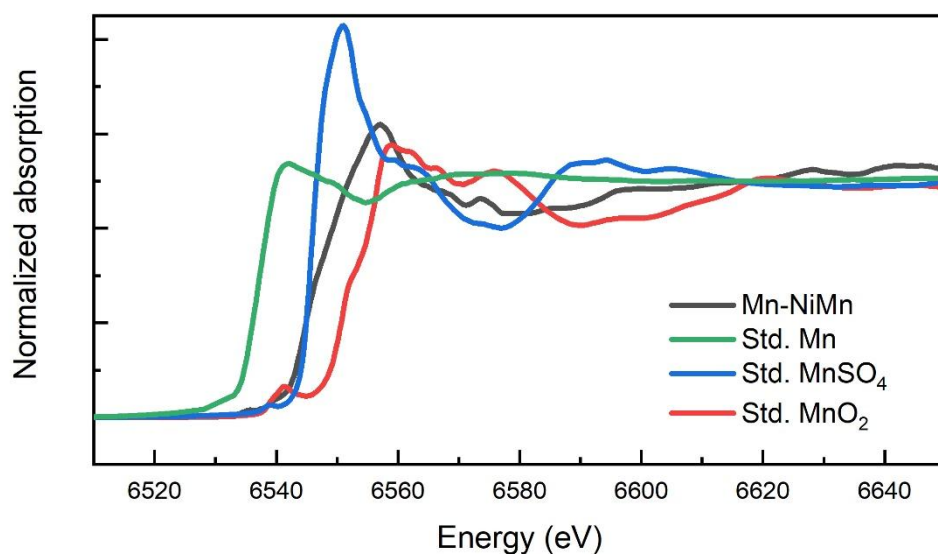


Figure 4-5 The Mn K-edge XANES spectra of NiMn catalyst after reduction at 750 °C for 4 h as well as those of Mn foil, and its oxide standards

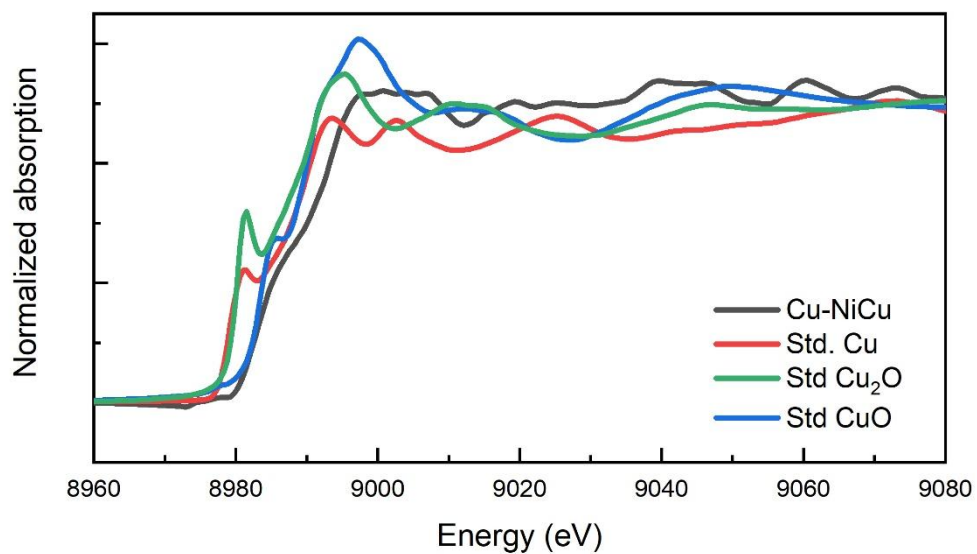


Figure 4-6 The Cu K-edge XANES spectra of NiCu catalyst after reduction at 750 °C for 4 h as well as those of Cu foil, and its oxide standards

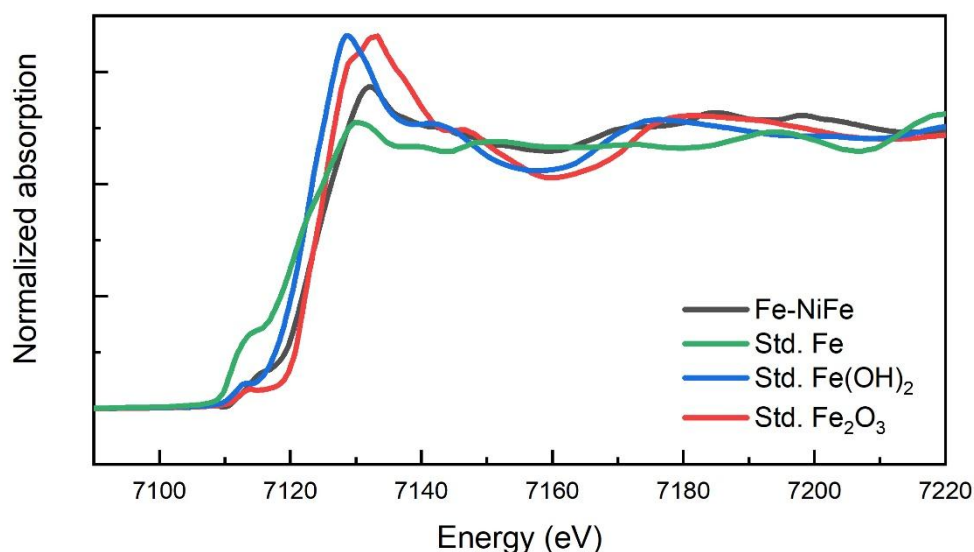


Figure 4-7 The Fe K-edge XANES spectra of NiFe catalyst after reduction at 750 °C for 4 h as well as those of Fe foil, and its oxide standards

To identify the extent of reduction of the metals in the catalyst samples, XANES linear combination fitting in the range of -20 to +30 eV of edge energy (Shakouri, 2018) was used to provide quantitative results shown in Table 4-3. The reduction extents of Ni in the catalysts Ni, NiFe, and NiCu were higher, 58 %, 54 %, and 47 % respectively, as compared to those in the catalysts NiCo and NiMn, which were only ~ 32 %. The results indicated that the Ni reduction in different catalysts was mitigated by M2. However, the degree of impact was different based on the attribute of M2.

The effects of M2 on the reduction of Ni were first noticed by Wang and co-workers (Wang et al., 2013) during the study on metal nanoparticle growth and bimetallic interaction of Ni-based catalysts for CRM. Then Alabi (Alabi, 2018) determined that the ratios of spinel and MgO phases in catalysts could also affect the extent of metal reduction. The Ni distributed in MgO phase was

reduced more easily than that in the spinel phase. Thus, the presence of the second metals changed the distribution of Ni in spinel and MgO phases, which impacted the extent of reduction of Ni.

The extent of reduction of second metal was also different. There were 28 % of Co^0 and 72 % of Co^{2+} species in the reduced NiCo catalyst. There were only Mn^{2+} and Mn^{4+} on the NiMn catalyst with the percentage of 46 and 49, respectively. The reduction of Cu and Fe on NiCu and NiFe catalysts were larger as compared to other NiM2 catalysts. 46 % of Cu^0 was formed in the NiCu catalyst after reduction at 750 °C for 4 h, and 64 % of Fe^0 was in the NiFe catalyst. The extent of reduction of M2 metals depended on their nature and interaction of Ni.

The amounts of reduced metals were calculated based on the composition of each metal and its extent of reduction. The results are shown in Table 4-4. Among these five catalysts, Ni had the most amount of metallic Ni formed after the reduction and the value was much larger than that of other catalysts. The extent of Ni reduction in the bimetallic catalysts NiM2 was similar, followed the order: $\text{NiFe} > \text{NiCu} > \text{NiCo} \approx \text{NiMn}$. Since Mg and Al in their oxide phase were not reduced at this reduction conditions, the reduction procedure does not change the total mass of the catalyst significantly.

Table 4-3 The contents of metals and metal oxides in reduced catalysts measured by the linear combination fitting of XANES.

Catalysts	Ni ⁰ /Ni ²⁺	Co ⁰ /Co ²⁺ /Co ³⁺	Mn ⁰ /Mn ²⁺ /Mn ⁴⁺	Cu ⁰ /Cu ⁺ /Cu ²⁺	Fe ⁰ /Fe ²⁺ /Fe ³⁺
Ni	0.58/0.42				
NiCo	0.32/0.68	0.28/0.72/0			
NiMn	0.32/0.68		0.05/0.46/0.49		
NiCu	0.47/0.53			0.48/0/0.52	
NiFe	0.54/0.46				0.64/0/0.36

Table 4-4 Metal compositions on the monometallic Ni and bimetallic NiM2 catalysts after reduction at 750 °C for 4 h

Catalysts	Reduced Ni	Reduced M2	Reduced metals
	(wt%)		
Ni	3.0	-	3.0
NiCo	0.8	1.3	2.1
NiMn	0.6	0.1	0.7
NiCu	0.9	0.6	1.4
NiFe	0.9	1.0	2.0

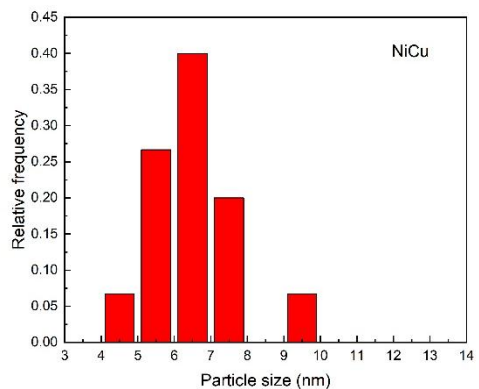
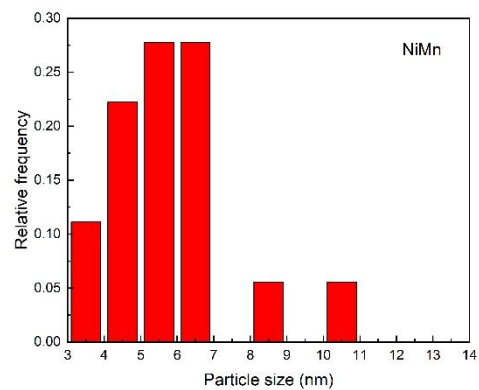
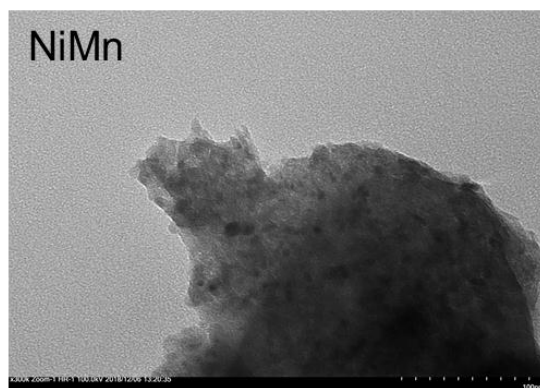
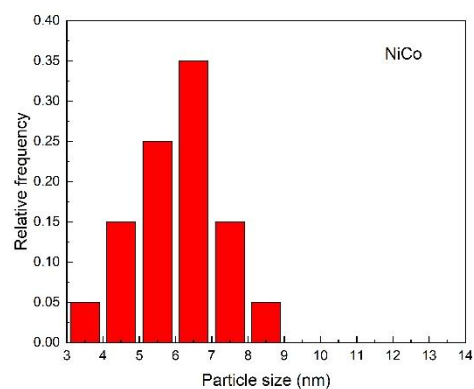
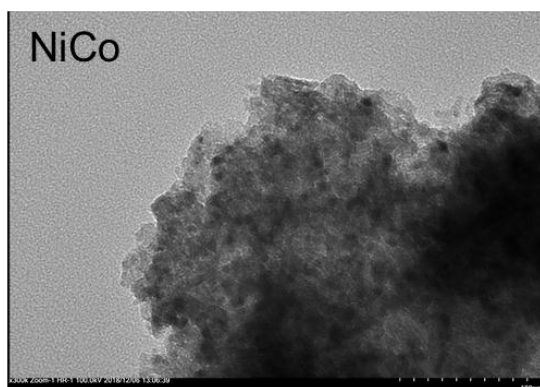
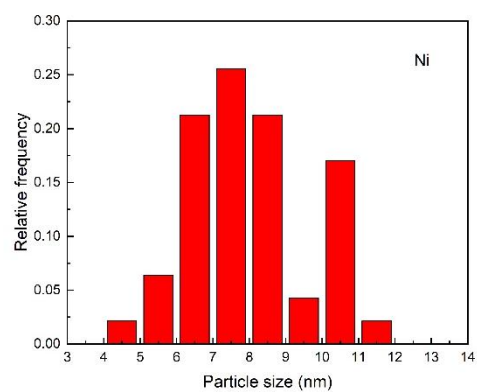
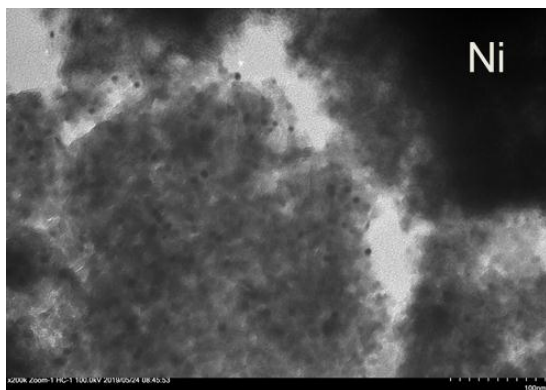
4.2.2 Particle size and distribution

If a reaction occurs on the single site of a catalyst, there is no issue of the contiguity. The contiguity is a description of how dual or multiple catalytic sites were next to each other in the

desired orientation to allow collision among different active species on them for reaction to take place. For CRM reaction, only metallic sites and basic sites that exist next to each other can allow carbon species on metallic sites, resulting in CH_4 dissociation, for the oxidation by the activated CO_2 on the basic sites. Most of the time, there was no direct measurement of the contiguity. However, many measurements from the catalyst characterizations can indicate the quality of contiguity of the catalytic sites. Metal particle size from TEM measurement is one of the indications of the catalytic sites' contiguity. Assuming the distribution of smaller metal particles in the same basic sites, they would allow more metallic sites to be exposed to basic sites as compared to larger particles. 9 nm was reported as a critical size for metallic particles for CRM below which the carbon deposition can be mitigated effectively (Rostrup-Nielsen et al., 2002; Alabi, 2018), meaning that the carbon species on such sites can be reached by activated CO_2 and consumed.

The TEM images and the particle size distribution of the catalysts reduced at 750 °C are shown in Figure 4-8. The micrographic analysis was done and the average metallic particle size was obtained and are shown in Table 4-5. Also, the percentage of those particles whose size was less than 9 nm is given in the table. This percentage can help to discuss the contiguity of metallic and basic sites.

Compared to the Ni catalyst with an average particle size of 8.1 nm, in the range of 4-12 nm and 77 % of particles smaller than 9 nm, there were smaller metallic particles formed on NiMn, NiCu, and NiCo catalysts, and more than 90 % of these particles were smaller than 9 nm, and most of the particles were in the range of 3-10 nm. The NiFe catalyst had bigger particles formed with an average size of 9.0 nm, in the range of 5-14 nm and only 55 % of the particles were smaller than 9 nm.



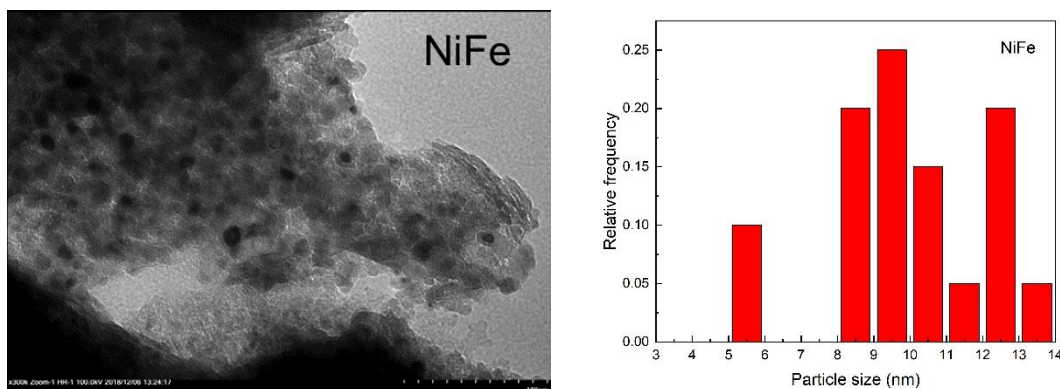


Figure 4-8 TEM images and the particle size distribution of the catalysts reduced at 750 °C

Table 4-5 Average particle size and particle size distribution from the TEM micrographs of catalysts reduced at 750 °C

Catalysts	Average particle size (nm)	Relative percentage < 9 nm (%)
Ni	8.1	76.6
NiCo	7.0	100
NiMn	5.8	94.4
NiCu	6.5	93.3
NiFe	9.0	55.0

According to the size of particle formed and their distributions from the TEM images, addition of Mn, Co, or Cu as the second metal to Ni-based bimetallic catalysts was helpful in reducing the metal size, further in the formation of good contiguity of metallic and basic sites. There were some explanations of the capability of M2 in controlling the size of metallic particles. Fan et al., 2010 and Lee et al., 2004 proposed that there was a synergistic effect displayed by NiCu and NiCo catalysts due to the formation of alloy. The integrity of Ni ensembles on the surface of the catalysts

was broken by Co or Cu, decreasing the size of the metallic particles during reduction. Yao et al., 2013 reported that the addition of Mn encouraged the dispersion of Ni species on the catalyst.

In this work, it was found that the particle size was basically proportional to the extent of reduced metal. It meant that with more active metal reduced at 750 °C in the catalysts, the bigger particles were formed. So, the effect of M2 on the size of metallic particles was based on how M2 affected the extent of reduction of active metal. The addition of Mn, Co, and Cu mitigated the reduction of Ni, then reduced the size of Ni particles in the catalysts formation. This may be due to the interaction between Ni and Mn, Co, or Cu.

4.2.3 Number of metallic sites and metal dispersion

During the CRM reaction, CH₄ was adsorbed and dissociated on the metallic sites. Thus, the number of metallic sites and metal dispersion was a critical property to evaluate the catalyst performance. The properties of metallic sites were detected by CO chemisorption, shown in Table 4-6. The number of metallic sites was obtained by the amount of CO uptake during the analysis, and all the CO molecules were linearly chemisorbed on the metal molecules on the surface of the catalyst. The metal dispersion is defined as surface metal over total metal atoms in the catalyst. Compared to the Ni catalyst, Fe favored increase in the surface metallic sites from 19 to 55 $\mu\text{mol}\cdot\text{g}^{-1}$ and metal dispersion from 2.2 to 11.3 %. However, Co, Mn, and Cu lowered the number of metallic sites to 9-11 $\mu\text{mol}\cdot\text{g}^{-1}$ and metal dispersion to about 2 %. Among these, the NiCo catalyst showed the lowest metal dispersion of 0.9 %.

Table 4-6 The number of metallic sites and metal dispersion of catalysts based on CO chemisorption analysis

Catalysts	CO adsorption ($\mu\text{mol}\cdot\text{g}^{-1}$)	Metal dispersion (%)
Ni	19	2.2
NiCo	11	0.9
NiMn	10	1.9
NiCu	9	1.7
NiFe	55	11.3

It seemed that the number of metallic sites and the metal dispersion of the catalysts were both associated with the extent of reduction of metals. The presence of Co, Mn, or Cu in the Ni-based catalysts lowered the extent of reduction of metals, thus the number of metallic sites and the metal dispersion.

4.3 Basicity of the monometallic Ni and bimetallic NiM2 catalysts

The basicity of the monometallic Ni and bimetallic NiM2 catalysts was detected by CO₂-TPD. Based on the studies in the literature (Di-Cosimo et al., 1998; Debecker et al., 2009; Alabi, 2018) on the basicity of the catalysts supported by MgO-spinel, the CO₂-TPD curves of some catalysts showed three desorption peaks at around 100, 400 and 650 °C. These peaks were assigned to weak, moderate, and strong basic sites, respectively. During the CO₂-TPD analysis, the amounts of CO₂ desorption at these three temperatures were the number of weak, moderate, and strong basic sites, respectively. The CO₂-TPD profiles for different catalysts and the support (MgO-spinel) are shown

in Figure 4-9, and the information related to each basic site is summarized and displayed in Table 4-7.

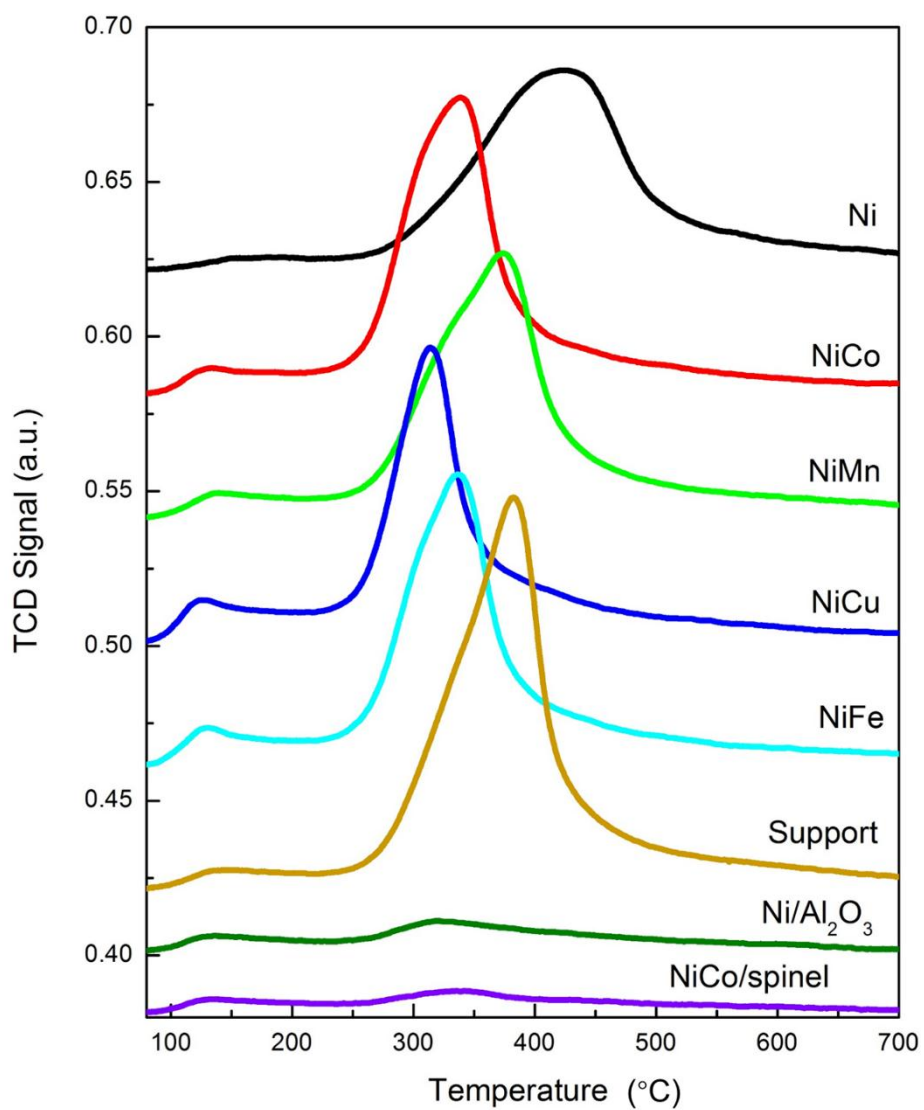


Figure 4-9 CO₂-TPD curves of the Ni and NiM2 catalysts, support, Ni/Al₂O₃, and NiCo/spinel

Table 4-7 Basic properties of Ni and NiM2 catalysts, support, Ni/Al₂O₃, and NiCo/spinel

Catalysts	Weak basic sites	Moderate basic sites		Total number of basic sites ($\mu\text{mol}\cdot\text{g}^{-1}$)
	Number of basic sites ($\mu\text{mol}\cdot\text{g}^{-1}$)	Number of basic sites ($\mu\text{mol}\cdot\text{g}^{-1}$)	Percentage of moderate sites (%)	
Ni	20	6810	99.7	6830
NiCo	101	5878	98.3	5979
NiMn	53	6203	99.2	6256
NiCu	175	4498	96.2	4674
NiFe	194	5874	96.8	6068
Support	24	7643	99.7	7667
Ni/Al ₂ O ₃	218	786	78.3	1004
NiCo/spinel	184	580	75.9	764

Two desorption peaks were shown in the profiles of CO₂-TPD at the desorbed temperatures of 130 °C and 350 °C. In this study, the CO₂-TPD curves of the monometallic Ni and bimetallic NiM2 catalysts only showed two desorption peaks, which were assigned to the weak and moderate basic sites, separately. On the basis of the literature, the weak basic sites were related to the OH⁻ groups. The moderate basic sites were ascribed to the M-oxygen pairs (M=Mg, Al, Ni, and M2) (Debecker et al., 2009).

The main peak was the moderate one in the CO₂-TPD curves of the catalysts Ni, NiM2, and support, which accounted for 96 % of the total amount. The moderate basic site is known as the main basic sites responsible for the reaction, and the discussion on the basic sites focuses on the moderate one in this study. Using support as the benchmark, with only Ni loaded catalyst, the

desorption temperature of moderate peak shifted from 382 °C to higher temperature 423 °C, but for Ni and M2 loaded catalysts, that shifted to a lower temperature. The desorption temperatures of the moderate peak on the NiCo, NiCu, and NiFe catalysts are at the same level, 314-339 °C. It shows that the addition of M2 had little influence on the strength of the basic sites.

According to the XRD profiles of monometallic Ni and bimetallic NiM2 catalysts, there two structures shown in the catalysts, MgO and spinel. There were two main crystals belonging to spinel structure, MgAl_2O_4 and Al_2O_3 (Alabi, 2018). Thus, the Ni/ Al_2O_3 (Ni monometallic catalyst supported by Al_2O_3) and NiCo/spinel (NiCo supported by the MgAl_2O_4 spinel) catalysts were prepared by co-precipitation method at the same conditions with catalysts Ni and NiM2. The profiles and the information of the desorption peaks of these catalysts are also shown in Figure 4-9 and Table 4-7. The number of moderate basic sites on the catalysts supported by MgO-spinel (Ni, NiM2) was in the range of 4500-6800 $\mu\text{mol}\cdot\text{g}^{-1}$, which was much higher than that supported by Al_2O_3 or spinel (Ni/ Al_2O_3 or NiCo/spinel). The number of moderate basic sites on the catalysts Ni/ Al_2O_3 and NiCo/spinel was 786 and 580 $\mu\text{mol}\cdot\text{g}^{-1}$, respectively.

Since the moderate basic site is associated with M-oxygen pairs, this basic site was related to the Mg-O and Al-O pairs on these catalysts and support. To determine the property of moderate basic sites, the catalysts Ni/ Al_2O_3 and NiCo/spinel were used to compare with monometallic Ni and bimetallic NiM2 catalysts. When there was only Al_2O_3 working as the support (catalyst Ni- Al_2O_3), the moderate basic site was only associated with the Al-O pair in structure of Al_2O_3 . The number of basic sites was 786 $\mu\text{mol}\cdot\text{g}^{-1}$, which was obviously less than that in the catalysts with MgO-spinel as the support. It indicated that most of the moderately basic sites on the catalysts supported by MgO-spinel were related to the Mg-O pair in MgO or spinel, or Al-O pair in spinel instead of Al-O in Al_2O_3 . When the MgAl_2O_4 spinel was used as support (catalyst NiCo/spinel),

the number of the basic sites was only $580 \mu\text{mol}\cdot\text{g}^{-1}$. This value was also much less than that on the catalysts supported by MgO-spinel (Ni and NiM2). Since on the catalyst NiCo/spinel, the moderate basic sites were only related to Mg-O pair and Al-O pair in the structure of spinel, in the catalysts of Ni and NiM2, the most moderate basic sites were ascribed to the Mg-O pair in the MgO solution.

Based on this discussion, the amount of Mg loading is the main factor in the basicity or number of basic sites of the catalysts. The addition of M2 to Ni on the Ni-based bimetallic catalysts didn't have much effect on the number of basic sites. But it seemed that adding M2 changed the desorption temperature on the moderate peak. Since the chemical composition, metal interaction, and the bulk structure all can affect the basicity of the catalysts (Muñoz et al., 2012), in this study, the addition of second metal also had chance to alter the strength of the M-O bond, resulting in different CO₂-desorption temperatures. Based on the CO₂-TPD curve of the support, the presence of Ni added to stronger the strength of the Mg-O bond. The CO₂-TPD curve of the catalyst NiMn showed a similar trend with that of the support. The catalysts NiCo, NiFe, and NiCu all had weaker moderate basic sites belonging to Mg-O pairs in the solution.

The loading of Mg was the main factor to increase the number of basic sites on the catalysts. The addition of second metal also had an impact on the basic sites, mainly the strength of the moderate basic sites. But the impact was not as critical as the influence of the second metal on the metallic sites.

4.4 Pulse Adsorption Experiments and Pulling-Pushing Theory

It had been recognized that CO₂ was activated by basic sites on the catalyst surface and that CH₄ was activated by the metallic sites on the surface (Papadopoulou et al., 2012). Catalyst basicity measurement by CO₂-TPD showed that when CO₂ was adsorbed on the basic sites of the catalyst

before reduction, no dissociation of CO₂ was observed because there was no CO to be detected in TPD exiting gas stream. Obviously in the reaction another factor or driving force, or called pulling force, must play roles to “help” the activated CO₂ decompose. On the other hand, when CH₄ was adsorbed on the metallic sites, the breakage of carbon-hydrogen bonds was expected to form product hydrogen. The carbon must somehow “pull” an O atom from the activated CO₂ to form a CO. It can be imagined that either O of the CO₂ molecule was “pushed” away from C when CO₂ was adsorbed on the basic sites. Help in “pulling” was needed to pull an O away from the metallic site nearby. The remaining CO was released from the basic sites. During the reaction, it was too fast to study how the two activated species (reactants) were interacted/reacted. In this section, it was hoped that the procedure could be “slowed” down by feeding the two reactants alternatively. “Pulse adsorption-reaction” was used to describe this experiment which hopefully, can reveal the mechanism of CO₂ and CH₄ on the relevant catalytic sites and the interaction of the two activated species.

4.4.1 Pulse adsorption experiments

The adsorption-reaction of CO₂ or CH₄ occurred at the moment that the reactant reached the corresponding sites, thus, the time to trigger the GC to sampling the products was crucial. To ensure the GC can sample the most amounts of products, different waiting times before the analysis by GC were tested, determining 1 min was the most suitable time.

CO₂ pulse adsorption experiments were conducted with catalysts before and after reduction. Catalysts including the material without Ni or other metallic sites before reduction did not give rise to any CO based on the TCD minimum detection capacity (no CO can be detected if CO < 0.5 v/v % by GC). This indicated no CO₂ dissociative adsorption for all the catalyst materials before reduction.

However, when the catalysts were reduced for CO₂ pulse adsorption, CO production was observed. When CO₂ molecule had been activated on the basic sites, the C-O bonds were activated but not broken. A pulling force was needed to help pull one O atom from it. The reduced metals, when close enough to the activated CO₂, can play a role in pulling the O away from it through oxidation. In other words, activated CO₂ can be decomposed only on parts of basic sites. Only those on the basic sites that were accessible to metallic sites can. The metal (M₂ or NiM₂ alloy) properties on metallic sites and the contiguity of the metallic sites with basic sites could affect this pulling force or effect. Thus, CO formation and how many CO formed per metallic sites can be taken as a measure of the CO₂ decomposition capacity of a combination of a basic site and a metallic site of the catalyst, as well as the rate of CO₂ decomposition reaction.

When CH₄ was dissociated on the metallic sites of fresh-reduced catalyst, carbon species (C*) and H₂ were formed. The latter released immediately, but carbon species stayed on the sites until all the metallic sites were covered by it. H₂ can be detected in the exhausting gas. The exhaust gas was sampled, one minute after feeding CH₄ to the reactor, and the H₂ production rate was determined by a metallic site. This value in the unit of s⁻¹ can be defined as the capacity of CH₄ dissociation on metallic sites, as well as the rate of CH₄ dissociation reaction.

Then the pulse adsorption experiments with pre-adsorbed catalysts were performed. The freshly reduced catalyst was first saturated by CH₄ through the injection of CH₄ into the reactor until no CH₄ could be chemisorbed by the catalyst. During this process, the carbon species were formed via CH₄ dissociation on the metallic sites. After the reactor was well purged with N₂ to remove the unreacted CH₄ and produced H₂, CO₂ was introduced into the reactor. CO₂ was activated by the basic sites and reduced by active metal and carbon species on the metallic sites. Thus, during the CO₂ decomposition, the pulling force comes not only from active metal but mainly

from the carbon species on the metallic sites. Whether there is a difference in CO formation compared to that with reduced catalyst, this difference represents the enhancement or inhibition of the CO₂ activation by CH₄ adsorption on metallic sites.

A similar experiment was also done with the catalyst, which had been saturated by CO₂ and purged by N₂ to remove unreacted CO₂ and produced CO. CH₄ was then fed into the reactor, then carbon species and H₂ were formed on the metallic sites, the latter released immediately. Since there were already activated CO₂ or oxygen species on the basic sites, the carbon species can be oxidized (burned) by them which were sitting on the basic sites nearby this metallic site. The difference in hydrogen formation per metallic sites compared to that with reduced catalyst showed to have enhancing or inhibiting effect on CH₄ dissociation by CO₂ adsorption.

The pulse adsorption experiment results are shown in Table 4.8. The formation rate in the Table was the first data collected after one min of the reactant purged into the reactor.

Table 4-8 The formation rate of H₂ and CO over the reduced and pre-chemisorbed catalysts in pulse adsorption experiments

Catalysts	Formation rate by the fresh-reduced catalyst (s ⁻¹)		Formation rate by the pre-adsorbed catalyst (s ⁻¹)	
	[CO] ₁	[H ₂] _{1/2}	[CO] _{2/2}	[H ₂] _{2/2}
Ni	211	105	158	579
NiCo	909	455	865	1091
NiMn	300	1000	500	1400
NiCu	0	222	333	667
NiFe	109	182	109	327

The formation rate (s^{-1}) of CO was calculated based on the number of metallic sites. Since the number of basic sites on one gram of catalyst was much higher than that of metallic sites, there were some basic sites far away from the metallic sites. Even if these basic sites absorb CO_2 , they may not participate in reaction. Only the basic sites and metallic sites that were close to each other participated in the CRM reaction. The number of basic sites involved in the reaction was unknown in fact but much closer to the number of metallic sites than that of basic sites. Thus, the CO formation rate was calculated based on the number of metallic sites. NiCo catalyst had the highest formation rate of CO compared to the NiMn, Ni, and NiFe catalysts. No CO was detected when CO_2 was injected into the reactor with reduced NiCu catalyst. Among these five catalysts, NiMn catalyst had the highest formation rate of H_2 activated by a fresh-reduced catalyst on a metallic site, which was 1000 s^{-1} . The value for NiCo was also higher, 455 s^{-1} , as compared to those of NiCu, NiFe, and Ni catalysts.

The formation rate of CO with pre-adsorbed NiCo, NiMn, NiCu, Ni, and NiFe catalysts based on metallic sites improved as compared to those with fresh-reduced catalyst. These values were 865, 500, 333, 158, and 109 s^{-1} , respectively. When the CH_4 was introduced into the system with a pre-adsorbed catalyst with CO_2 , NiMn and NiCo catalysts had a higher level of formation rate of H_2 among these catalysts.

Compared to the Ni catalyst, addition of M2 improved the formation rate of H_2 on the metallic site, as well as the reaction rate of CH_4 dissociation. It was summarized by Bian et al., 2017 as a result of the alloy formation. Addition of M2 also changed the reaction rate of CO_2 decomposition. The addition of Co to the catalyst improved this reaction greatly, which was attributed to the strong affinity of Co to oxygen species (Ruckenstein and Wang, 2002). But with NiCu catalyst, there was no CO formation. As it was discussed before, this didn't mean there was no basic sites present

on this catalyst. It meant even with the help of active Ni, Cu, or NiCu alloy on the metallic sites, the basic site on catalyst NiCu still cannot push one of oxygen out of the CO₂ molecule. It may be due to the contiguity of Ni and support not good enough or the activity of metallic sites not strong enough. There was only activated CO₂ formation, not CO.

As reported, the relative reaction rate of CH₄ dissociation and CO₂ decomposition was crucial in the evaluation of the stability of the catalyst. On the NiMn, NiCu, or NiFe catalysts, the carbon species formation rate was higher than those of the oxygen species formation rate or carbon species oxidation rate. The carbon deposition may happen on these catalysts, which was the reason for deactivation of these catalysts. However, pulse adsorption experiments showed that only a trace amount of H₂ or CO was detected in a short period of time when CH₄ or CO₂ alone was feed to the catalytic reactor. Feeding CH₄ and CO₂ together facilitated continuous operation, producing H₂ and CO.

4.4.2 The pulling-pushing theory

For a reaction such as CO₂ reforming of CH₄, where two kinds of reactants were activated on two types of catalytic sites, respectively, the reactants must be activated on each type of catalytic site first. For example, CO₂ was activated on the basic site and CH₄ was activated on metallic sites. Then, the resultant activated species must have interacted with each other such that the reaction could proceed and be completed. This step was even more important because how it proceeded determined the direction of the reaction and the selectivity of the desired product(s). Since the two activated species must interact with each other, the contiguity of the two sites determined this interaction qualitatively and quantitatively.

Based on the results of pulse adsorption experiments, a theory of pulling-pushing by the catalytic sites was proposed to help understand the process of CO₂ activation and the CH₄ dissociation. If the activation ability of the sites was defined by “pushing force” or “pulling force” for short, “pulling force” or “pulling force” from the other kind of sites was required for the “self” sites to be refreshed and the reaction to be continued. In particular, CO₂ could be activated by all the basic sites which were assumed evenly distributed. But the basic sites that were involved in the reaction were those which were accessible to the metallic ones. During the reaction, CO₂ was activated on the basic sites. The force from the basic sites was trying to “push” one oxygen atom out of the molecular CO₂. But one of the oxygen atoms didn’t go until the “pulling force”, the carbon species (C*) or active metal on metallic sites, pulled one oxygen atom away. On the other hand, CH₄ was dissociated to carbon species and H₂ on the metallic sites by “pushing”. The carbon stayed on the metallic sites. It didn’t go and the CH₄ dissociation stopped until there was a pulling force to “draw away (burn)” the carbon species. This “pulling force” can be supplied by the activated CO₂ formed from CO₂ activation on the basic sites. The pushing force was determined by the properties of the site themselves. The pulling force is determined by the properties of the other site, and the contiguity of one kind of sites to the other kind.

Then the results of pulse adsorption experiments have a new way to explain using pushing and pulling forces from each catalytic site, which are shown in Table 4-9. The force here is represented by the formation rate of CO or H₂ in a unit of s⁻¹.

Table 4-9 The pulling or pushing forces from metallic or basic sites based on the pulse adsorption experiments.

Catalysts	Ni	NiCo	NiMn	NiCu	NiFe
Pushing force to O* from basic sites or Pulling force to O* from metallic sites	211	909	300	0	109
Pushing force to C* from metallic sites or Pulling force to C* from basic sites	105	455	1000	222	182
Pushing force to O* from basic sites and Pulling force to O* from C*	158	865	500	333	109
Pushing force to C* from metallic sites or Pulling force from CO ₂ * or O*	579	1091	1400	667	327
Numbers of basic sites around one metallic site	5.5	2.4	1.4	3.0	1.8

The pulse adsorption experiments provided quantitative or semiquantitative measurement of the pushing force and pulling force. When CO₂ was fed to fresh reduced catalysts, the pulling force may be given by reduced metals. When CO₂ was fed to the catalysts to which CH₄ had been adsorbed previously, the pulling force was given by C* on metallic sites, leading to the formation of another CO. The pulling force by different species on metallic sites can be quantified by the formation rate of CO when CO₂ was fed to catalysts reduced or adsorbed by CH₄. On the other hand, the pushing force of metallic sites to CH₄ can be quantified by the formation rate of H₂ with reduced catalysts. The pulling force by activated CO₂ can be quantified by the H₂ formation rate with pre-adsorption of CO₂.

The comparison of the oxidizing ability of CO₂ species on the basic sites surrounding the metallic particles, which was the pushing force from basic sites, and the pushing force of the metallic sites to C* can give the stability information of the catalyst. Meanwhile, the comparison

of the H_2 production rates with freshly reduced catalyst and pre-chemisorbed catalysts by CO_2 , the contiguity of two catalytic sites on different catalysts can be determined. During the pulse adsorption reaction with the pre-chemisorbed catalyst, CH_4 was introduced into the reactor. CH_4 was activated by the metallic sites to form carbon species and H_2 , the latter released immediately. Since there were already activated CO_2 or oxygen species on the basic sites, the carbon species can be oxidized (burned) by activated CO_2 or oxygen species which sat on the basic sites nearby this metallic site. Then the metallic sites were regenerated. Then CH_4 dissociation and carbon species oxidation happened repeatedly until there was no activated CO_2 or oxygen species left on the basic site which can access the metallic sites. The value of the H_2 formation rate on a metallic site with freshly reduced catalyst represented how much H_2 could be formed on one metallic site with occurrence of one time of CH_4 dissociation. Then, the value of the H_2 formation rate on a metallic site with the pre-chemisorbed catalyst with CO_2 represented how much H_2 could be formed on one metallic site with the occurrence of several times of CH_4 dissociation. Thus, the ratio of these two values (the latter value to the former) was how many times the CH_4 dissociation and carbon species oxidation happened. Assuming that there was only one oxygen species or activated CO_2 adsorbed on each nearby basic site, then the ratio was also the number of basic sites around one metallic site.

As the results shown in Table 4-9, the value of the pulling force from carbon species is also related to the contiguity of two catalytic sites. Since the NiMn, NiCu, and NiCo catalysts had smaller Ni particle formation, and most of the particles were smaller than 9 nm, these catalysts showed stronger pulling force from carbon species to reduce CO_2 activated on the basic sites. The Ni and NiFe catalysts on the contrary, had less Ni particles which were smaller, most of the metallic sites were too far from the basic sites. Thus, the average pulling force of carbon species was weaker. As discussed, the contiguity was expressed by the ratio of $[H_2]_2/2$ and $[H_2]_1/2$, as well as how many

times the CH₄ dissociation and carbon species oxidation happened and the number of basic sites were around one metallic site. Compared to the monometallic Ni catalyst, this value decreased with the addition of Cu and Co, from 5.5 to around 2.7, then decreased further by adding Fe and Mn to around 1.6. It seemed that the addition of M₂ decreased the number of basic sites around a metallic site.

4.5 Catalyst Performances

The activity and stability of the catalysts were investigated under the condition of 750 °C, 1 atm, and GHSV of 110 L·g_{cat}⁻¹·h⁻¹, and the results were reproducible. According to the thermodynamic calculation, the equilibrium conversion of CH₄ was 91.5 % at this reaction condition (Zhang et al., 2007). The CH₄ conversions of monometallic Ni and bimetallic NiM₂ catalysts are shown in Figure 4-10. The addition of Co, Mn, and Cu to Ni on the Ni-based catalysts improved the initial conversion of CH₄, with the highest value of 89 % on NiCo. However, Fe decreased the initial conversion of CH₄ as compared to the catalyst Ni. The conversion of CO₂ with NiCo was close to those from our earlier work (Zhang et al., 2007) and much better than those reported in recent years (Bian et al., 2017).

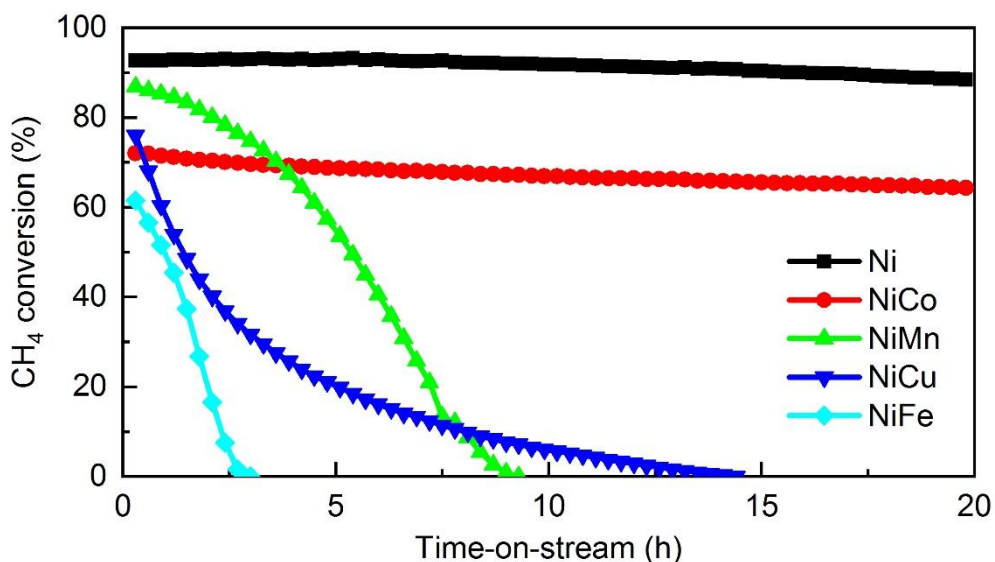
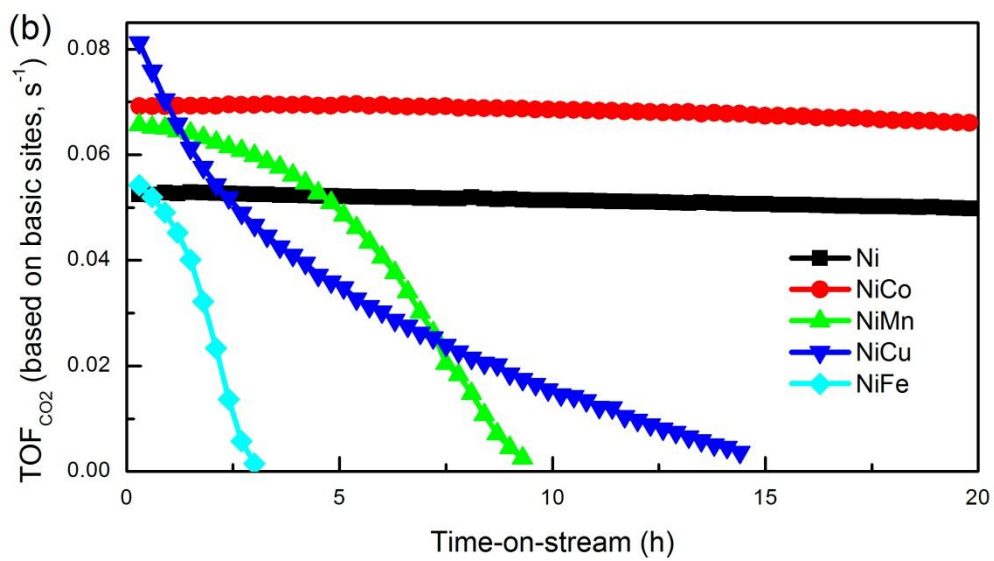
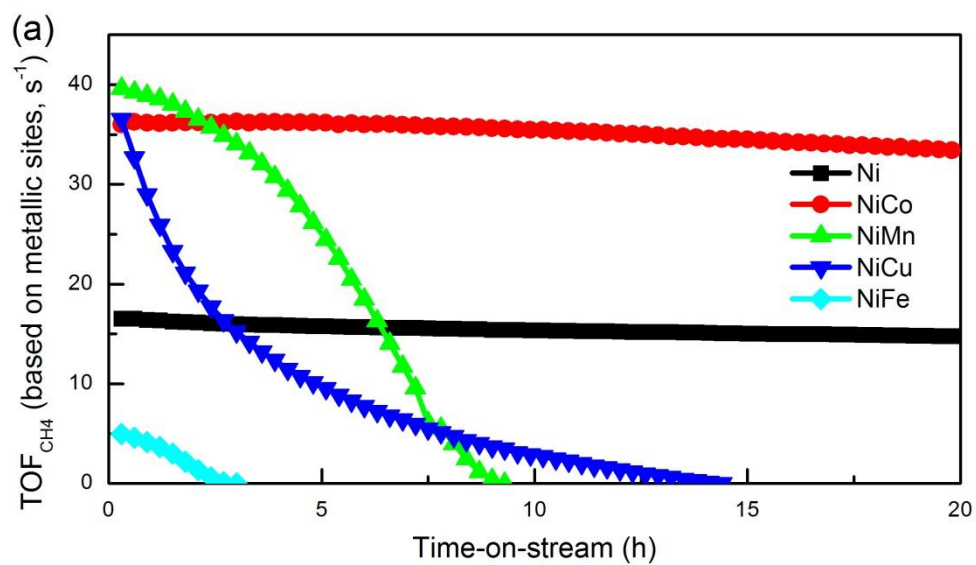


Figure 4-10 CH₄ conversion as a function of time-on-stream over monometallic Ni and bimetallic NiM2 catalysts

According to the amount of CO uptake from the CO chemisorption, turnover frequency (TOF) of CH₄ based on the metallic sites on the surface of the catalysts was calculated, which is shown in Figure 4-11 (a). Among these five catalysts, the NiMn, NiCu, and NiCo catalysts showed higher initial TOF_{CH₄} at the level of 35-40 s⁻¹. However, the value of Ni was only 17 s⁻¹, and that of NiFe was the lowest, 5 s⁻¹. Only NiCo and Ni catalysts were stable during the reaction. NiMn, NiCu, and NiFe catalysts were deactivated after 14 h, 9 h, and 3 h since the reaction began. TOF represents the reaction rate on every active site. The activity of every active sites is supposed to be the same during the reaction. Thus, the change on the TOF is due to the change of number of active sites which are working. In other words, the decrease of TOF is because that some of the active sites are deactivated.

TOF_{CO₂} based on basic sites and metallic sites were all calculated, which are shown in Figure 4-13 (b and c). The former was very low and the latter displayed the same trend with TOF_{CH₄}. A

comparison between the amounts of CO and CO₂ chemisorption indicates that the number of basic sites is much greater than that of the metallic sites. As mentioned in pulse adsorption experiments, those basic sites were far away from the metallic sites, even though they may have adsorbed CO₂, could not participate in the reaction. Thus, only a small portion of the basic sites participated in the reaction. In other words, metallic sites had to be involved to pull the O from activated CO₂ to complete its conversion. The basic sites and metallic sites that were close to each other (close enough to enable the pulling force to play a role) made the CO₂ reforming of CH₄ reaction completed. The number of basic sites involved in the reaction was unknown in fact but much closer to the number of metallic sites than that of basic sites. Therefore, it did make sense to use TOF_{CO2} based on the metallic site number to express the reaction rate of CO₂ on the active site. The CO₂ reaction rate based on metallic sites (Figure 4-13 (c)) showed the same trend with the CH₄ reaction rate based on metallic sites. The agreement between CH₄ and CO₂ reaction rate based on metallic sites indicated that pushing and pulling forces worked together.



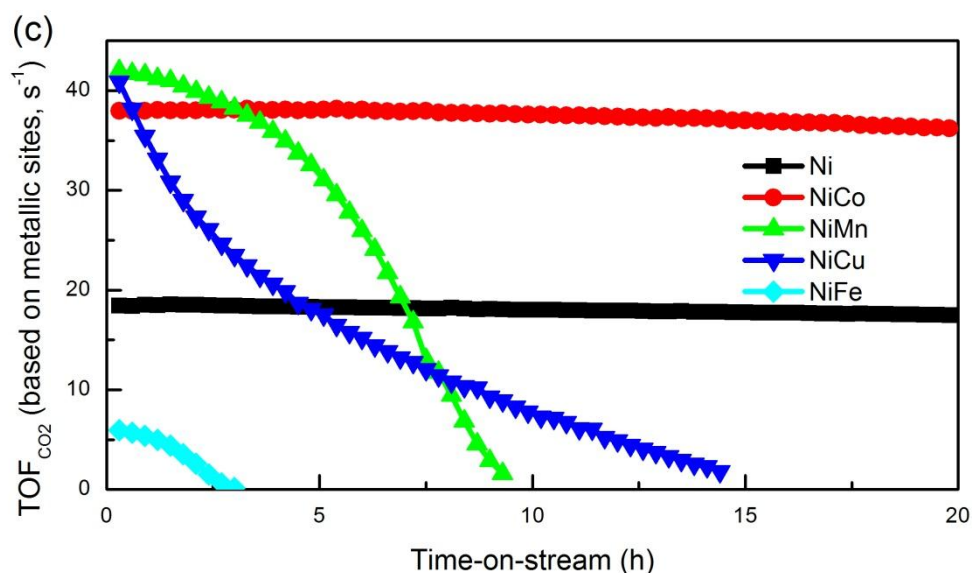


Figure 4-11 Activity and stability of monometallic Ni and bimetallic NiM2 catalysts at reaction condition: $T = 750\text{ }^{\circ}\text{C}$, $P = 1\text{ atm}$, $\text{GHSV} = 110\text{ L}\cdot\text{g}_{\text{cat}}^{-1}\text{h}^{-1}$, $\text{CH}_4/\text{CO}_2/\text{N}_2 = 1/1/1$, 0.05 g catalyst . (a) TOF of CH_4 reacted based on the metallic sites on the surface of the catalysts; (b) TOF of CO_2 reacted based on the basic sites on the surface of the catalysts; (c) TOF of CO_2 reacted based on the metallic sites on the surface of the catalysts.

To determine the relationship between the activity of metallic sites and the contiguity of the metallic sites to the basic ones, the correlations of initial TOF_{CH_4} and TOF_{CO_2} , and the average size of metallic particles are shown in Figure 4-13. The catalysts with smaller metallic sites had a higher initial reaction rate based on the metallic sites. During the reaction, CH_4 dissociation happened on the metallic sites to form carbon species. On the catalyst with larger metallic particles, more metallic sites isolated in the center of particles surface cannot access to the basic sites around. There were not enough activated CO_2 supplied to the metallic sites. In other words, the contiguity of basic and metallic sites was not good enough. Then the extra carbon species gathered and formed coke. The metallic sites far from the basic sites were encapsulated by coke and deactivate, resulting in low TOF_{CH_4} and TOF_{CO_2} .

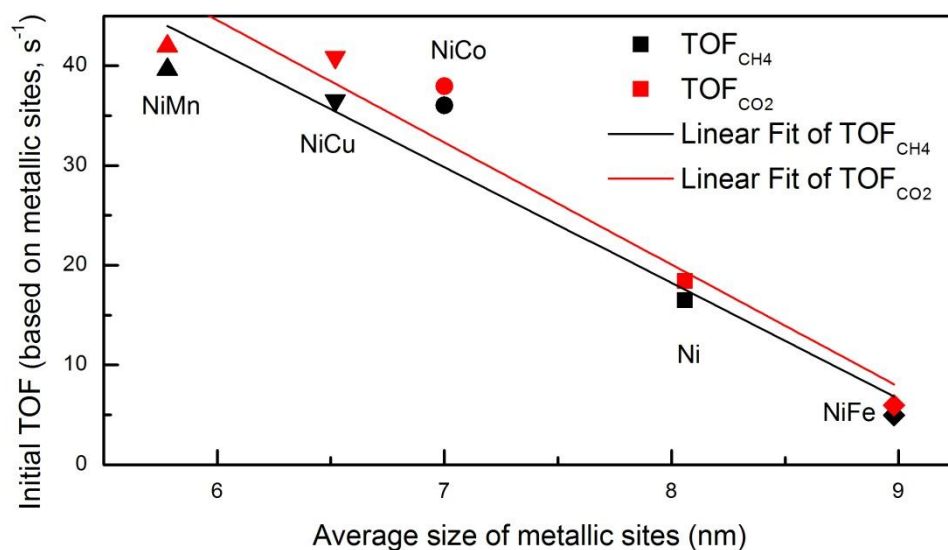


Figure 4-12 Correlations of initial TOF_{CH_4} and TOF_{CO_2} and the average size of metallic particles

The deactivation of the NiMn, NiCu, and NiFe catalysts are due to the formation of the coke (Arora and Prasad, 2016). The deactivation of NiFe catalyst can be due to the poor contiguity of basic and metallic sites, which was by much bigger particles formed. Most of metallic sites were far away from the basic site, as well as oxygen species or activated CO_2 , resulting to cover by the carbon species. The deactivation of NiMn, NiCu, and NiFe catalysts can be also explained based on the results of pulse adsorption experiments. As it was discussed before, the relative reaction rate of CH_4 dissociation and CO_2 decomposition was crucial for the carbon formation, resulting in the deactivation of the catalysts. The summary of the rate of each reaction from the pulse adsorption experiments and the catalysts' deactivation in the experiments is shown in Table 4-10. The reaction rate of CO_2 decomposition was higher than that of CH_4 dissociation over the NiCo and Ni catalysts. Thus, these two catalysts were stable during the reaction. On the contrary, the reaction rate of CO_2 decomposition was lower than that of CH_4 dissociation over the NiMn, NiCu, and NiFe catalysts, which resulted in the deactivation of these three catalysts in a short time after the reaction began.

This also can be explained with the pushing-pulling theory. When the oxidizing ability of CO₂ species on the basic sites surrounding the metallic particles, which was the pushing force from basic sites, was stronger than the pushing force of the metallic sites to C*, the catalysts were carbon-resistant.

Table 4-10 The relative reaction rate of CH₄ dissociation and CO₂ decomposition and deactivation of catalysts

Catalysts	CH ₄ dissociation	CO ₂ decomposition	Relative reaction rate	t _{1/2}
Ni	105	211	CH ₄ dissociation < CO ₂ decomposition	-
NiCo	455	909	CH ₄ dissociation < CO ₂ decomposition	-
NiMn	1000	300	CH ₄ dissociation > CO ₂ decomposition	5.8 h
NiCu	222	0	CH ₄ dissociation > CO ₂ decomposition	2.3 h
NiFe	182	109	CH ₄ dissociation > CO ₂ decomposition	1.7 h

It was believed that reverse water-gas shift reaction was the main side reaction that led to the H₂/CO ratio below one in CO₂ reforming of CH₄. However, the study on the H₂/CO ratio with those three deactivating catalysts gave a different result. The results of the H₂/CO molar ratio as a function of time-on-stream over monometallic Ni and bimetallic NiM2 catalysts are shown in Figure 4-12. Among these five catalysts, the NiCo catalyst had the highest selectivity to the CRM reaction with the ratio of H₂/CO of 1 (initial) and 0.95 (20 h). The ratio of H₂/CO over the catalyst Ni was around 0.85 during the reaction. The value with NiMn, NiCu, or NiFe catalysts decreased with the decrease of CH₄ reaction rate and the deactivation of the catalysts.

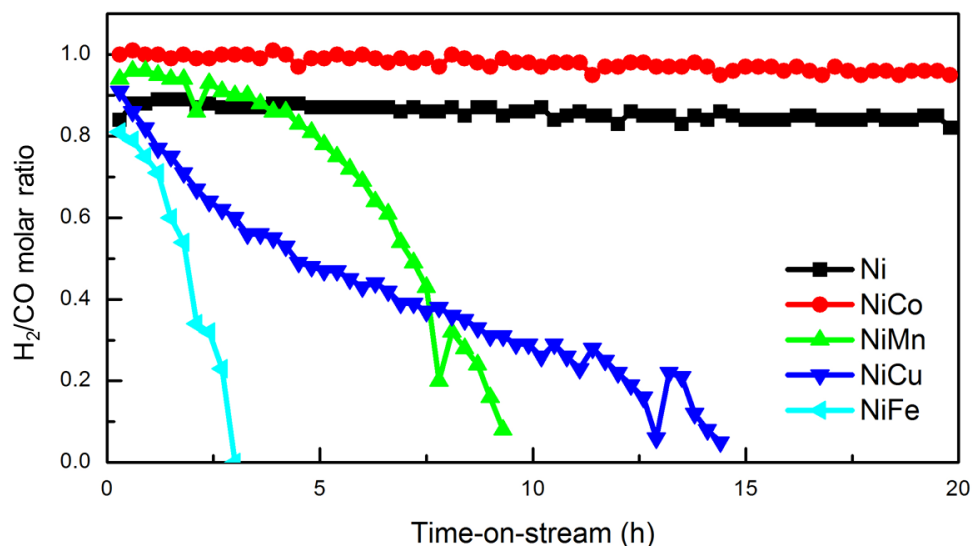


Figure 4-13 H₂/CO molar ratio as a function of time-on-stream over monometallic Ni and bimetallic NiM₂ catalysts

For those three fast deactivating catalysts, NiMn, NiCu, and NiFe, it was noticed that when the H₂/CO ratio was 0.5, the TOF of CO₂ was 1.5 times than that of CH₄. If the reverse water gas shift reaction occurred as the side reaction, when the H₂/CO ratio was 0.5, the TOF of CO₂ to that of CH₄ should be 5/3. Another explanation was that there was not only C* formed from CH₄ dissociation, but also methyl-like species (CH_x*) formed. The later may also react with CO₂ on basic sites. During the CO₂ reforming of CH₄ over the fast deactivating catalysts, the following reactions that might occur.



and,



Then the activated CO₂ (CO₂*) reacted with S**C* to form CO and released the metallic sites,



or the activated CO_2 reacted with S^*CH_4 to form CO and H_2O , and left carbon on the metallic sites.



This mechanism could perfectly explain the results of CH_4 and CO_2 TOF and H_2/CO ratio. According to the steps of CRM reaction, the degree of methane decomposition depended on the active metal and the nature of the support (Papadopoulou et al., 2012). Thus, the reason for methyl-like species (S^*CH_x) formation instead of S^*C on these catalysts, NiMn, NiCu, and NiFe, may due to the weaker pushing force of metallic sites as compared to that of Ni and NiCo catalysts.

4.6 Catalyst Study with Larger Metallic Particles

Section 4.5 showed that there was an obvious correlation between initial TOF of CO_2 and CH_4 and the average metallic particle size. The average metallic particle size somehow reflected the contiguity between basic sites and metallic sites. The smaller metallic particles resulted in more metallic sites close to or next to basic sites. To confirm this correlation, a higher reduction temperature, 850 °C, was used to purposely make the metallic particles larger. XANES was used to confirm the extent of reduction of Ni and second metal elements for monometallic Ni catalyst and bimetallic NiM2 catalyst. TEM was used to quantify the metallic particle size for all five catalysts.

4.6.1 Reduction properties of active metals by XANES at higher reduction temperature

The spectra of Ni, Co, Mn, Cu, and Fe K-edge XANES of catalysts reduced at 850 °C are shown in Appendix G. The Ni, Co, Mn, Cu, and Fe K-edge XANES LCF in the range of -20 to

+30 eV of edge energy of the catalyst Ni and bimetallic catalysts NiM2 after their reduction at 850 °C for 4 h are shown in Table 4-11.

Table 4-11 The metal and metal oxide content in catalysts reduced at 850 °C for 4 h measured by the linear combination fitting of XANES.

Catalysts	Ni ⁰ /Ni ²⁺	Co ⁰ /Co ²⁺ /Co ³⁺	Mn ⁰ /Mn ²⁺ /Mn ⁴⁺	Cu ⁰ /Cu ⁺ /Cu ²⁺	Fe ⁰ /Fe ²⁺ /Fe ³⁺
Ni	0.77/0.23				
NiCo	0.70/0.30	0.55/0.45/0			
NiMn	0.69/0.31		0.10/0.46/0.44		
NiCu	0.65/0.34			0.41/0/0.59	
NiFe	0.76/0.24				0.82/0/0.18

Compared to the metal content of Ni and M2 in the catalysts reduced at 750 °C, more Ni and M2 were reduced at higher reduction temperature (850 °C). The extents of reduction of Ni in the monometallic Ni and bimetallic NiM2 catalysts were similar, from 0.65 to 0.77, indicating that at high reduction temperature, 850 °C, the extent of Ni reduction was not affected by M2. There were two times of Co²⁺ reduced at 850 °C as compared that at 750 °C. But the reduction extents of Mn⁴⁺, Cu²⁺ in different reduction temperatures were similar, indicating that a part of Mn⁴⁺, Cu²⁺ was easy to be reduced at a lower temperature, and the other part cannot be reduced even at high reduction temperature. The extent of reduction of Fe³⁺ increased from 0.64 at a reduction temperature of 750 °C to 0.82 at the reduction temperature of 850 °C.

4.6.2 Particles formed at a higher reduction temperature

The information on metallic particle size, especially the percentage of particles whose size was smaller than 9 nm, was used to study the contiguity of metallic and basic sites. The TEM images of the monometallic Ni and bimetallic NiM2 catalysts reduced at 850 °C and their metallic particle size distributions are shown in Appendix G. The metal particle size and distribution of the reduced catalysts investigated from the TEM images are given in Table 4-12.

Table 4-12 Average particle size and particle size distribution from the TEM micrographs of catalysts reduced at 850 °C

Catalysts	Average particle size, nm	Relative percentage < 9 nm, %
Ni	8.5	70.3
NiCo	7.6	70.2
NiMn	9.3	55.0
NiCu	7.4	85.7
NiFe	10.7	35.7

With the increase in reduction temperature, the metallic particles formed on Ni or NiM2 catalysts became larger. The changes of particle size on the Ni and NiCu were not substantial with different reduction temperatures, from 8.1 and 7.1 nm (reduced at 750 °C) to 8.5 and 7.4 nm (reduced at 850 °C). The percentage of particles smaller than 9 nm on these two catalysts didn't decrease much, either. Compared to the NiCo bimetallic catalyst reduced at 750 °C, the catalyst reduced at 100 °C higher formed larger particles with the average size of 7.6 nm, and the percentage of particles smaller than 9 nm decreased from 100 % to 70 %. However, the particles formed on the NiMn and NiFe catalyst reduced at 850 °C were much larger than those reduced at 750 °C, with

the increase in average size from 5.8 and 9.0 nm to 9.3 and 10.7 nm, respectively. Thus, the contiguity of basic and metallic sites on monometallic Ni and bimetallic NiM₂ catalysts was changed or got worse with higher reduction temperature.

4.6.3 Performance of catalysts reduced at a higher temperature

The activity and stability of the catalysts were investigated under the condition of 850 °C, 1 atm, and GHSV of 110 L·g_{cat}⁻¹·h⁻¹, which are shown in Figure 4-14.

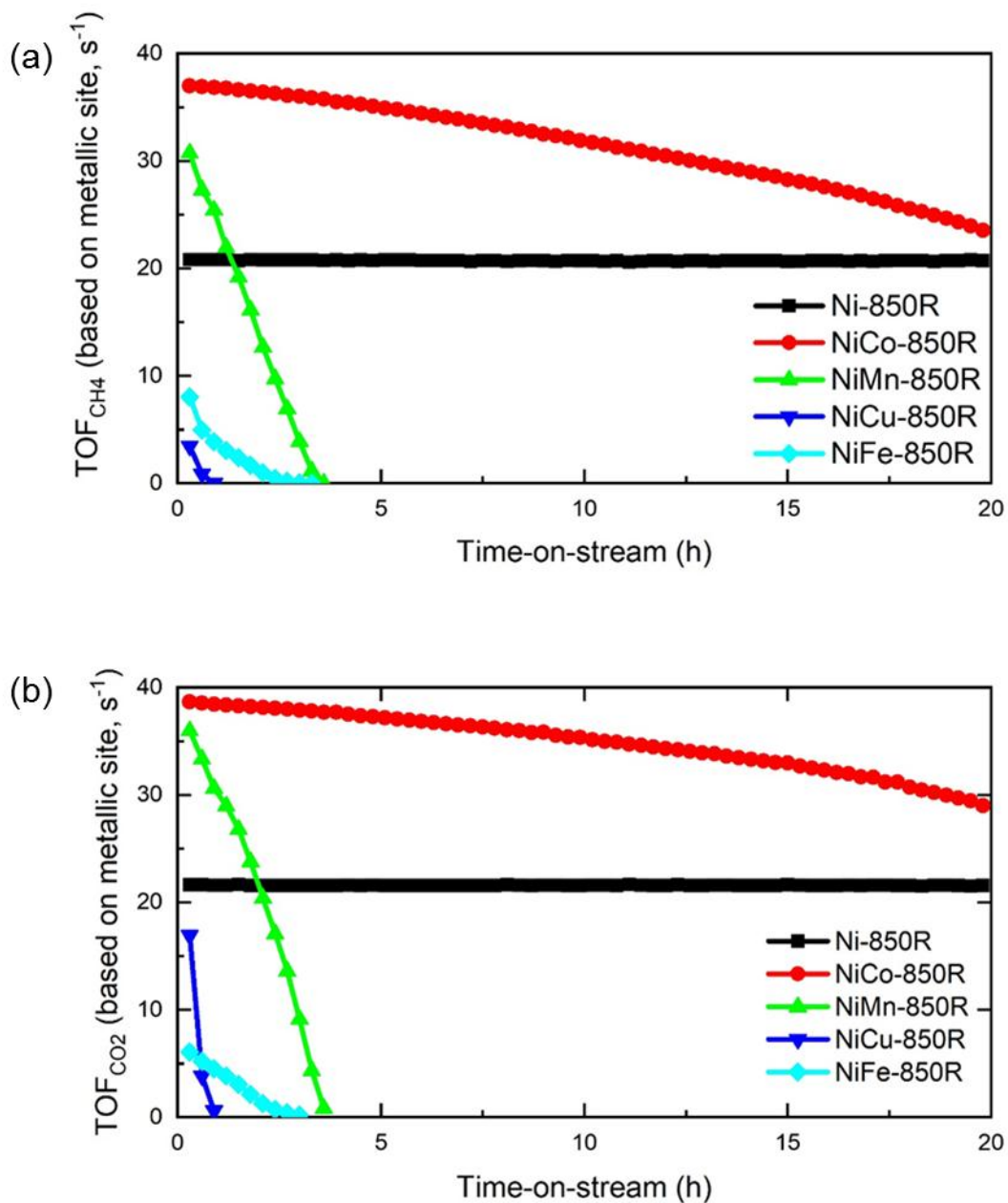


Figure 4-14 Activity and stability of Ni monometallic and NiM2 bimetallic catalysts at reaction condition: reduction $T=850\text{ }^{\circ}\text{C}$, reaction $T = 750\text{ }^{\circ}\text{C}$, $P = 1\text{ atm}$, $F = 90\text{ mL/min}$, $CH_4/CO_2/N_2 = 1/1/1$, 0.05 g catalyst . (a) TOF of CH_4 reacted based on the metallic sites on the surface of the catalysts; (b) TOF of CO_2 reacted based on the metallic sites on the surface of the catalysts.

The Ni catalyst was stable during the reaction period, with the TOF based on the number of metallic sites on CH₄ of 21 s⁻¹. However, the Ni-based catalysts with the addition of Mn, Cu, and Fe, deactivated during the reaction, and the NiCo catalyst also appeared the trend of deactivation. The TOF of CO₂ based on the number of metallic sites are also shown in Figure 4-13. The trend of this curve was similar to the TOF of CH₄.

Since the increase of reduction temperature led to higher metallic Ni and M2 contents in the reduced NiM2 catalysts, the larger metallic particles were formed on the catalysts. With larger particle formation, more metallic sites were far away from the basic sites. These metallic sites were hard to access to the basic sites. There were not enough oxygen species or activated CO₂ supplied to oxidize the carbon species formed on the metallic sites, resulting in the coke formation and deactivation of the catalysts (El Hassan et al., 2016; Ahmad et al., 2017).

This study determined that the bigger metallic particle, as well as the poor contiguity of metallic sites and basic ones, was an important factor that aggravates carbon formation and deactivation of the catalysts.

4.7 Catalyst Study with Different Support

The contents in Chapter 4 so far focused on the metallic particle size and the potential quantification of their contiguity with basic sites, and how they work together to impact the catalytic performance. There was still a lack of geographic information on where the basic sites were, where the metallic sites were and where they were potentially together.

From earlier work (Alabi, 2018), four catalyst samples were chosen to study these questions. The bulk structures of the four samples were chosen such that two samples had spinel structures only (gamma-Al₂O₃ showed spinel structure), and two had the combination of MgO solid solution

structure and spinel structure (MgO-spinel). Over each structure, Ni metallic sites, and the other had bimetallic NiCo sites were present. The catalysts were Ni catalysts supported by Al₂O₃ and MgO-spinel, and NiCo catalysts supported by spinel and MgO-spinel.

4.7.1 Extent of reduction of metals

The bulk properties of catalysts Ni/Al₂O₃, Ni/MgO-spinel, NiCo/spinel, and NiCo/MgO-spinel are shown in Appendix H. The Ni and Co K-edge XANES of reduced catalysts were scanned. XANES linear combination fitting (LCF) in the range of -20 to +30 eV of edge energy was used to provide quantitative results, shown in Table 4-13. The results indicated that the reduction rate of both Ni and Co increased with an increase in the Mg/Al ratio in the catalysts. The presence of MgO increased the reduction of both Ni and Co, significantly. Spinel structure led to no Co reduction and a few percentages of Ni reduction.

Table 4-13 Extent of Ni and Co reduction in catalysts

Catalysts	Ni (%)	NiO (%)	Co (%)	CoO (%)
Ni/Al ₂ O ₃	33	67	-	-
Ni/MgO-spinel	88	12	-	-
NiCo/spinel	12	88	2	98
NiCo/ MgO-spinel	90	10	32	68

4.7.2 Number of metallic and basic sites

The properties of metallic sites and basic sites studied by CO chemisorption and CO₂-TPD are shown in Table 4-14. With the addition of MgO as the support of Ni catalyst, the number of

metallic sites increased from 5 to 15 $\mu\text{mol}\cdot\text{g}^{-1}$, and that of moderate basic sites increased from 786 to 6810 $\mu\text{mol}\cdot\text{g}^{-1}$. Similar trend displayed on the NiCo/spinel and NiCo/MgO-spinel catalysts. The number of metallic sites on NiCo/spinel was 9 $\mu\text{mol}\cdot\text{g}^{-1}$, and the value of NiCo/MgO-spinel catalyst was 24 $\mu\text{mol}\cdot\text{g}^{-1}$. The number of the moderate basic sites on the NiCo/spinel catalyst was 580 $\mu\text{mol/g}$, the value of the NiCo/MgO-spinel catalyst was 5878 $\mu\text{mol/g}$. From the study of these two sets of catalysts, it was determined that the support had some influence on the properties of metallic sites, but much more on the basic sites.

Table 4-14 Properties of metallic sites of catalysts from the analysis of CO chemisorption, and basic properties of catalysts based on CO₂-TPD analysis.

Catalysts	Metallic sites		Basic sites				
	Number ($\mu\text{mol}\cdot\text{g}^{-1}$)	Metal dispersion (%)	Weak basic sites		Moderate basic sites		Total number ($\mu\text{mol}\cdot\text{g}^{-1}$)
			T (°C)	Number ($\mu\text{mol}\cdot\text{g}^{-1}$)	T (°C)	Number ($\mu\text{mol}\cdot\text{g}^{-1}$)	
Ni/Al ₂ O ₃	5	0.9	136	218	318	786	1004
Ni/MgO- spinel	15	1.5	147	20	423	6810	6830
NiCo/spinel	9	1.4	130	184	333	580	764
NiCo/ MgO-spinel	24	1.7	129	101	339	5878	5979

4.7.3 Distribution of the active metal on the support

The quantitative analysis of the STEM-EDX images was used to study the contiguity of the basic and metallic sites (Alabi, 2018). Figure 4-15 shows the elements Al and Mg distributed on

the catalyst Ni/Al₂O₃. The Ni displayed a non-homogeneous distribution on the support of Al₂O₃. There was phase segregation of Ni with a bigger particle size formation.

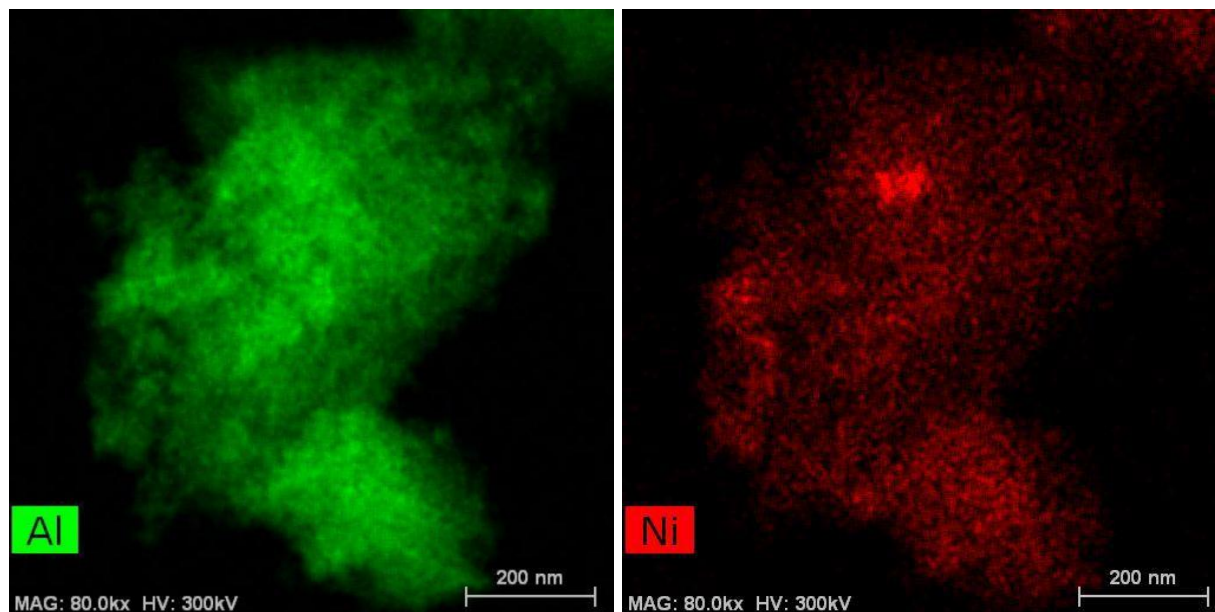


Figure 4-15 STEM-EDX of Ni/Al₂O₃ catalyst. Ni and Al interaction

The distribution of elements Al, Mg, and Ni on the catalyst are displayed in Figure 4-16. After the support was modified by MgO, the distribution of Ni on the surface of support was much better. Based on the result of the line scan, the intensity peaks of Ni seem not to be “linked” to Al, yet Ni showed a potential maximum where the Mg maximum was found. Thus, compared to the Ni phase distributed on the Al, it showed better distribution on the Mg phase.

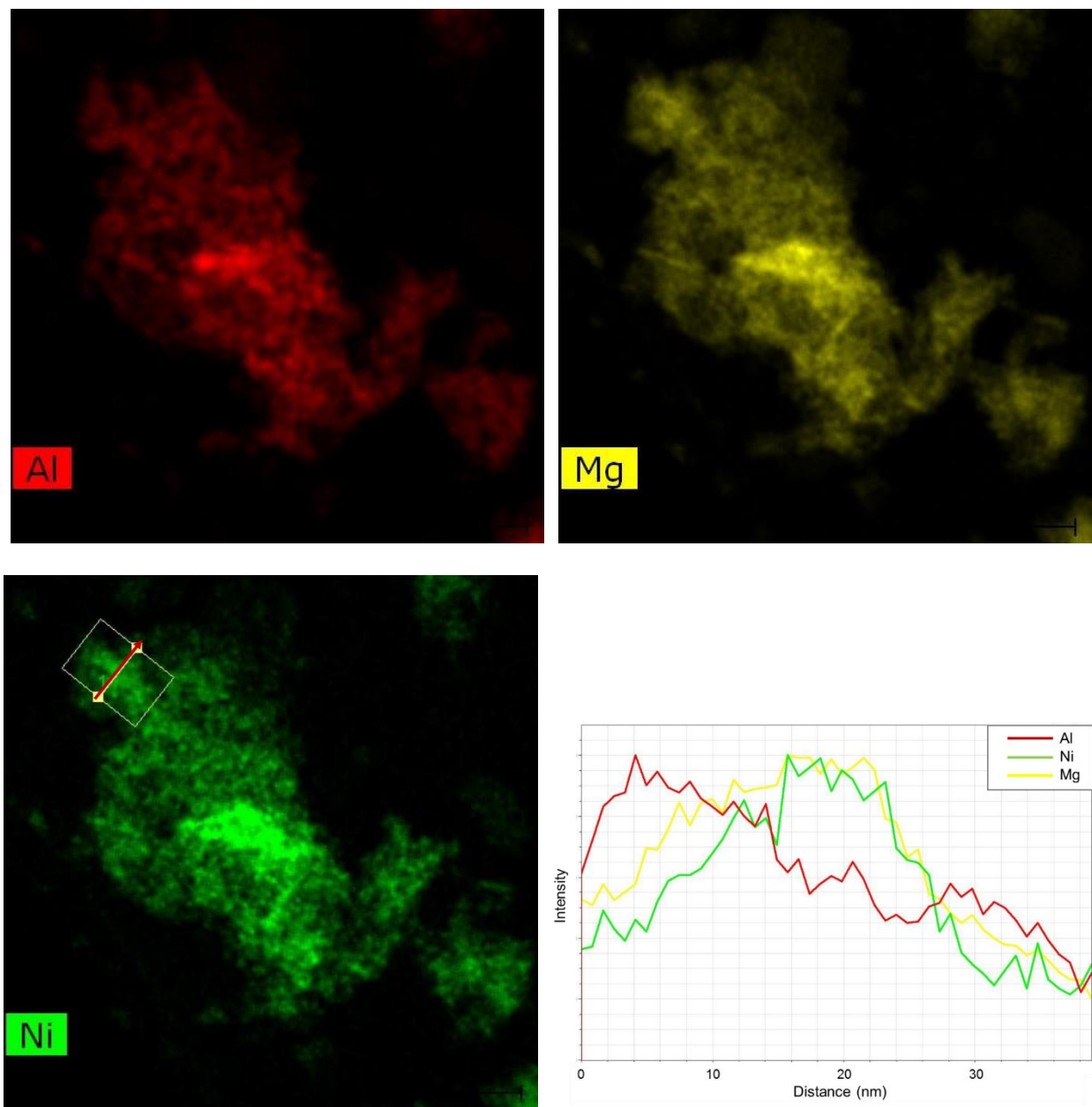


Figure 4-16 STEM-EDX of Ni/MgO-spinel catalyst. Ni and Al interaction, Ni and Mg interaction, Mg and Al interaction

The images determined that on the support Al_2O_3 , the Ni and Al interaction was not strong enough to have a homogeneous distribution of Ni phase. Then on the support MgO-spinel, the interaction of Ni and Al was much improved by the modification of MgO. The Ni phase also had stronger interaction with Mg. There was a correlation between Ni and Mg. As a conclusion, the

interaction of active metal and support on the catalysts Ni-Al₂O₃ and Ni/MgO-spinel was different, further, the contiguity of basic and metallic sites was different. As discussed before, the MgO phase was the main basic sites on the catalysts. Thus, the metallic sites of catalyst Ni/MgO-spinel can more easily access the main basic sites due to the stronger interaction, as well as the better correlation between Ni and Mg.

This conclusion had also been confirmed by the comparison of NiCo catalyst supported by spinel and MgO-spinel. The distributions of each element on the catalysts NiCo/spinel were studied by STEM-EDX and shown in Figure 4-17. The Al atoms were concentrated in a few spots, so were the most of Mg, Ni, and Co atoms. Mg, Ni, and Co can form spinel with Al. However, Mg, Ni, and Co were seen everywhere other than where Al was. This part was too small to be detected by XRD. The spinel phase (MgAl₂O₄) was as the support for this catalyst, and barely MgO solid existed according to the XRD analysis, which was the reason for the Al and Mg phases staying together. The active metals, Ni and Co dispersed well on the support.

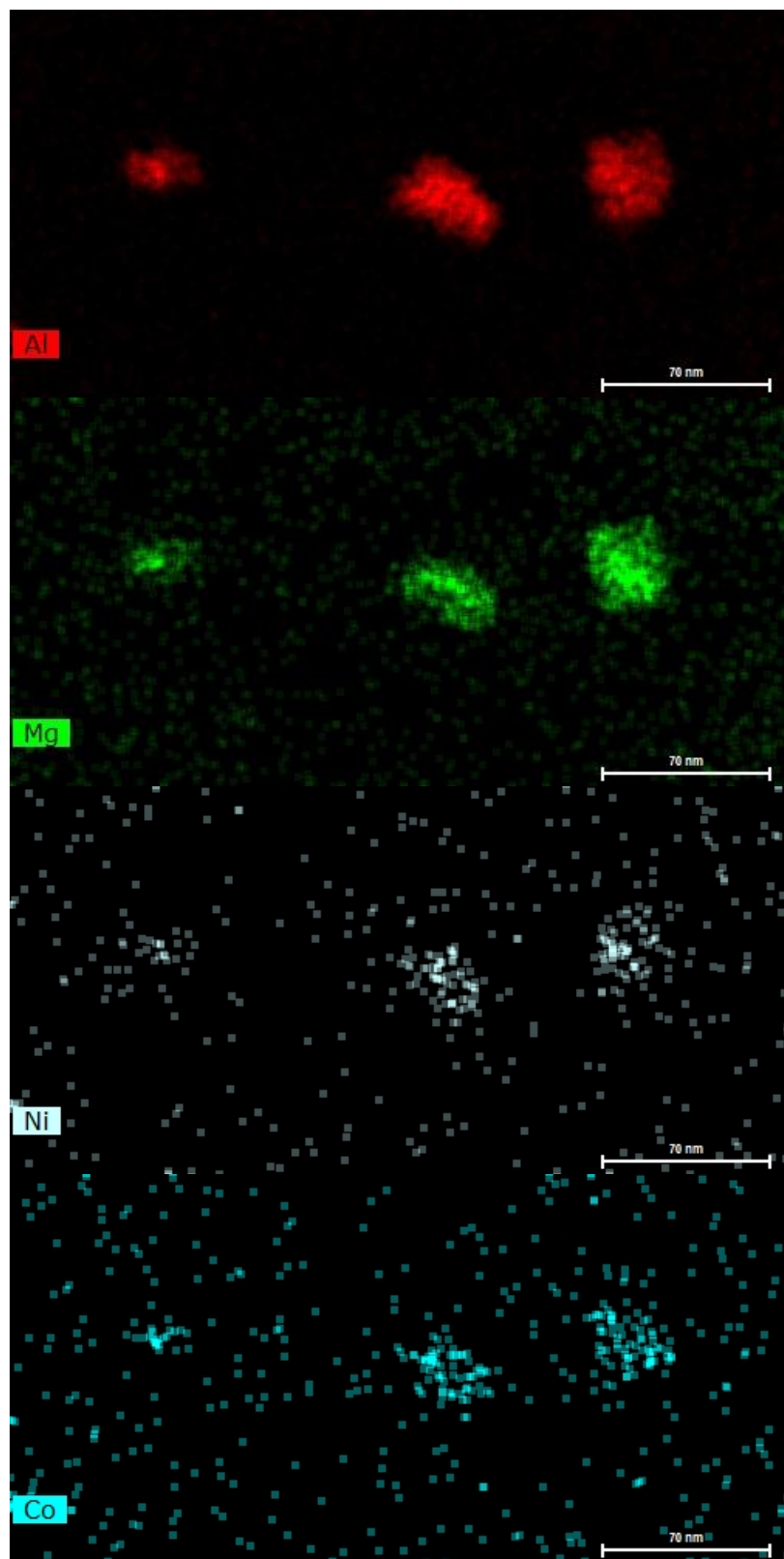


Figure 4-17 STEM-EDX of NiCo-spinel catalyst.

The distributions of each element on the catalysts NiCo/MgO-spinel were also studied by STEM-EDX. The results are shown in Figure 4-18. It was obvious that the distribution of Al was very different from that of elements Mg, Ni, and Co. The latter three elements stayed in the same location. According to the XRD analysis of this catalyst, there were two phases, spinel and MgO. The difference between Al and Mg distribution was due to the fact that these two elements were not in the same structure. The Al only stayed in the structure of spinel, but Mg also stayed in the MgO phase.

The catalyst particle shown in Figure 4-19 was divided into six parts. In parts A, more Al gathered in these areas than the other three elements. Oppositely, Mg along with Ni and Co displayed more in parts B. It indicated that the active metals Ni and Co had a stronger interaction with Mg, instead of with Al. The element Mg was mostly in the structure of the MgO solid solution, which was the main basic site working during the reaction. Thus, in part B, Ni and Co can have better interaction with the MgO, as well as better correlation with MgO, implying good contiguity of metallic and main basic sites.

To quantify the elements' content in each part, the mean grey value was determined using software ImageJ. Then the contents of the element were calculated and shown in Table 4-15. There was more Al in part A, with the molar percentage of 16.8, but the value in part B was 13.6. On the contrary, the contents of Mg, Ni, and Co were more in part B than in part A. There were 38.2 mol% of Mg, 2.7 mol% of Ni and 3.0 mol% of Co in part B, but the values in part A were 22.6, 1.2 and 1.9 mol%, respectively. The Mg/Al ratio was 0.8 in part A and 1.6 in part B.

As it was proposed, the measurement of elements' content in different parts also confirmed that most of Mg was not in the same structure with Al. The Mg/Al ratio even determined that the main structure of support in part A was spinel, but MgO solid in part B. Since the MgO was the

stronger basic sites on the catalysts and mainly in part B, the CRM reaction will mainly happen on part B instead in part A.

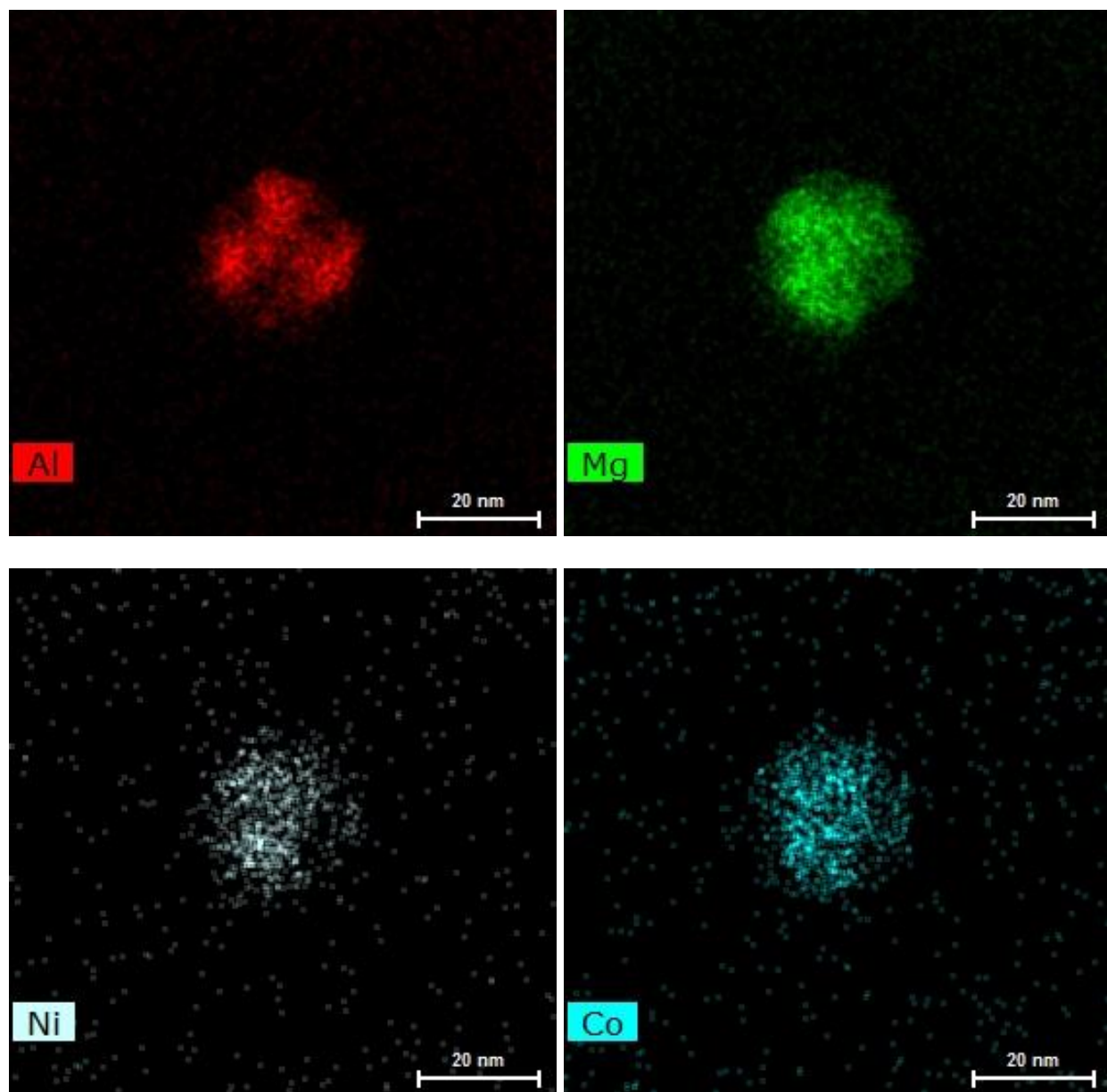


Figure 4-18 STEM-EDX of NiCo- MgO-spinel catalyst.

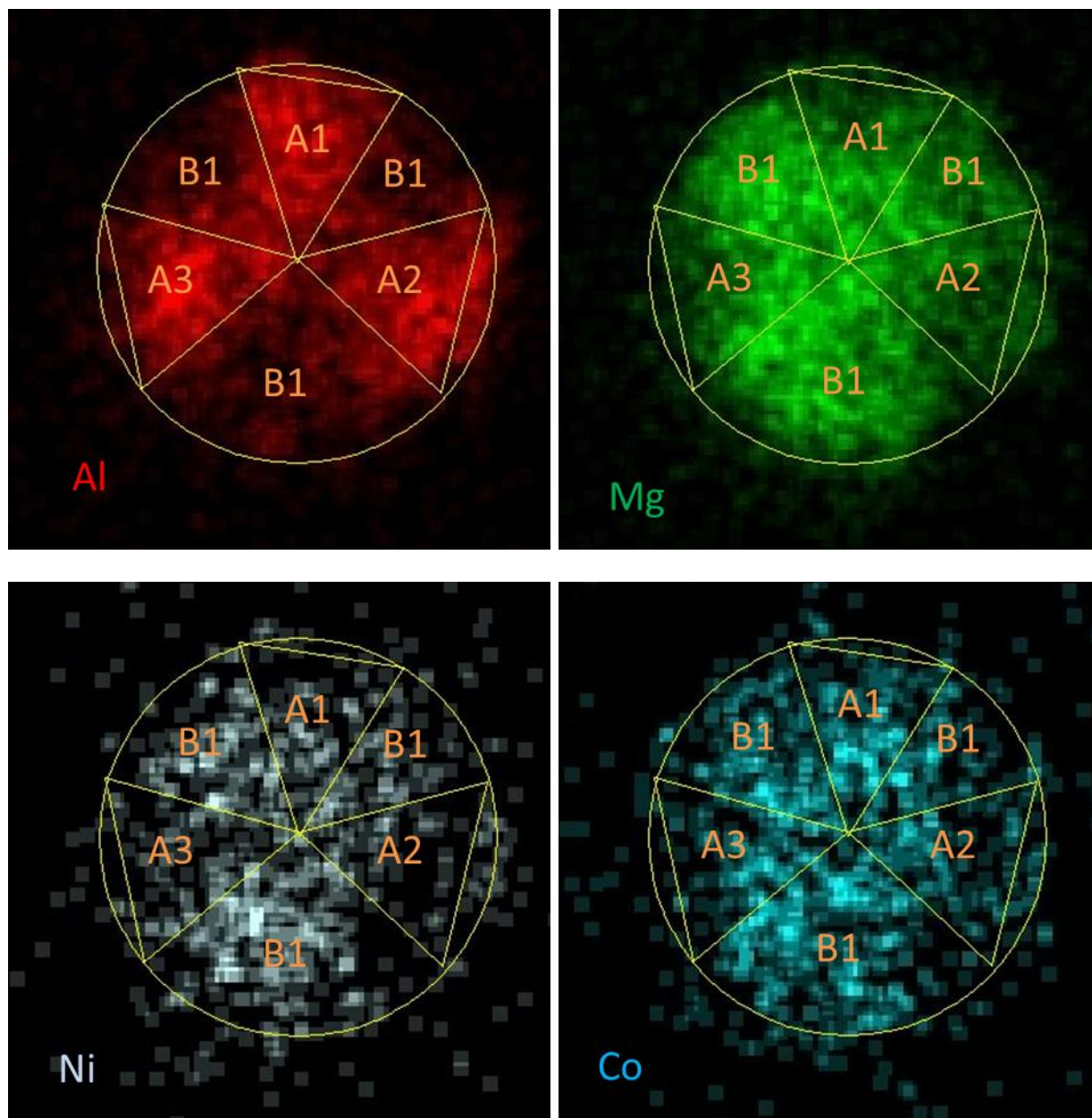


Figure 4-19 STEM-EDX of NiCo/MgO-spinel catalyst to calculate the element content in each part.

Table 4-15 The element content in different parts of the catalyst.

Parts	Mole (%)				Mg/Al ratio
	Al	Mg	Ni	Co	
A	16.8	22.6	1.2	1.9	0.8
B	13.6	38.2	2.7	3.0	1.6

4.7.4 Performance of the catalyst

The activity and stability of Ni/Al₂O₃ and Ni/MgO-spinel catalysts were investigated under the condition of 755 °C, 1 atm, and GHSV of 1200 L·g_{cat}⁻¹·h⁻¹. The reaction rate of CH₄ as a function of time-on-stream based on the number of metallic sites is shown in Figure 4-20. The catalyst Ni/Al₂O₃ had a lower reaction rate of 1.8 mmol·g_{cat}⁻¹·s⁻¹ as compared to 3.8 mmol·g_{cat}⁻¹·s⁻¹ with catalyst Ni/MgO-spinel. The same trend was seen in the performance of NiCo supported by spinel and MgO-spinel. The activity and stability of these two catalysts are shown in Figure 4-21. the reaction rate of CH₄ over the catalyst NiCo/spinel was around 1.0 mmol·g_{cat}⁻¹·s⁻¹, however that over catalyst NiCo/MgO-spinel was much higher, around 4.2 mmol·g_{cat}⁻¹·s⁻¹. Among these four catalysts, only NiCo/spinel had a trend of deactivation. It determined that the emergence of moderate basic sites, more metallic sites, and good contiguity of these two catalytic sites in catalyst Ni/MgO-spinel and NiCo/MgO-spinel led them to have higher catalytic activity in terms of per gram of catalyst as compared to catalysts Ni/Al₂O₃ and NiCo-spinel.

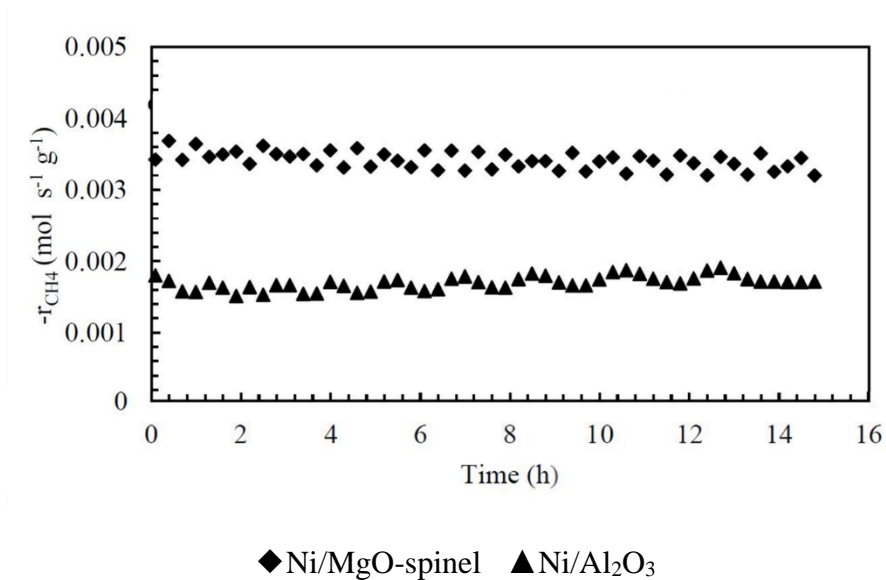


Figure 4-20 Activity and stability of Ni/Al₂O₃ and Ni/MgO-spinel catalysts at reaction condition: T = 755 °C, P = 1 atm, GHSV = 1200 L·g_{cat}⁻¹·h⁻¹, CH₄/CO₂/N₂ = 1/1/1. The reaction rate of CH₄ as a function of time-on-stream (Alabi, 2018).

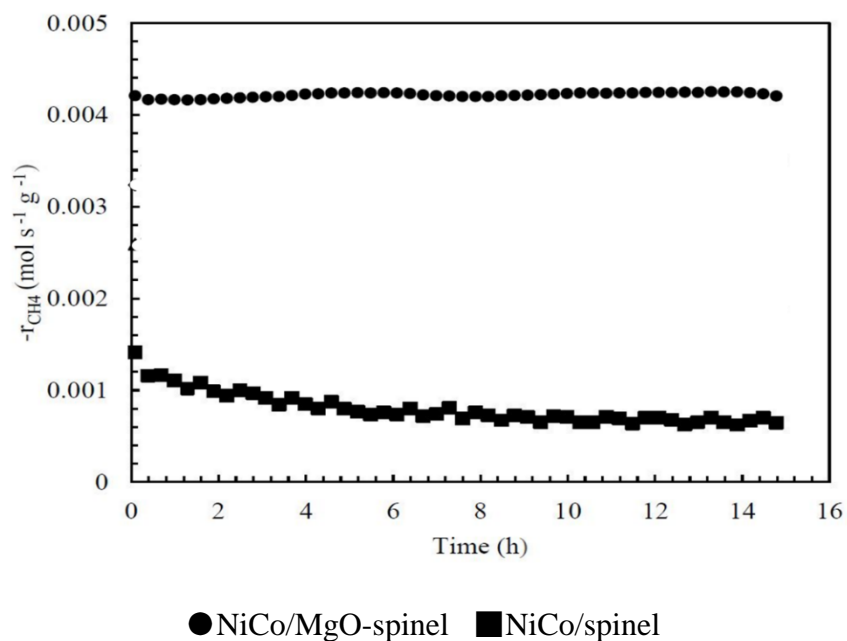


Figure 4-21 Activity and stability of NiCo/spinel and NiCo/MgO-spinel catalysts at reaction condition: T = 755 °C, P = 1 atm, GHSV = 1200 L·g_{cat}⁻¹·h⁻¹, CH₄/CO₂/N₂ = 1/1/1. The reaction rate of CH₄ as a function of time-on-stream (Alabi, 2018).

4.8 Conclusion

In this chapter, the effects of the different second metallic components in addition to Ni in the NiM2 (M2=Co, Mn, Cu, and Fe) bimetallic MgO-spinel structure catalysts on their catalytic performances in CO₂ reforming of CH₄ were studied. The study led to the understanding not only on the CO₂ catalytic activation mechanism but also on the interaction between species on basic sites and metallic sites. The study also led to one's thinking of contiguity, the geographic distribution and orientation of the basic sites and metallic sites, of the catalysts when dual sites or multiple sites participate in reactions. Here were some conclusions that were drawn from this study:

1. By using the coprecipitation method, a highly stable CO₂ reforming of CH₄ catalyst was created. MgO determined the number and strength of the basic sites of the catalysts. It also determined the reduction behavior of Ni and other metallic elements that form metallic sites after reduction. The use of the second metal or other metal elements chosen from Co, Cu, Fe, and Mn affected the metallic particle sizes and it also affected the basicity of the catalysts slightly. A look at a group of catalysts with varying contents of Mg revealed that stronger basic sites, or moderate basic sites according to CO₂-TPD, were on the MgO solid solution phase in the catalysts. The metallic sites were there, too. This granted that the catalyst with good contiguity of the two types of sites works for CO₂ reforming of CH₄.
2. The order of initial TOF of CO₂ and CH₄ based on the number of metallic sites with respect to the second metal was NiMn > NiCu > NiCo > Ni-monometallic > NiFe. This also had a good correlation with the average metallic particle size. The smaller particles had more chances for metallic sites in them to contact basic sites around them, as well as good contiguity of metallic and basic sites, thus leading to higher activities.

3. The deactivation behavior of the catalysts was explained by a pushing-pulling theory proposed in this study. The pushing force and pulling force of the catalytic sites were quantified from the pulse adsorption-reaction experiments. A stable, or good carbon-resistant catalyst had to be such that the pulling force, i.e., the oxidizing ability of CO₂ species on the basic sites surrounding the metallic particles, was stronger than the pushing force of the metallic sites to CH₄.
4. The analysis resulted in a new understanding of the reaction and side reaction of the CO₂ reforming of CH₄ system. It was believed that reverse water-gas shift reaction was the main side reaction that led to the H₂/CO ratio in CO₂ reforming of CH₄ below one. This study revealed that the incomplete dissociation of CH₄ on the metallic sites should be blamed. Two activated C-H bonds on metallic sites react with one activated CO₂ to form one CO, two H₂O, and one carbon on the metallic sites, which resulted in carbon deposition and catalyst deactivation.

CHAPTER 5 CO₂ Catalytic Activation for CO₂ Hydrogenation to Synthesize Methanol over ZnO Over-coated Cu/SiO₂ Catalysts

Based on the literature study, it had been recognized that during the reaction of CO₂ hydrogenation for methanol synthesis over the Cu-ZnO catalyst, CO₂ was activated by one type of sites, say ZnO or ZnO related, which was the basic sites, and H₂ by another type, say metallic Cu or Cu related, which was the metallic sites. The metallic sites and basic sites must be next to each other to form the right structures to facilitate the formation of methanol. If not, the two catalytic sites may form the wrong structures to help the formation of CO. Different catalysts for this reaction were developed, but no one had proposed a catalyst can show both high CO₂ conversion and selectivity to methanol until now. More works are needed to be done to study CO₂ catalytic activation in this reaction, especially on the aspect of the contiguity of the catalytic sites.

For the reaction of CO₂ hydrogenation to produce methanol, which involved two reactants to be activated on different types of activation sites, not only the number and activity of the sites but also the site distribution and orientation, namely site contiguity, determined the reaction mechanism and kinetics. Thus, the study to determine the effect of the contiguity of basic and metallic sites on the catalytic performance was necessary. To study the effects of the neighborhood, the accessibility, and the orientation of these two types of sites, two extreme catalyst models were proposed. The first model of catalyst contained isolated Cu particles distributed in a layer of ZnO atoms, and the second showed isolated ZnO phases distributed in a layer of Cu or surrounded by

sufficient Cu nanoparticles. In this part of the work, only the first model was studied due to the limitation of equipment.

In this part, the Cu-ZnO catalysts containing isolated Cu-related particles distributed in ZnO atoms with different distribution were studied to investigate the influence of distribution and uniformity of metallic Cu particles and ZnO, and their contiguity on the catalyst activity and selectivity to methanol.

Part of the contents in this chapter has been published in Catalysis cited blow.

Citation: Gao, J.; Boahene, P. E.; Hu, Y.; Dalai, A.; Wang, H. Atomic Layer Deposition Over-coated Cu-ZnO Catalysts for Methanol Synthesis from CO₂ Hydrogenation. Catalysts 2019, 9(11), 922

Contribution of authors: Conceptualization, J.G. and H.W.; Data curation, J.G.; Formal analysis, J.G.; Funding acquisition, H.W. and A.D.; Investigation, J.G. and P.B.; Methodology, J.G.; Resources, Y.H., A.D. and H.W.; Supervision, H.W. and A.D.; Writing—original draft, J.G.; Writing—review and editing, P.B., Y.H., A.D. and H.W.

5.1 Formation of Cu Particles with Uniformed Distribution

To develop the Cu-ZnO catalysts with isolated Cu particles and ZnO atoms with a different distribution, the Cu particles were prepared first. In this section, the Cu particles had been prepared with the different methods, dry impregnation or strong electronic adsorption, at different calcination temperatures, 250 °C or 500 °C, and with different reduction temperatures, 250 °C or 500 °C. Then, the sample with uniformed Cu particles was chosen as the precursor to over-coated ZnO and further studied in the next section.

5.1.1 Reduction properties of samples from H₂-TPR

The H₂-TPR results of samples Imp-5Cu-CT250, Imp-5Cu-CT500, SEA-5Cu-CT250, SEA-5Cu-CT500, SEA-10Cu-CT250 and SEA-10Cu-CT500 are shown in Figure 5-1. For samples calcined at 250 °C, two hydrogen consumption peaks were observed at the range of 186-194 °C (referred to as α -peak) and 206-240 °C (β -peak) in the H₂-TPR profile. For samples calcined at 500 °C, there was only one hydrogen consumption peak displayed at 180 °C (Imp-5Cu-CT500 and SEA-10Cu-CT500) or 240 °C (SEA-5Cu-CT500). The consumption peak area of samples calcined at 500 °C was much smaller than that of samples calcined at 250 °C.

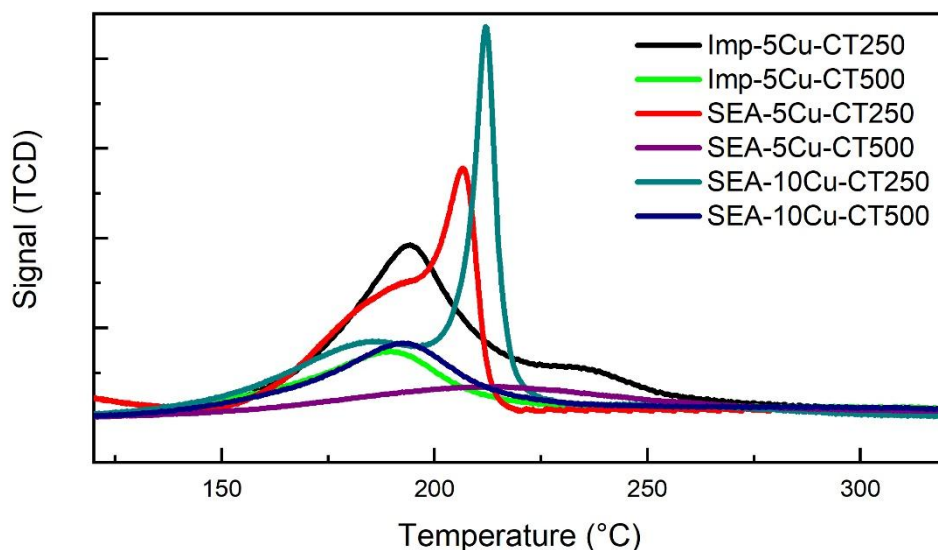


Figure 5-1 H₂-TPR profiles of samples prepared by Imp or SEA method with different Cu content and different calcined temperature.

On the basis of literature, the α -peak was ascribed to the reduction of the highly dispersed CuO phases (Ren et al., 2015; Din et al., 2017), while the β -peak was attributed to the reduction of the CuO species having relatively stronger interactions with the support (Ren et al., 2015). Imp-5Cu-CT250 sample was prepared by impregnation results in more formation of the dispersed CuO

species, shown by the higher α -peak intensity. SEA-5Cu-CT250 and SEA-10Cu-CT250, prepared by the SEA method with 5 wt% and 10 wt% of Cu loading, exhibited larger β -peak. The difference between these two types of catalysts on the H₂-TPR profiles was due to their preparation method. During the preparation of SEA samples, the silica gel was first pretreated with ammonia solution at a certain pH to adjust the surface charge before mixing with the Cu complex of the opposite charge to form the CuO species. Thus, the catalysts prepared by the SEA method showed more CuO species which had stronger interactions with the support. For the samples calcined at 500 °C, the small consumption peak meant that not all the Cu species were reduced in the temperature range of the TPR procedure we used.

According to the reduction properties of each sample, the reduction temperature of 250 °C was used to reduce the samples Imp-5Cu-CT250, SEA-5Cu-CT250 and SEA-10Cu-CT250, and that of 500 °C to reduce the sample Imp-5Cu-CT250, Imp-5Cu-CT500, SEA-5Cu-CT250, SEA-5Cu-CT500, SEA-10Cu-CT250 and SEA-10Cu-CT500, to prepare uniform Cu particles.

5.1.2 Samples screened by TEM images

TEM images of reduced samples were used to screen them. Figure 5-2 shows the TEM images of the samples Imp-5Cu-CT250-RT250 (the sample prepared by dry impregnation, calcined at 250 °C and reduced at 250 °C), Imp-5Cu-CT500-RT500, SEA-5Cu-CT250-RT250, SEA-5Cu-CT500-RT500, SEA-10Cu-CT250-RT250, and SEA-10Cu-CT500-RT500. And there were no many metallic Cu nanoparticles formed on the surface of these samples.

Figure 5-3 shows the TEM images and the histograms of the samples calcined at 250 °C and reduced at 500 °C. The sample Imp-250 reduced at 500 °C had Cu particles with different sizes in a wide range of 2-21 nm. Since the CuO species prepared by the SEA method showed relatively

stronger interactions with the support, the pretreatment in SEA to adjust the surface charge resulted in better distribution of the metal particles. The average particle sizes of sample SEA-5Cu was 8.4 nm. The particles formed in a narrow range, which was bigger than 5nm and smaller than 13 nm. The average particle sizes of sample SEA-10Cu was 8.6 nm. The sizes of metallic particles on the sample SEA-10Cu were in the range of 3-23 nm. In the further comparison of the particle-size distribution between SEA-5Cu and SEA-10Cu, showed that SEA-5Cu should be used for further study.

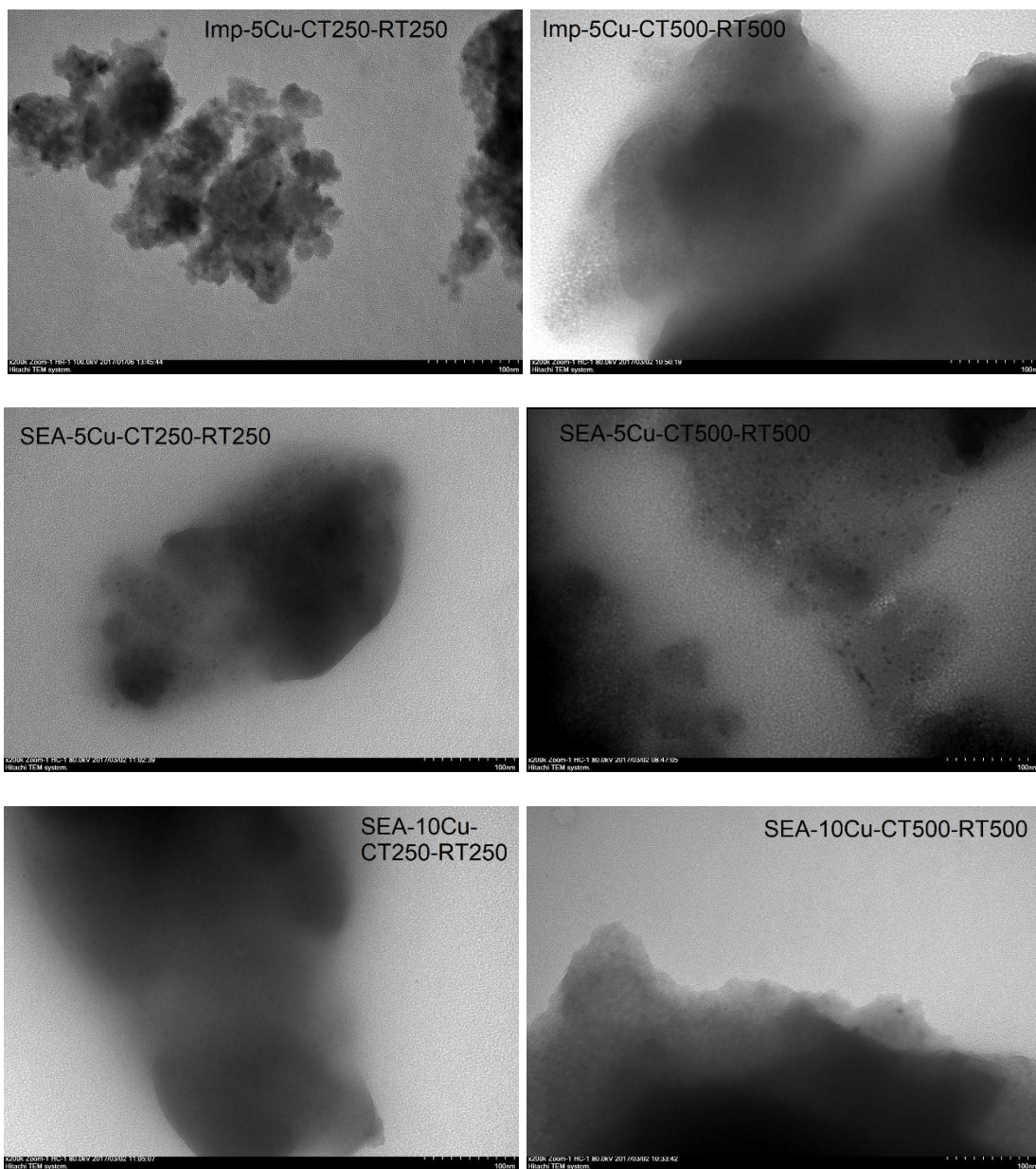


Figure 5-2 TEM images of samples Imp-5Cu, SEA-5Cu and SEA-10Cu calcined at 250 °C and reduced at 250 °C, and samples calcined at 500 °C and reduced at 500 °C

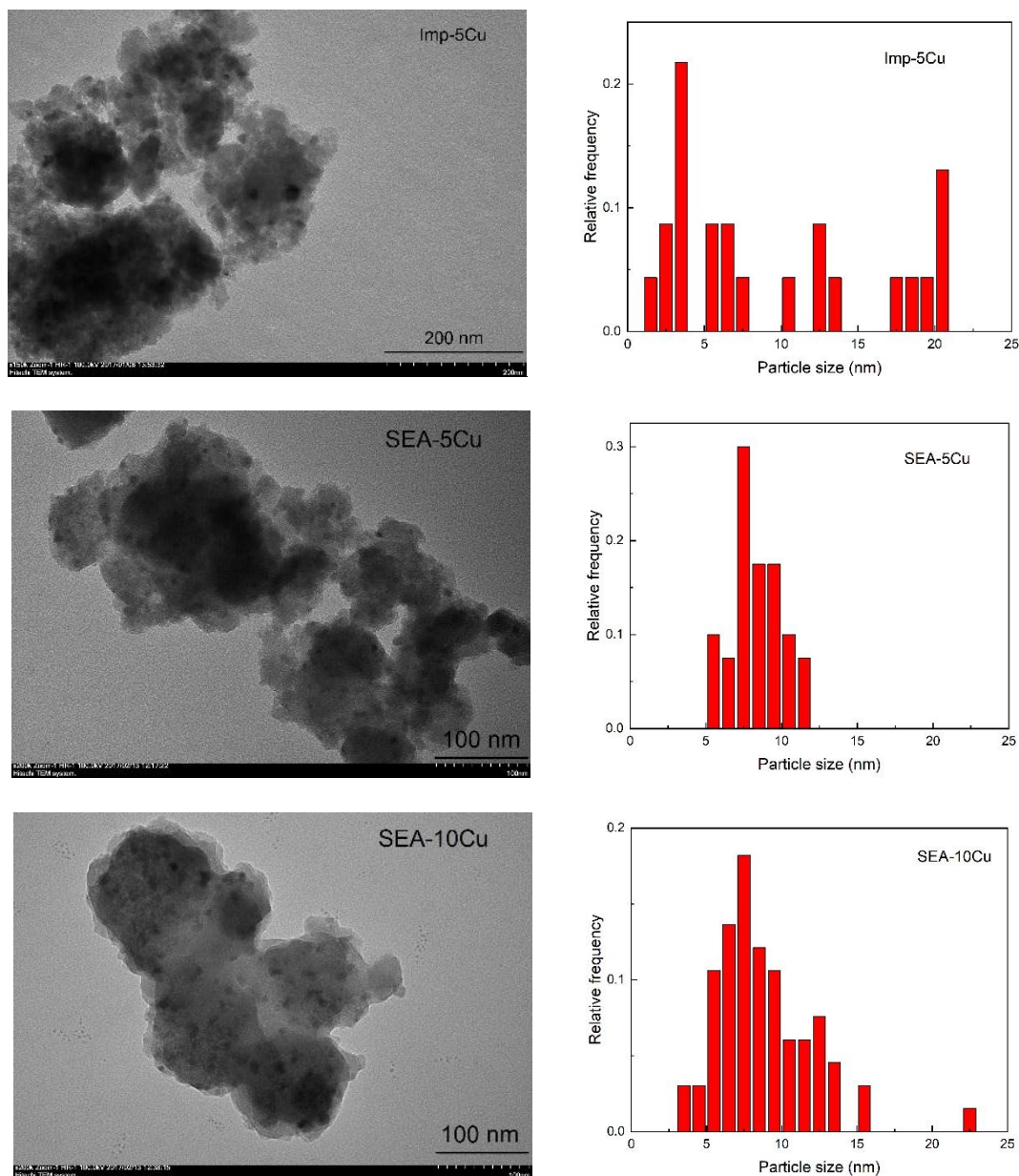


Figure 5-3 TEM images and particle-size distribution of samples Imp-5Cu, SEA-5Cu, and SEA-10Cu calcined at 250 °C and reduced at 500 °C.

The final catalysts were prepared by using ALD to deposit ZnO with different exposure time and cycles on SEA-5Cu calcined at 250 °C. The catalysts were denoted as 5Cu-1CyZn-5s, 5Cu-1CyZn-30s, and 5Cu-5CyZn-5s (called ZnO over-coated Cu/SiO₂ catalysts). 1Cy and 5Cy

represented the number of cycles of ALD performed. 5s and 30s represented the exposure time of the SEA-5Cu to the Zn precursor in each cycle.

5.2 Bulk Properties of the CO₂ Hydrogenation Catalysts of Oxide State

The ZnO over-coated Cu/SiO₂ catalysts with isolated Cu phase and ZnO phase in different uniformity were prepared by SEA and ALD method. The solid structure and basic sites had been formed. The bulk properties meant the composition, the specific surface area, and porous structures. They were measured by ICP-MS, N₂ adsorption, respectively. The detailed procedures have been given in Chapter 3.

5.2.1 Metal composition by ICP analysis

Table 5-1 shows the ICP results of the substrate silica gel (SiO₂), SEA-5Cu, and the ZnO over-coated Cu/SiO₂ catalysts. The reproducibility of the ICP results has been studied and shown in Appendix A. The Cu contents in these samples were approximately 4.4 wt% as expected; however, the Zn content varied depending on the exposure time and ALD cycles. With a single-cycle deposition, the content of Zn increased from 0.3 wt% (exposure time of 5 seconds) to 1.5 wt% (exposure time of 30 seconds). With the same exposure time (5 seconds), the Zn content increased from 0.3 wt% (1 cycle of ALD) to 1.3 wt % (5 cycles of ALD).

Table 5-1 ICP results of SiO₂, SEA-5Cu, and ZnO over-coated Cu/SiO₂ catalyst

Samples	Cu (wt%)	Zn (wt%)
Silica gel	-	-
SEA-5Cu	4.4	-
5Cu-1CyZn-5s	4.4	0.3
5Cu-1CyZn-30s	4.5	1.5
5Cu-5CyZn-5s	4.3	1.3

5.2.2 Surface area and porous structures by N₂ adsorption-desorption

The isotherm results of N₂ adsorption-desorption of SiO₂, SEA-5Cu, and ZnO over-coated Cu/SiO₂ catalyst are shown in Figure 5-5. According to the IUPAC classification of Sing et al. (Sing et al., 1985), all the catalysts had the hysteresis loop which was the characteristic feature of the Type IV isotherm. The loop was associated with capillary condensation which took place in mesoporous material. However, the support, silica gel showed Type H4 loop, which was associated with narrow slit-like pores, and SEA-5Cu and ZnO over-coated Cu/SiO₂ catalysts displayed Type H1 hysteresis loop, which was related to solid materials with a narrow distribution of pore size. It determined along with Cu loaded, the narrow slit-like pores were blocked, and the ZnO over-coated didn't affect the pore size and distribution much.

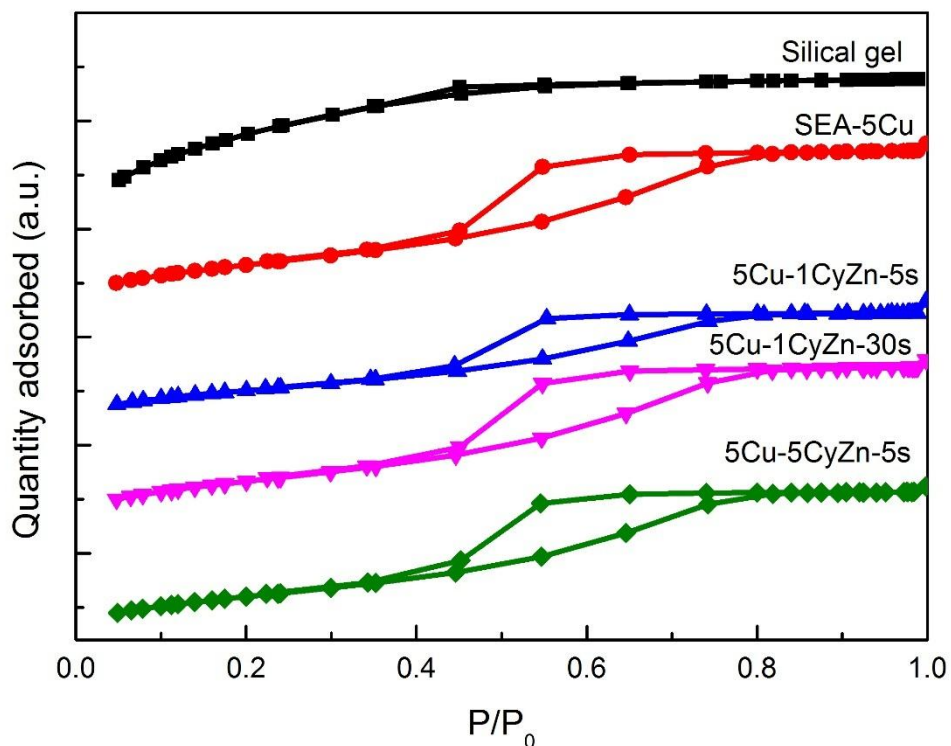


Figure 5-4 N₂ adsorption-desorption isotherms of SiO₂, SEA-5Cu, and ZnO over-coated Cu/SiO₂ catalysts

As the BET results shown in Table 5-2, the loading of Cu by the SEA method dramatically decreased the specific surface area and pore volume of SiO₂. The average pore size increased from 3.0 nm to 4.5 nm, indicating blockage of smaller mesopores. The surface area and pore volume were decreased further by ZnO ALD, but to a smaller extent on the basis of the Cu loading.

Table 5-2 BET and XRD results of SiO₂, SEA-5Cu, and ZnO over-coated Cu/SiO₂ catalysts

Samples	BET surface area (m ² g ⁻¹)	Pore volume (cm ³ g ⁻¹)	Average pore size (nm)	Cu ⁰ lattice constant (Å)
Silica gel	718	0.41	3.0	
SEA-5Cu	264	0.30	4.5	3.62
5Cu-1CyZn-5s	200	0.21	4.2	3.62
5Cu-1CyZn-30s	210	0.24	4.3	3.65
5Cu-5CyZn-5s	238	0.28	4.6	3.66

5.3 Catalysts Characterization after Reduction

The material formed during the reduction was the catalyst used for the reaction. Properties after reduction had more direct impacts on reaction performances. The reduction was the key step where the metallic sites formed.

In this section, the reduction condition of the catalysts ZnO over-coated Cu/SiO₂ was studied by H₂-TPR first. Then the reduction temperature which can reduce Cu species, but not Zn species was chosen. The crystal structure of the reduced catalysts was studied by XRD patterns. Through the TEM-EDX analysis, the distribution of Cu and ZnO phase, and the metal particle size and distribution were obtained. Then metal dispersion and the number of metallic sites were determined by the CO chemisorption analysis.

5.3.1 Reduction condition study by H₂-TPR

The H₂-TPR results of ZnO over-coated Cu/SiO₂ catalysts with the different ZnO over-coated procedure are shown in Figure 5-5. Two hydrogen consumption peaks were seen at the range of 148-194 °C (referred to as α -peak) and 206-254 °C (β -peak) in the TPR spectra. According to the study on the Imp-5Cu, SEA-5Cu and SEA-10Cu, the two peaks were ascribed to the reduction of the highly dispersed CuO phases and the CuO species, which had a strong interaction with the support (Ren et al., 2015; Din et al., 2017). Along with the increase in the amount of ZnO, the β -peak clearly shifted to high temperatures. Since adding ZnO can improve the dispersion of Cu particles, which was confirmed by TEM results, the interaction between smaller Cu particles and support was stronger. This right shift could also be due to the coverage of ZnO on CuO species, and causing them harder to be reduced. The H₂-TPR profiles also verified that using 500 °C as the reduction temperature was sufficient to activate the catalysts.

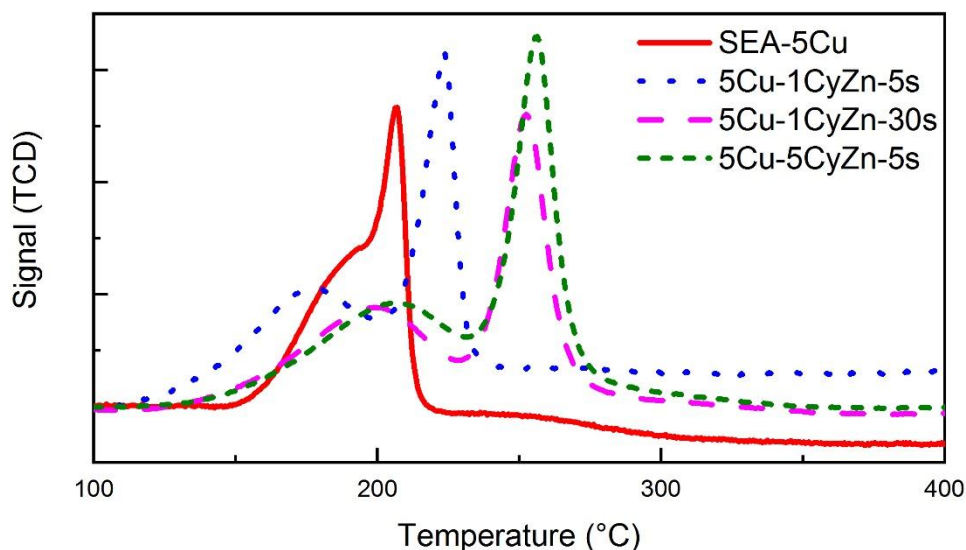


Figure 5-5 H₂-TPR profiles of SEA-5Cu and catalysts ZnO over-coated Cu/SiO₂

5.3.2 Crystal structure by XRD

XRD patterns of SiO₂ and reduced SEA-Cu, ZnO over-coated Cu/SiO₂ catalysts are shown in Figure 5-6. The diffraction peak relative to amorphous SiO₂ at 2θ can be seen at $2\theta = 22^\circ$. After reduction, most of CuO was reduced to metallic Cu. For the reduced SEA-5Cu, the Cu phase was assigned to face-centered cubic copper structure with characteristic diffraction peak 2θ at 43° , 50° , and 74° . (Tisseraud et al., 2018) The ALD over-coating of ZnO did not change much of the Cu signals. No new peaks were formed for ZnO species, which indicated that the structure of ZnO prepared by ALD was not large enough to be detected by XRD. The value of Cu⁰ lattice constant calculated (Table 5-2) increased with the increase in ZnO deposition, from 3.62 to 3.66 Å. Kanai et al. (Kanai et al., 1994) believed that the increase of lattice constant from 3.62 to 3.67 Å in their study on the Cu-ZnO catalysts was attributable to the formation of a Cu-Zn alloy. In our case, the increase in the lattice constant upon the deposition of ZnO may be also associated with the formation of the Cu-Zn surface alloy, which implying chemical interaction of Cu and ZnO, further good contiguity of metallic and basic sites.

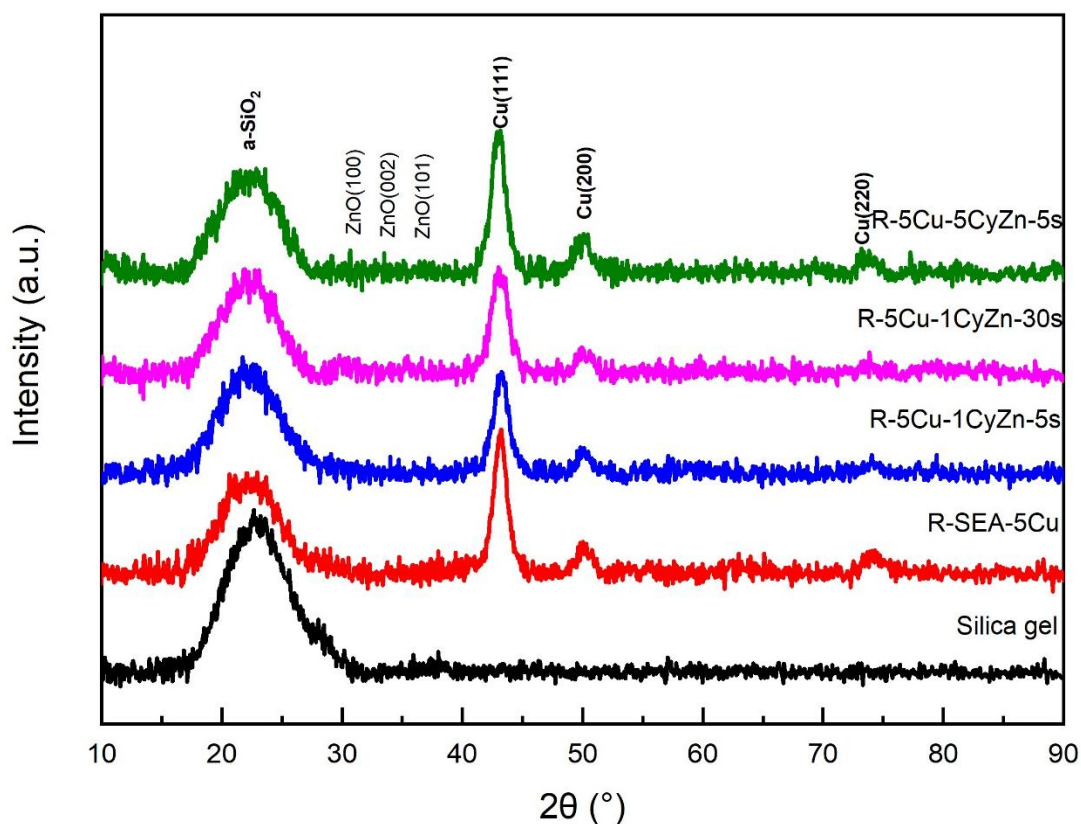


Figure 5-6 XRD patterns corresponding to support and reduced ZnO over-coated Cu/SiO₂ catalysts

5.3.3 ZnO and Cu phase distribution

With the help of TEM-EDX, the distributions of the elements of the reduced catalysts were obtained and shown in Table 5-3, which revealed the structure of ZnO formed by the ALD procedure. The spots were chosen randomly and the diameter of the chosen area was 1 μm . According to EDX results of catalyst 5Cu-1CyZn-5s, at the different spots, there are varying ZnO over-coated. Three spots showed a similar content of ZnO over-coated, whose value was around 0.25 wt%. At another spot, Zn content was 1.9 wt%. However, on the catalyst of 5Cu-1CyZn-30s, the Zn contents showed a similar value of 1.1 wt% (minimum) and 1.9 wt% (maximum) at various spots. There was much more difference in the Zn content on the catalyst 5Cu-5CyZn-5s. There was

barely over-coating of ZnO on spot 1 with the Zn content of 0.1 wt%. On the spot 2, this value was 4.1 wt%. Compared to the Cu content on the various spot of the catalysts 5Cu-1CyZn-5s and 5Cu-5CyZn-5s, which showed a huge difference, quite similar Cu content was shown on the various spot of the catalyst 5Cu-1CyZn-30s.

Table 5-3 The content of elements on the reduced catalysts detected by TEM-EDX.

Catalysts	Spots	Zn	Cu	Si	O
5Cu-1CyZn-5s Elements (wt%)	1	1.9 (± 0.8)	87.0 (± 9.2)	1.8 (± 0.5)	9.3 (± 1.8)
	2	0.2 (± 0.1)	22.6 (± 2.3)	42.0 (± 1.0)	35.2 (± 3.4)
	3	0.3 (± 0.1)	17.7 (± 1.7)	46.8 (± 0.8)	35.1 (± 3.3)
	4	0.2 (± 0.1)	7.8 (± 0.7)	45.2 (± 0.5)	46.8 (± 4.3)
5Cu-1CyZn-30s Elements (wt%)	1	1.1 (± 0.2)	10.9 (± 1.1)	43.7 (± 0.5)	44.3 (± 4.1)
	2	1.9 (± 0.2)	12.3 (± 1.2)	48.6 (± 0.6)	37.2 (± 3.4)
	3	1.1 (± 0.1)	8.5 (± 0.8)	52.8 (± 0.3)	37.6 (± 3.4)
	4	1.8 ± 0.2	8.3 ± 0.8	50.1 ± 0.2	39.8 ± 3.6
5Cu-5CyZn-5s Elements (wt%)	1	0.1 (± 0.0)	5.0 (± 0.5)	60.7 (± 0.5)	34.2 (± 3.1)
	2	4.1 (± 0.4)	8.0 (± 0.8)	43.1 (± 0.4)	44.8 (± 4.1)
	3	2.4 (± 0.3)	9.0 (± 0.9)	43.2 (± 0.4)	45.4 (± 4.1)
	4	1.0 (± 0.2)	26.5 (± 2.6)	34.6 (± 0.8)	37.9 (± 3.6)

Previous investigation of in situ XAS of ZnO growth on SiO₂ demonstrated that ZnO film initially grew through an embryonic step in which three-dimensional nanoislands form, then coalesce to trigger a layer-by-layer growth mode. In our case, on the catalyst 5Cu-1CyZn-5s, there may be nanoislands of ZnO because of short exposure time. The ZnO was located on 5Cu-1CyZn-

5s as molecules and not enough to totally connect to each other and form an atomic layer. Similar Zn contents were shown at the different spots on the catalyst 5Cu-1CyZn-30s, which indicated there was a uniform atomic ZnO layer over-coated on the surface of the catalyst. The content of Zn on the catalyst 5Cu-5CyZn-5s was larger than that on catalyst 5Cu-1CyZn-5s. With multiple cycles and short exposure time, there may be different sizes of ZnO nanoparticles formation on the catalyst 5Cu-5CyZn-5s. At some of the spots, multiple ZnO layers were formed, and at some spots, there was barely any ZnO deposited.

During the reduction, CuO species migrated to the surface and formed metallic Cu particles. (Gawande et al., 2016) Since the ZnO deposited on the catalysts were shown to have the different structure on various catalysts, different sizes of Cu particles were formed during reduction. On the catalyst 5Cu-1CyZn-30s, with a uniform ZnO layer over-coated, all the CuO species had similar resistance while migrating to the surface, so there were similar Cu contents on different spots on the reduced catalyst. On the contrary, there was non-uniform ZnO deposited on the catalysts 5Cu-1CyZn-5s and 5Cu-5CyZn-5s, which resulted in different Cu content showing on various spots. The distribution of the metallic particle size was also obtained by the TEM images of reduced catalysts, which verified the conclusion from the results of TEM-EDX. (Figure 5-7)

5.3.4 Metallic particle size and distribution

For CO₂ hydrogenation for methanol synthesis reaction, only metallic sites and basic sites that are next to each other can allow activated CO₂ on the basic sites, to be reduced by hydrogen species formed on metallic sites resulted from H₂ activation. The basic and metallic sites should sit in the right orientation to allow hydrogen species to pull one oxygen out, and insert H at the same time to form O-H and C-H bond. Thus, the accessibility of metallic and basic sites, or their contiguity

is important for the occurrence reaction in the right direction. At least, two catalytic sites should be close to each other enough. Most of the time, there is no direct measure of contiguity. However, many measures of the characterization methods can become the indicator of contiguity of the catalytic sites. TEM metal particle size is one of the indications of the sites' contiguity. Assumed to be distributed in the same basic sites, smaller metal particles allow more metallic sites to be exposed to basic sites, but larger particles isolate more metallic sites in the middle of particles.

Compared to the TEM image of SEA-Cu, the ZnO coating leads to a reduction of the particle size, which is from 8.4 nm to 8.1, 6.7, or 6.9 nm on the catalysts 5Cu-1CyZn-5s, 5Cu-1CyZn-30s, or 5Cu-5CyZn-5s, respectively (Table 5-4). The crystallite sizes of Cu calculated using the Scherrer's equation are reported in Table 5-4. These values are a little smaller than those from TEM images, however, a similar trend can be observed. The catalyst 5Cu-1CyZn-30s has the smallest Cu particles formed on the catalysts, and only Cu particles on catalyst 5Cu-1CyZn-30s showed uniform particle size, in a range of 4-10 nm. There are both much bigger and smaller particles formed on the catalysts 5Cu-1CyZn-5s (particle sizes in the range of 3-15 nm) and 5Cu-5CyZn-5s (particle sizes in the range of 2-11 nm). The difference of the particle size on these three catalysts is due to the distinct ZnO structure formed on the surface of the catalysts by ALD as discussed earlier. The catalyst 5Cu-1CyZn-30s with smaller metal particles, allows more metallic sites to be exposed to basic sites, which means better contiguity of metallic and basic sites.

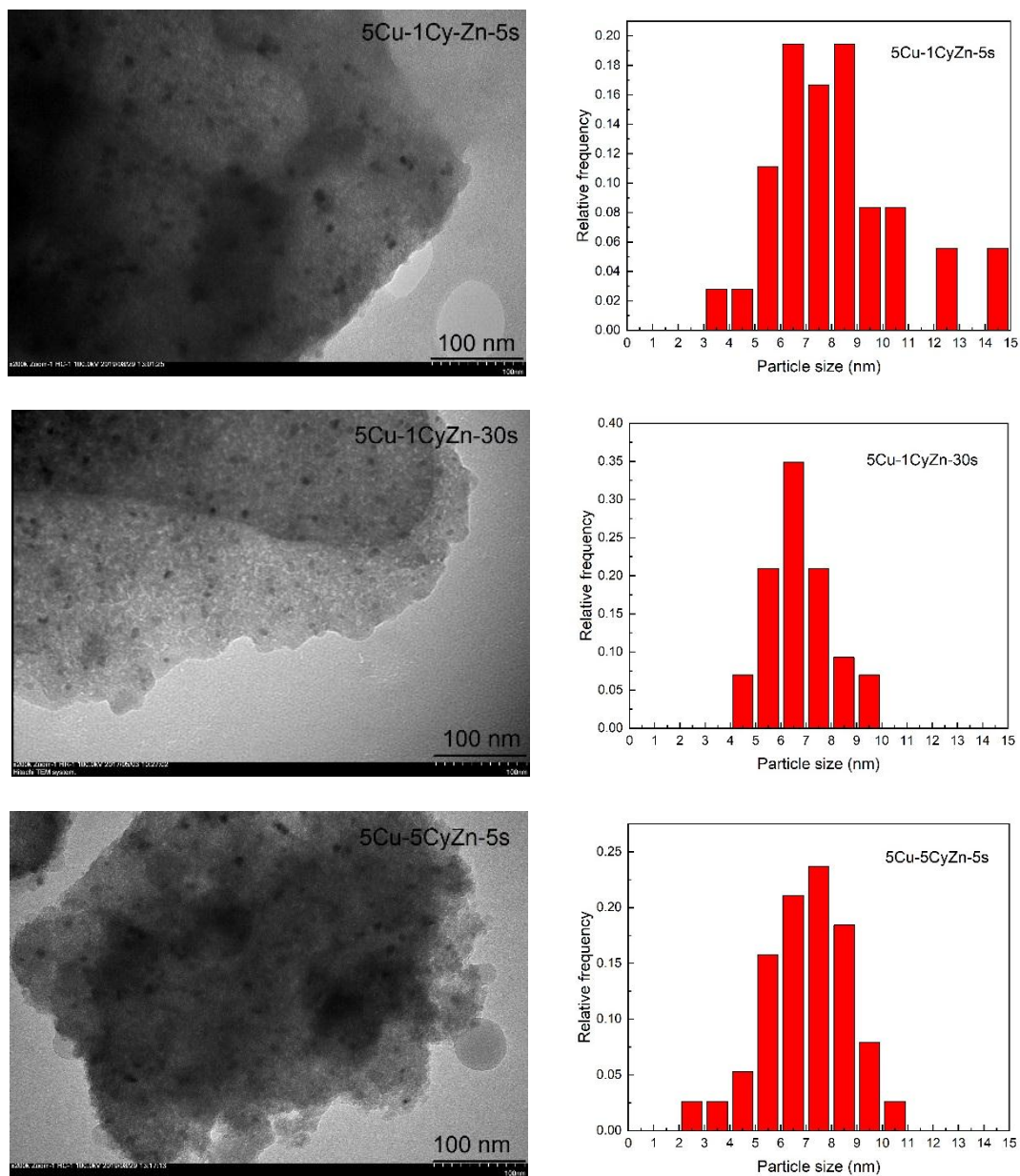


Figure 5-7 TEM images, particle size, and distribution of Cu-ZnO catalysts.

Table 5-4 Metallic particle size measured by TEM and XRD

Samples	Metal particle size (nm)	
	TEM	XRD
SEA-5Cu	8.4	7.1
5Cu-1CyZn-5s	8.1	6.5
5Cu-1CyZn-30s	6.7	5.3
5Cu-5CyZn-5s	6.9	6.4

5.3.5 Number of metallic sites and metal dispersion

The properties of metallic sites were detected by CO chemisorption, shown in Table 5-4. The number of metallic sites was obtained by the amount of CO uptake during the analysis, and all the CO molecules were linearly chemisorbed on the metal molecules on the surface of the catalyst. The Cu dispersion decreased with the longer exposure time of ZnO over-coating. The Cu dispersion decreased from 1.9 (5Cu-1CyZn-5s) to 1.7 % (5Cu-1CyZn-30s). This value decreased much more with multiple cycles of ZnO over-coated, which was from 1.9 to 1.3 % (5Cu-5CyZn-5s). The Cu surface area on the catalysts 5Cu-1CyZn-5s and 5Cu-1CyZn-30s showed a similar value of 0.65 and 0.69 $\text{m}^2 \cdot \text{g}_{\text{cat}}^{-1}$. This value became less for the catalyst 5Cu-5CyZn-5s, which was 0.53 $\text{m}^2 \cdot \text{g}_{\text{cat}}^{-1}$. The number of metallic sites on these catalysts showed the same trend. The lower Cu dispersion of 5Cu-5CyZn-5s may be due to the multiple layers or nanoparticles of ZnO formation on the surface, which provided different resistance for Cu species migrating to the surface during the reduction of the catalyst. And Cu surface area was also lower on the 5Cu-5CyZn-5s because CuO species may be covered by multiple layers of ZnO and harder to be reduced, which was also

confirmed by the results of H₂-TPR. The number of metallic sites was related to the ability of H₂ dissociation and how much H atoms can be provided to the basic sites.

Table 5-5 Cu dispersion, metallic surface area of reduced catalysts, and number of metallic sites.

Samples	Cu dispersion (%)	Cu surface area (m ² ·g _{cat} ⁻¹)	The number of metallic sites (μmol·g ⁻¹)
SEA-5Cu	-	-	-
5Cu-1CyZn-5s	1.9	0.69	304
5Cu-1CyZn-30s	1.7	0.65	286
5Cu-5CyZn-5s	1.3	0.53	228

5.4 Basicity of the catalysts from CO₂-TPD

The basicity of the SEA-5Cu and Cu-ZnO catalysts was detected using CO₂-TPD, which revealed the species and number of basic sites. The CO₂-TPD curves of the SEA-5Cu and Cu-ZnO catalysts are shown in Figure 5-8. There were three peaks shown in the profiles. The adsorption temperatures of each peak were centered around 140 °C, 340 °C, and 570 °C, which can be assigned to the weak, moderate, and strong basic sites. According to the literature, the weak basic sites were ascribed to the OH⁻ groups. The moderate basic sites were related to the M-oxygen pairs (M=metal). The strong basic sites were associated with the coordinatively unsaturated O²⁻ ions, which was a low coordination oxygen atom. (Liu et al., 2010; Gao et al., 2014; Huang et al., 2015; Ayodele et al., 2017)

From the peak fitting results based on the Gaussian distribution using software Origin, there were small weak and strong CO₂ desorption peak and a big moderate peak showing. The amounts

of CO₂ desorption for the catalysts are shown in Table 5-5. There was the most amount of moderate basic site on the 5Cu-1CyZn-30s and 5Cu-5CyZn-5s catalysts, 1260 $\mu\text{mol}\cdot\text{g}^{-1}$. The catalyst 5Cu-1CyZn-30s also had the greatest number of total basic site, the value was 1428 $\mu\text{mol}\cdot\text{g}^{-1}$.

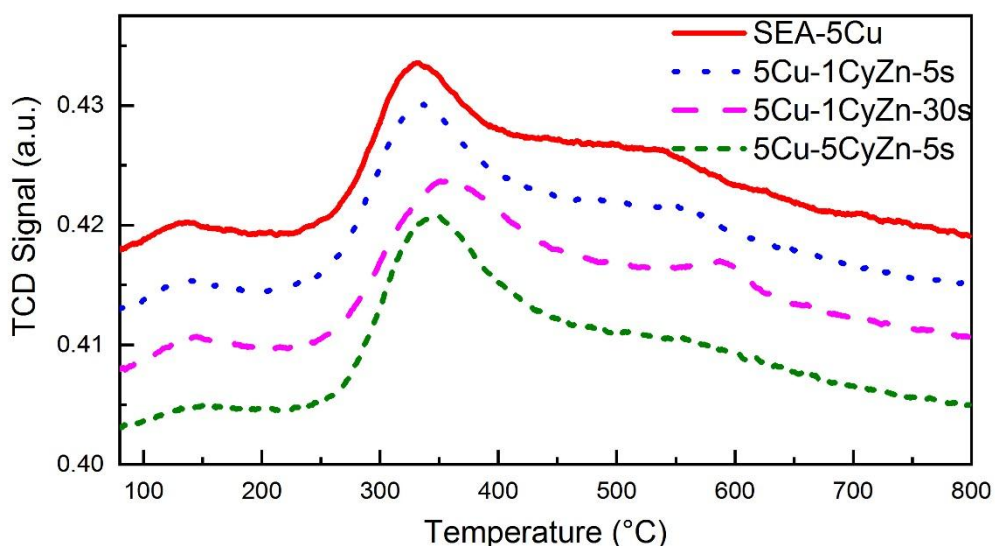


Figure 5-8 CO₂-TPD curves of the SEA-5Cu and Cu-ZnO catalysts

Table 5-6 Basic properties of the SEA-5Cu and Cu-ZnO catalysts.

Catalysts	Weak basic sites		Moderate basic sites		Strong basic sites		Total number of basic sites ($\mu\text{mol}\cdot\text{g}^{-1}$)
	T (°C)	Number ($\mu\text{mol}\cdot\text{g}^{-1}$)	T (°C)	Number ($\mu\text{mol}\cdot\text{g}^{-1}$)	T (°C)	Number ($\mu\text{mol}\cdot\text{g}^{-1}$)	
SEA-5Cu	136	67	328	682	543	35	784
5Cu-1CyZn-5s	133	77	330	1036	558	45	1158
5Cu-1CyZn-30s	144	75	351	1260	587	93	1428
5Cu-5CyZn-5s	138	34	340	1260	556	17	1311

According to the CO₂-TPD curves of the Cu-ZnO catalysts, the three desorption peaks of catalyst 5Cu-1CyZn-30s appeared at a higher temperature compared to those of the other two, which demonstrated that the basic sites on the catalyst 5Cu-1CyZn-30s were stronger. Since the moderate basic sites were related to the M-O pairs, the moderate basic sites on SEA-5Cu were only associated with Cu-O pair, which would be removed after reduction. So during the reaction, the actual basic sites on the Cu-ZnO catalysts should be calculated by deduction of the basic sites provided by Cu-O pair. Comparing the number of basic sites of the Cu-ZnO catalysts, there were more basic sites on the catalyst 5Cu-1CyZn-30s. The basic sites were where the CO₂ adsorption and activation happen.

5.5 Chemical Structure from XAS spectra

For the reaction of CO₂ hydrogenation to produce methanol, it had been considered that CO₂ was adsorbed on the basic sites, H₂ was dissociated on the metallic ones, and the contiguity of the metallic and basic is crucial for the catalyst performance. The number of basic and metallic sites had been studied by CO₂-TPD and CO chemisorption, the physical location of these two sites was determined by the TEM images. The catalyst 5Cu-1CyZn-30s with smaller metal particles, allowed more metallic sites to be exposed to basic sites, which meant better contiguity of metallic and basic sites. In this section, the contiguity of metallic and basic was identified by the chemical interaction through the XAS study. Then the right orientation of basic and metallic sites for methanol formation can be further determined. The reproducibility of the XANES results has been studied and shown in Appendix A.

5.5.1 XANES for Cu K edge of SEA-5Cu and ZnO over-coated Cu/SiO₂ catalysts

The local structure and electronic state of Cu and Zn in the catalysts were investigated by XAS. The Cu K edge XANES spectra of SEA-5Cu and ZnO over-coated Cu/SiO₂ catalysts are shown in Figure 5-9. Compared with Cu, Cu₂O and CuO standard, the Cu K edge spectra of calcined SEA-5Cu and Cu-ZnO catalysts exhibited similar profiles as that of CuO, which showed adsorption edge at 8984 eV. The absence of the pre-edge at approximately 8981 eV, which was the characteristic Cu¹⁺ 1s–4d transition feature (Bhuiyan et al., 2014), indicated that the copper in all the calcined catalysts consists mainly of Cu²⁺.

The XANES derivative spectra of the Cu K edge are shown in Figure 5-10. The weak peak at around 8977 eV in the reference derivative spectrum of CuO was frequently observed in Cu²⁺ compounds, which was because of a 1s–3d quadrupole-allowed pre-edge transition. The stronger peak at 8984 eV in CuO was assigned to the 1s–4p transition shakedown contributions. Another peak at approximately 8991 eV in CuO represents the main 1s–4p transition. (Bhuiyan et al., 2014) The Cu K edge spectra of catalysts with the ZnO layer over-coated were similar to that of SEA-5Cu. Compared to the spectra of CuO, the peaks representing 1s-3d and 1s-4p transitions in the SEA-5Cu and Cu-ZnO catalysts were all shifted by 1–3 eV to higher energy, which suggested a noncentrosymmetric CuO attributable to the ligand donor effect (Bhuiyan et al., 2014).

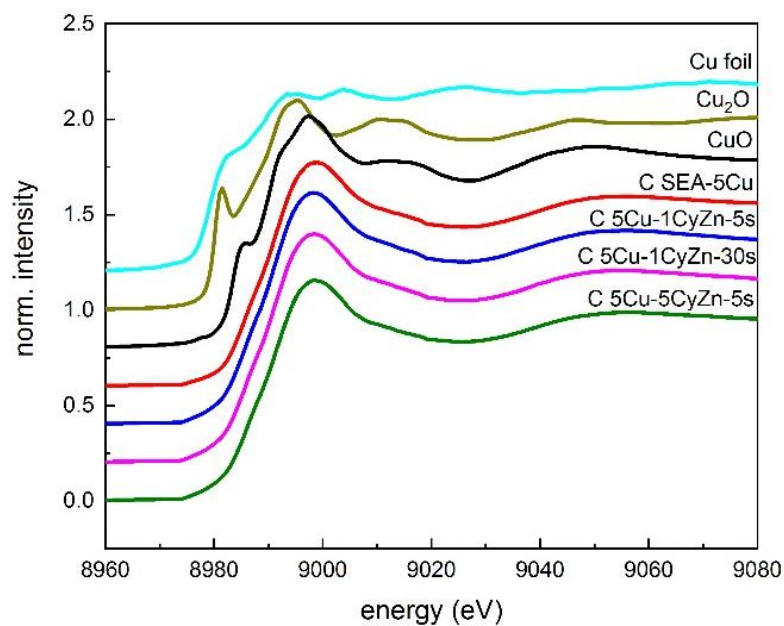


Figure 5-9 Experimental XANES spectra registered Cu K edge of catalysts SEA-5Cu and Cu-ZnO

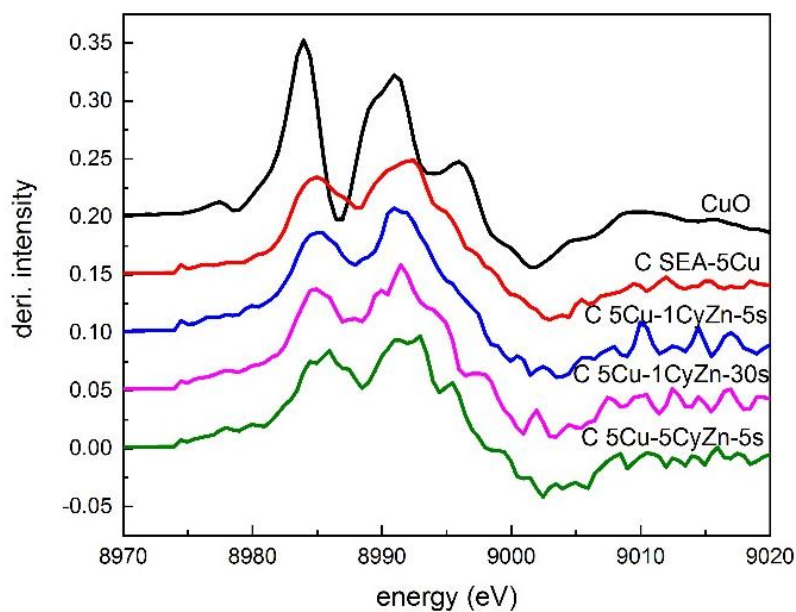


Figure 5-10 Experimental derivative XANES spectra registered Cu K edge of catalysts SEA-5Cu and Cu-ZnO

The Cu K edge XANES spectra of reduced SEA-5Cu and ZnO over-coated Cu/SiO₂ catalysts are shown in Figure 5-11. Cu foil showed the absorption edge at 8979 eV assigned to 1s–4p transitions, and two resonance features at E₀+15 eV and E₀+24 eV (Velu et al., 2002). The spectra of SEA-5Cu and Cu-ZnO catalysts showed the same shape with Cu foil and similar absorption edge, which meant the chemical environment of Cu species in SEA-5Cu and Cu-ZnO catalysts was close to that of the Cu foil reference. The catalyst 5Cu-1CyZn-30s showed better-shaped peaks corresponding to resonance features, which indicated the Cu species on the catalyst has better dispersion. This conclusion had been certified by the TEM images.

To further confirm the oxidation state of Cu, linear combination fitting (LCF) of XANES was then used for reduced SEA-5Cu and ZnO over-coated Cu/SiO₂ catalysts (Table 5-7). There were approximately 75 % of metallic Cu formation in SEA-5Cu and the catalysts.

The Cu K edge XANES derivative spectra of reduced SEA-5Cu and ZnO over-coated Cu/SiO₂ catalysts are shown in Figure 5-12. There was the main peak at approximately 8979 eV in the derivative spectrum of Cu foil, which is assigned to 1s–4p transitions. According to the derivative spectra of reduced 5Cu-1CyZn-5s and 5Cu-1CyZn-30s catalysts, the peak drifted towards higher energy compared to that of SEA-5Cu. This demonstrated that the chemical environments of Cu species on these two catalysts were affected by the ZnO over-coated, and metallic Cu may be oxidized by the ZnO. Higher energy was needed to make the electron transition from 1s to 4p orbital. Thus, there was an interaction between Cu and ZnO, which might be a dissolution of a part of the Cu in the ZnO lattice. However, the spectrum of the reduced catalyst 5Cu-5CyZn-5s showed no shift compared to that of SEA-5Cu, which meant that with multiple layers of ZnO, the interaction of Cu and ZnO became weaker. As we discussed about the mechanism of CO₂ hydrogenation to methanol reaction, the chemical interaction between Cu and ZnO from the

XANES derivative spectra was also an indicator of contiguity of metallic and basic sites. The stronger interaction between metallic and basic sites indicated better contiguity of these two catalytic sites. Thus, the catalysts 5Cu-1CyZn-5s and 5Cu-1CyZn-30s showed better contiguity of basic and metallic sites compared to the catalyst 5Cu-5CyZn-5s.

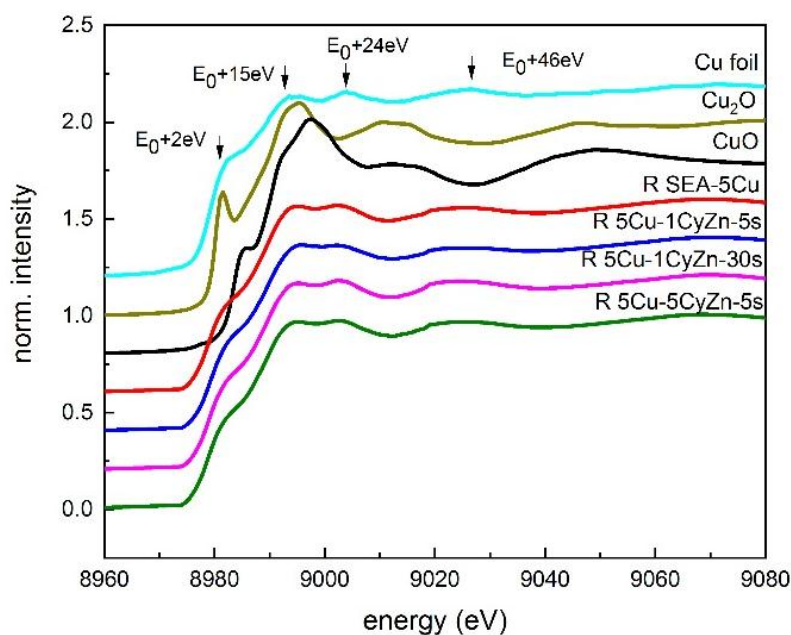


Figure 5-11 Experimental XANES spectra registered Cu K edge of reduced SEA-5Cu and ZnO over-coated Cu/SiO₂ catalysts

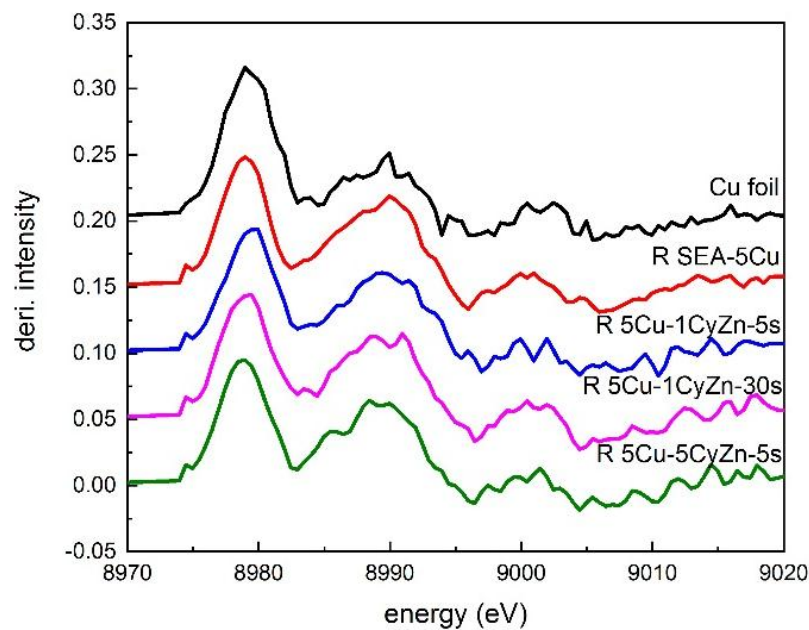


Figure 5-12 Experimental derivative XANES spectra registered Cu K edge of reduced SEA-5Cu and ZnO over-coated Cu/SiO₂ catalysts

Table 5-7 Cu species in the reduced SEA-5Cu and ZnO over-coated Cu/SiO₂ catalysts based on linear combination fitting

Samples	Cu ⁰	Cu ¹⁺	Cu ²⁺
SEA-5Cu	0.75	0.01	0.24
5Cu-1CyZn-5s	0.75	0	0.25
5Cu-1CyZn-30s	0.75	0	0.25
5Cu-5CyZn-5s	0.79	0	0.21

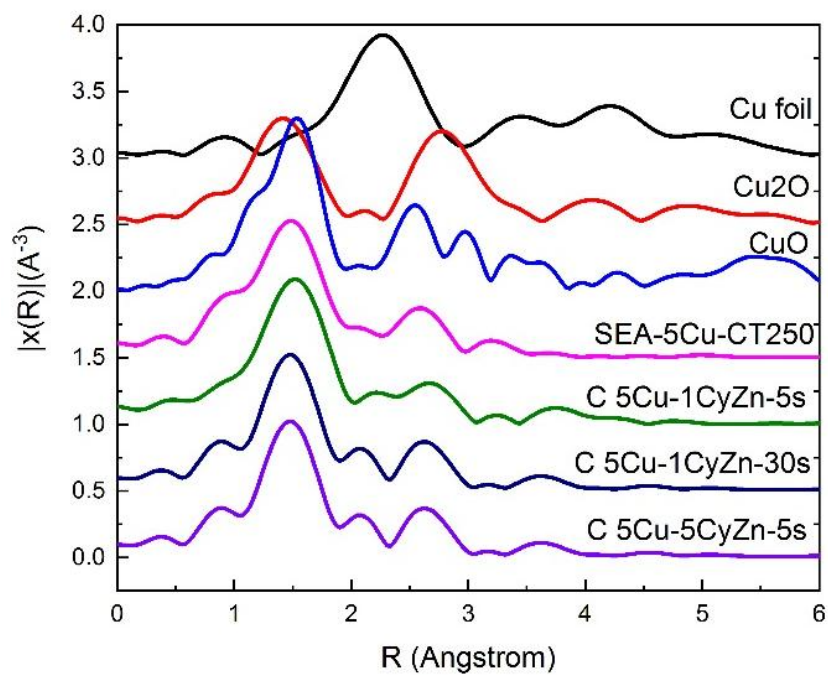
5.5.2 EXAFS for Cu K edge of SEA-5Cu and ZnO over-coated Cu/SiO₂ catalysts

The EXAFS spectra of Cu foil, Cu₂O, and CuO are shown in Figure 5-13, and the information about bond length is shown in Table 5-7. The EXAFS spectra of SEA-5Cu and ZnO over-coated Cu/SiO₂ catalysts displayed two peaks at around 1.47 and 2.58 Å, which were assigned to the lengths of Cu-O bond and Cu-(O)-Cu bond. The lengths of these two bonds were both in the middle of those of Cu₂O and CuO. Compared to the spectra of SEA-5Cu, the peaks represented to the length of these two bonds in calcined Cu-ZnO catalysts were both right-shifted, which indicated with ZnO over-coated, the bonds of Cu-O and Cu-(O)-Cu became longer.

The EXAFS spectra of reduced SEA-5Cu and ZnO over-coated Cu/SiO₂ catalysts are shown in Figure 5-14. There were two peaks in the spectra of catalysts on behalf of two bonds, respectively Cu-O bond whose length was in the range from 1.41 Å to 1.47 Å, and Cu-Cu bond whose length was in the range from 2.22 Å to 2.24 Å. The spectra of catalysts showed an obviously similar trend to Cu foil. Using SEA-5Cu as benchmark, which had two absorption peaks at around 1.42 Å and 2.24 Å, the first peak went righter to 1.47 Å with more ZnO deposition, which meant with ZnO over-coated, the length of Cu-O bond became longer. The intensity of this peak became less with the increase of exposure time and cycles of ZnO deposition, which disclosed that ZnO over-coated helped the reduction of the Cu. The Cu-Cu bond length of ZnO over-coated Cu/SiO₂ catalysts was similar to that of SEA-5Cu.

Table 5-8 Basic information of Cu reference in EXAFS spectra

Compound	Bond	R (Angstrom)
Cu foil	Cu-Cu	2.27
Cu ₂ O	Cu-O	1.41
	Cu-(O)-Cu	2.76
CuO	Cu-O	1.53
	Cu-(O)-Cu	2.55

**Figure 5-13** Experimental EXAFS spectra registered Cu K edge of calcined ZnO over-coated Cu/SiO₂ catalysts

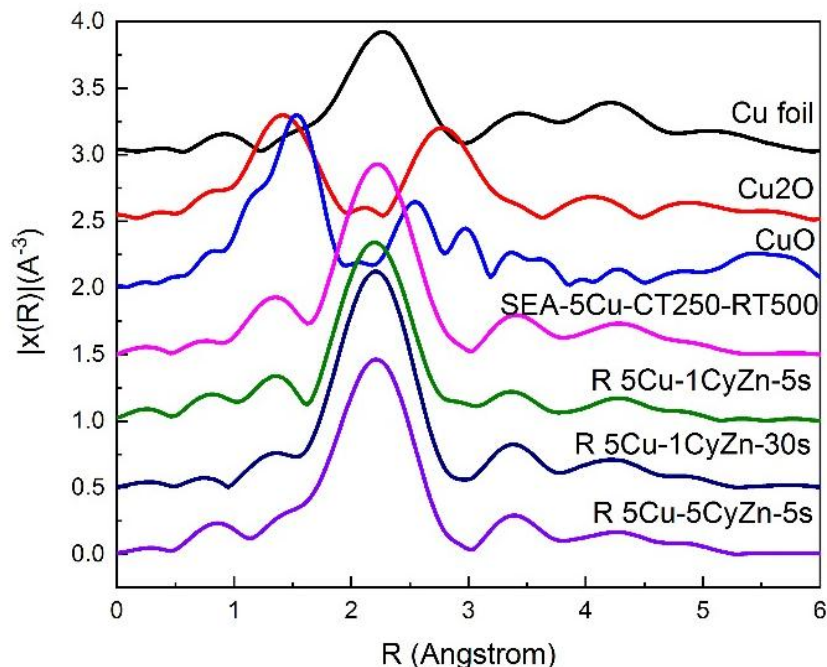


Figure 5-14 Experimental EXAFS spectra registered Cu K edge of reduced ZnO over-coated Cu/SiO₂ catalysts

5.5.3 XANES for Zn K edge of ZnO over-coated Cu/SiO₂ catalysts

The Zn XANES spectra of calcined ZnO over-coated Cu/SiO₂ catalysts are shown in Figure 5-15. The absorption edge was at 9662 eV coincided with ZnO, which indicated the existence of bivalent Zn. However, the spectra of Cu-ZnO catalysts were considerably different from ZnO. Compared to the spectrum of ZnO, the peaks at 9663.8 eV and 9668.4 eV assigned to 1s-4sp and 1s-4p transitions, were merged to one peak at 9667.5 eV. The peaks at 9679.3 eV and 9683.4 eV were smoothed and became a shoulder (9681.1 eV) which was only shown in the spectrum of 5Cu-5CyZn-5s, assigned to multiple scattering (midrange order and short-range order) (Dadlani et al., 2017). In the range 9700-9760 eV, there was a single broad peak instead of two. The peak assigned to multiple scattering didn't show in the spectra of ZnO over-coated Cu/SiO₂ catalysts with one cycle of ZnO deposition. With the deposition of 1 or 5 layer(s) of Zn²⁺ species, no ZnO structure

formation in these catalysts. The difference between the spectra of Cu-ZnO and the spectrum of ZnO was also due to the Zn^{2+} on the catalysts which existed as molecules or very smaller particles, may be mostly influenced by the substrate, SiO_2 . The spectra of calcined and reduced ZnO over-coated Cu/ SiO_2 catalysts didn't show the difference.

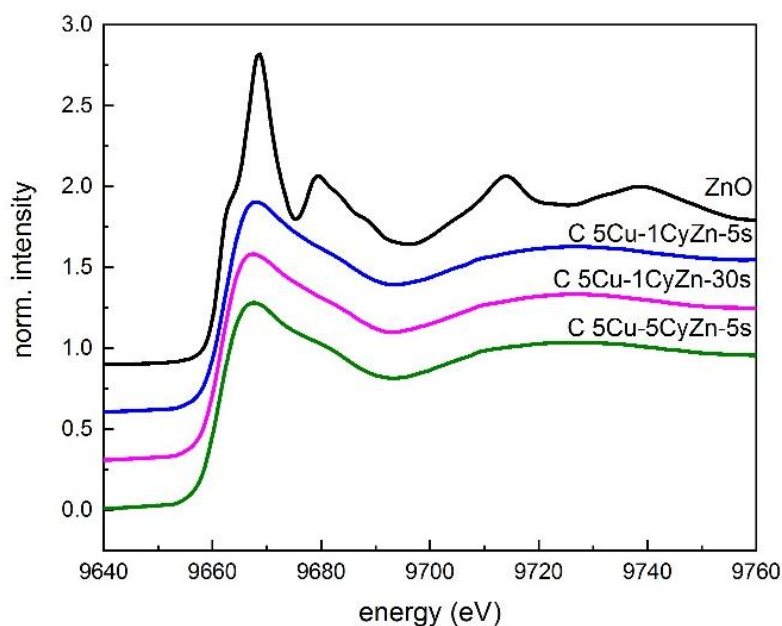


Figure 5-15 Experimental XANES spectra registered Zn K edge of calcined ZnO over-coated Cu/ SiO_2 catalysts

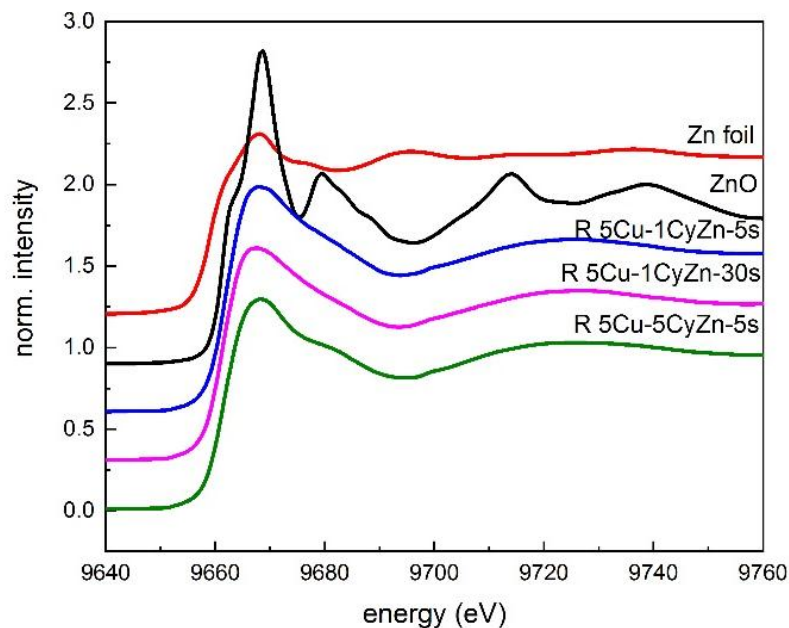


Figure 5-16 Experimental XANES spectra registered Zn K edge of reduced ZnO over-coated Cu/SiO₂ catalysts

5.5.4 EXAFS for Zn K edge of ZnO over-coated Cu/SiO₂ catalysts

The Zn EXAFS spectra of calcined and reduced ZnO over-coated Cu/SiO₂ catalysts are shown in Figure 5-17 and Figure 5-18. In the EXAFS spectra of the ZnO standard, the bond length between the central zinc atom and the first shell atom, which was an oxygen atom, was 1.60 Å. The second peak was at 2.85 Å, which was attributed to Zn-(O)-Zn interaction. According to the EXAFS spectra of Zn foil, the bond length of Zn-Zn was 2.28 Å. There was a Zn-O bond in the spectra of calcined ZnO over-coated Cu/SiO₂ catalysts, and no much difference showed in the spectra of reduced Cu-ZnO. It was worth noting there was no peak shown represent to the bond of Zn-(O)-Zn which meant no bigger ZnO particles or many layers of ZnO formed.

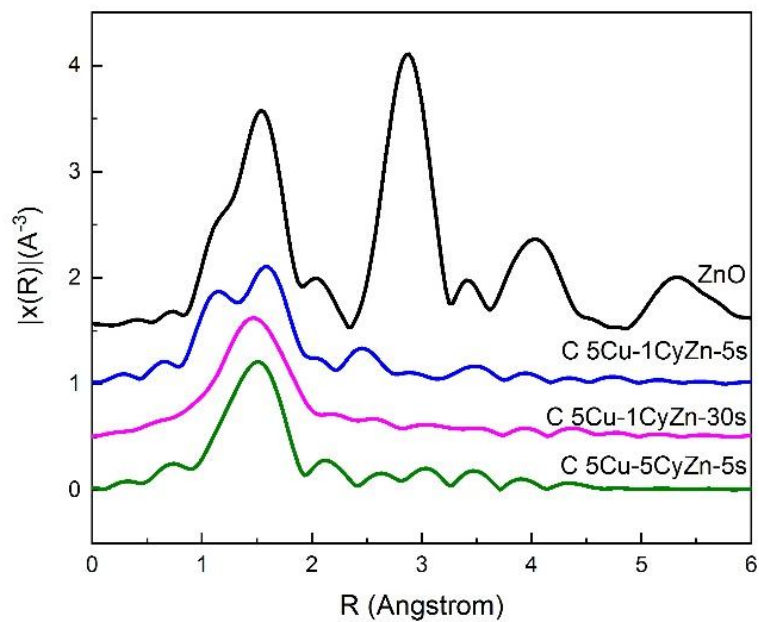


Figure 5-17 Experimental EXAFS spectra registered Zn K edge of ZnO over-coated Cu/SiO₂ catalysts

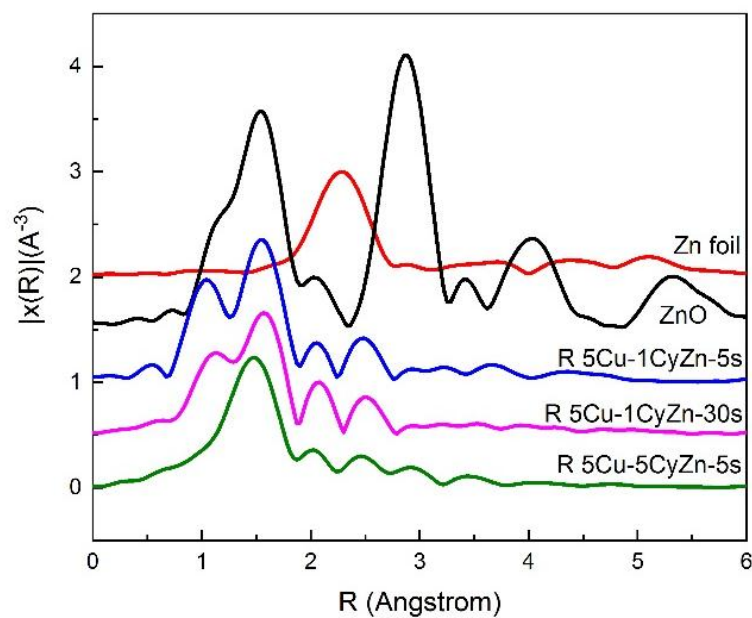


Figure 5-18 Experimental EXAFS spectra registered Zn K edge of reduced ZnO over-coated Cu/SiO₂ catalysts

5.6 CO₂ Conversion and Methanol Synthesis

Catalytic evaluations of the ZnO over-coated Cu/SiO₂ catalysts are shown in Table 5-8. The blank experiments using Cu or ZnO supported by SiO₂ catalysts were done, and the catalysts showed no activity. The CO₂ reaction rate and CO formation rate barely changed during a run (acted for 24 h), and the average values are shown in Table 5-8. The reproducibility of the results has been studied and shown in Appendix A. The liquid products were analyzed at the end of the run. No other product besides methanol and CO was formed. The CO₂ reaction rate of catalyst 5Cu-1CyZn-5s was 4.90 mmol·g⁻¹h⁻¹, which decreased to 4.77 mmol·g⁻¹h⁻¹ with an exposure time of 30 s, and becomes even smaller (4.06 mmol·g⁻¹h⁻¹) with 5 cycles of ZnO over-coated. The CO₂ conversion showed the same trend. The formation rate of CO had the same trend as the CO₂ reaction rate. The methanol formation rate of catalyst 5Cu-1CyZn-30s was 0.48 mmol·g⁻¹h⁻¹, which was higher than that of catalyst 5Cu-1CyZn-5s (0.33 mmol·g⁻¹h⁻¹) and 5Cu-5CyZn-5s (0.21 mmol·g⁻¹h⁻¹). The methanol selectivity of catalyst 5Cu-1CyZn-30s was 10.1 %, which was higher than 6.7 % for 5Cu-1CyZn-5s, and 5.2 % for 5Cu-5CyZn-5s.

Table 5-9 Catalytic performances of the ZnO over-coated Cu/SiO₂ catalysts: reaction rate and selectivity.

Catalysts	CO ₂ conversion (%)	CO ₂ reaction	Methanol formation	CO formation	methanol selectivity (%)
		Rate (mmol·g ⁻¹ h ⁻¹)			
5Cu-1CyZn-5s	4.58	4.90	0.33	4.57	6.7
5Cu-1CyZn-30s	4.45	4.77	0.48	4.32	10.1
5Cu-5CyZn-5s	3.79	4.06	0.21	3.89	5.2

Reaction conditions: T = 250 °C, P = 4.0 MPa, F = 9.6 L·h⁻¹, 1.0 g catalyst.

The ratios of the number of metallic sites to the number of basic sites also are shown in Table 5-9, which were 0.26, 0.19, and 0.17 on the catalysts 5Cu-1CyZn-5s, 5Cu-1CyZn-30s, and 5Cu-5CyZn-5s, respectively. The TOF of CO₂ is calculated based on the number of basic sites from the results of CO₂-TPD. The TOF of H₂ is calculated based on the number of metallic sites from the results of CO chemisorption. Among these catalysts, 5Cu-1CyZn-5s had higher TOF_{CO₂} of 4.2 h⁻¹, and lower TOF_{H₂} of 18.3 h⁻¹. 5Cu-1CyZn-30s and 5Cu-5CyZn-5s showed similar TOF_{CO₂} of 3.3 h⁻¹ and 3.1 h⁻¹, and the similar TOF_{H₂} of 20.0 h⁻¹ and 19.7 h⁻¹, respectively.

Table 5-10 Catalytic performances of the ZnO over-coated Cu/SiO₂ catalysts: TOF of reactants.

Catalysts	The ratio of metallic to basic sites	TOF _{CO₂} by ZnO	TOF _{H₂} by Cu
		(h ⁻¹)	
5Cu-1CyZn-5s	0.26	4.2	18.3
5Cu-1CyZn-30s	0.19	3.3	20.0
5Cu-5CyZn-5s	0.17	3.1	19.7

During the reaction, the activated CO₂ needed assistance from the active H to pull one O away and to insert H in at the same time to form C-H and O-H bonds. When the activated CO₂ lacked surrounding H atoms, only O can be pulled away from the activated CO₂, resulting in the formation of CO. To form methanol only, three metallic sites should be next to one basic site to supply three moles of activated H₂ to react with the activated CO₂ in molecular form. In our case, much more basic sites were formed than the metallic sites on the ZnO over-coated Cu/SiO₂ catalysts. During the reaction, the basic sites were enough to adsorb and activate CO₂. It was more important if there were enough metallic sites to activate H₂ and provided atom H to the basic sites. Since more metallic sites were formed on the 5Cu-1CyZn-5s, it showed a higher CO₂ reaction rate as observed

by other researchers (Behrens et al., 2012; Dong et al., 2016; B. Hu et al., 2018). It indicated that the CO₂ reaction rate and CO₂ conversion was related to the number of metallic sites.

When it came to the selectivity of the catalyst, another factor should be considered, which was if the basic and metallic sites are close enough to each other, as well as the good contiguity of metallic and basic sites. To study if there is good contiguity of basic and metallic sites on each catalyst, the characterization of TEM, XRD patterns, XANES, and EXAFS spectra were used as the indicators of the catalytic sites' contiguity. The TEM image of reduced catalysts gave the physical location of the metallic and basic sites. There were uniform and smaller Cu particles formed with good distribution on the catalyst 5Cu-1CyZn-30s, allowing more metallic sites to be exposed to basic sites, which meant better contiguity of metallic and basic sites. The other characterizations, XRD patterns, XANES, and EXAFS spectra gave the information of the chemical interaction of metallic and basic sites. The value of Cu⁰ lattice constant of 5Cu-1CyZn-30s was 3.65 Å, but this value for sample SEA-5Cu was 3.62 Å. The increase in the lattice constant upon the deposition of ZnO may be attributable to the formation of the Cu-Zn surface alloy. (Kanai et al., 1994) From the XANES spectra registered Cu K edge of reduced 5Cu-1CyZn-5s and 5Cu-1CyZn-30s, the peaks assigned to 1s–4p transition drifted towards higher energy compared to that of SEA-5Cu, which demonstrated the chemical environment of Cu species were affected by the ZnO over-coated and metallic Cu may be oxidized by the ZnO. Thus, there was an interaction between Cu and ZnO. More ZnO exposure time helped this dissolution, but multiple layers didn't. Compared to the EXAFS spectrum of calcined SEA-5Cu, the bond lengths of Cu-O and Cu-(O)-Cu in the spectra of calcined Cu-ZnO catalysts become longer due to the interaction between Cu and over-coated ZnO. These characters all can indicate that better contiguity of basic and metallic

sites on the catalyst 5Cu-1CyZn-30s compared to other catalysts, which was the reason for better selectivity to methanol.

5.7 Evidence from Others' Work

In the last section, the catalyst ZnO over-coated on Cu/SiO₂, which contained isolated Cu-related particles distributed in a layer of ZnO atoms, had been studied. According to the study of the relationship between catalyst structure and activity, a theory of CO₂ catalytic activation can be proposed. The mechanism is shown in Figure 5-19. During the reaction on the 5Cu-1CyZn-30s, CO₂ is chemisorbed and activated by the basic site, ZnO, which tried to push the atom O out of the CO₂ molecule. Then the H₂ was activated by the metallic site, Cu to form H atom which then diffused to the basic site. Since more points where Cu and the ZnO were close to each other exist, as well as good contiguity of metallic and basic sites, enough H atoms help to pull out the O atom and add into the CO₂ to form C-H and O-H bonds which result in methanol formation. Due to the synergistic effects of both the basic and metallic sites to provide the forces of pushing and pulling, CO₂ can be activated and reacted with H₂ to form methanol.

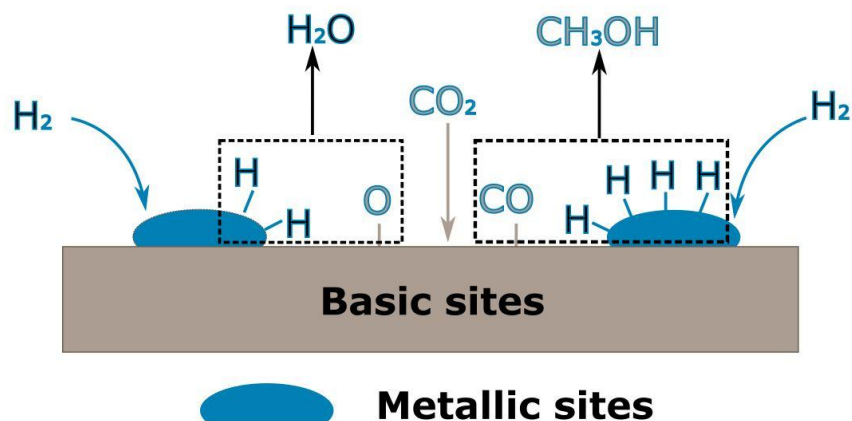


Figure 5-19 Mechanism of CO₂ hydrogenation process to produce methanol on a common catalyst

The reaction mechanism on the other catalyst model we proposed, the catalyst Cu over-coated on ZnO/SiO₂, which contained isolated ZnO phases distributed in a layer of Cu or surrounded by sufficient Cu nanoparticles, is shown in Figure 5-20. The sufficient metallic sites can provide enough hydrogen atoms to access the activated CO₂ to produce methanol instead of CO.

To certify this hypothesis, much work had been done to review other's work on the characterization and performance Cu-ZnO catalysts used for CO₂ hydrogenation to produce methanol. The catalysts with better CO₂ conversion had lower selectivity to methanol, however, the catalysts with higher selectivity to methanol showed lower CO₂ conversion. Bare catalysts had both high CO₂ conversion and good selectivity to methanol. Two Cu-ZnO catalysts were chosen as the representatives of each situation.

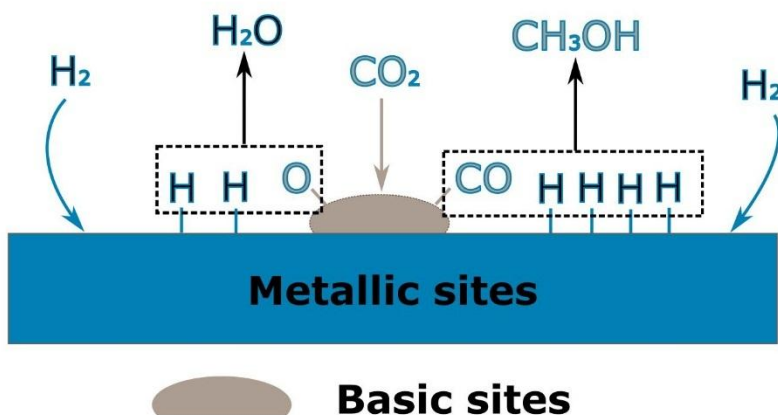


Figure 5-20 Mechanism of CO₂ hydrogenation process to produce methanol on the second catalyst model

5.7.1 The catalyst CuZn/N-rGO with promising CO₂ conversion

The catalyst CuZn/N-rGO was prepared and studied by Deerattrakul and co-workers. There were four papers published according to their studies on this catalyst. The role of nitrogen species on graphene aerogel, the effect of hydrothermal temperature, the effect of Cu-Zn loading, and the

influence of reduction time of the catalyst were studied. (Deerattrakul et al., 2016, 2017, 2018, 2019) But they did not answer the question of why this catalyst had better CO₂ conversion than others. In this part, this question was discussed based on the properties of the catalytic sites, especially the contiguity of metallic and basic sites.

The catalyst was prepared as the scheme shown in Figure 5-21. Based on the Hummers' method, the graphene oxide was prepared from graphite. Then the reduced graphene oxide aerogel was made by the hydrothermal method. At last, the catalyst CuZn/N-rGO was synthesized by the incipient wetness impregnation method (Deerattrakul et al., 2018).

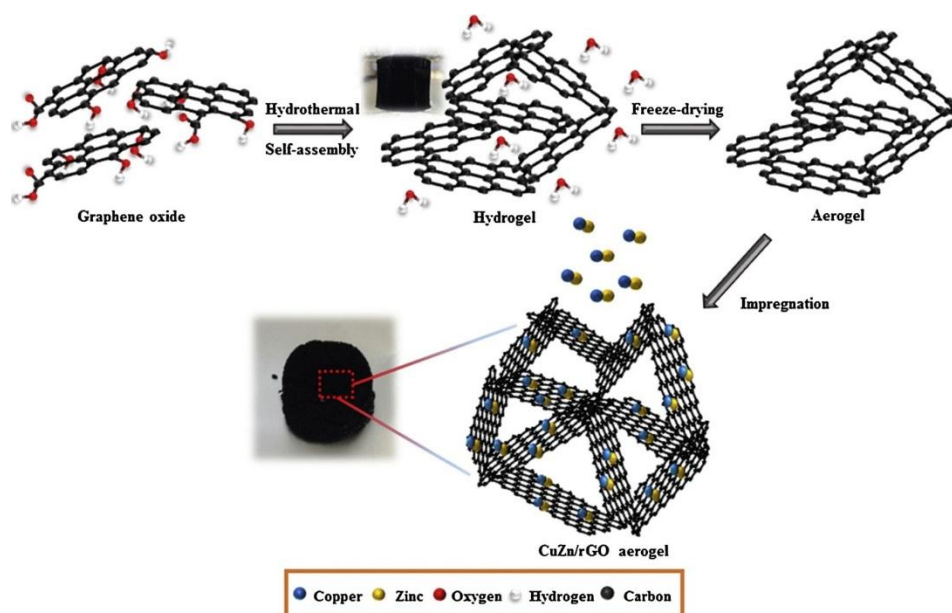


Figure 5-21 Schematic illustration for the synthesis of Cu-Zn/N-rGO (Deerattrakul et al., 2018)

The distribution of each element on the catalyst was determined by FE-SEM images and EDX mapping images in Figure 5-22. The FE-SEM images (Figure 5-22 a, b) exhibited that the layers of N-rGO provided a smooth surface as the anchoring site for the active metals, and the metals Cu and Zn displaying a spherical shape deposit on N-rGO nanosheets. The EDS mapping images (Figure 5-22 c-f) confirmed the good dispersion of Cu and Zn atoms.

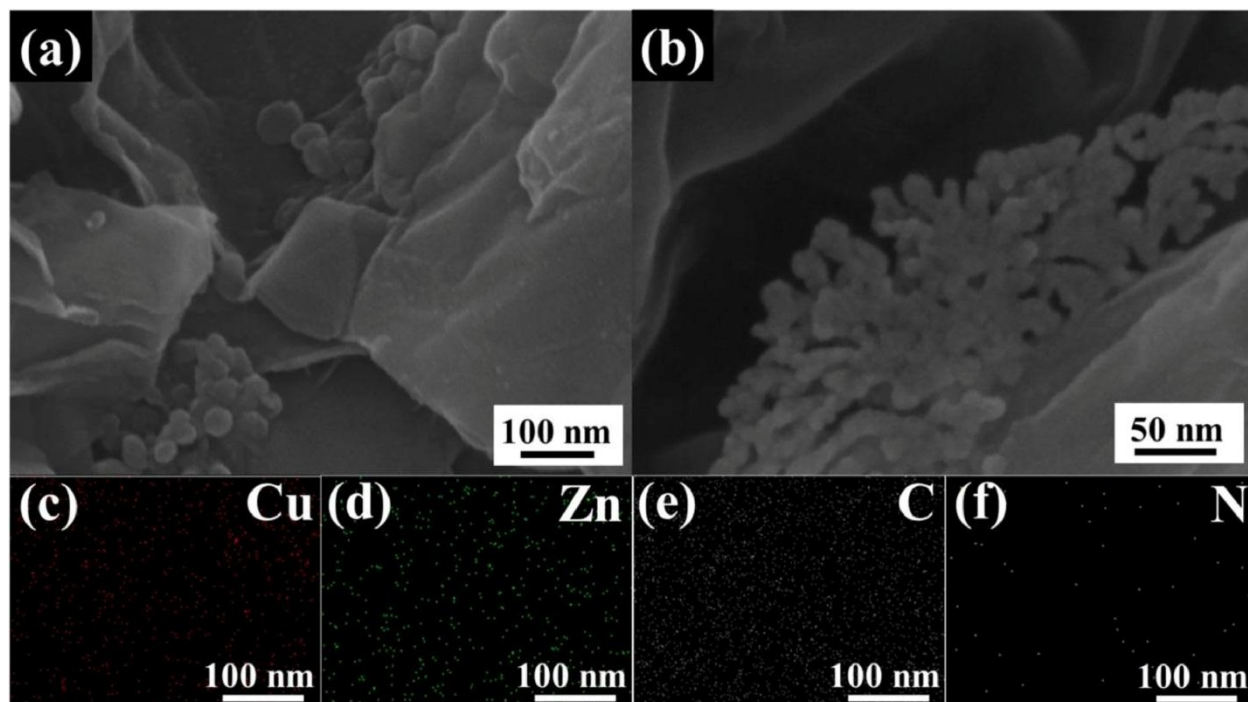


Figure 5-22 FE-SEM images of CuZn/N-rGO (a, b) and EDS mapping of CuZn/N-rGO catalyst showing Cu (c), Zn (d), C (e) and N (f) (Deerattrakul et al., 2017)

To understand the size of metallic particles, further the size of metallic sites, the TEM analysis was done, the images are shown in Figure 5-23 with low and high magnification. The Cu-Zn particles appeared with a good distribution on the surface of N-rGO nanosheets. This was in good agreement with the FE-SEM images. The distribution of particle size was analyzed and shown in Figure 5-23 (b). The sizes of particles were in the range of 2 to 16 nm. The average size of the metallic nanoparticles was 8-10 nm approximately.

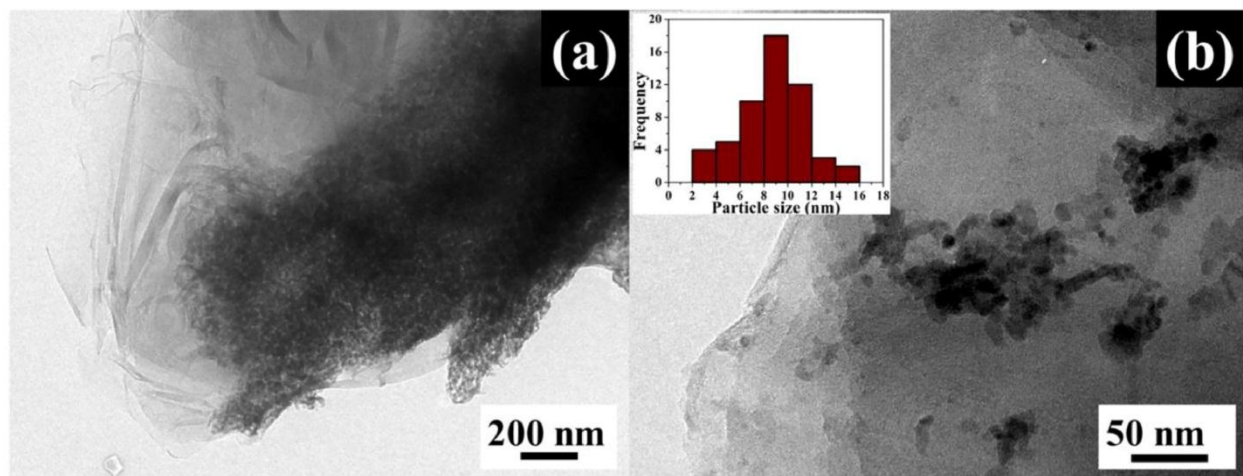


Figure 5-23 (a) Low- and (b) high-magnification TEM images of CuZn/N-rGO. (Deerattrakul et al., 2017)

According to the study on the material of nitrogen-doped graphene (Yu et al., 2011; Zhang and Xia, 2011; Liao et al., 2013), the edges of nitrogen-doped graphene can reduce the energy barrier of H_2 adsorption and dissociation due to its high electronegativity. Thus, this structure can attribute to enhance the performance of the catalyst for CO_2 hydrogenation.

The catalyst CuZn/N-rGO had greatly even-dispersed Cu and ZnO phases, which indicated excellent metallic and basic sites. And the support can help to enhance the H_2 dissociation to active H atoms, lots of which were needed in the reactions of both producing CO and methanol. Thus, the activity of metallic sites was improved by the particular property of nitrogen-doped graphene. Due to the contribution of these two catalytic sites, the catalyst had a high CO_2 conversion. Since they just randomly connected to each other, the selectivity of methanol was not outstanding.

5.7.2 The catalyst Cu@ZnO_x with 100 % selectivity to methanol

Le Valant, Tisseraud, and co-workers prepared Cu@ZnO_x core-shell structure catalyst by surface modification precipitation method. The Cu powder was used as the substrate and then treated using citric acid. ZnO was deposited on the surface of Cu by precipitation method. This

catalyst showed 100 % selectivity to methanol. Then the impact of the composition of the Cu@ZnO_x core-shell catalyst, and the catalysts prepared using ZnO powder as the substrate with Cu species deposited by the wet impregnation method was studied to elucidate the relationship of catalytic performance and the structure of the catalyst. (Le Valant et al., 2015; Tisseraud et al., 2015, 2016, 2018)

To study the morphology property of the catalyst Cu@ZnO_x, the TEM and EDX analysis were done. The TEM image and the corresponding EDX result are shown in Figure 5-24 and Table 5-10, respectively.

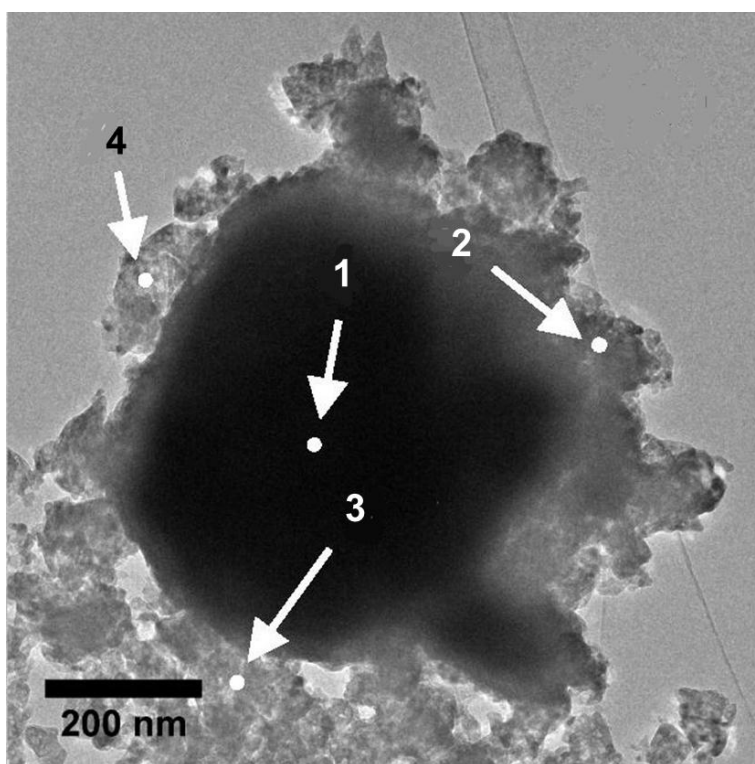


Figure 5-24 TEM images for the catalyst Cu@ZnO_x. Spots in figure correspond to EDX analysis. (Tisseraud et al., 2016)

Table 5-11 EDX results for Cu, Zn, and O on the catalyst Cu@ZnO_x. Spots refer to Figure 5-24.

Spot	Mole fraction			O/(Cu+Zn)
	Cu	Zn	O	
1	89.65	8.11	2.24	0.02
2	2.98	73.65	23.37	0.30
3	7.73	56.94	35.32	0.55
4	5.26	58.38	36.37	0.57

Obliviously, there was a core-shell structure observed on the TEM image of catalyst Cu@ZnO_x. The core was composed of Cu, like spot 1 shown in Figure 5-24. The remaining Zn was detected on the shell. When the beam moved away from the core, the Cu depletion along with Zn enrichment was observed. At the interface between core and shell, the Cu and Zn were both rich, which was related to the formation of CuZn alloy, shown as spot 2. The ratio of O/(Cu+Zn) less than 1 confirmed there was the presence of oxygen vacancies and Cu^{δ+} species (+1 and/or +2) at the zone of the shell, especially at the interface between core and shell. The Cu^{δ+} was identified to be contributing to the catalytic reaction. The intimate interaction between metallic sites, Cu and basic sites, ZnO was the key for controlling the metal electronic properties and the reducibility of the ZnO phase, further the activity of catalysts on CO₂ hydrogenation to produce methanol. This conclusion consistent with ours, the catalytic site for methanol synthesis was the interface of metallic sites and basic ones.

The number of metallic sites and basic sites were determined by H₂ and CO₂ chemisorption. The number of metallic sites was the 2.0 μmol·g⁻¹, and the number of basic sites is 3.0 μmol·g⁻¹. Even though the ratio of numbers of metallic sites to basic ones is 0.67, less than 3, the relatively

higher ratio than other catalysts still has a benefit for the high selectivity of the catalyst. As a contrast, this ratio of the catalyst 5Cu-1CyZn-30s we prepared is only 0.2.

There was a correlation between the amount of hydrogen chemisorption with catalytic activity (methanol production). This correlation was said to be associated with hydrogen spillover, which meant how much hydrogen species atoms could come to the ZnO, the basic sites, to reduce the activated CO₂ molecule. This conclusion agreed with ours. Enough active H atoms should supply to the basic sites to form methanol, instead of CO.

The catalyst had a very small amount of ZnO precipitated on the surface of metallic Cu, which represented a bit amount of basic sites, a large number of metallic sites, and very good contiguity between them. During the reaction, there were enough H atoms formation and spillover to the basic sites, to reduce the activated CO₂ to methanol. But this catalyst had very low CO₂ conversion due to the weak basic sites.

Based on the study of these two catalysts, either having most CO₂ conversion, or 100 % selectivity to methanol, it was determined that the catalyst which contained isolated ZnO phases distributed in a layer of Cu or surrounded by sufficient Cu nanoparticles, met the criterion of these two catalysts, and should have both high activity and selectivity.

5.8 Conclusion

This chapter studied the influence of Cu-ZnO catalysts with different metallic particle size, ZnO distribution, and contiguity of basic and metallic sites on their catalytic performance in CO₂ hydrogenation for methanol synthesis reaction. Through this study, the understanding of CO₂ catalytic activation mechanism on the aspects of not only the activity and number of metallic and

basic sites, but also the interaction between them had been improved. Here were conclusions obtained from this part of work:

1. The catalyst ZnO over-coated Cu/SiO₂, which contained isolated Cu particles (metallic sites) deposited on the layer of ZnO atoms (basic sites), was successfully developed on the surface of silica gel by the combination of strong electronic adsorption and atomic layer deposition methods.
2. During the reaction, the activated CO₂ needed assistance from the active H to pull one O away and to insert H in at the same time to form C-H and O-H bonds. On the catalysts ZnO over-coated Cu/SiO₂, where the much more basic sites were formed than the metallic sites, the CO₂ conversion or CO₂ reaction rate was related to the number of metallic sites.
3. In the reaction of CO₂ hydrogenation, CO₂ and H₂ were activated on different sites. thus, the interaction or orientation of basic and metallic sites affected the catalyst selectivity to methanol. The catalyst 5Cu-1CyZn-30s with better metallic sites (smaller Cu particles with good distribution) and basic sites (uniform ZnO layer) formation, as well as the good contiguity between them, showed higher selectivity to methanol compared to other catalysts. The contiguity of basic and metallic sites was indicated using the characterization methods of TEM, XRD, and XAS analysis.
4. As we proposed, the catalyst, which contained isolated metallic sites distributed in a layer of basic sites, prefer to form CO, instead of methanol. And the catalyst, which contained isolated ZnO phases distributed in a layer of Cu or surrounded by sufficient Cu nanoparticles, was certified to meet the criterion of both high activity and selectivity according to the literature study.

CHAPTER 6 Conclusions and Recommendations

The conclusions for this work are summarized and then the recommendations for future work are also mentioned in this chapter.

6.1 Conclusions

The CO₂ catalytic activation mechanism by considering the effect of contiguity of the two activation sites in the CO₂ reforming of methane system and CO₂ hydrogenation for methanol systems was studied as the principal objective of this work. The Ni-based catalysts or Cu-ZnO catalysts with different properties and structures were studied for these two CO₂ utilization reactions to understand the effects of the interaction between species on basic sites and metallic sites, further the geographic distribution and orientation of the basic sites and metallic sites.

For the reaction of CRM, different second metallic components in addition to Ni in the NiM₂ (M₂=Co, Mn, Cu, and Fe) bimetallic MgO-spinel structure catalysts were prepared. It was determined that the second metal affected the metallic particle sizes and it also affected the basicity of the catalysts slightly. The catalysts with varying contents of Mg from revealed that stronger basic sites were related to MgO solid solution phase, where metallic sites preferred to sit. The MgO phase was responsible for the good contiguity of the two types of sites that worked for CO₂ reforming of CH₄. During the reaction, the initial TOF of CO₂ and CH₄ based on the number of metallic sites had a good correlation with the average metallic particle size. The smaller particles created more chance for the activated reactant on metallic sites to reach the other reactant activated on the basic sites around it, as well as good contiguity of metallic and basic sites, thus leading to higher activities. The deactivation behavior of the catalysts was explained by a pushing-pulling theory proposed in this study. The pushing force and pulling force of the catalytic sites were

quantified from the pulse adsorption-reaction experiments. A stable, or good carbon-resistant catalyst should have stronger oxidizing ability of CO₂ species on the basic sites surrounding the metallic particles than the pushing force of the metallic sites to CH₄. This study also revealed the incomplete dissociation of CH₄ on the metallic sites, which may be the reason leading to lower H₂/CO instead of reverse water-gas shift reaction.

For the reaction of CO₂ hydrogenation to synthesize methanol, the synthesis of the catalysts led to the formation of isolated Cu nanoparticles (metallic sites) distributed in ZnO layer(s) (basic sites), by the combination of strong electronic adsorption and atomic layer deposition methods. With varying the exposure time of the Zn-containing precursor and the number of ZnO deposition layers, there was a slight change in the environment of ZnO sites to Cu sites and vice versa, and their contiguity. The more uniformed Cu site and ZnO site distribution in 5Cu-1CyZn-30s allowed it to have relatively more methanol formation, due to the good contiguity in both physical location and chemical interaction. This was confirmed with characterization methods of TEM, XRD and XAS analysis. As expected, these catalysts facilitate more CO formation rate than the methanol formation rate. This study partially supports the mechanism theory for CO₂ hydrogenation to form methanol that activated CO₂ on the ZnO sites needs activated hydrogen in the right position. The other catalyst we proposed, which contained isolated ZnO phases distributed in a layer of Cu or surrounded by sufficient Cu nanoparticles, was certified to meet the criterion of both high activity and selectivity according to the literature study.

Through this work, the concept of site contiguity was proposed, and the understanding of site contiguity help to study the mechanism of the CO₂ catalytic activation. So far, the site contiguity is recognized as the property of the catalyst which cannot be quantified. However, some of the characterization methods can be used as an indicator of site contiguity, like TEM image to study

the physical location of active sites, XAS spectra to study the chemical interaction of active sites. The theory of pushing-pulling was proposed to describe the effect from two active sites for one reactant, further to explain the mechanism of CO₂ utilization reactions.

For these catalytic reactions, involving two reactants to be activated on different types of activation sites, not only the number and activity of the sites but also the site distribution and orientation, namely site contiguity, can affect the performance of the catalysts. In conclusion, the mechanism of CO₂ catalytic activation was analyzed based on the CRM and CO₂ hydrogenation reaction, especially on the aspect of contiguity of metallic sites and basic sites. According to this study, the common recognition of the CO₂ utilization catalyst used in this reaction system was obtained. For CO₂ utilization, enough and strong basic sites should be created on the catalysts for CO₂ activation. The properties of metallic sites, like the number or activity of metallic sites, can lead to different product formation. In the reaction of CRM, with stronger metallic sites, the ability of carbon formation through CH₄ dissociation on the metallic sites was stronger than the oxidizing ability of CO₂ species on the basic sites surrounding the metallic particles, then coke was formed instead of the desired product, CO. During the CO₂ hydrogenation reaction, with relatively more metallic sites, the catalyst has higher selectivity to methanol, instead of CO. The good contiguity of basic and metallic sites on the catalysts was necessary for these reaction systems to give enough chance to let the reactants activated on these two catalytic sites reach and react with each other, further improving the stability and activity of the catalyst. These conclusions can be instrumental in developing effective catalysts for CO₂ utilization in future.

6.2 Recommendations

To further understand the CO₂ catalytic activation during converting to value-added products, the following work is recommended.

6.2.1 CO₂ reforming of methane

To further study the CO₂ catalytic activation during CRM reaction, in situ characterization methods, like in situ FTIR or in situ XAS, and computational investigation, like density functional theory (DFT), can be carried out.

From the result of in situ FTIR during the reaction of CO₂ reforming of methane, the intermediates of the reaction can be determined. The change of valence of active metal in the catalysts can be detected via the in situ XAS during the reaction. This information can help to picture the pathway of reaction and the mechanism of CO₂ catalytic activation. The study could help to further understand the effect of each catalytic site and the contiguity of metallic and basic sites.

Studies on the computational investigation on this reaction would assist in determining the reaction mechanism over the catalysts with different properties and structures, which can reveal the effect of structure of the catalysts on the reaction pathway. Through the study of adsorption and activation energy of each reactant, the pushing-pulling effect of each active site on the reactant can be determined. The combination of experimental and simulated study is possible to give comprehensive analysis and understanding on the theory of pushing-pulling between the metallic and basic sites of the catalyst and the mechanism of CO₂ catalytic activation.

6.2.2 CO₂ hydrogenation reaction for methanol synthesis

For the study of CO₂ catalytic activation on the CO₂ hydrogenation reaction, only one extreme catalyst model has been studied. The ZnO over-coated Cu/SiO₂ catalyst is indicated to prefer to form CO, instead of methanol. To complete this, the study on the Cu-ZnO catalyst with isolated basic sites surrounded by sufficient metallic sites should be facilitated.

This catalyst is certified to meet the criterion of both high activity and selectivity according to the literature study, but experimental analysis is still needed. To prepare the catalyst with certain structure, especially the desired interaction between metallic and basic sites, the uniformed Cu layer phase in the catalysts can be deposited by ALD method with proper precursors, and isolated ZnO phase can be prepared by the SEA method. Then, the same characterization and evaluation as studying the ZnO over-coated Cu/SiO₂ catalyst should be carried out for this catalyst. This study can fully support the mechanism theory in CO₂ hydrogenation to form methanol, that activated CO₂ on the ZnO sites needs activated hydrogen in the right position. Based on these results, the pushing-pulling theory can be used to describe and understand the CO₂ activation mechanism during the reaction.

Then in situ characterization methods and computational investigation can be used to further study the CO₂ catalytic activation during the reaction of CO₂ hydrogenation to form methanol.

6.2.3 Other CO₂ utilization reactions

Other reactions for CO₂ utilization can be studied to understand the process of CO₂ catalytic activation and develop effective catalysts for CO₂ utilization.

Thermochemical conversion of CO₂ can use high temperature of concentrated solar power to split CO₂ into CO and O₂. The process of electrocatalytic reduction of CO₂ can produce CH₄, C₂H₄,

or CO with proper catalyst. Photoelectrocatalytic conversion of CO₂ is also a promising process for CO₂ utilization. These technologies are still in their infancy and needed more research.

REFERENCES

- Ahmad, M. N., Aramouni, N. A. K., Tarboush, B. A., Touma, J. G., Zeaiter, J. (2017). Catalyst design for dry reforming of methane: Analysis review. *Renewable and Sustainable Energy Reviews*, 82, 2570–2585.
- Ahouari, H., Soualah, A., Le Valant, A., Pinard, L., Magnoux, P., Pouilloux, Y. (2013). Methanol synthesis from CO₂ hydrogenation over copper based catalysts. *Reaction Kinetics, Mechanisms and Catalysis*, 110(1), 131–145.
- Al-Daous, M. A., Manda, A. A., Hattori, H. (2012). Acid-base properties of γ -Al₂O₃ and MgO-Al₂O₃ supported gold nanoparticles. *Journal of Molecular Catalysis A: Chemical*, 363–364, 512–520.
- Alabi, W. O. (2018). *A study of structural properties and performance of Ni-Co-Mg-Al-O_x catalysts for carbon dioxide reforming of methane*. Ph.D. Thesis, University of Saskatchewan.
- Alabi, W. O., Wang, H., Huang, W., Li, X. (2018). A study of CO₂ reforming of CH₄ for coal delivered gases over Ni-based catalysts. *Catalysis Today*, 309, 77–82.
- Angelo, L., Kobl, K., Tejada, L. M. M., Zimmermann, Y., Parkhomenko, K., Roger, A. C. (2015). Study of CuZn MO_x oxides (M = Al, Zr, Ce, CeZr) for the catalytic hydrogenation of CO₂ into methanol. *Comptes Rendus Chimie*, 18(3), 250–260.
- Annesini, M. C., Piemonte, V., Turchetti, L. (2007). Carbon Formation in the Steam Reforming Process: a Thermodynamic Analysis Based on the Elemental Composition. *Climate Change 2013 - The Physical Science Basis*, 11, 1–30.
- Arena, F., Mezzatesta, G., Zafarana, G., Trunfio, G., Frusteri, F., Spadaro, L. (2013). Effects of oxide carriers on surface functionality and process performance of the Cu-ZnO system in the synthesis of methanol via CO₂ hydrogenation. *Journal of Catalysis*, 300, 141–151.

- Arora, S., Prasad, R. (2016). An overview on dry reforming of methane: Strategies to reduce carbonaceous deactivation of catalysts. *RSC Advances*, 6(110), 108668–108688.
- Ayodele, O. B., Tasfy, S. F. H., Zabidi, N. A. M., Uemura, Y. (2017). Co-synthesis of methanol and methyl formate from CO₂ hydrogenation over oxalate ligand functionalized ZSM-5 supported Cu/ZnO catalyst. *Journal of CO₂ Utilization*, 17, 273–283.
- Behrens, M. (2009). Meso- and nano-structuring of industrial Cu/ZnO/(Al₂O₃) catalysts. *Journal of Catalysis*, 267(1), 24–29.
- Behrens, M., Studt, F., Kasatkin, I., Kühl, S., Hävecker, M., Abild-pedersen, F., Zander, S., Girgsdies, F., Kurr, P., Knief, B., Tovar, M., Fischer, R. W., Nørskov, J. K., Schlögl, R. (2012). The Active Site of Methanol Synthesis over Cu/ZnO/Al₂O₃ Industrial Catalysts. *Science*, 759, 893–898.
- Bhuiyan, M. M. R., Lin, S. D., Hsiao, T. C. (2014). Effect of calcination on Cu-Zn-loaded hydrotalcite catalysts for C-C bond formation derived from methanol. *Catalysis Today*, 226, 150–159.
- Bian, Z., Das, S., Wai, M. H., Hongmanorom, P., Kawi, S. (2017). A Review on Bimetallic Nickel-Based Catalysts for CO₂ Reforming of Methane. *ChemPhysChem*, 18(22), 3117–3134.
- Bonura, G., Cordaro, M., Cannilla, C., Arena, F., Frusteri, F. (2014). The changing nature of the active site of Cu-Zn-Zr catalysts for the CO₂ hydrogenation reaction to methanol. *Applied Catalysis B: Environmental*, 152, 152–161.
- Centi, G., Perathoner, S. (2009). Opportunities and prospects in the chemical recycling of carbon dioxide to fuels. In *Catalysis Today*, 148(3–4), 191–205.
- Choi, Y., Futagami, K., Fujitani, T., Nakamura, J. (2001). The difference in the active sites for CO₂ and CO hydrogenations on Cu/ZnO-based methanol synthesis catalysts. *Catalysis Letters*, 73(1), 27–31.

Dadlani, A., Acharya, S., Trejo, O., Nordlund, D., Peron, M., Razavi, J., Berto, F., Prinz, F. B., Torgersen, J. (2017). Revealing the Bonding Environment of Zn in ALD Zn(O,S) Buffer Layers through X-ray Absorption Spectroscopy. *Appl. Mater. Interfaces*, 9, 39105–39109.

Dasireddy, V. D. B. C., and Likozar, B. (2019). The role of copper oxidation state in Cu/ZnO/Al₂O₃ catalysts in CO₂ hydrogenation and methanol productivity. *Renewable Energy*, 140, 452–460.

Dang, S., Yang, H., Gao, P., Wang, H., Li, X., Wei, W., Sun, Y. (2019). A review of research progress on heterogeneous catalysts for methanol synthesis from carbon dioxide hydrogenation. *Catalysis Today*, 330, 61–75.

Debecker, D. P., Gaigneaux, E. M., Busca, G. (2009). Exploring, tuning, and exploiting the basicity of hydrotalcites for applications in heterogeneous catalysis. *Chemistry - A European Journal*, 15(16), 3920–3935.

Deerattrakul, V., Dittanet, P., Sawangphruk, M., Kongkachuichay, P. (2016). CO₂ hydrogenation to methanol using Cu-Zn catalyst supported on reduced graphene oxide nanosheets. *Journal of CO₂ Utilization*, 16, 104–113.

Deerattrakul, V., Limphirat, W., Kongkachuichay, P. (2017). Influence of reduction time of catalyst on methanol synthesis via CO₂ hydrogenation using Cu-Zn/N-rGO investigated by in situ XANES. *Journal of the Taiwan Institute of Chemical Engineers*, 80, 495–502.

Deerattrakul, V., Puengampholsrisook, P., Limphirat, W., Kongkachuichay, P. (2018). Characterization of supported Cu-Zn/graphene aerogel catalyst for direct CO₂ hydrogenation to methanol: Effect of hydrothermal temperature on graphene aerogel synthesis. *Catalysis Today*, 314, 154–163.

- Deerattrakul, V., Yigit, N., Rupprechter, G., Kongkachuichay, P. (2019). General The roles of nitrogen species on graphene aerogel supported Cu-Zn as efficient catalysts for CO₂ hydrogenation to methanol. *Applied Catalysis A, General*, 580, 46–52.
- Di-Cosimo, J. I., Diez, V. K., Xu, M., Iglesia, E. (1998). Structure and Surface and Catalytic Properties of Mg-Al Basic Oxides. *Journal of Catalysis*, 178, 499–510.
- Din, I. U., Shaharun, M. S., Naeem, A., Tasleem, S., Johan, M. R. (2017). Carbon nanofiber-based copper/zirconia catalyst for hydrogenation of CO₂ to methanol. *Journal of CO₂ Utilization*, 21, 145–155.
- Dong, X., Li, F., Zhao, N., Xiao, F., Wang, J., Tan, Y. (2016). CO₂ hydrogenation to methanol over Cu/ZnO/ZrO₂ catalysts prepared by precipitation-reduction method. *Applied Catalysis B Environmental*, 191, 8–17.
- Duan, H., Yang, Y., Singh, R., Chiang, K., Wang, S., Xiao, P., Patel, J., Danaci, D., Burke, N., Zhai, Y., Webley, P. A. (2014). Mesoporous carbon-supported Cu/ZnO for methanol synthesis from carbon dioxide. *Australian Journal of Chemistry*, 67(6), 907–914.
- Dugué A., Cormier, L., Dargaud, O., Galois, L., Calas, G. (2012). Evolution of the Ni²⁺ environment during the formation of a MgO-Al₂O₃-SiO₂ glass-ceramic: A combined XRD and diffuse reflectance spectroscopy approach. *Journal of the American Ceramic Society*, 95(11), 3483–3489.
- El Hassan, N., Kaydouh, M. N., Geagea, H., El Zein, H., Jabbour, K., Casale, S., El Zakhem, H., Massiani, P. (2016). Low temperature dry reforming of methane on rhodium and cobalt based catalysts: Active phase stabilization by confinement in mesoporous SBA-15. *Applied Catalysis A: General*, 520, 114–121.
- English, N., El-Hendawy, M., Mooney, D., MacElroy, J. (2014). Perspectives on atmospheric CO₂ fixation in inorganic and biomimetic. *Coordination Chemistry Reviews*, 269, 85–95.

- Fan, M., Abdullah, A. Z., Bhatia, S. (2009). Catalytic Technology for Carbon Dioxide Reforming of Methane to Synthesis Gas. *Chem.Cat.Chem*, 1, 192–208.
- Fan, M. S., Abdullah, A. Z., Bhatia, S. (2010). Utilization of greenhouse gases through carbon dioxide reforming of methane over Ni-Co/MgO-ZrO₂: Preparation, characterization and activity studies. *Applied Catalysis B: Environmental*, 100(1–2), 365–377.
- Fan, X., Liu, Z., Zhu, Y. A., Tong, G., Zhang, J., Engelbrekt, C., Ulstrup, J., Zhu, K., Zhou, X. (2015). Tuning the composition of metastable Co_xNi_yMg_{100-x-y}(OH)(OCH₃) nanoplates for optimizing robust methane dry reforming catalyst. *Journal of Catalysis*, 330, 106–119.
- Feng, H., Elam, J. W., Libera, J. A., Setthapun, W., Stair, P. C. (2010). Palladium Catalysts Synthesized by Atomic Layer Deposition for Methanol Decomposition. *Chemistry of Materials*, 22(16), 3133–3142.
- Foo, S. Y., Cheng, C. K., Nguyen, T. H., Adesina, A. A. (2012). Syngas production from CH₄ dry reforming over Co-Ni/Al₂O₃ catalyst: Coupled reaction-deactivation kinetic analysis and the effect of O₂ co-feeding on H₂:CO ratio. *International Journal of Hydrogen Energy*, 37(22), 17019–17026.
- Friedlingstein, P., Jones, M. W., O’Sullivan, M., Andrew, R. M., Hauck, J., Peters, G. P., Peters, W., Pongratz, J., Sitch, S., Le Quéré C., DBakker, O. C. E., Canadell, J. G., Ciais, P., Jackson, R. B., Anthoni, P., Barbero, L., Bastos, A., Bastrikov, V., Becker, M., ... Zaehle, S. (2019). Global carbon budget 2019. *Earth System Science Data*, 11(4), 1783–1838.
- Fujimoto, K., Yu, Y. (1993). Spillover effect on the stabilization of Cu-Zn catalyst for CO₂ hydrogenation to methanol. *Studies in Surface Science and Catalysis*, 77(C), 393–396.
- Gao, P., Li, F., Zhan, H., Zhao, N., Xiao, F., Wei, W., Zhong, L., Sun, Y. (2014). Fluorine-modified Cu/Zn/Al/Zr catalysts via hydrotalcite-like precursors for CO₂ hydrogenation to methanol. *Catalysis Communications*, 50, 78–82.

Gawande, M. B., Goswami, A., Felpin, F. X., Asefa, T., Huang, X., Silva, R., Zou, X., Zboril, R., Varma, R. S. (2016). Cu and Cu-Based Nanoparticles: Synthesis and Applications in Catalysis. *Chemical Reviews*, 116(6), 3722–3811.

Gesmanee, S., Koo-Amornpattana, W. (2017). Catalytic hydrogenation of CO₂ for methanol production in fixed-bed reactor using Cu-Zn supported on gamma-Al₂O₃. *Energy Procedia*, 138, 739–744.

Goeppert, A., Czaun, M., Jones, J. P., Surya Prakash, G. K., Olah, G. A. (2014). Recycling of carbon dioxide to methanol and derived products-closing the loop. *Chemical Society Reviews*, 43(23), 7995–8048.

Hasan, F., Webly, P. A. (2017). Utilization of CO₂ for Fuels and Chemicals. In *Sustainable Utilization of Natural Resources* 417–439.

Hu, B., Yin, Y., Liu, G., Chen, S., Hong, X., Tsang, S. C. E. (2018). Hydrogen spillover enabled active Cu sites for methanol synthesis from CO₂ hydrogenation over Pd doped CuZn catalysts. *Journal of Catalysis*, 359, 17–26.

Hu, Y. H., Ruckenstein, E. (2004). Catalytic Conversion of Methane to Synthesis Gas by Partial Oxidation and CO₂ Reforming. *Adv. Catal.*, 48, 297–345.

Huang, C., Chen, S., Fei, X., Liu, D., Zhang, Y. (2015). Catalytic hydrogenation of CO₂ to methanol: Study of synergistic effect on adsorption properties of CO₂ and H₂ in CuO/ZnO/ZrO₂ system. *Catalysts*, 5(4), 1846–1861.

Huang, Chunlei, Wen, J., Sun, Y., Zhang, M., Bao, Y., Zhang, Y., Liang, L., Fu, M., Wu, J., Ye, D., and Chen, L. (2019). CO₂ hydrogenation to methanol over Cu/ZnO plate model catalyst: Effects of reducing gas induced Cu nanoparticle morphology. *Chemical Engineering Journal*, 374, 221–230.

- Jadhav, S. G., Vaidya, P. D., Bhanage, B. M., Joshi, J. B. (2014). Catalytic carbon dioxide hydrogenation to methanol: A review of recent studies. *Chemical Engineering Research and Design*, 92(11), 2557–2567.
- Janocha, E. (2011). *Electronic Properties of ALD Zinc Oxide Interfaces and its Implication for Chalcopyrite Absorber Materials*. M.Sc. Thesis, Helmholtz Zentrum Berlin.
- Kanai, Y., Watanabe, T., Fujitani, T., Saito, M., Nakamura, J., Uchijima, T. (1994). Evidence for the migration of ZnOx in a Cu/ZnO methanol synthesis catalyst. *Catalysis Letters*, 27(1–2), 67–78.
- Karelovic, A., Bargibant, A., Fernández, C., Ruiz, P. (2012). Effect of the structural and morphological properties of Cu/ZnO catalysts prepared by citrate method on their activity toward methanol synthesis from CO₂ and H₂ under mild reaction conditions. *Catalysis Today*, 197(1), 109–118.
- Kawi, S., Kathiraser, Y., Ni, J., Oemar, U., Li, Z., Saw, E. T. (2015). Progress in Synthesis of Highly Active and Stable Nickel-Based Catalysts for Carbon Dioxide Reforming of Methane. *ChemSusChem*, 8(21), 3556–3575.
- Kim, S. M., Abdala, P. M., Margossian, T., Hosseini, D., Foppa, L., Armutlulu, A., Van Beek, W., Comas-Vives, A., Copéret, C., Müller, C. (2017). Cooperativity and dynamics increase the performance of NiFe dry reforming catalysts. *Journal of the American Chemical Society*, 139(5), 1937–1949.
- Klym, H. (2017). Study of phase composition in the technologically modified MgO-Al₂O₃ nanoceramics using XRD and XPS methods. *2017 IEEE 1st Ukraine Conference on Electrical and Computer Engineering, UKRCON 2017 - Proceedings*, 713–716.
- Kobl, K., Thomas, S., Zimmermann, Y., Parkhomenko, K., Roger, A. C. (2016). Power-law kinetics of methanol synthesis from carbon dioxide and hydrogen on copper-zinc oxide catalysts with alumina or zirconia supports. *Catalysis Today*, 270, 31–42.

- Kurhade, A. (2019). *Synthesis and Characterization of Supported Solid Acid Catalysts for Conversion of Green Seed Canola Oil to Biodiesel*. Ph.D. Thesis, University of Saskatchewan
- Le Valant, A., Comminges, C., Tisseraud, C., Canaff, C., Pinard, L., & Pouilloux, Y. (2015). The Cu-ZnO synergy in methanol synthesis from CO₂, Part 1: Origin of active site explained by experimental studies and a sphere contact quantification model on Cu+ZnO mechanical mixtures. *Journal of Catalysis*, 324, 41–49.
- Lee, J. H., Lee, E. G., Joo, O. S., Jung, K. D. (2004). Stabilization of Ni/Al₂O₃ catalyst by Cu addition for CO₂ reforming of methane. *Applied Catalysis A: General*, 269(1–2), 1–6.
- Lei, H., Hou, Z., Xie, J. (2016). Hydrogenation of CO₂ to CH₃OH over CuO/ZnO/Al₂O₃ catalysts prepared via a solvent-free routine. *Fuel*, 164, 191–198.
- Liang, Z., Gao, P., Tang, Z., Lv, M., Sun, Y. (2017). Three dimensional porous Cu-Zn/Al foam monolithic catalyst for CO₂ hydrogenation to methanol in microreactor. *Journal of CO₂ Utilization*, 21, 191–199.
- Liao, T., Sun, C., Sun, Z., Du, A., Smith, S. (2013). Chemically modified ribbon edge stimulated H₂ dissociation: a first-principles computational study. *Physical Chemistry Chemical Physics*, 15, 8054–8057.
- Liang, B., Ma, J., Su, X., Yang, C., Duan, H., Zhou, H., Deng, S., Li, L., and Huang, Y. (2019). Investigation on Deactivation of Cu/ZnO/Al₂O₃ Catalyst for CO₂ Hydrogenation to Methanol. *Industrial and Engineering Chemistry Research*, 58(21), 9030–9037.
- Liu, Y., Sun, K., Ma, H., Xu, X., Wang, X. (2010). Cr, Zr-incorporated hydrotalcites and their application in the synthesis of isophorone. *Catalysis Communications*, 11(10), 880–883.
- Liu, Z. J., Tang, X. J., Xu, S., Wang, X. L. (2014). Synthesis and Catalytic Performance of Graphene Modified CuO-ZnO-Al₂O₃ for CO₂ Hydrogenation to Methanol. *Journal of Nanomaterials*, 2014.

- Lu, J., Lei, Y., Elam, J. W. (2012). Atomic Layer Deposition of Noble Metals – New Developments in Nanostructured Catalysts. In *Noble Metals* 159-178.
- Ma, J., Sun, N., Zhang, X., Zhao, N., Xiao, F., Wei, W., Sun, Y. (2009). A short review of catalysis for CO₂ conversion. *Catalysis Today*, 148(3–4), 221–231.
- Masango, S. S., Peng, L., Marks, L. D., Duyne, R. P. Van, Stair, P. C. (2014). Nucleation and Growth of Silver Nanoparticles by AB and ABC-Type Atomic Layer Deposition. *The Journal of Physical Chemistry*, 118, 17655–17661.
- Muñoz, M., Moreno, S., Molina, R. (2012). Synthesis of Ce and Pr-promoted Ni and Co catalysts from hydrotalcite type precursors by reconstruction method. *International Journal of Hydrogen Energy*, 37(24), 18827–18842.
- Muraza, O., Galadima, A. (2015). A review on coke management during dry reforming of methane. *International Journal of Energy Research*, 39, 1196–1216.
- Nikoo, M. K., Amin, N. A. S. (2011). Thermodynamic analysis of carbon dioxide reforming of methane in view of solid carbon formation. *Fuel Processing Technology*, 92(3), 678–691.
- Olah, G. A. (2005). Beyond oil and gas: The methanol economy. *Angewandte Chemie - International Edition*, 44(18), 2636–2639.
- Olah, G. A., Goeppert, A., Prakash, G. K. S. (2009). Chemical recycling of carbon dioxide to methanol and dimethyl ether: From greenhouse gas to renewable, environmentally carbon neutral fuels and synthetic hydrocarbons. *Journal of Organic Chemistry*, 74(2), 487–498.
- Oneill, B. J., Jackson, D. H. K., Lee, J., Canlas, C., Stair, P. C., Marshall, C. L., Elam, J. W., Kuech, T. F., Dumesic, J. A., Huber, G. W. (2015). Catalyst design with atomic layer deposition. *ACS Catalysis*, 5(3), 1804–1825.
- Pakhare, D., Spivey, J. (2014). A review of dry (CO₂) reforming of methane over noble metal catalysts. *Chem. Soc. Rev.*, 43, 7813–7837.

- Papadopoulou, C., Matralis, H., Verykios, X. (2012). Utilization of biogas as a renewable carbon source: dry reforming of methane. Catalysis for alternative energy generation. In *Springer Nature*.
- Pérez-fortes, M., Schöneberger, J. C., Boulamanti, A., Tzimas, E. (2016). Methanol synthesis using captured CO₂ as raw material : Techno-economic and environmental assessment. *Applied Energy*, 161, 718–732.
- Preston, C. K. (2015). *Integrated Carbon Capture and Storage Project At Saskpower's Boundary Dam Power Station*.
- Rathod, V., Bhale, P. V. (2014). Experimental investigation on biogas reforming for syngas production over an alumina based nickel catalyst. *Energy Procedia*, 54, 236–245.
- Ren, H., Xu, C.-H., Zhao, H.-Y., Wang, Y.-X., Liu, J. J.-Y., Liu, J. J.-Y. (2015). Methanol synthesis from CO₂ hydrogenation over Cu/ γ -Al₂O₃ catalysts modified by ZnO, ZrO₂ and MgO. *Journal of Industrial and Engineering Chemistry*, 28, 261–267.
- Rikkinen, E., Santasalo-aarnio, A., Airaksinen, S., Borghei, M., Viitanen, V., Sainio, J., Kauppinen, E. I., Kallio, T., Krause, A. O. I. (2011). Atomic Layer Deposition Preparation of Pd Nanoparticles on a Porous Carbon Support for Alcohol Oxidation. *The Journal of Physical Chemistry*, 115, 23067–23073.
- Rostrup-Nielsen, J. R., Sehested, J., Nørskov, J. K. (2002). Hydrogen and synthesis gas by steam- and CO₂ reforming. *Advances in Catalysis*, 47, 65–139.
- Ruckenstein, E., Wang, H. Y. (2002). Carbon deposition and catalytic deactivation during CO₂ reforming of CH₄ over Co/ γ -Al₂O₃ catalysts. *Journal of Catalysis*, 205(2), 289–293.
- Shakouri, M. (2018). *Industrial Ni-Based Catalyst Development for Carbon Dioxide Reforming of Methane*. Ph.D. Thesis, University of Saskatchewan.

- Sing, K. S. W., Everett, D. H. G., Haul, R. A. W., Moscou, L., Pierotti, R. A., Rouquerol, J., Siemieniewska, T. (1985). Reporting Physisorption Data for Gas/Solid System: International Union of Pure and Applied Chemistry, IUPAC. *Pure Applied Chemistry*, 57(4), 603–619.
- Theofanidis, S. A., Batchu, R., Galvita, V. V., Poelman, H., Marin, G. B. (2016). Carbon gasification from Fe-Ni catalysts after methane dry reforming. *Applied Catalysis B: Environmental*, 185, 42–55.
- Theofanidis, S. A., Galvita, V. V., Poelman, H., Marin, G. B. (2015). Enhanced carbon-resistant dry reforming Fe-Ni catalyst: Role of Fe. *ACS Catalysis*, 5(5), 3028–3039.
- Tisseraud, C., Comminges, C., Belin, T., Ahouari, H., Soualah, A., Pouilloux, Y., Le Valant, A. (2015). The Cu-ZnO synergy in methanol synthesis from CO₂, Part 2: Origin of the methanol and CO selectivities explained by experimental studies and a sphere contact quantification model in randomly packed binary mixtures on Cu-ZnO coprecipitate cataly. *Journal of Catalysis*, 330, 533–544.
- Tisseraud, C., Comminges, C., Habrioux, A., Pronier, S., Pouilloux, Y., Le Valant, A. (2018). Cu-ZnO catalysts for CO₂ hydrogenation to methanol: Morphology change induced by ZnO lixiviation and its impact on the active phase formation. *Molecular Catalysis*, 446, 98–105.
- Tisseraud, C., Comminges, C., Pronier, S., Pouilloux, Y., Le Valant, A. (2016). The Cu-ZnO synergy in methanol synthesis Part 3: Impact of the composition of a selective Cu@ZnOxcore-shell catalyst on methanol rate explained by experimental studies and a concentric spheres model. *Journal of Catalysis*, 343, 106–114.
- Tomishige, K., Himeno, Y., Matsuo, Y., Yoshinaga, Y., Fujimoto, K. (2002). Catalytic Performance and Carbon Deposition Behavior of a NiO-MgO Solid Solution in Methane Reforming with Carbon Dioxide under Pressurized Conditions. *Industrial & Engineering Chemistry Research*, 39(6), 1891–1897.

- Trimm, D. L. (1999). Catalysts for the control of coking during steam reforming. *Catalysis Today*, 49(1–3), 3–10.
- Velu, S., Suzuki, K., Gopinath, C. S., Yoshida, H., Hattori, T. (2002). XPS, XANES and EXAFS investigations of CuO/ZnO/Al₂O₃/ZrO₂ mixed oxide catalysts. *Physical Chemistry Chemical Physics*, 4(10), 1990–1999.
- Wang, H., Miller, J. T., Shakouri, M., Xi, C., Wu, T., Zhao, H., Akatay, M. C. (2013). XANES and EXAFS studies on metal nanoparticle growth and bimetallic interaction of Ni-based catalysts for CO₂ reforming of CH₄. *Catalysis Today*, 207, 3–12.
- Wang, H. Y., Ruckenstein, E. (2001). CO₂ reforming of CH₄ over Co/MgO solid solution catalysts-effect of calcination temperature and Co loading. *Applied Catalysis A: General*, 209(1–2), 207–215.
- Wang, H., Zaidi, S. (2013). Catalyst Development for CO₂ Activation to Produce Syn-Gas through CO₂ Reforming of CH₄: Mitigation of Carbon Formation on Ni-Based. In *New and Future Developments in Catalysis*, 455–479.
- Wang, W., Wang, S., Ma, X., Gong, J. (2011). Recent advances in catalytic hydrogenation of carbon dioxide. *The Royal Society of Chemistry*, 40, 3703–3727.
- Waugh, K. C. (1992). Methanol Synthesis. *Catalysis Today*, 15, 51–75.
- Yao, L., Zhu, J., Peng, X., Tong, D., Hu, C. (2013). Comparative study on the promotion effect of Mn and Zr on the stability of Ni/SiO₂ catalyst for CO₂ reforming of methane. *International Journal of Hydrogen Energy*, 38(18), 7268–7279.
- Yu, L., Pan, X., Cao, X., Hu, P., Bao, X. (2011). Oxygen reduction reaction mechanism on nitrogen-doped graphene : A density functional theory study. *Journal of Catalysis*, 282, 183–190.
- Zhang, J. (2008). *Research and development of Nickel based catalysts for carbon dioxide reforming of methane*. Ph.D. Thesis, University of Saskatchewan.

Zhang, J., Wang, H., Dalai, A. K. (2007). Development of stable bimetallic catalysts for carbon dioxide reforming of methane. *Journal of Catalysis*, 249(2), 300–310.

Zhang, L., Xia, Z. (2011). Mechanisms of Oxygen Reduction Reaction on Nitrogen-Doped Graphene for Fuel Cells. *The Journal of Physical Chemistry*, 115, 11170–11176.

Appendix A: Reproducibility of the Experimental Results

ICP analysis: one of the catalysts for the reaction CRM and one for the reaction of CO₂ hydrogenation to produce methanol were characterized twice, to determine whether the characterization results are reproducible. The percent difference of two values (a₁ and a₂) is calculated using Equation

$$\text{Diff.} = \left| \frac{(a_1 - a_2)}{(a_1 + a_2)/2} \right| \times 100 \% \quad \text{A-1}$$

The compositions of elements on the catalyst NiMn and catalyst 5Cu-1CyZn-30s were measured twice and the results are shown in Table A-1 and A-2, which reveal that the results in ICP analysis were reproducible.

XAS analysis:

In the analysis of XAS, two spectra of the same sample were collected. As the example, the Ni K-edge spectra for the reduced CRM catalyst NiCo, and Cu K-edge spectra for the reduced catalyst 5Cu-1CyZn-30s are shown in Figure A-1,2. The spectra are almost identical, and significant difference is displayed.

Catalyst activity test:

The activity test of the catalyst NiCo for the CRM reaction was repeated. The CH₄ and CO₂ reaction rate of NiCo are shown in Figure A-3. The same test for the Cu-Zno catalyst was done for the CO₂ hydrogenation reaction, and the results are shown in Table A-3. Both of the differences of reaction rates in these two reaction were in the range of $\pm 4.1\%$, meaning that the activity test of catalysts for these two reactions were reproducible.

Table A-1 Repeatability results for ICP analysis for catalyst NiMn

	a ₁	a ₂	Diff. (%)
Ni (%)	2.90	2.93	0.1
Mn (%)	1.94	1.99	2.0
Mg (%)	64.46	64.52	2.0
Al (%)	30.68	30.56	2.0

Table A-2 Repeatability results for ICP analysis for catalyst 5Cu-1CyZn-30s

	a ₁	a ₂	Diff. (%)
Cu (wt%)	4.49	4.38	5.6
Zn (wt%)	1.47	1.39	2.5

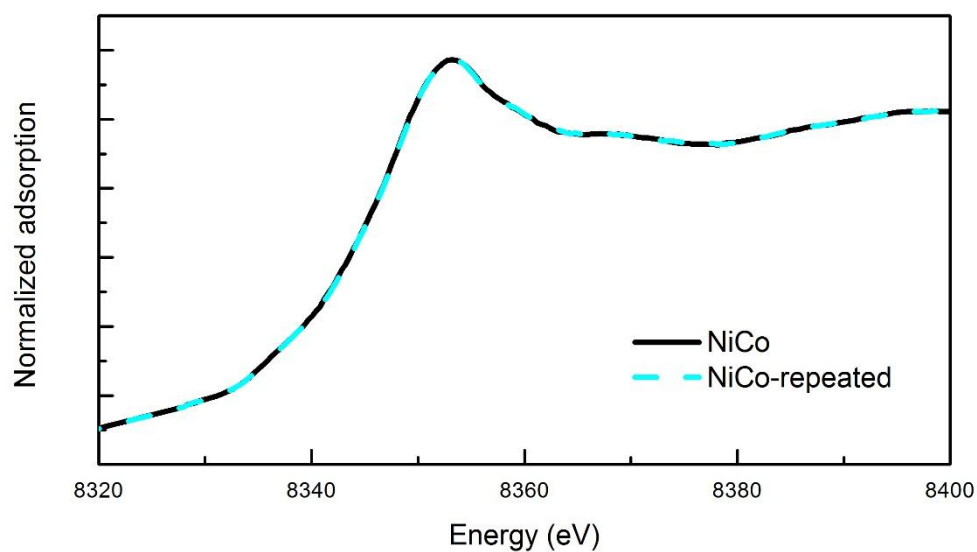


Figure A-1 Reproducibility of XANES analysis for the reduced catalyst NiCo

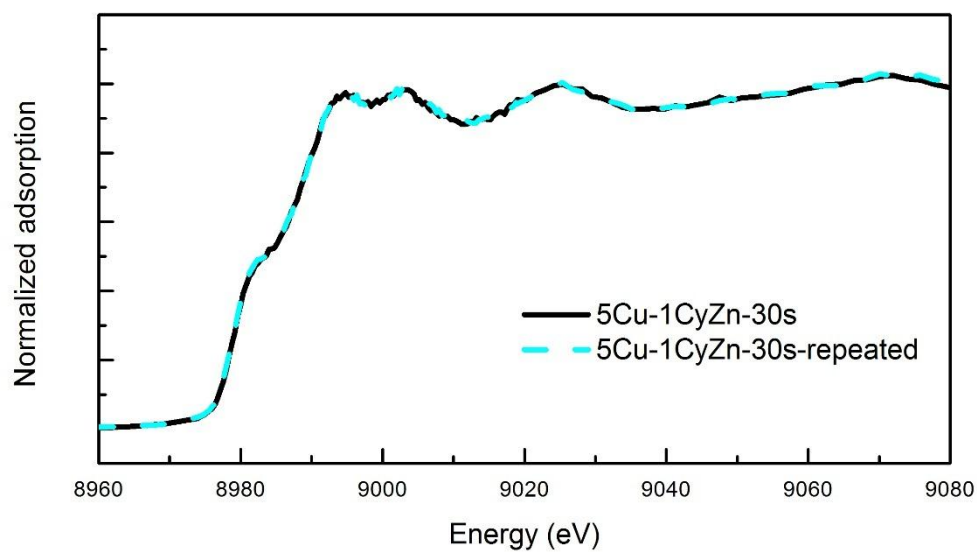


Figure A-2 Reproducibility of XANES analysis for the reduced catalyst 5Cu-1CyZn-30s

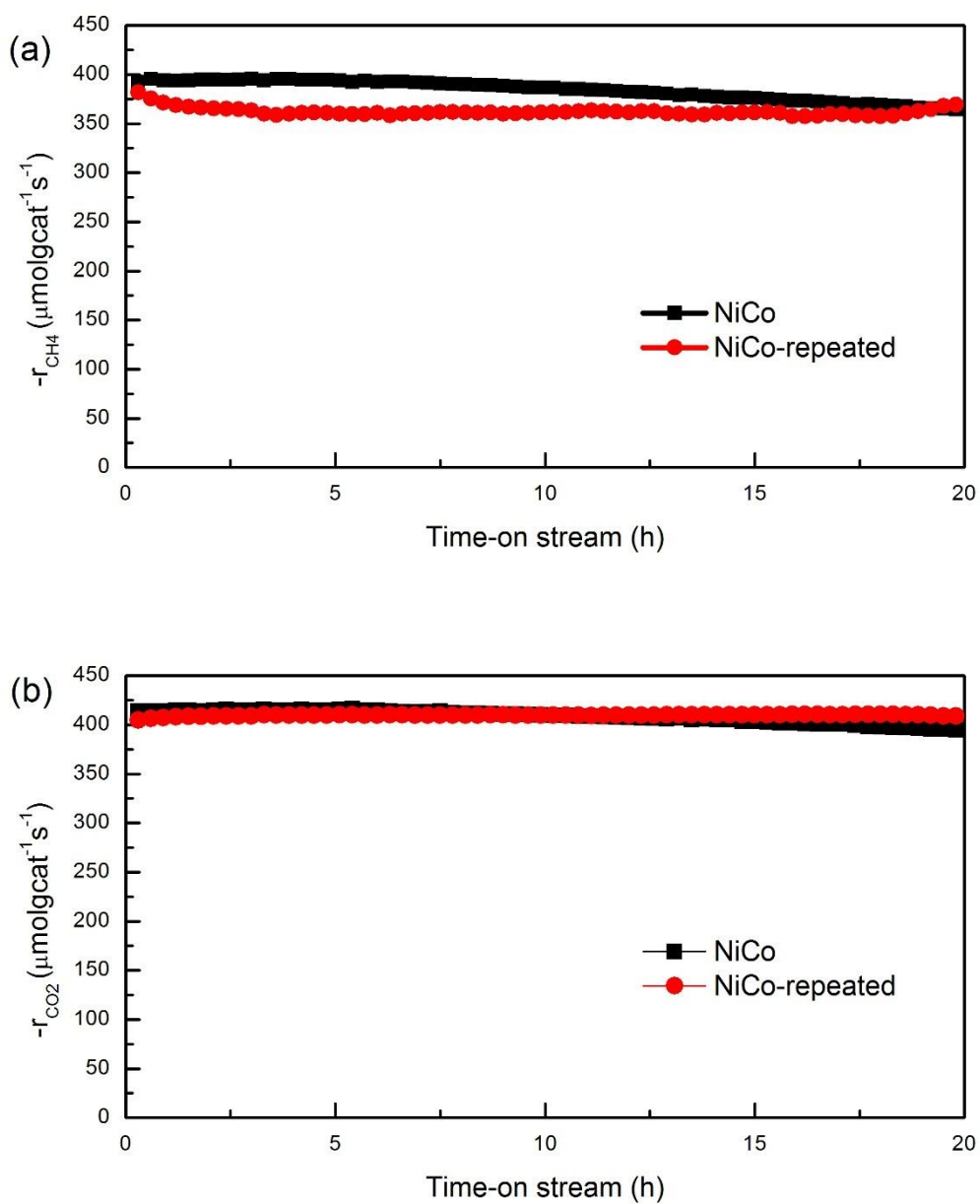


Figure A-3 Repeated catalyst performance evaluation experiments. Activity test of NiCo catalysts at reaction condition: $T = 750\text{ }^{\circ}\text{C}$, $P = 1\text{ atm}$, $F = 90\text{ mL}\cdot\text{min}^{-1}$, $\text{CH}_4/\text{CO}_2/\text{N}_2 = 1/1/1$, 0.05 g catalyst . (a) The reaction rate of CH₄ as a function of time-on-stream; (b) The reaction rate of CO₂ as a function of time-on-stream.

Table A-3 Repeated catalytic performances of the catalyst 5Cu-1CyZn-30s

Rate (mmol·g ⁻¹ h ⁻¹)	a ₁	a ₂	Diff. (%)
CO ₂ reaction	4.82	4.72	2.1
Methanol formation	0.49	0.47	4.1
CO formation	4.38	4.26	2.8

Reaction conditions: T = 250 °C, P = 4.0 MPa, F = 9.6 L·h⁻¹, 1.0 g catalyst.

Appendix B: Calibration of Mass Flow Controller

There are four channels in the mass flow controller (MFC) for the reaction of CRM, N₂, CO₂, CH₄, and H₂, respectively. Figure B-1 shows the calibration curves of MFC for these four gases. There are two channels of MFC for the reaction of CO₂ hydrogenation to methanol, CO₂ and H₂. Figure B-2 displays the calibration curves of MFC. Each point represents the average of 10 measured flow rates at that set-point. The R² of each curve was more than 0.999.

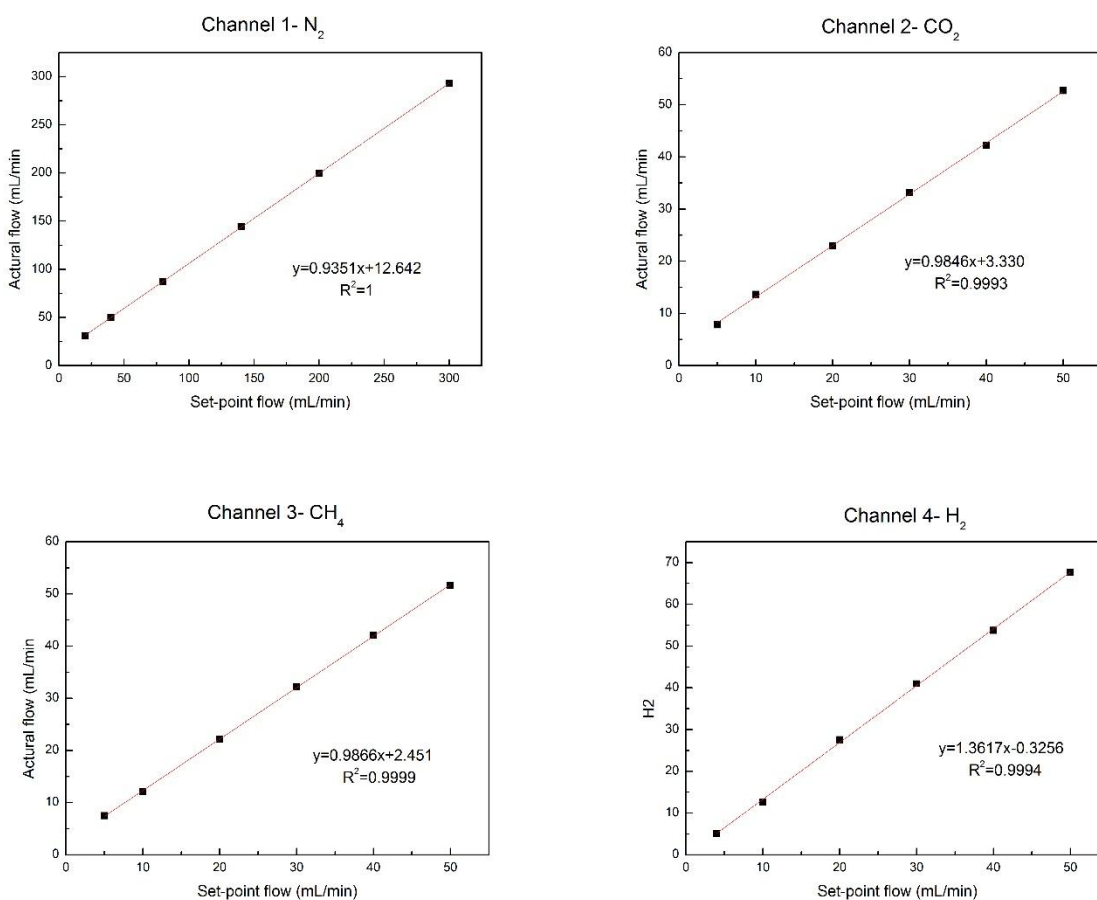


Figure B-1 MFC calibration curves of each channel for CRM reaction

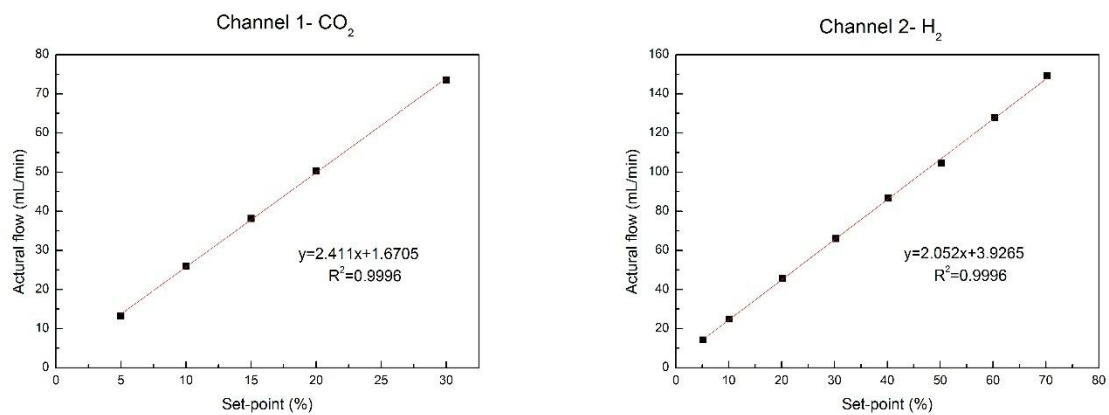


Figure B-2 MFC calibration curves of each channel for the reaction of CO₂ hydrogenation

Appendix C: Calibration of Gas Chromatography

The gas chromatography (GC) was calibrated using at least four concentrations. And at least three times injections were conducted at each concentration. For the reaction of CRM, the calibration of gases N_2 , CO_2 , CH_4 , CO and H_2 were carried out with Agilent 6890N GC equipped with a TCD. The calibration curves are shown in Figure C-1. For the reaction of CO_2 hydrogenation to produce methanol, the calibration of gases H_2 , CO , and CO_2 were done with Agilent Technologies 7890A GC equipped with two thermal conductivity detectors (TCD) and a flame ionization detector (FID). The liquid product methanol was detected with an off-line Agilent Technologies 7890A GC equipped with a DB-Wax capillary column and FID detector. The calibration curves are shown in Figure C-2,3.

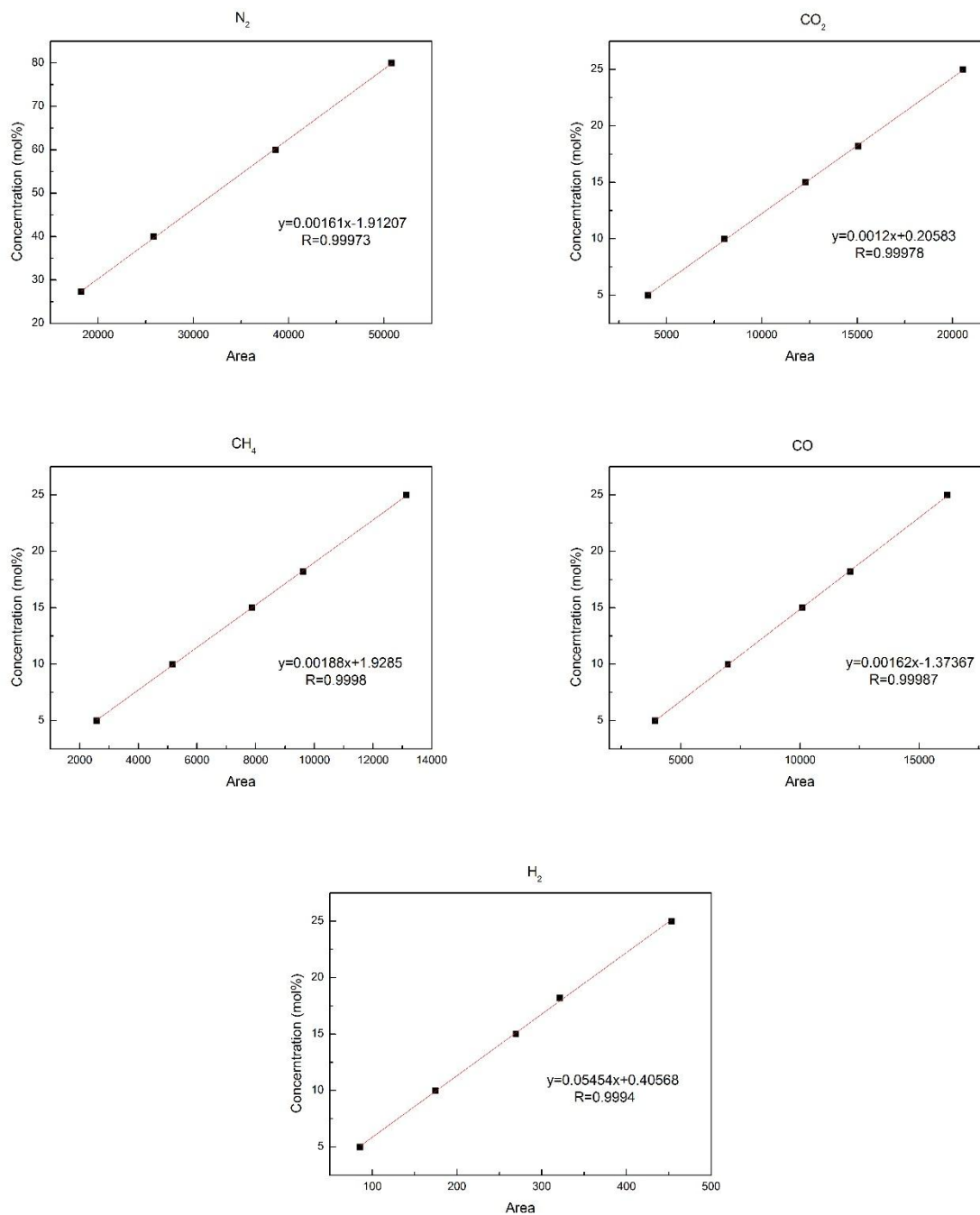


Figure C-1 Calibration curves for the Agilent 6890N GC equipped with an TCD for CRM reaction

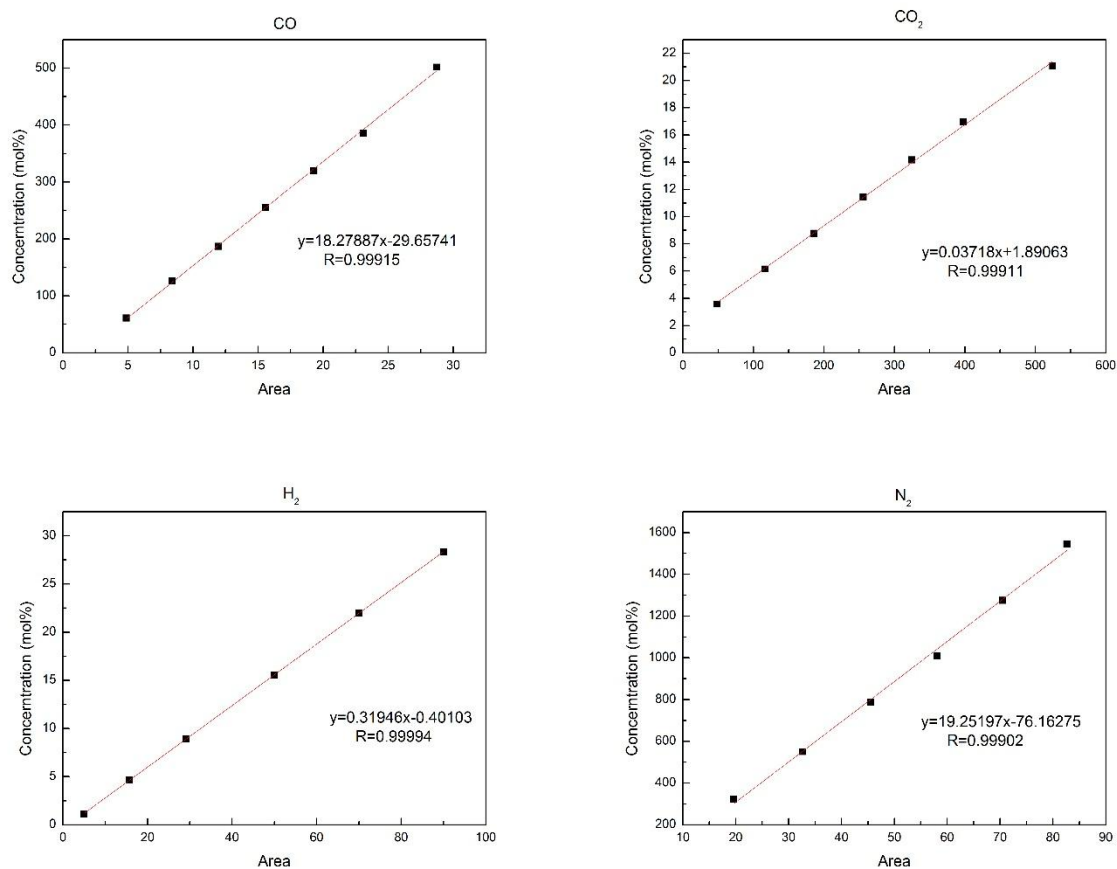


Figure C-2 Calibration curve of Methanol for the Agilent Technologies 7890A GC equipped with TCD and FID detectors

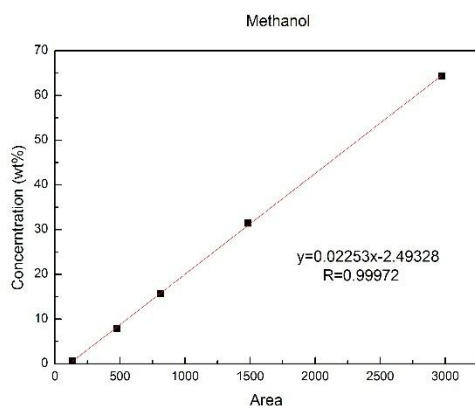


Figure C-3 Calibration curve of Methanol for the Agilent Technologies 7890A GC equipped with a DB-Wax capillary column and FID detector

Appendix D: Temperature Profiles of Reactors

The temperatures profile inside the reactors were obtained with N₂ gas passing through the reactor. The temperature inside the reactor were measured with a K-type thermocouple at various position while the furnace is setting at different temperatures. Each measurement was repeated 3 times and the average value was used. Figure D-1 shows (a) the calibration of the actual temperature (from the thermocouple) and the setting temperature (of the furnace), and (b) the constant-temperature zone of the reactors for the CRM reaction. Figure D-2 displayed (a) the calibration of the actual temperature and the setting temperature, and (b) the constant-temperature zone of the reactors for the CO₂ hydrogenation reaction.

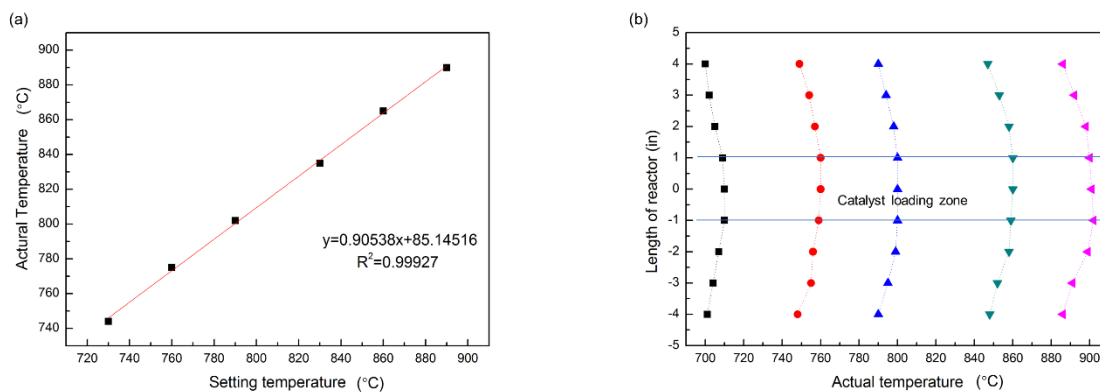


Figure D-1 Temperature profiles of CRM reactor

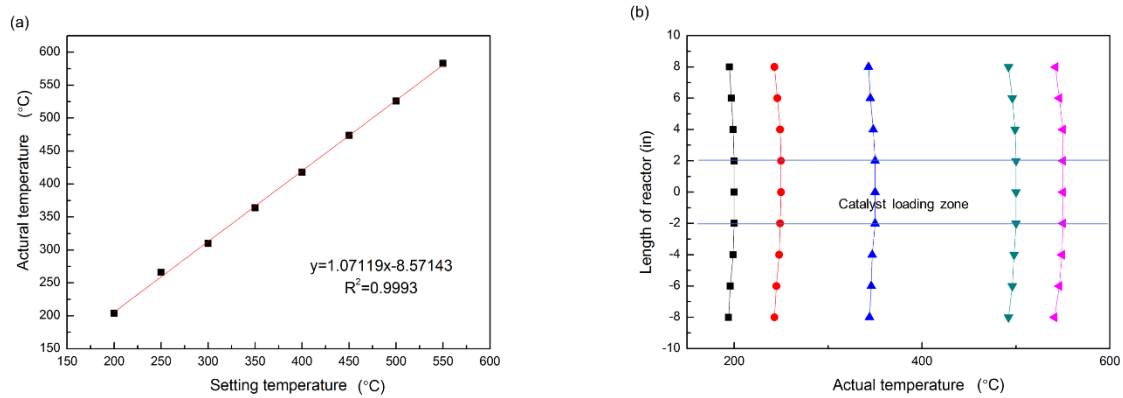


Figure D-2 Temperature profiles of CO₂ hydrogenation reactor

Appendix E: Carbon and Hydrogen Balance

The carbon and hydrogen balance in CRM reaction could be calculated in the unit of mole. The C and H balance during CRM reaction over catalyst NiCo is shown in Table E-1 as an example with the reaction time of 20 h.

$$C_{in} = (CH_4 + CO_2)_{in}$$

$$C_{out} = (CH_4 + CO_2 + CO)_{out}$$

$$\Delta C = C_{in} - C_{out}$$

$$H_{in} = (4 \times CH_4)_{in}$$

$$H_{out} = (4 \times CH_4 + 2 \times H_2)_{out}$$

$$\Delta H = H_{in} - H_{out}$$

The carbon and hydrogen balance in CO₂ hydrogenation reaction could also be calculated. The balance of these two elements over catalyst 5Cu-1CyZn-30s is shown in Table E-2 with the reaction time of 24 h.

$$C_{in} = (CO_2)_{in}$$

$$C_{out} = (CO_2 + CH_3OH + CO)$$

$$\Delta C = C_{in} - C_{out}$$

$$H_{in} = (2 \times H_2)_{in}$$

$$H_{out} = (2 \times H_2 + 4 \times CH_3OH + 2 \times H_2O)_{out}$$

$$\Delta H = H_{in} - H_{out}$$

Table E-1 Carbon and Hydrogen balance for CRM over NiCo during 20 h. Reaction conditions: 0.05 g catalyst, temperatures: 750 °C, 1atm, GHSV of 110 L g⁻¹ h⁻¹, CH₄/CO₂/N₂ = 1/1/1

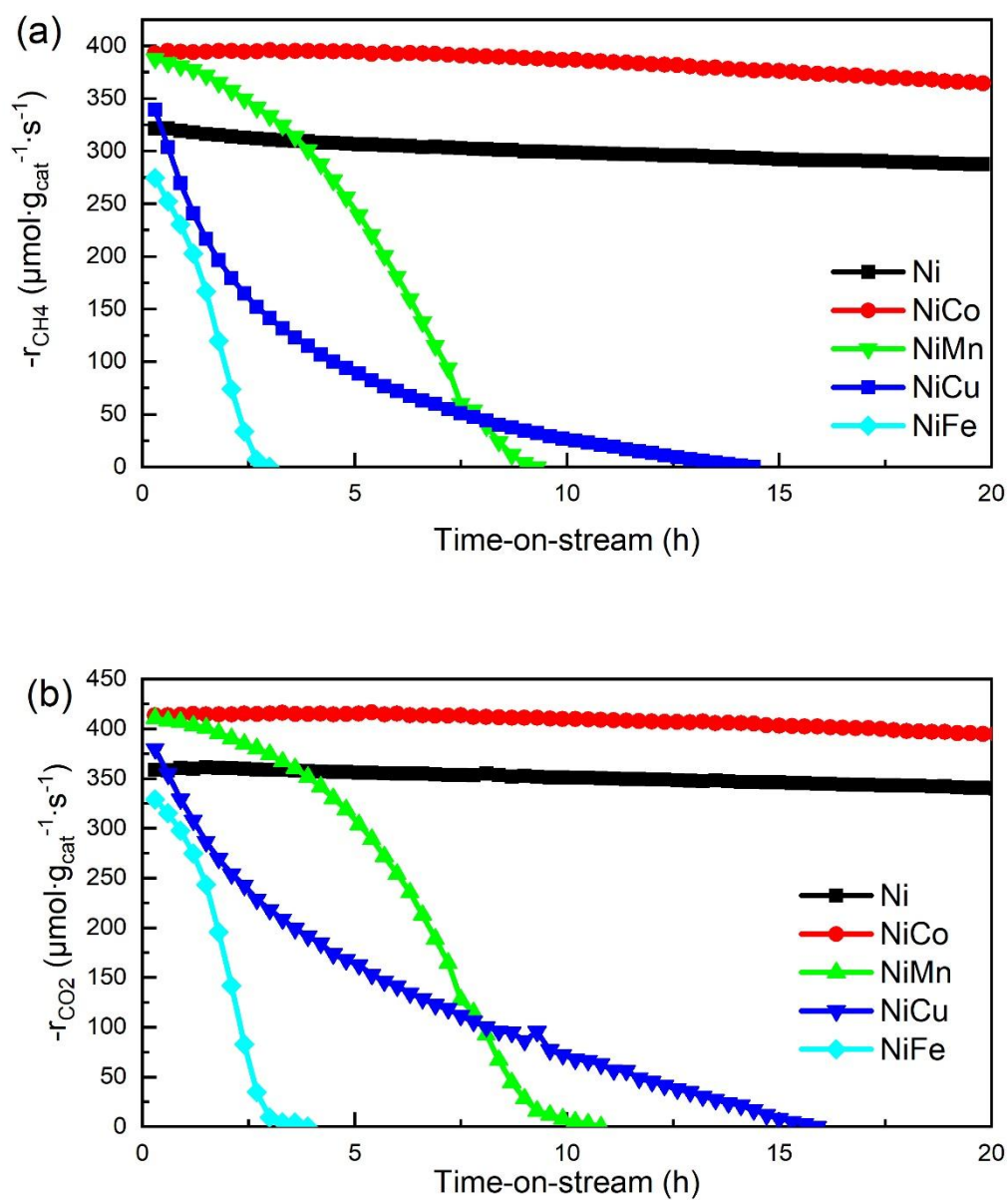
Carbon				Hydrogen			
In (mole)	Out (mole)	Balance (mole)	Diff. (%)	In (mole)	Out (mole)	Balance (mole)	Diff. (%)
3.57	3.43	0.14	4.00	7.14	6.94	0.19	2.69

Table E-2 Carbon and Hydrogen balance for CO₂ hydrogenation reaction over catalyst 5Cu-1CyZn-30s during 24 h. Reaction conditions: 1.0 g catalyst, temperatures: 250 °C, 4 MPa, F = 9.6 L h⁻¹, H₂/CO₂ = 3/1

Carbon				Hydrogen			
In (mole)	Out (mole)	Balance (mole)	Diff. (%)	In (mole)	Out (mole)	Balance (mole)	Diff. (%)
2.57	2.46	0.11	4.37	15.43	14.98	0.45	4.41

Appendix F: Performance of Monometallic Ni and Bimetallic NiM2 Catalysts for CRM Reaction at 750 °C

The CH₄ and CO₂ reaction rates, and the H₂ and CO formation rates of catalysts Ni and NiM2 are shown in Figure F-1.



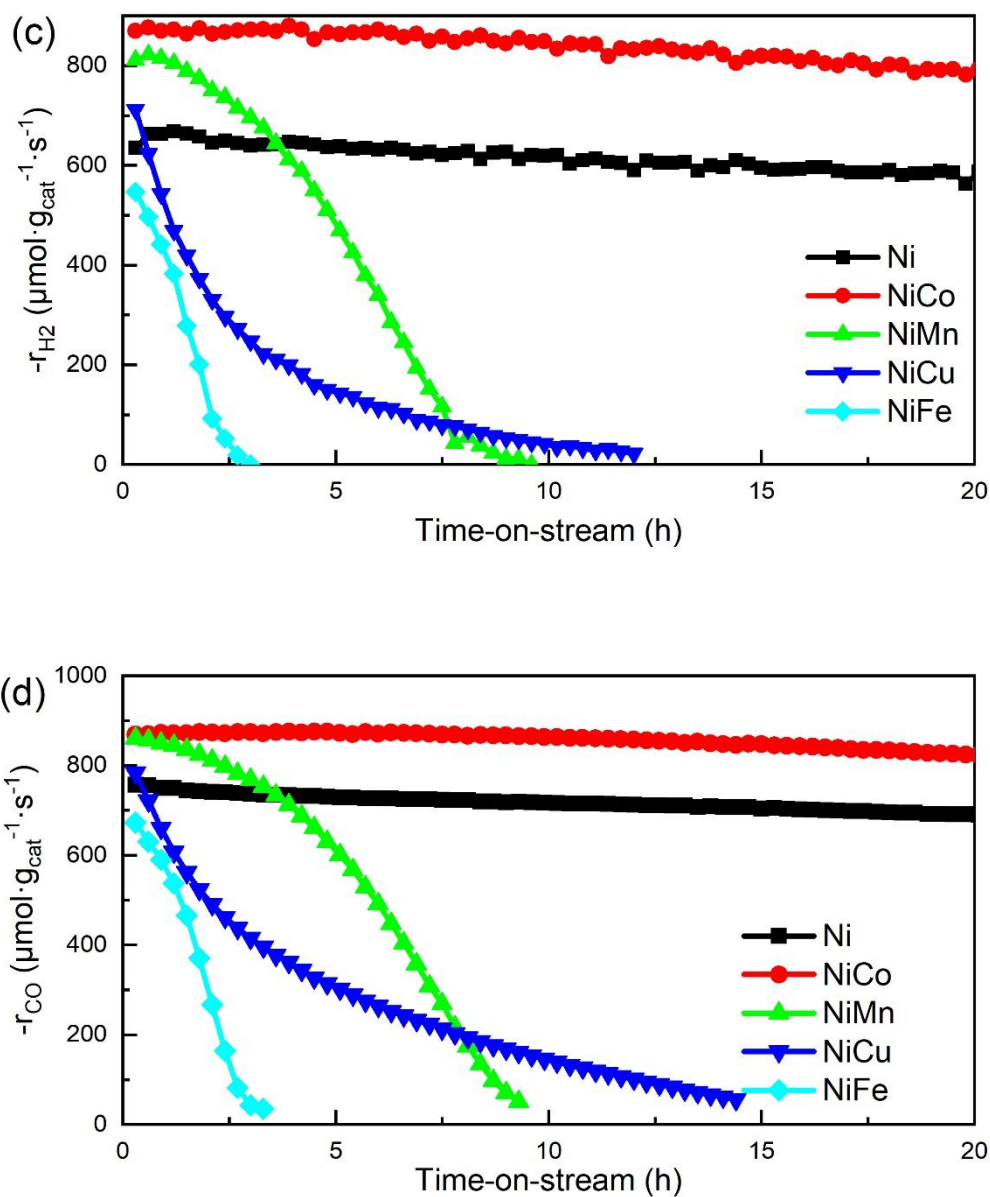


Figure F-1 Activity and stability of monometallic Ni and bimetallic NiM2 catalysts at reaction condition: $T = 750\text{ }^{\circ}\text{C}$, $P = 1\text{ atm}$, $\text{GHSV} = 110\text{ L} \cdot g_{\text{cat}}^{-1} \cdot \text{h}^{-1}$, $\text{CH}_4/\text{CO}_2/\text{N}_2 = 1/1/1$, 0.05 g catalyst . (a) The reaction rate of CH_4 as a function of time-on-stream; (b) The reaction rate of CO_2 as a function of time-on-stream; (c) The formation rate of H_2 as a function of time-on-stream; (d) The formation rate of CO as a function of time-on-stream

Appendix G: Characterization of Monometallic Ni and Bimetallic NiM₂ Catalysts Reduced at 850 °C

The spectra of Ni, Co, Mn, Cu, and Fe K-edge XANES of catalysts reduced at 850 °C are shown in Figure G-1,2,3,4, and 5.

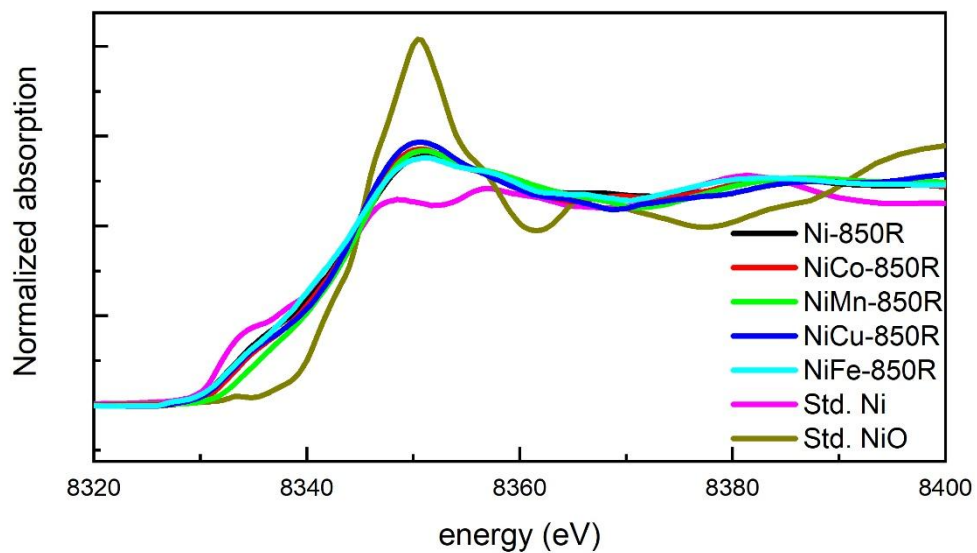


Figure G-1 The Ni K-edge XANES spectra of monometallic Ni and bimetallic NiM₂ catalysts after reduction at 850 °C for 4 h as well as those of Ni and its oxide standards

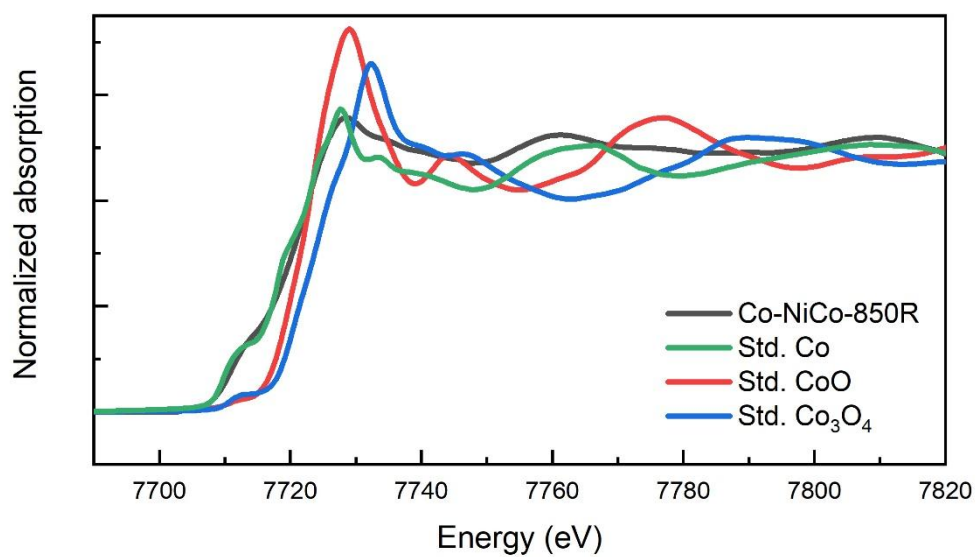


Figure G-2 The Co K-edge XANES spectra of NiCo catalyst after being reduction 850 °C for 4 h as well as those of Co foil, and its oxide standards

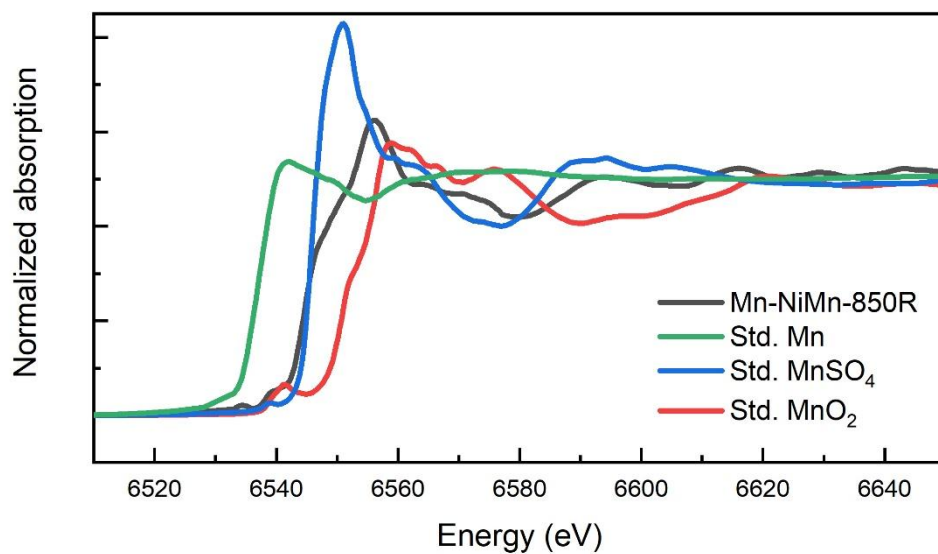


Figure G-3 The Mn K-edge XANES spectra of NiMn catalyst after reduction at 850 °C for 4 h as well as those of Mn foil, and its oxide standards

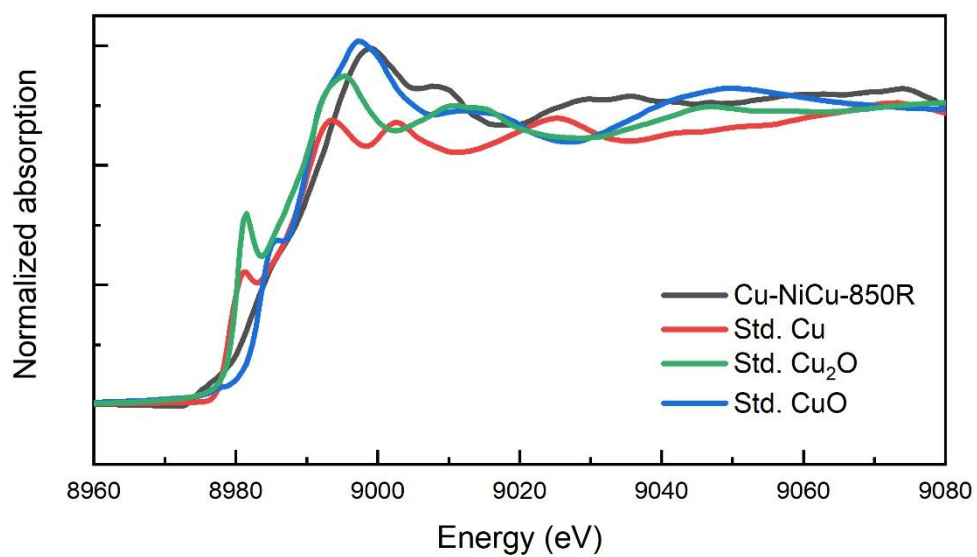


Figure G-4 The Cu K-edge XANES spectra of NiCu catalyst after reduction at 850 °C for 4 h as well as those of Cu foil, and its oxide standards

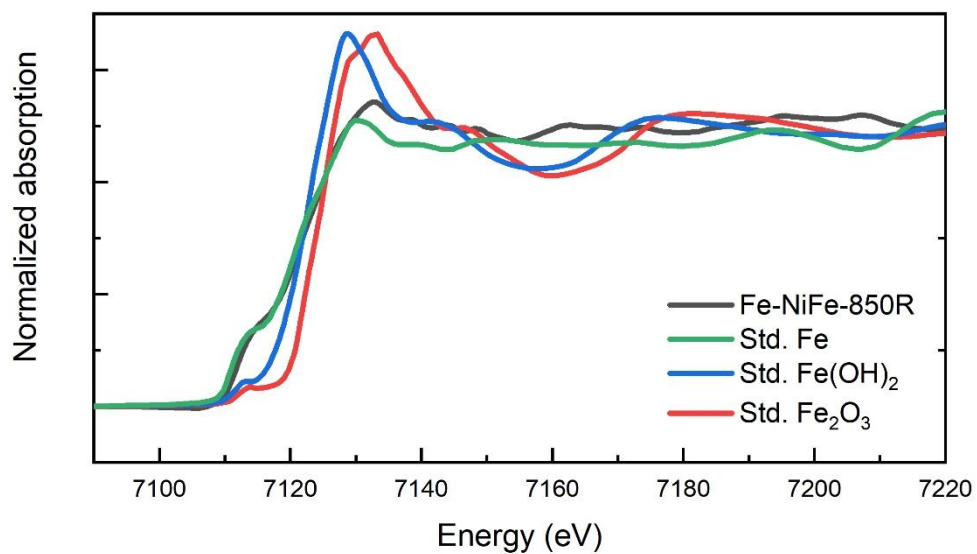
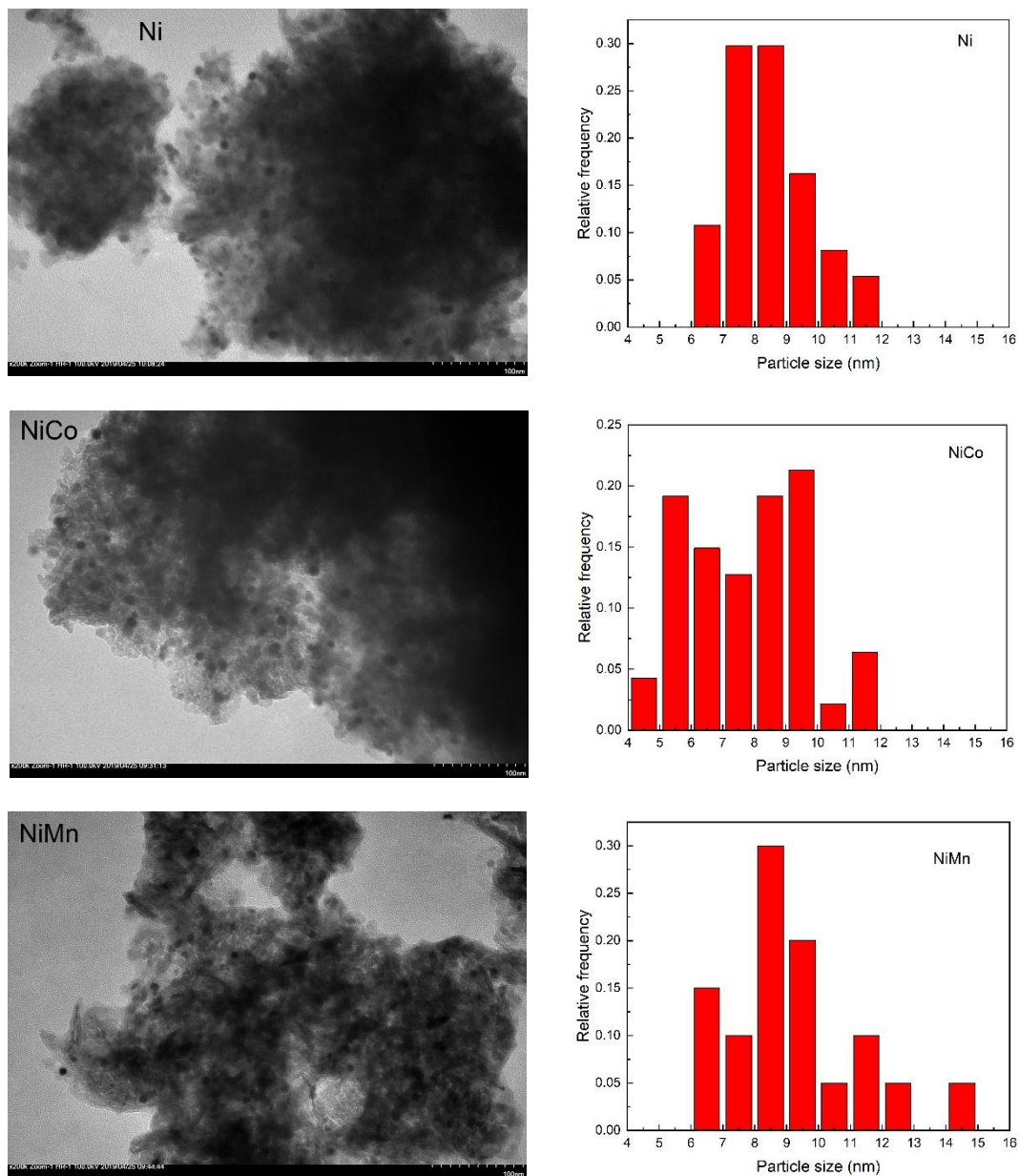


Figure G-5 The Fe K-edge XANES spectra of NiFe catalyst after reduction at 850 °C for 4 h as well as those of Fe foil, and its oxide standards

The TEM images of the monometallic Ni and bimetallic NiM2 catalysts reduced at 850 °C and their metallic particle size distributions are shown in Figure G-6.



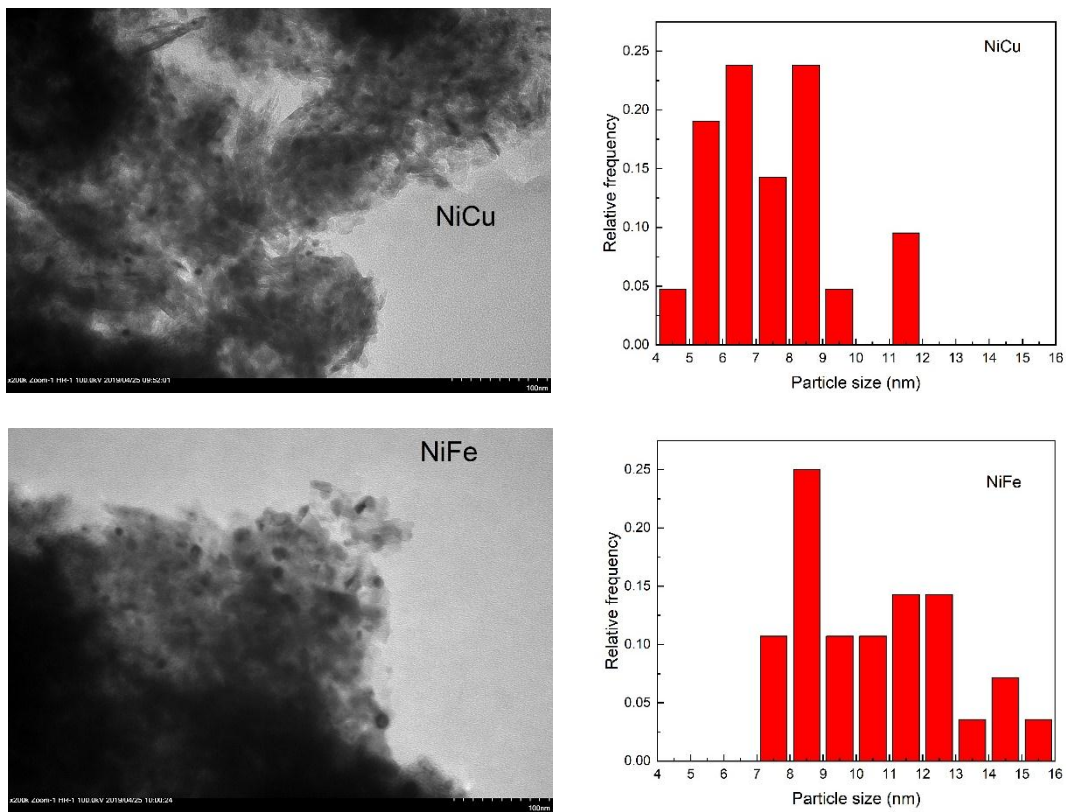


Figure G-6 TEM images and the particle size distribution of the catalysts reduced at 850 °C

Appendix H: Characterization of Catalysts with Different Supports

The bulk structure of catalysts Ni/Al₂O₃, Ni/MgO-spinel, NiCo/spinel, and NiCo/MgO-spinel is shown in Tabel H-1 and Figure H-1,2. The phase percentages of spinel and MgO were calculated and shown in Table H-2.

Table H-1 ICP and BET results

Catalysts	Elements composition (mol%)		Mg/Al	BET surface area, m ² ·g ⁻¹	Pore volume, cm ³ ·g ⁻¹	Average pore size, nm
	Ni	Co				
Ni/Al ₂ O ₃	3.0	-	0	182	0.34	75.8
Ni/MgO- spinel	4.8	-	1.6	91	0.19	84.0
NiCo/spinel	1.6	1.7	0.3	95	0.32	116.3
NiCo/MgO- spinel	3.9	4.9	2.0	74	0.22	130.4

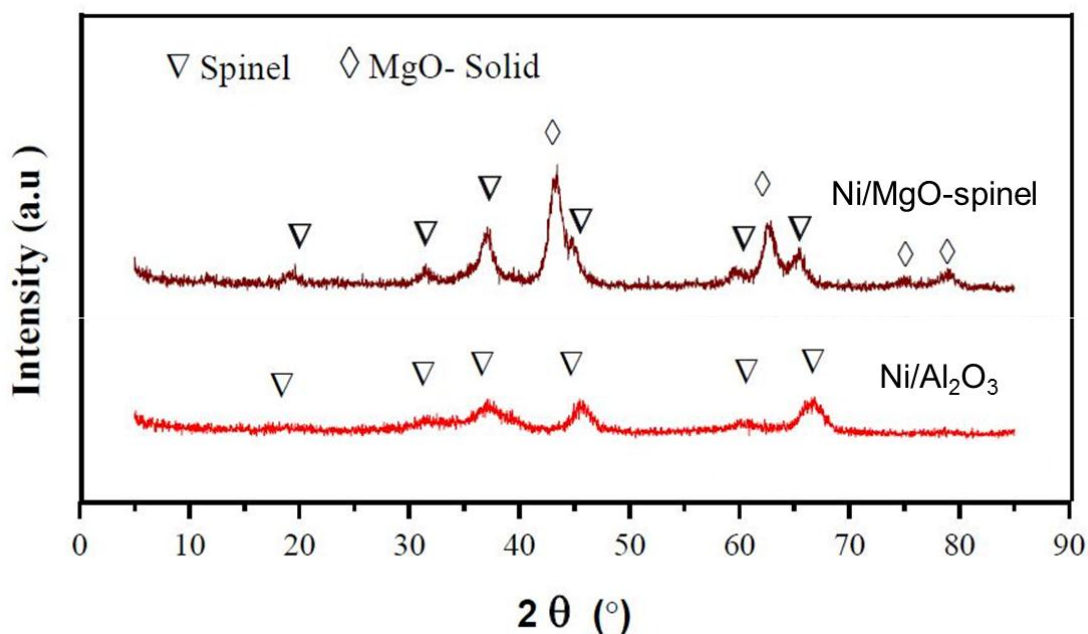


Figure H-1 XRD patterns of Ni catalysts supported by Al₂O₃ and MgO-spinel (Alabi, 2018)

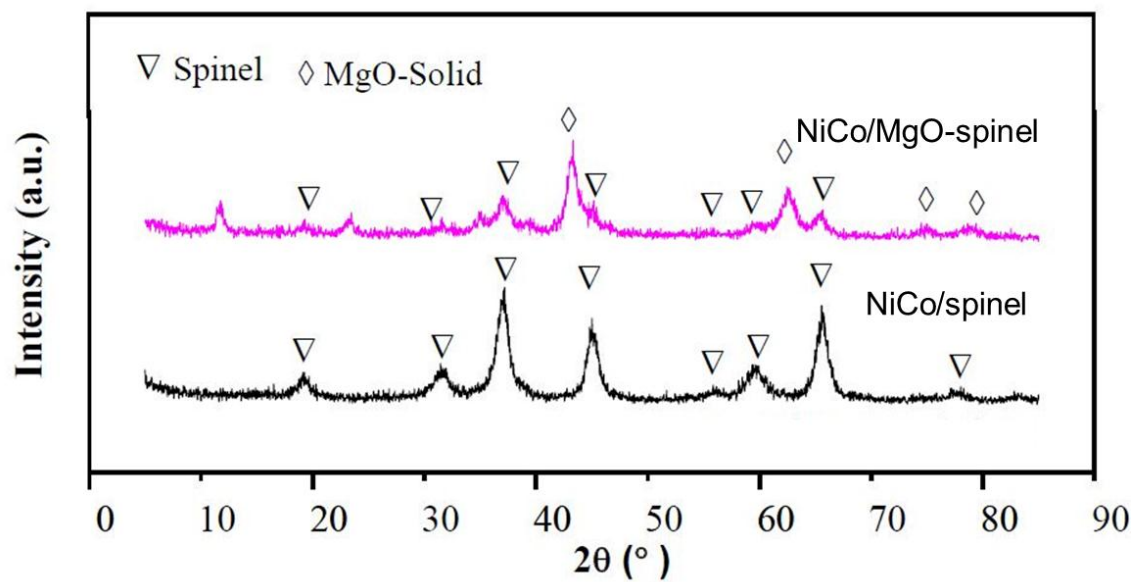


Figure H-2 XRD patterns of NiCo catalysts supported by spinel and MgO-spinel (Alabi, 2018)

Table H-2 Phase quantification of catalysts based on the XRD patterns



Catalysts	MgO phase (%)	Spinel phase (%)
Ni/Al ₂ O ₃	0	100
Ni/MgO-spinel	55	45
NiCo/spinel	0	100
NiCo/MgO-spinel	62	38


Appendix I: Permission to Use


1. Permission to use the published figure in “Development of stable bimetallic catalysts for carbon dioxide reforming of methane”.


License Number	4850850658051
License date	Jun 16, 2020
Licensed Content Publisher	Elsevier
Licensed Content Publication	Journal of Catalysis
Licensed Content Title	Development of stable bimetallic catalysts for carbon dioxide reforming of methane
Licensed Content Author	Jianguo Zhang,Hui Wang,Ajay K. Dalai
Licensed Content Date	Jul 25, 2007
Licensed Content Volume	249
Licensed Content Issue	2
Licensed Content Pages	11
Type of Use	reuse in a thesis/dissertation
Portion	figures/tables/illustrations
Number of figures/tables/illustrations	1
Format	electronic
Are you the author of this Elsevier article?	No
Will you be translating?	No
Title	A Study of Carbon Dioxide Catalytic Activation for Its Conversion to Value-added Products
Institution name	University of Saskatchewan
Expected presentation date	Sep 2020
Portions	Figure 1
Requestor Location	Ms. Jinglin Gao 57 Campus Dr Saskatoon, SK S7N 5A9 Canada Attn: Ms. Jinglin Gao GB 494 6272 12
Publisher Tax ID	
Total	0.00 CAD


2. Permission to use the published figure in “Cooperativity and Dynamics Increase the Performance of NiFe Dry Reforming Catalysts”.




 Home

 Help

 Email Support

 Jinglin Gao ▾



Cooperativity and Dynamics Increase the Performance of NiFe Dry Reforming Catalysts
Author: Sung Min Kim, Paula Macarena Abdala, Tigran Margossian, et al
Publication: Journal of the American Chemical Society
Publisher: American Chemical Society
Date: Feb 1, 2017
Copyright © 2017, American Chemical Society

PERMISSION/LICENSE IS GRANTED FOR YOUR ORDER AT NO CHARGE

This type of permission/license, instead of the standard Terms & Conditions, is sent to you because no fee is being charged for your order. Please note the following:

- Permission is granted for your request in both print and electronic formats, and translations.
- If figures and/or tables were requested, they may be adapted or used in part.
- Please print this page for your records and send a copy of it to your publisher/graduate school.
- Appropriate credit for the requested material should be given as follows: "Reprinted (adapted) with permission from (COMPLETE REFERENCE CITATION). Copyright (YEAR) American Chemical Society." Insert appropriate information in place of the capitalized words.
- One-time permission is granted only for the use specified in your request. No additional uses are granted (such as derivative works or other editions). For any other uses, please submit a new request.

If credit is given to another source for the material you requested, permission must be obtained from that source.

3. Permission to use the published figure in “The Cu–ZnO synergy in methanol synthesis from CO₂, Part 1: Origin of active site explained by experimental studies and a sphere contact quantification model on Cu+ZnO mechanical mixtures”.

License Number	4850990505642
License date	Jun 16, 2020
Licensed Content Publisher	Elsevier
Licensed Content Publication	Journal of Catalysis
Licensed Content Title	The Cu–ZnO synergy in methanol synthesis from CO ₂ , Part 1: Origin of active site explained by experimental studies and a sphere contact quantification model on Cu+ZnO mechanical mixtures
Licensed Content Author	Anthony Le Valant, Clément Comminges, Céline Tisseraud, Christine Canaff, Ludovic Pinard, Yannick Pouilloux
Licensed Content Date	Apr 1, 2015
Licensed Content Volume	324
Licensed Content Issue	n/a
Licensed Content Pages	9
Type of Use	reuse in a thesis/dissertation
Portion	figures/tables/illustrations
Number of figures/tables/illustrations	4
Format	print
Are you the author of this Elsevier article?	No
Will you be translating?	No
Title	A Study of Carbon Dioxide Catalytic Activation for Its Conversion to Value-added Products
Institution name	University of Saskatchewan
Expected presentation date	Sep 2020
Portions	Figure 4
Requestor Location	Ms. Jinglin Gao 57 Campus Dr Saskatoon, SK S7N 5A9 Canada Attn: Ms. Jinglin Gao GB 494 6272 12
Publisher Tax ID	
Total	0.00 CAD

4. Permission to use the published figure in “Characterization of supported Cu-Zn/graphene aerogel catalyst for direct CO₂ hydrogenation to methanol: Effect of hydrothermal temperature on graphene aerogel synthesis”.

License Number	4851000064732
License date	Jun 16, 2020
Licensed Content Publisher	Elsevier
Licensed Content Publication	Catalysis Today
Licensed Content Title	Characterization of supported Cu-Zn/graphene aerogel catalyst for direct CO ₂ hydrogenation to methanol: Effect of hydrothermal temperature on graphene aerogel synthesis
Licensed Content Author	Varisara Deerattrakul, Pralachoak Puengampholsrisook, Wanwisa Limphirat, Paisan Kongkachuichay
Licensed Content Date	Sep 15, 2018
Licensed Content Volume	314
Licensed Content Issue	n/a
Licensed Content Pages	10
Type of Use	reuse in a thesis/dissertation
Portion	figures/tables/illustrations
Number of figures/tables/illustrations	1
Format	print
Are you the author of this Elsevier article?	No
Will you be translating?	No
Title	A Study of Carbon Dioxide Catalytic Activation for Its Conversion to Value-added Products
Institution name	University of Saskatchewan
Expected presentation date	Sep 2020
Portions	Figure 1
Requestor Location	Ms. Jinglin Gao 57 Campus Dr Saskatoon, SK S7N 5A9 Canada Attn: Ms. Jinglin Gao GB 494 6272 12
Publisher Tax ID	
Total	0.00 CAD

5. Permission to use the published figure in “Influence of reduction time of catalyst on methanol synthesis via CO₂ hydrogenation using Cu–Zn/N-rGO investigated by in situ XANES’.

License Number	4851000384218
License date	Jun 16, 2020
Licensed Content Publisher	Elsevier
Licensed Content Publication	Journal of the Taiwan Institute of Chemical Engineers
Licensed Content Title	Influence of reduction time of catalyst on methanol synthesis via CO ₂ hydrogenation using Cu–Zn/N-rGO investigated by in situ XANES
Licensed Content Author	Varisara Deerattrakul, Wanwisa Limphirat, Paisan Kongkachuichay
Licensed Content Date	Nov 1, 2017
Licensed Content Volume	80
Licensed Content Issue	n/a
Licensed Content Pages	8
Type of Use	reuse in a thesis/dissertation
Portion	figures/tables/illustrations
Number of figures/tables/illustrations	1
Format	print
Are you the author of this Elsevier article?	No
Will you be translating?	No
Title	A Study of Carbon Dioxide Catalytic Activation for Its Conversion to Value-added Products
Institution name	University of Saskatchewan
Expected presentation date	Sep 2020
Portions	Figure 1,2
Requestor Location	Ms. Jinglin Gao 57 Campus Dr Saskatoon, SK S7N 5A9 Canada Attn: Ms. Jinglin Gao GB 494 6272 12
Publisher Tax ID	
Total	0.00 CAD

6. Permission to use the published figure in “Catalyst Design with Atomic Layer Deposition”.



Dear Dr. Gao,

Your permission requested is granted and there is no fee for this reuse. In your planned reuse, you must cite the ACS article as the source, add this direct link <https://pubs.acs.org/doi/abs/10.1021/cs501862h> and include a notice to readers that further permissions related to the material excerpted should be directed to the ACS.

If you need further assistance, please let me know.

Sincerely,
Simran Mehra
ACS Publications Support
Customer Services & Information
Website: <https://help.acs.org/>

Incident Information:

Incident #: 3613373
Date Created: 2020-06-17T03:25:03
Priority: 3
Customer: Jinglin Gao,
Title: Asking permission to use published material
Description: Hello,

This is Jinglin Gao, from University of Saskatchewan. I would like to use a figure in the article "

Catalyst Design with Atomic Layer Deposition" published in ACS, <https://pubs-acscs.org/cyber.usask.ca/doi/abs/10.1021/cs501862h>.

The figure number is Figure 2 which I would like to use in my thesis "A Study of Carbon Dioxide Catalytic Activation for Its Conversion to Value-added Products". May I have the permission, please?

Thank you
Regards
Jinglin

Jinglin Gao
Department of Chemical and Biological Engineering
University of Saskatchewan
Tel. (306)261-0063

Room 1C142 Engineering Building
57 Campus Drive
Saskatoon, SK, CANADA S7N 5A9

7. Permission to use the published figures in “Effect of spinel inversion and metal-support interaction on the site activity of Mg-Al-O_x supported Co catalyst for CO₂ reforming of CH₄”.

License Number	4852650255725
License date	Jun 19, 2020
Licensed Content Publisher	Elsevier
Licensed Content Publication	Journal of CO2 Utilization
Licensed Content Title	Effect of spinel inversion and metal-support interaction on the site activity of Mg-Al-O _x supported Co catalyst for CO ₂ reforming of CH ₄
Licensed Content Author	Wahab O. Alabi,Kazeem O. Sulaiman,Hui Wang,Yongfeng Hu,Christian Patzig
Licensed Content Date	Apr 1, 2020
Licensed Content Volume	37
Licensed Content Issue	n/a
Licensed Content Pages	8
Type of Use	reuse in a thesis/dissertation
Portion	figures/tables/illustrations
Number of figures/tables/illustrations	4
Format	print
Are you the author of this Elsevier article?	No
Will you be translating?	No
Title	A Study of Carbon Dioxide Catalytic Activation for Its Conversion to Value-added Products
Institution name	University of Saskatchewan
Expected presentation date	Sep 2020
Portions	Figure 4,5
Requestor Location	Ms. Jinglin Gao 57 Campus Dr Saskatoon, SK S7N 5A9 Canada Attn: Ms. Jinglin Gao GB 494 6272 12
Publisher Tax ID	
Total	0.00 CAD